Fermilab

FERMILAB-THESIS-1996-16

Probing Hadroproduction Processes with Charm Meson Pairs from 500 GeV π^- Interactions

by

Judy Leslie

B.A. (Carleton College, Northfield, MN) 1989

A dissertation submitted in partial satisfaction of the
requirements for the degree of
Doctor of Philosophy

in

Physics

in the

GRADUATE DIVISION
of the
UNIVERSITY of CALIFORNIA at SANTA CRUZ

Committee in charge:

Professor Patricia Burchat, Chair
Professor Howard Haber
Professor Abe Seiden

1996

The dissertation of Judy Leslie is approved:

Chair Date

Date

Date

University of California at Santa Cruz

1996

Probing Hadroproduction Processes with Charm Meson Pairs from 500 GeV π^- Interactions

by
Judy Leslie

Abstract

Probing Hadroproduction Processes
with
Charm Meson Pairs
from
500 GeV π^- Interactions

by

Judy Leslie
Doctor of Philosophy in Physics

University of California at Santa Cruz

Professor Patricia Burchat, Chair

We have fully reconstructed approximately 800 $D\overline{D}$ events from data gathered by the fixed-target hadroproduction experiment E791 at Fermi National Accelerator Laboratory — the largest sample of charm-pair events collected to date. We find slight correlations between the D and $\overline{D}$ longitudinal momenta and between the amplitudes of the transverse momenta. As with previous charm-pair experiments, we find significant correlations between the directions of the D and $\overline{D}$ mesons in the plane transverse to the beam axis. We also find that the difference between the D and $\overline{D}$ azimuthal angles, $\Delta\phi$, is strongly correlated to the scalar sum of the squares of the transverse momenta, Σp_t^2. The larger Σp_t^2 is, the more peaked at 180° the $\Delta\phi$ distribution is. In a leading-order perturbative QCD calculation, the charm and anti-charm particle are produced back-to-back in the plane transverse to the beam axis. Hence, at leading-order, the $\Delta\phi$ distribution is a delta function at $\Delta\phi = 180°$. As the energy scale of the partonic hard-scattering that produces the charm pair increases (*i.e.*, as Σp_t^2 increases), we expect higher-order corrections to play a smaller role and, consequently, we expect the leading-order prediction to become more accurate.

We compare all measured charm-pair distributions to predictions from the fully differential next-to-leading calculation as well as to prediction from the PYTHIA/JETSET Monte Carlo event generator. Due to the smallness of the charm quark mass, the theoretical

uncertainties are large and preclude a quantitative comparison between theory and data.

Professor Patricia Burchat
Dissertation Committee Chair

Contents

List of Figures **v**

List of Tables **xiii**

1 Introduction and Motivation **1**
1.1 Charm Hadroproduction: A Theoretical Framework 2
1.1.1 Leading Order Prediction 3
1.1.2 Higher-Order Perturbative Corrections 5
1.1.3 Intrinsic Transverse Momenta 6
1.1.4 Hadronization 7
1.2 Theoretical Predictions for Charm-Pair Distributions 14

2 The E791 Experiment **32**
2.1 The Beam 32
2.2 The Target 33
2.3 The Spectrometer 34
2.3.1 Tracking the π^- Beam 35
2.3.2 Vertexing 35
2.3.3 Tracking and Determining the Momenta of Charged Particles 36
2.3.4 Identifying particles 37
2.4 Data Acquisition 38
2.5 Data Processing 39

3 Event Selection **42**
3.1 Philosophy and Methodology 42
3.1.1 Candidate-Driven Approach 42
3.1.2 Parallel Search Algorithm 43
3.1.3 Iterative Optimization Procedure 44
3.1.4 Comparison with Other Approaches to Signal Optimization 48
3.2 Highlights of the Event Selection Procedure 49
3.2.1 Definition of Discrimination Variables 49
3.2.2 Preliminary Selection Criteria 50
3.2.3 First Iteration Results 54
3.3 Final Selection Criteria 56

4 Data Analysis **68**
4.1 Determining Yields and Significances 68
4.1.1 Normalized Mass 68
4.1.2 Binned Method for Background Subtraction 72
4.1.3 Unbinned Maximum Likelihood Fit 74
4.2 Acceptance and Smearing Corrections 75
4.2.1 One-Variable Case 78
4.2.2 Two-Variable Toy Model 81
4.2.3 From the Two-Variable Toy Model to Eight-Variable Reality 83

5 Results and Conclusions **98**
5.1 Single-Charm Predictions 99
5.2 Two-Dimensional Distributions 104
5.3 Comparisons with Theory 109
5.4 Asymmetries Among the Four Types of $D\overline{D}$ Pairs 118
5.5 Conclusions 125

Bibliography **127**

List of Figures

1.1 Feynman diagrams that contribute to the leading order perturbative QCD calculation of the $c\overline{c}$ cross section. 4

1.2 A sample of the Feynman diagrams that contribute to the next-to-leading order perturbative QCD calculation of the $c\overline{c}$ cross section. 6

1.3 Recent results from an E791 analysis for the function $A(x_F) = \frac{\sigma_{D^-} - \sigma_{D^+}}{\sigma_{D^-} + \sigma_{D^+}}$, showing significant asymmetries between the production of inclusive D^- and D^+ mesons. The next-to-leading order perturbative QCD prediction includes no hadronization mechanism; the PYTHIA/JETSET predictions include a final-state coalescence mechanism; and the Vogt-Brodsky prediction includes an initial-state coalescence mechanism. 8

1.4 Scatter plots, y_c versus $y_{\overline{c}}$ and y_D versus $y_{\overline{D}}$, from 100,000 PYTHIA/JETSET $D\overline{D}$ events, showing the "forward-backward" correlation introduced by the PYTHIA/JETSET hadronization model. As discussed in Chapter 4, we are only able to reconstruct $D\overline{D}$ events in the region $-0.5 < y_{D,\overline{D}} < 2.5$. 10

1.5 Common fragmentation functions: The PYTHIA/JETSET default for the hadronization of light quarks (LUND) for two values of $m_t \equiv \sqrt{M^2 + p_{x_s}^2 + p_{y_s}^2}$; the PYTHIA/JETSET default for heavy quarks (Bowler); and, lastly, the function commonly used to analyze e^+e^- data (Peterson), where $\epsilon = 0.135$ is derived from fits to CLEO and ARGUS D^0 data[19, 20]. See Eqs. 1.4-1.6. 12

1.6 Comparison of the gluon distribution functions for Sets (1) through (4), defined in Table 1.2. The pion and nucleon functions for each set are obtained from PDFLIB after imposing the constraint $\sqrt{x_\pi x_N} \geq \frac{2m_c}{E_{CM}}$, where E_{CM} is the center-of-mass energy of the colliding hadrons. 21

1.7 Sensitivity of single-charm and charm-pair distributions to higher-order perturbative corrections. The leading-order (LO) and next-to-leading order (NLO) distributions are obtained from the HVQMNR generator; the parton-shower (PS) distributions from the PYTHIA/JETSET generator. Table 1.3 shows the settings used for each set of distributions. 26

1.8 Sensitivity of single-charm and charm-pair distributions to variations in the mass of the charm quark. All distributions are obtained from HVQMNR next-to-leading order calculations using the default values for all parameters — except for m_c (see Table 1.3). 27

1.9 Sensitivity of single-charm and charm-pair distributions to variations in the parton distribution functions. Sets (1) through (4) are defined in Table 1.2. All distributions are obtained from HVQMNR next-to-leading order calculations using the default values for all parameters — except for the parton distribution functions (see Table 1.3). 28
1.10 Sensitivity of single-charm and charm-pair distributions to variations in the factorization and renormalization scales. All distributions are obtained using HVQMNR next-to-leading order calculation. Equation 1.7 defines the energy scale Q. Rather than using the default set of parton distribution functions, we use the GRV functions, which are evolved down to $\mu_0^2 = 0.3$ GeV^2. See Tables 1.2 and 1.3. 29
1.11 Sensitivity of the single-charm and charm-pair distributions to the parton shower evolution, the addition of intrinsic transverse momentum, and the hadronization process. All distribution are obtained using the PYTHIA/JETSET event generator. The **solid** distributions include all three effects; the dashed distributions include *only* the parton shower evolution: the dotted distributions include *only* intrinsic transverse momentum; the solid distributions include *only* hadronization. See Table 1.3 30
1.12 Sensitivity of single-charm and charm-pair distributions to variations in the amount of intrinsic transverse momenta added to the hard-scattering partons. All distributions are obtained using PYTHIA/JETSET event generator, using default settings for all parameters except σ_{k_t} (see Table 1.3). 31

2.1 The E791 Tagged Photon Spectrometer 34
2.2 The E791 data-processing scheme, beginning with 24,000 raw data tapes and ending with approximately 30 different analyses processing 1 to 10 tapes each. See Table 2.1. 40

3.1 An illustration of how selection criteria of the form V^n and/or $V^{\overline{n}} > p$, which are symmetric between the two D candidates, can lead to cuts of the form ($\vec{V}^{MAX} > \vec{h}$ and $\vec{V}^{MIN} > \vec{l}$). 44
3.2 Scatter plot of $M^{K^-n\pi}$ versus $M^{K^+n\pi}$ for the final data sample of $D\overline{D}$ candidates. The plot contains four types of events: combinatoric background events spread over the entire region; D- and $\overline{D}$-ridge events, containing one real D and one fake D meson; and real $D\overline{D}$ events in the central signal region. 45
3.3 Results from the first iteration of optimizing 2-pronged single-charm selection criteria: (a) $N'_{MC}/\sqrt{N'_{BK}}$ (given $\Delta N_{MC}/N_{MC} \approx 0.05$) vs. Cut Variable, indicating that PTDK is the best cut variable for the first iteration. The constraint $\Delta N_{MC}/N_{MC} \approx 0.05$ determines the value at which the cut is made. (b) PTDK distributions, normalized to the same area, for both the Monte Carlo signal events and the weighted and unweighted background events (c) Scatter plot of PTDK versus the reconstructed mass of the 2-prong D meson from the Monte Carlo sample, indicating that PTDK is not significantly correlated to the mass of the D meson for PTDK < 0.45 GeV^2. 53

3.4 Results from the first iteration of optimizing 3-3 pronged charm-pair selection criteria: A plot of $N'_{MC}/\sqrt{N'_{BK}}$ (given $\Delta N_{MC}/N_{MC} \approx 0.05$) versus cut variable, indicating that an or-type cut on the variable SDZ is the best first iteration cut. The constraint $\Delta N_{MC}/N_{MC} \approx 0.05$ determines at what value the cut is made. The Monte Carlo and data samples are normalized such that $N_{MC}/\sqrt{N_{BK}} = 0.01$ before any cuts are applied. Open circles show results for or-type cuts and solid circles for and-type cuts. 55

3.5 Monte Carlo (signal) and data (background) SDZ distributions for the 3-3 pronged candidates. (a) Single-charm SDZ distributions normalized to unit area. (b) $\mathrm{SDZ_D}$ versus $\mathrm{SDZ_{\overline{D}}}$ for Monte Carlo signal events. (c) $\mathrm{SDZ_D}$ versus $\mathrm{SDZ_{\overline{D}}}$ for background events from data. The boxes in the lower left-hand corner of (b) and (c) show the candidates that are eliminated by the cut ($\mathrm{SDZ_3}$ or $\mathrm{SDZ_{\overline{3}}}$) > 10. 55

3.6 Results from the first iteration of optimizing 2-3 pronged charm-pair selection criteria. Each plot shows $N'_{MC}/\sqrt{N'_{BK}}$ (given $\Delta N_{MC}/N_{MC} \approx 0.05$) versus the 3-pronged cut variables. And each plot is associated with a particular 2-pronged cut variable. Open circles show results for or-type cuts and solid circles for and-type cuts. The left-most open circle in the bottom left-hand plot, for example, indicates that applying the cut ($\mathrm{TAU_2} > p$ or $\mathrm{SDZ_3} > q$) brings the significance, $N'_{MC}/\sqrt{N'_{BK}}$, to approximately 0.025. The values of p and q, not shown in the plot, meet the requirement that $\Delta N_{MC}/N_{MC} \approx 0.05$. The Monte Carlo and data samples are normalized such that $N_{MC}/\sqrt{N_{BK}} = 0.01$ before any cuts are applied. 57

3.7 Normalized distributions of cut variables for the Monte Carlo sample (solid), the background-subtracted data sample (dashed), and the combinatoric background sample (dotted) after all selection criteria have been applied. The distributions of both D candidates from each $D\overline{D}$ candidate are added. The cut variables are defined in Section 3.2.1. 62

3.8 Normalized distributions of cut variables for the Monte Carlo sample (solid), the background-subtracted data sample (dashed), and the combinatoric background sample (dotted) after all selection criteria have been applied. The distributions of both D candidates from each $D\overline{D}$ candidate are added. The cut variables are defined in Section 3.2.1. 63

3.9 Normalized distributions of cut variables for the Monte Carlo sample (solid), the background-subtracted data sample (dashed), and the combinatoric background sample (dotted) after all selection criteria have been applied. The distributions of both D candidates from each $D\overline{D}$ candidate are added. The cut variables are defined in Section 3.2.1. 64

3.10 The distribution of selection criteria for the cut variables DIP, SDIP, PTB, SDZ, TAU, and STRG. The x-axes indicate the value at which a cut is made; the y-axes indicate on what type of candidate a cut is made. For example, the y label "4-2" indicates that a cut is made on the 4-pronged candidates from the 4-2 pronged pairs. The symbols on the plots indicate whether the cut is an and-type (solid circle), an or-type (open circle), or a single-charm (star) cut. The cut variables are defined in Section 3.2.1. 65
3.11 The distribution of selection criteria for the cut variables SPISO, SPRAT, SSISO and SSRAT. The x-axes indicate the value at which a cut is made; the y-axes indicate on what type of candidate a cut is made. For example, the y label "4-2" indicates that a cut is made on the 4-pronged candidates from the 4-2 pronged pairs. The symbols on the plots indicate whether the cut is an and-type (solid circle), an or-type (open circle), or a single-charm (star) cut. The cut variables are defined in Section 3.2.1. 66
3.12 The distribution of selection criteria for the cut variables KPRB, CHIS, and PTDK. The x-axes indicate the value at which a cut is made; the y-axes indicate on what type of candidate a cut is made. For example, the y label "4-2" indicates that a cut is made on the 4-pronged candidates from the 4-2 pronged pairs. The symbols on the plots indicate whether the cut is an and-type (solid circle), an or-type (open circle), or a single-charm (star) cut. The cut variables are defined in Section 3.2.1. 67

4.1 One-dimensional measured mass distributions from the final data sample with fits to a Gaussian plus linear distribution superimposed. The parameters of the Gaussians extracted from the fits are given in Table 4.1. 69
4.2 One-dimensional normalized mass distributions from the final data sample with fits to a Gaussian plus linear distribution superimposed. The parameters of the Gaussians extracted from the fits are given in Table 4.3. 71
4.3 Distribution of normalized masses for the final sample of $D\overline{D}$ candidates. (The length, not the area, of the boxes in each bin is proportional to the number of events in the bin.) 73
4.4 The function $N_{D\overline{D}} f(\vec{z};\hat{\alpha})$ that maximizes the likelihood function for the final sample of $D\overline{D}$ candidates shown in Figures 3.2 and 4.3. 76
4.5 One-dimensional projections of charm-pair normalized mass distributions for both the maximum-likelihood fit function (dashed histogram) and the final data sample (solid histogram). The top plots are projections of the full data sample shown in Figure 3.2. The bottom plots include only the data from the $\overline{D}$-ridge region (left plot) and the D-ridge region (right plot). 77

4.6 (a) Normalized Monte Carlo distributions of the invariant mass of $D\overline{D}$ pairs: the original generated distribution (P^{MC}), the generated distribution for accepted $D\overline{D}$ events (Q^{MC}), and the reconstructed distribution for accepted $D\overline{D}$ events (R^{MC}). (b) The acceptance as a function of the invariant mass (arbitrary vertical scale). (c) Reconstructed $M_{D\overline{D}}$ vs. generated $M_{D\overline{D}}$ for the subset of Monte Carlo events that survive all selection criteria. (d) The smearing matrix ($\times$ 100) for the invariant mass, obtained from (c) by normalizing each column to 1. 79

4.7 Distributions of the invariant mass of the $D\overline{D}$ pair from the final data sample: uncorrected distribution (solid circle), acceptance corrected distribution (open circle), acceptance and smearing corrected distribution (triangle). . . 80

4.8 Two-variable toy model discussed in Section 4.2.2. (a) Monte Carlo probability distribution function for parameters x and y. (b) Acceptance function for parameters x and y. 82

4.9 A^{MC}, defined in Eq. 4.7, as a function of rapidity. The meaning of the solid, dashed, and dotted curves is given in the table below the figures. All distributions are normalized to the same area. 87

4.10 A^{MC}, defined in Eq. 4.7, as a function of transverse momentum. The meaning of the solid, dashed, and dotted curves is given in the table below the figures. All distributions are normalized to the same area. 88

4.11 A^{MC}, defined in Eq. 4.7, as a function of azimuthal angle. The meaning of the solid, dashed, and dotted curves is given in the table below the figures. All distributions are normalized to the same area. 89

4.12 A^{MC}, defined in Eq. 4.7, as a function of the number of decay tracks. The meaning of the solid, dashed, and dotted curves is given in the table below the figures. All distributions are normalized to the same area. 90

4.13 The nine $A^{MC}(y_D, y_{\overline{D}};\ n_D, n_{\overline{D}})$ projections (one for each $n_D n_{\overline{D}}$ combination). Each projection is normalized to the same area and plotted on the same scale. 92

4.14 Using the estimates for the $c^D_{n_D}(y_D)$ and $c^{\overline{D}}_{n_{\overline{D}}}(y_{\overline{D}})$ distributions in Figure 4.15, we construct nine two-dimensional functions: $c^D_{n_D}(y_D)c^{\overline{D}}_{n_{\overline{D}}}(y_{\overline{D}})$, one for each $n_D n_{\overline{D}}$ combination. Comparing these distributions to the nine distributions in Figure 1.13 confirms that $A^{MC}(y_D, y_{\overline{D}};\ n_D, n_{\overline{D}})$ approximately factorizes. 93

4.15 Estimates for $c^D_{n_D}(y_D)$ and $c^{\overline{D}}_{n_{\overline{D}}}(y_{\overline{D}})$ obtained by summing and integrating over the two-dimensional projection $A^{MC}(y_D, y_{\overline{D}};\ n_D, n_{\overline{D}})$. 94

4.16 (a) The distribution of weights, $w \propto \frac{1}{A(\vec{x})B(D)B(\overline{D})}$, for the final sample of $D\overline{D}$ candidates. The mean of the distribution, by construction, is one; the standard deviation about the mean is 1.3, with the largest weight (not shown) at 23. (b) The distribution of the fractional errors on the weights, with a mean of 12%. 96

5.1 Single-charm distributions for the variables x_F, y, p_t^2 and ϕ, obtained from summing the D and $\overline{D}$ distributions from our signal $D\overline{D}$ events. The total number of signal D mesons, N_D, is simply twice the number of signal $D\overline{D}$ events N_s. 100
5.2 Charm-pair distributions for $\Delta x_F = x_{F,D} - x_{F,\overline{D}}$ and $\Sigma x_F = x_{F,D} + x_{F,\overline{D}}$. The single-charm predictions for Δx_F and Σx_F are defined in Eqs. 5.1 and 5.2. 102
5.3 Charm-pair distributions for $\Delta y = y_D - y_{\overline{D}}$ and $\Sigma y = y_D + y_{\overline{D}}$. The single-charm predictions for Δy and Σy are defined in Eqs. 5.1 and 5.2. 102
5.4 Charm-pair distributions for $|\Delta p_t^2| = |p_{t,D}^2 - p_{t,\overline{D}}^2|$ and $\Sigma p_t^2 = p_{t,D}^2 + p_{t,\overline{D}}^2$. The single-charm predictions for Δp_t^2 and Σp_t^2 are defined in Eqs. 5.1 and 5.2. . 103
5.5 Charm-pair distributions for $\Delta\phi =$ (minimum of $|\phi_D - \phi_{\overline{D}}|$ and $360° - |\phi_D - \phi_{\overline{D}}|$) and $\Sigma\phi = (\phi_D + \phi_{\overline{D}}$ modulo $360°)$. The single-charm predictions for $\Delta\phi$ and $\Sigma\phi$ are defined in Eqs. 5.1 and 5.2. 104
5.6 Charm-pair distributions for $p_{t,D\overline{D}}^2$ and $M_{D\overline{D}}$. The solid histograms show the single-charm predictions. The dashed $p_{t,D\overline{D}}^2$ histogram assumes that $x_{F,D}$ and $x_{F,\overline{D}}$ are uncorrelated and that $p_{t,D}^2$ and $p_{t,\overline{D}}^2$ are uncorrelated, but that ϕD and $\phi\overline{D}$ are correlated as shown in Figure 5.5. 105
5.7 (a) Number of acceptance-corrected $D\overline{D}$ signal events dN_s found in nine ($x_{F,D}$, $x_{F,\overline{D}}$) bins. (b) $x_{F,D}$ distribution $N_i(dN_s/dx_{F,D})$ for each $x_{F,\overline{D}}$ bin, where N_i is chosen such that the integral over $x_{F,D}$ equals one. (c) $x_{F,\overline{D}}$ distribution for each $x_{F,D}$ bin. (d)-(f) $x_{F,D}$ ($x_{F,\overline{D}}$) distribution for the first, second and third $x_{F,\overline{D}}$ ($x_{F,D}$) bins, respectively. The open symbols show the x_D distributions; the closed symbols the $x_{\overline{D}}$ distributions. 106
5.8 (a) Number of acceptance-corrected $D\overline{D}$ signal events dN_s found in nine (y_D, $y_{\overline{D}}$) bins. (b) y_D distribution $N_i(dN_s/dy_D)$ for each $y_{\overline{D}}$ bin, where N_i is chosen such that the integral over y_D equals one. (c) $y_{\overline{D}}$ distribution for each y_D bin. (d)-(f) y_D ($y_{\overline{D}}$) distribution for the first, second and third $y_{\overline{D}}$ (y_D) bins, respectively. 107
5.9 (a) Number of acceptance-corrected $D\overline{D}$ signal events dN_s found in nine ($p_{t,D}^2$, $p_{t,\overline{D}}^2$) bins. (b) $p_{t,D}^2$ distribution $N_i(dN_s/dp_{t,D}^2)$ for each $p_{t,\overline{D}}^2$ bin, where N_i is chosen such that the integral over $p_{t,D}^2$ equals one. (c) $p_{t,\overline{D}}^2$ distribution for each $p_{t,D}^2$ bin. (d)-(f) $p_{t,D}^2$ ($p_{t,\overline{D}}^2$) distribution for the first, second and third $p_{t,\overline{D}}^2$ ($p_{t,D}^2$) bins, respectively. 107
5.10 (a) Number of acceptance-corrected $D\overline{D}$ signal events dN_s found in nine ($\Delta\phi$, Σp_t^2) bins. (b) $\Delta\phi$ distribution $N_i(dN_s/d\Delta\phi)$ for each Σp_t^2 bin, where N_i is chosen such that the integral over $\Delta\phi$ equals one. (c) Σp_t^2 distribution for each $\Delta\phi$ bin. (d) Number of acceptance-corrected $D\overline{D}$ signal events dN_s found in 9 ($\Delta\phi$,$|\Delta p_t^2|$) bins. (e) $\Delta\phi$ distribution for each $|\Delta p_t^2|$ bin. (f) $|\Delta p_t^2|$ distribution for each $\Delta\phi$ bin. 108

5.11 Experimental single-charm distributions for x_F, y, p_t^2 and ϕ compared to three sets of theoretical predictions: the next-to-leading order perturbative QCD prediction, the PYTHIA/JETSET charm quark prediction, and the PYTHIA/JETSET D meson prediction. All distributions are obtained from summing the charm and anti-charm distributions from charm-pair events. . 110
5.12 Experimental Δx_F and Σx_F distributions compared to three sets of theoretical predictions: the next-to-leading order perturbative QCD prediction, the PYTHIA/JETSET $c\overline{c}$ prediction, and the PYTHIA/JETSET $D\overline{D}$ prediction. 111
5.13 Experimental Δy and Σy distributions compared to three sets of theoretical predictions: the next-to-leading order perturbative QCD prediction, the PYTHIA/JETSET $c\overline{c}$ prediction, and the PYTHIA/JETSET $D\overline{D}$ prediction. . 112
5.14 PYTHIA/JETSET $D\overline{D}$ prediction for Δy compared to the PYTHIA/JETSET single-charm prediction, which is obtained by assuming that the D and $\overline{D}$ mesons are completely uncorrelated (See Eq. 5.4). 112
5.15 Experimental $|\Delta p_t^2|$ and Σp_t^2 distributions compared to three sets of theoretical predictions: the next-to-leading order perturbative QCD prediction, the PYTHIA/JETSET $c\overline{c}$ prediction, and the PYTHIA/JETSET $D\overline{D}$ prediction. 113
5.16 Experimental $\Delta\phi$ and $\Sigma\phi$ distributions compared to three sets of theoretical predictions: the next-to-leading order perturbative QCD prediction, the PYTHIA/JETSET $c\overline{c}$ prediction, and the PYTHIA/JETSET $D\overline{D}$ prediction. 113
5.17 Experimental $p^2_{t,D\overline{D}}$ and $M_{t,D\overline{D}}$ distributions compared to three sets of theoretical predictions: the next-to-leading order perturbative QCD prediction, the PYTHIA/JETSET $c\overline{c}$ prediction, and the PYTHIA/JETSET $D\overline{D}$ prediction. 114
5.18 (a) The NLO perturbative QCD prediction for the number of $c\overline{c}$ events in 9 ($x_{F,D}$,$x_{F,\overline{D}}$) bins, normalized such that the number of generated NLO events equals the number of acceptance-corrected $D\overline{D}$ signal events. (b) Experimental $x_{F,D}$ distribution for each $x_{F,\overline{D}}$ bin compared to the NLO perturbative QCD predictions. Each $x_{F,D}$ distribution is normalized such that the integral over $x_{F,D}$ equals one. (c) Same as (b) for the $x_{F,\overline{D}}$ distributions. (d)-(f) Same as (a)-(c) for the PYTHIA/JETSET $c\overline{c}$ prediction. (g)-(i) Same as (a)-(c) for the PYTHIA/JETSET $D\overline{D}$ prediction. 116
5.19 (a) The NLO perturbative QCD prediction for the number of $c\overline{c}$ events in 9 (y_D,$y_{\overline{D}}$) bins, normalized such that the number of generated NLO events equals the number of acceptance-corrected $D\overline{D}$ signal events. (b) Experimental y_D distribution for each $y_{\overline{D}}$ bin compared to the NLO perturbative QCD predictions. Each y_D distribution is normalized such that the integral over y_D equals one. (c) Same as (b) for the $y_{\overline{D}}$ distributions. (d)-(f) Same as (a)-(c) for the PYTHIA/JETSET $c\overline{c}$ prediction. (g)-(i) Same as (a)-(c) for the PYTHIA/JETSET $D\overline{D}$ prediction. 117

5.20 (a) The NLO perturbative QCD prediction for the number of $c\overline{c}$ events in 9 ($p^2_{t,D}$,$p^2_{t,\overline{D}}$) bins, normalized such that the number of generated NLO events equals the number of acceptance-corrected $D\overline{D}$ signal events. (b) Experimental $p^2_{t,D}$ distribution for each $p^2_{t,\overline{D}}$ bin compared to the NLO perturbative QCD predictions. Each $p^2_{t,D}$ distribution is normalized such that the integral over $p^2_{t,D}$ equals one. (c) Same as (b) for the $p^2_{t,\overline{D}}$ distributions. (d)-(f) Same as (a)-(c) for the PYTHIA/JETSET $c\overline{c}$ prediction. (g)-(i) Same as (a)-(c) for the PYTHIA/JETSET $D\overline{D}$ prediction. 118

5.21 (a) The NLO perturbative QCD prediction for the number of $c\overline{c}$ events in 9 ($\Delta\phi$,Σp^2_t) bins, normalized such that the number of generated NLO events equals the number of acceptance-corrected $D\overline{D}$ signal events. (b) Experimental $\Delta\phi$ distribution for each Σp^2_t bin compared to the NLO perturbative QCD predictions. Each $\Delta\phi$ distribution is normalized such that the integral over $\Delta\phi$ equals one. (c) Same as (b) for the Σp^2_t distributions. (d)-(f) Same as (a)-(c) for the PYTHIA/JETSET $c\overline{c}$ prediction. (g)-(i) Same as (a)-(c) for the PYTHIA/JETSET $D\overline{D}$ prediction. 119

5.22 (a) The NLO perturbative QCD prediction for the number of $c\overline{c}$ events in 9 ($\Delta\phi$,$|\Delta p^2_t|$) bins, normalized such that the number of generated NLO events equals the number of acceptance-corrected $D\overline{D}$ signal events. (b) Experimental $\Delta\phi$ distribution for each $|\Delta p^2_t|$ bin compared to the NLO perturbative QCD predictions. Each $\Delta\phi$ distribution is normalized such that the integral over $\Delta\phi$ equals one. (c) Same as (b) for the Δp^2_t distributions. (d)-(f) Same as (a)-(c) for the PYTHIA/JETSET $c\overline{c}$ prediction. (g)-(i) Same as (a)-(c) for the PYTHIA/JETSET $D\overline{D}$ prediction. 120

5.23 Several 2-dimensional projections onto the (P_{nn}, P_{nc}, P_{cn}, P_{cc}, f) parameter space, showing the regions that are one (solid line), two (dashed), and three (dotted) standard deviations from our experimental results. The default PYTHIA/JETSET prediction and the no-coalescence prediction are also shown. 122

5.24 PYTHIA/JETSET prediction for the (y_D, $y_{\overline{D}}$) distribution for each of the four types of $D\overline{D}$ pairs. The dashed lines help define the asymmetry functions $A_v(i)$ (Eq. 5.5) which are shown, for both theory and data, in Fig. 5.25. . . 124

5.25 The asymmetry function $A_v(i) = \frac{N_i(v>a)-N_i(v<a)}{N_i(v<a)+N_i(v<a)}$, where i =($D^0\overline{D^0}$, D^0D^-, $D^+\overline{D^0}$,D^+D^-) and N_i is the number of signal $D\overline{D}$ events of type i, for (v, a) = (Δy, 0), (Σy, 1.2), (y_D, 0.6), and ($y_{\overline{D}}$, 0.6). All functions are obtained after excluding any PYTHIA/JETSET $D\overline{D}$ events and $D\overline{D}$ candidates from data in which the center-of-mass rapidity of either the D or $\overline{D}$ is less than -0.5 or greater than 2.5. 125

List of Tables

1.1 A summary of fixed-target charm hadroproduction experiments, including the number of partially and fully reconstructed single-charm and charm-pair events for each experiment. 2
1.2 The pairs of pion and nucleon parton distribution functions considered in this section, obtained from the CERN FORTRAN package PDFLIB. The functions have been extracted from fits to data assuming a fixed value of Λ_{QCD}; and the functions are undefined below the minimum scale μ_0 16
1.3 The settings used by the HVQMNR and PYTHIA/JETSET generators to obtain the single-charm and charm-pair distribution shown in Figures 1.7-1.12. The set of pion and nucleon parton distribution functions (PDF), labeled (1) through (5), are defined in Table 1.2. A "Y" indicates that parton showers (PS) are included in the PYTHIA/JETSET event generator; an "N" indicates that they are not included. 18

2.1 The number of different output streams, as well as the number of tapes and events per output, at each level in the E791 data-processing scheme. 39

3.1 Selection criteria applied to all D candidates before beginning the charm-pair optimization procedure. Variables are defined in Sec. 3.2.1. 54
3.2 Charm-pair selection criteria for $n-n$ pronged events. The entry "90" in the first row, for example, means all 4-4 pronged candidates must pass the cut ($\mathrm{DIP}_4 < 90\mu$m AND $\mathrm{DIP}_{\overline{4}} < 90\ \mu$m). Variables are defined in Section 3.2.1. 58
3.3 Charm-pair selection criteria for 2-3 pronged events. The third entry "1 OR 5.4" in the first row, for example, means all 2-3 pronged candidates must pass the cut ($\mathrm{PTB}_2 < 1\,\mathrm{GeV}$ OR $\mathrm{STRG}_3 > 5.4$). Variables are defined in Section 3.2.1. 59
3.4 Charm-pair selection criteria for 2-4 pronged events. The entry "0.18 OR 0.01" in the first row, for example, means all 2-4 pronged candidates must pass the cut ($\mathrm{KPRB}_2 > 0.18$ OR $\mathrm{SSRAT}_4 < 0.01$). Variables are defined in Section 3.2.1. 60

3.5 Charm-pair selection criteria for 3-4 pronged events. The entry "23 OR 0.4" in the first row, for example, means all 3-4 pronged candidates must pass the cut ($DIP_3 < 23$ μm OR $PTB_4 < 0.4$ GeV). Variables are defined in Section 3.2.1. 61

4.1 The parameters of the Gaussian extracted from the fits to the one-dimensional measured mass distributions from the final data sample shown in Figure 4.1 70
4.2 The sigma σ_{M_D}, in MeV, of the Gaussian extracted from the fits to the one-dimensional measured mass distributions from the final data sample. The means of the Gaussians are fixed to the values shown in Table 4.1. 70
4.3 The parameters of the Gaussian extracted from the fits to the one-dimensional normalized mass M_n distributions from the final data sample shown in Figure 4.2, where $M_n = (M - M_D)/\sigma_{M_D}$ and M_D and σ_{M_D} are taken from Tables 4.1 and 4.2, respectively. 70
4.4 Correlation coefficients $\rho(x_i, x_j) = V_{ij}/(\sigma_i \sigma_j)$ for the variables $((y, p_t, \phi, n)_D$, $(y, p_t, \phi, n)_{\overline{D}})$ from the original Monte Carlo sample of events. 85

5.1 The integrals, $\int_{v_{min}}^{v_{max}} P(v)dv$, for all single-charm and charm-pair acceptance-corrected distributions shown in Figures 5.1-5.6, showing the fraction of signal events within the domain $v_{min} < v < v_{max}$. 101
5.2 Experimental yields for the four types of $D\overline{D}$ pairs compared to predictions from the PYTHIA/JETSET event generator. Both experimental and theoretical yields are obtained after excluding any candidates in which the center-of-mass rapidity of either the D or $\overline{D}$ is less than -0.5 or greater than 2.5. 121

Acknowledgements

The shortest road ain't always the best.
Sometimes let a back road take you home.
Kate Wolf

Thanks to all those who guided me to and along this road and to all those who, now and again, guided me off the road.

To Pat for being a great friend and a great advisor. A brighter, more compassionate, more down-to-earth person could not exist.

To my family for still loving me even though I hardly ever call, I never write, and I never ever remember birthdays. I now have no excuse. To my mom for always simply assuming that I could and would do great things in my life. To my siblings for building my character.

To Johnny for always being so proud of my work in physics. For opening my eyes wider than ever before; wide enough to finally see myself.

To the physics faculty at Carleton College, especially Joel Weisberg and Bruce Thomas for being wonderful teachers and wonderful people. To Paul Wellstone for motivating me to quit school to work for ACORN.

To all the UCSC folks. To Judy, Marilyn, Georgia and Nora for putting up with me. Special thanks to Howie Haber, Tom Weiler, and Peter Young for some of my favorite classes. To Ron Ruby and his family for welcoming our R.V. in their driveway. To Nicolo and Alex for working long hours with me on problem sets, for sharing lots of pizza and laughs together. To John Hiser for making us play all that frisbee.

To all the E791 folks. To those Santa Cruz babes — Kathy, Renata, and Pauline — and that token Guy for simply being a great bunch of people to work, travel, and play with. To Jean Slaughter for many thoughtful and helpful words of wisdom. To Tom Carter for being... Tom Carter and a really wonderful friend.

To the staff at the Riviera Travelodge for all the tamales and Spanish lessons. I miss you all. To Bill, Kelly, and Gideon for being my family when I really, really needed one. To all the Single Payer folks for making sure I didn't take all this physics stuff too seriously. To the rest of my friends in this wonderful, loving town; and to those two who had the nerve to move to San Jose.

To Bruce for everything. Bread, love, movies, more love, more bread, bike rides, more movies. And to the rest of the crew: Athena, Kidney Bean (we miss you!), and Jagger for demanding food, walks, and warm bellies to lie on.

Chapter 1

Introduction and Motivation

The charm quark is the lightest of the heavy quarks. Because of its relatively *small* mass, charm particles are produced copiously at energies typical of fixed-target hadroproduction experiments. Because of its relatively *large* mass, one assumes that the large momentum-transfer processes responsible for producing $c\overline{c}$ pairs are calculable in perturbative quantum chromodynamics (QCD); one also assumes that there is no interference between these short-distance processes and the long-distance (non-perturbative) processes responsible for binding quarks and gluons into hadrons. The consequence of the charm quark being the lightest of the heavy quarks — more specifically, of having a mass that is not significantly larger than Λ_{QCD} — is that there are considerable uncertainties associated with these theoretical assumptions. Such large theoretical uncertainties combined with conflicting experimental results from early charm hadroproduction experiments have made systematic comparisons between theory and data difficult.

Recent experimental and theoretical progress, however, is encouraging. In the last decade, next-to-leading order calculations for the hadroproduction of heavy quarks have been developed by various authors. Most recently, a next-to-leading order calculation for the full differential cross section was presented by Mangano, Nason, Ridolfi (MNR)[1]. On the experimental front, the current generation of fixed-target experiments has reconstructed an unprecedented number of charm particles. A complete set of precise measurements is not yet available, but high statistics charm hadroproduction measurements from experiments WA92, E769, and E791 will continue to emerge in the next few years. A summary of charm hadroproduction experiments is shown in Table 1.1.

Typically, analyses use single-charm inclusive measurements, in which only one

Table 1.1: A summary of fixed-target charm hadroproduction experiments, including the number of partially and fully reconstructed single-charm and charm-pair events for each experiment.

Experiment		Beam [GeV]		Target	Single-Charm Full.	Single-Charm Part.	Charm-Pair Full.	Charm-Pair Part.	Charm-Pair Ref.
NA11	'82	175	π^-	Be	130				
NA27	'82	360	π^-	H_2		183	53[a]		[2]
	'84	400	p	H_2		425	233		[3]
E743	'85	800	p	H_2	33	148			
WA75		350	π^-	Emul.		288		102	[4]
NA32	'84	200	π^-,K,p	Si	170				
	'86	230	π^-	Cu	1300		20	557	[5, 6]
E653	'84-85	800	p	Emul.	146			35	[7]
	'87-88	600	π^-	Emul.	1000				
WA82	'87-89	340	π^-	Si,W,Cu					
	'88-89	370	p	Cu,W	3000				
E769	'87-88	250	π^-	Be,Al,Cu,W	4000				
WA92	'92-93	350	π^-	Cu	10,000			102[b]	[8]
E791	'91	500	π^-	Cu,Pt	200,000		791[c]		

[a] After the final selection criteria were applied, 12 fully reconstructed charm pairs remained.
[b] Represents 30% of the full data sample.
[c] Represents 90% of the full data sample.

charm particle in an event is reconstructed, to probe hadroproduction processes. Alternatively, analyses can reconstruct both the charm and anti-charm particle in the event. The advantage of the former approach is significantly higher statistics; the advantage of latter approach is more complete information about the hadroproduction process — specifically, information regarding the correlations between the charm and the anti-charm particle in a $c\overline{c}$ event. The focus of this dissertation is an analysis of approximately 800 fully reconstructed $D\overline{D}$ events from data gathered by the fixed-target hadroproduction experiment E791 at Fermi National Accelerator Laboratory. As shown in Table 1.1, this is the largest sample of fully reconstructed, hadroproduced charm-pair events collected to date.

1.1 Charm Hadroproduction: A Theoretical Framework

Our aim in this chapter is to determine how sensitive theoretical predictions are to variations in inputs such as the mass of the charm quark or the gluon distribution functions. In this section, we lay out the theoretical framework used to describe the hadroproduction of

charm pairs, focusing on the framework used by the following two packages: the FORTRAN program HVQMNR[9] which implements the MNR next-to-leading order perturbative QCD calculation, and the PYTHIA (Version 5.7) / JETSET (Version 7.4) Monte Carlo event generator[10]. In the following section, we examine predictions from these two packages using a wide range of theoretical assumptions.

Both packages use a perturbative QCD framework to obtain the differential cross section for producing a $c\overline{c}$ pair:

$$\mathrm{d}\sigma_{c\overline{c}} = \sum_{i,j} \int \mathrm{d}x_b \, \mathrm{d}x_t \, f_i^b(x_b, \mu_F) \, f_j^t(x_t, \mu_F) \, \mathrm{d}\hat{\sigma}_{ij}(x_b P_b, x_t P_t, p_c, p_{\overline{c}}, m_c, \mu_R), \qquad (1.1)$$

where

- P_b (P_t) is the momentum of the beam (target) in the center of mass of the colliding hadrons;
- x_b (x_t) is the fraction of P_b (P_t) carried by the hard scattering parton from the beam (target);
- f_i are the parton distribution functions, which give the number density of partons of type i with momentum xP, where the parton types are gluons, light quarks, and light anti-quarks; and, lastly,
- $\mathrm{d}\hat{\sigma}$ is the cross section for the two hard-scattering partons to produce a pair of charm quarks, each with mass m_c, and with 4-momenta p_c and $p_{\overline{c}}$.

The renormalization scales, μ_F and μ_R, are discussed below.

1.1.1 Leading Order Prediction

An examination of the leading-order perturbative QCD prediction for the $c\overline{c}$ cross section demonstrates why charm-pair distributions are particularly sensitive to higher order QCD effects. The gluon- and quark-fusion Feynman diagrams that contribute to the leading-order partonic cross section are shown in Figure 1.1. At fixed-target energies, the quark-fusion contribution is negligible. The leading-order charm and anti-charm quark are produced back-to-back in the center of mass of the two hard scattering partons; that is, the c and $\overline{c}$ momenta are completely correlated.

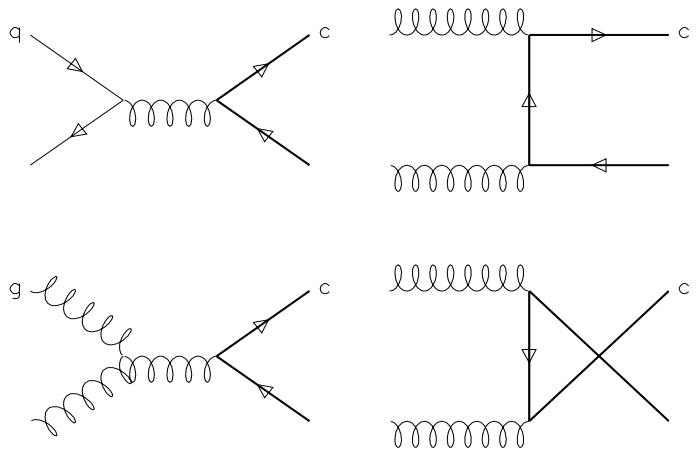

Figure 1.1: Feynman diagrams that contribute to the leading order perturbative QCD calculation of the $c\overline{c}$ cross section.

For each $c\overline{c}$ event, the partonic center-of-mass — which cannot be determined experimentally — is boosted with respect to the (known) hadronic center-of-mass along the beam axis. The amount of boost depends on the momentum fractions x_b and x_t, which are selected randomly from the gluon distribution functions f_g^b and f_g^t, respectively. Hence, the correlation between the c and $\overline{c}$ longitudinal momenta, even at leading order, is smeared. On the other hand, the correlation between the c and $\overline{c}$ momenta transverse to the beam axis is still perfect at leading order: $\vec{p}_{t,c} = -\vec{p}_{t,\overline{c}}$.

Typically, charm-pair analyses use the following two distributions to investigate correlations in the transverse degrees of freedom: $\Delta\phi$ — the minimum value between $|\phi_c - \phi_{\overline{c}}|$ and $360^\circ - |\phi_c - \phi_{\overline{c}}|$, where ϕ is the azimuthal angle of the charm quark with respect to the beam axis — and $p^2_{t,c\overline{c}} = |\vec{p}_{t,c} + \vec{p}_{t,\overline{c}}|^2$. The leading-order calculation predicts delta function distributions at $\Delta\phi = 180^\circ$ and at $p^2_{t,c\overline{c}} = 0$ GeV^2. These distributions, therefore, are optimally sensitive to higher-order effects.

To investigate correlations in the longitudinal degrees of freedom, charm-pair analyses can measure distributions for the variables $\Sigma x \equiv x_c + x_{\overline{c}}$ and $\Delta x \equiv x_c - x_{\overline{c}}$ where x_c is the longitudinal momentum of the charm quark in the hadronic center of mass divided by the center-of-mass beam momenta P_b. Charm-pair analyses have also used the rapidity distributions $\Sigma y \equiv y_c + y_{\overline{c}}$ and $\Delta y = y_c - y_{\overline{c}}$ where

$$y_c \equiv \left[\frac{1}{2}\ln\left(\frac{E_c + p_{z,c}}{E_c - p_{z,c}}\right)\right]_{CM}. \tag{1.2}$$

If the longitudinal momenta of the charm and anti-charm particles are completely uncorre-

lated, then the Σx and Δx distributions (or the charm-pair rapidity distributions) contain no more information — and significantly less statistical power — than the x_F distribution from a single-charm analysis.[1] Due to the random boost along the beam axis the charm and anti-charm longitudinal momenta are not significantly correlated at leading order. However, some models of higher-order effects — for example, the PYTHIA/JETSET hadronization scheme discussed below — introduce significant correlations between the longitudinal momenta of the charm and anti-charm hadrons.

For the transverse momenta, the degree to which correlations are *smeared* provides a measure of higher-order effects. In contrast, for the longitudinal momenta, the degree to which correlations are *present* provides a measure of higher-order effects.

1.1.2 Higher-Order Perturbative Corrections

The HVQMNR program and the PYTHIA/JETSET event generator use complementary methods for including higher-order perturbative corrections to the leading-order partonic cross section. Schematically, the partonic cross section is

$$\mathrm{d}\hat{\sigma} = \sum_{n=2}^{\infty} \sum_{m=0}^{n} c_{mn} \alpha_S^n \ \ln^m y \ \frac{dy}{y}$$

where $\sqrt{y}$ characterizes the energy scale of the hard-scattering process. The MNR next-to-leading order calculation sums all α_s^2 and α_s^3 terms. A sample of the diagrams that contribute to the α_s^3 terms are shown in Figure 1.2. At next-to-leading order, processes such as $gg \to c\overline{c}g$, in which the c and $\overline{c}$ are no longer back-to-back, smear the delta function distribution, $\delta(\vec{p}_{t,c} + \vec{p}_{t,\overline{c}})$, of the leading-order prediction.

When applying Feynman rules, the loops in the higher-order diagrams introduce infinities into the perturbative QCD calculation. The renormalization procedure — which transforms the QCD coupling constant and the π^- and nucleon wave functions in the Lagrangian from their "bare" (infinite) values to their physical (*i.e.*, finite and measurable) values — leaves us with a finite partonic cross section and two extra parameters. The renormalization scale μ_R results from re-parameterizing the color charge $g = \sqrt{4\pi\alpha_S}$; the factorization scale μ_F from re-parameterizing π^- and nucleon wave functions. Any dependence of a finite-order calculation on these arbitrary scales is an indication that higher-order corrections are important. The dependence of the next-to-leading order charm-pair distributions on these scales is examined in the following section.

[1] Generally, single-charm analyses use the symbol x_F rather than $x_{c/\overline{c}}$.

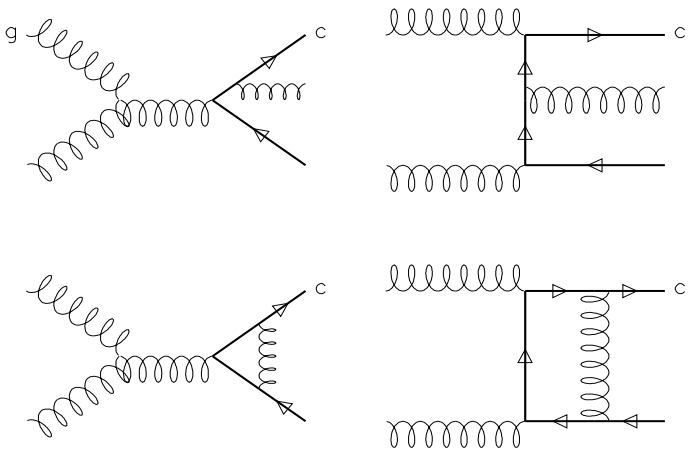

Figure 1.2: A sample of the Feynman diagrams that contribute to the next-to-leading order perturbative QCD calculation of the $c\overline{c}$ cross section.

An alternative approach to a finite-order calculation, used by the PYTHIA/JETSET event generator, is a leading-log calculation in which the cross section is determined by summing all "leading" $\ln^n y$ terms: $\mathrm{d}\hat{\sigma} = \sum_{n=2}^{\infty} c_{nn}\alpha_S^n \ \ln^n y \ dy/y$. This approach, referred to as parton showers, is often used in Monte Carlo event generators because it can be implemented iteratively. Each of the two incoming and two outgoing partons, whose distributions are based on leading-order matrix elements, can branch – backwards and forwards in time, respectively – into two partons, each of which can branch into two more parton, *etc.* This evolution continues until some small momentum scale is reached, at which point a non-perturbative hadronization scheme transforms the colored partons into color-neutral hadrons.

1.1.3 Intrinsic Transverse Momenta

The PYTHIA/JETSET event generator also allows the hard-scattering partons to have an intrinsic transverse momentum. The distribution is assumed to be Gaussian. One expects the variance of this distribution to be approximately 1 GeV^2[9]. Fits to single-charm and charm-pair distributions from experiments WA82, E769, WA75, and WA92 give conflicting results for the variance, ranging from 0.5 to 2 GeV^2[11]. Finding that a variance of 2 GeV^2 is necessary to fit the observed charm distributions would suggest that in processes initiated by gluons the intrinsic transverse momentum of the hard-scattering partons is on average larger than in processes initiated by quarks, such as the Drell-Yan process. More

experimental information may help clarify this issue. The cause of the apparent conflict, however, may also be due to the choice of hadronization models used in the fit.

1.1.4 Hadronization

Fragmentation functions parameterizing the hadronization of charm quarks to observable charm hadrons have been precisely measured by several e^+e^- experiments. The hadroproduction environment, however, is quite different from the e^+e^- environment and the role that the remnants of the colliding hadrons play in the hadronization process is not well understood.

Leading-Particle Effect

Almost all charm hadroproduction experiments in which a pion beam is collided into a nuclear target observe the so-called leading-particle[12]-[16]. That is, they observe an enhanced production at large x_F of "leading" H_c charm hadrons over the production of the charge-conjugate $\overline{H_c}$ hadrons, where the former have a valence quark (or anti-quark) in common with the beam and the latter do not. Therefore, in contrast to results from e^+e^- experiments, the hadroproduction hadronization process cannot be completely described by simply convoluting the partonic cross section with a fragmentation function that is independent of the quantum numbers of the incoming beam.

To quantify the leading-particle effect, single-charm analyses measure the asymmetry parameter

$$A \equiv \frac{\sigma_{H_c} - \sigma_{H_{\overline{c}}}}{\sigma_{H_c} + \sigma_{H_{\overline{c}}}}$$

as a function of x_F, where σ_H is the single-charm inclusive cross section for charm hadrons of type H. Results from a recent E791 analysis for $H_c = D^-(\overline{c}d)$ and $\overline{H_c} = D^+(c\overline{d})$ are shown in Figure 1.3[17]. The experimental results in this figure are compared to several theoretical predictions. The comparison with the next-to-leading order perturbative QCD prediction for charm quarks (*i.e.*, with no hadronization model implemented) clearly indicates that higher-order effects are responsible for the large asymmetries observed. The E791 data suggest that at large x_F there is a finite probability for the $\overline{c}$ quark to simply coalesce with the d valence quark from the $\pi^-(d\overline{u})$ beam particle. Both initial-state and final-state coalescence mechanisms must occur in QCD at some level. The PYTHIA/JETSET event generator implements a final-state mechanism as follows: the heavy-quark pair is produced

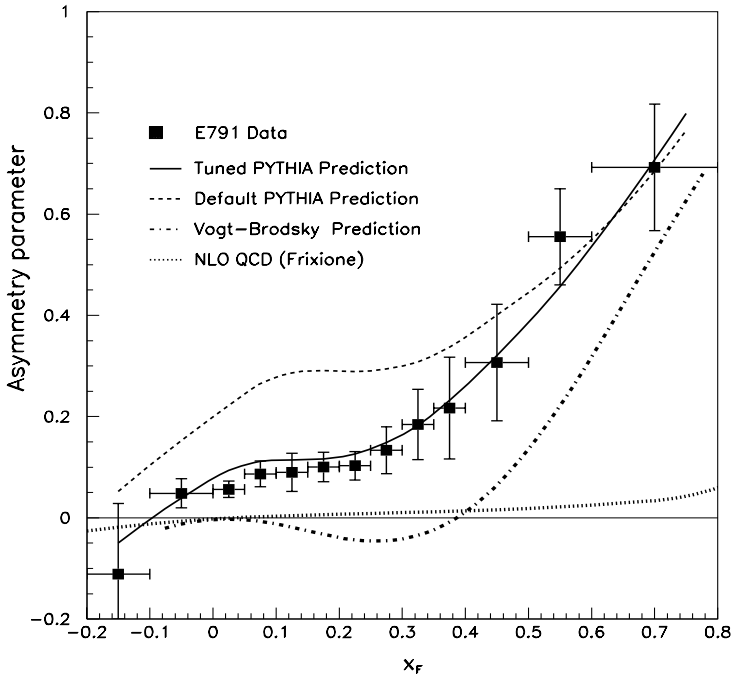

Figure 1.3: Recent results from an E791 analysis for the function $A(x_F) = \frac{\sigma_{D^-} - \sigma_{D^+}}{\sigma_{D^-} + \sigma_{D^+}}$, showing significant asymmetries between the production of inclusive D^- and D^+ mesons. The next-to-leading order perturbative QCD prediction includes no hadronization mechanism; the PYTHIA/JETSET predictions include a final-state coalescence mechanism; and the Vogt-Brodsky prediction includes an initial-state coalescence mechanism.

via a leading-order perturbative QCD process ($gg \to c\overline{c}$ or $q\overline{q} \to c\overline{c}$); then, if the $\overline{c}$ quark is moving with approximately the same velocity as the d valence quark from the π^- beam particle, this $\overline{c} + d$ color-singlet string can simply coalesce into a "leading" charm meson. The two predictions from the PYTHIA/JETSET event generator presented in Figure 1.3 both show the same trend as data.

An initial-state coalescence mechanism is implemented by R. Vogt and S. Brodsky[18]. In this case, the charm and anti-charm quark are not produced from the hard scattering of a beam parton with a target parton; but from a fluctuation of the π^- beam particle into a $|d\overline{u}c\overline{c}\rangle$ Fock state. The most probable fluctuations are those in which all four partons have approximately the same velocity (*i.e.*, a minimum invariant mass). Hence, during such fluctuations, the coalescence of $d + \overline{c}$ (or $\overline{u} + c$) into a "leading" charm meson is likely. As with the PYTHIA/JETSET final-state prediction, the Vogt-Brodsky initial-state prediction for $A(x_F)$ shows the same trend as data (Figure 1.3). The initial- and final-state contributions to the asymmetry parameter $A(x_F)$ cannot *both* be as large as pre-

dicted, respectively, by the Vogt-Brodsky intrinsic charm model and the PYTHIA/JETSET hadronization model. Additional high statistics single-charm analyses from a range of beam types (π^-, p, Σ) as well as from a range of "leading" hadron types may help clarify this issue.

One goal of this chapter is to determine if a charm-pair analysis — in particular, an analysis of $D\overline{D}$ events produced in π^--nucleon collisions — may also help clarify this issue. We focus only on predictions from the PYTHIA/JETSET event generator because charm-pair predictions from the Vogt-Brodsky intrinsic charm model are not yet available. Both the degree of correlation between the D and $\overline{D}$ longitudinal momenta as well as asymmetries among the four types of $D\overline{D}$ pairs — $D^0\overline{D^0}$, D^0D^-, $D^+\overline{D^0}$, and D^+D^- — provide information about the hadroproduction hadronization process. Below we outline the various elements of the PYTHIA/JETSET hadronization model for heavy quarks produced in π^--nucleon collisions.

PYTHIA/JETSET String Topology

When a gluon from a π^- in the beam and a gluon from a nucleon in the target collide to form a $c\overline{c}$ pair, the remnant π^- and target nucleon are no longer color-singlet particles. In the PYTHIA/JETSET event generator, the remnant π^- is split into two valence quarks; the remnant nucleon into and a valence quark plus a diquark. Following simple counting rules, two-thirds of the time, a proton (neutron) is split into a u (d) quark and a ud diquark; one-third of the time, into a d (u) quark and uu (dd) diquark. Color-singlet strings are then formed by connecting these remnant partons with the heavy-quark pair. Given this minimal set of partons — $(c,\, \overline{c})$, $(\overline{u},\, d)_\pi$, and $(qq, q)_N$, there are only two ways to make sets of color-singlet strings:

$$\begin{aligned} &(c,\, \overline{u}_\pi), \quad (\overline{c},\, q_N), \quad \text{and} \quad (d_\pi,\, qq_N); \text{ or} \\ &(\overline{c},\, d_\pi), \quad (c,\, qq_N), \quad \text{and} \quad (\overline{u}_\pi,\, q_N). \end{aligned} \tag{1.3}$$

Figure 1.4, which shows the scatter plot of the charm and anti-charm rapidities from 100,000 PYTHIA/JETSET $D\overline{D}$ events[2], demonstrates how the PYTHIA/JETSET string topologies tend to pull one charm quark in the forward (beam) direction, the other charm quark in the backward (target) direction. Comparing the scatter plot of the charm and anti-charm

[2]Default values are used for all PYTHIA/JETSET settings.

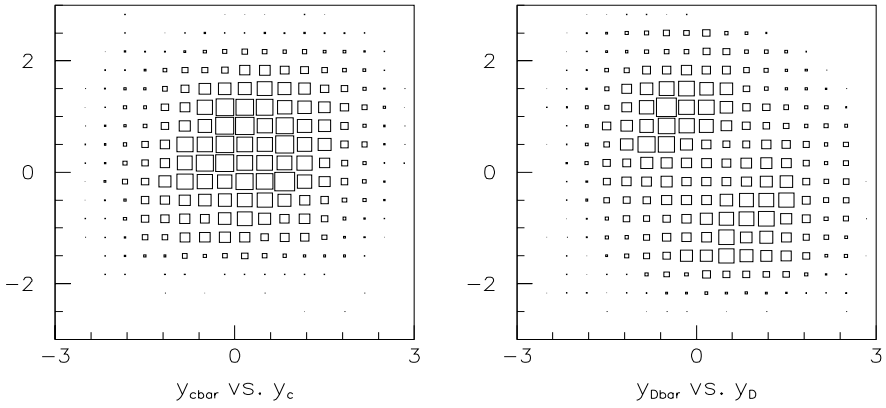

Figure 1.4: Scatter plots, y_c versus $y_{\overline{c}}$ and y_D versus $y_{\overline{D}}$, from 100,000 PYTHIA/JETSET $D\overline{D}$ events, showing the "forward-backward" correlation introduced by the PYTHIA/JETSET hadronization model. As discussed in Chapter 4, we are only able to reconstruct $D\overline{D}$ events in the region $-0.5 < y_{D,\overline{D}} < 2.5$.

quark rapidities (Fig. 1.4a) to the scatter plot of the D and $\overline{D}$ rapidities (Fig. 1.4b) clearly indicates that the forward-backward correlations are introduced at the hadronization level.

In the PYTHIA/JETSET model, partons originating from parton showers, as well as partons from the sea of either colliding hadron, are sometimes added to the strings listed in Equation 1.3. These extra partons, however, do not change the overall topology; each is simply added to one of the strings listed in Equation 1.3. Different string topologies do occur when the hard-scattering partons that produce the $c\overline{c}$ pair are quarks rather than gluons – roughly 5% of the time. Allowing sea quarks to play a more dominant role in determining the string topologies — for example, generating sets of strings in which neither the c nor the $\overline{c}$ are associated with valence quarks or, possibly, where both are associated with the same colliding hadron – would smear the correlations shown in Figure 1.4.

Lund String Model

In this section we describe the Lund string model: the iterative approach that the PYTHIA/JETSET event generator uses to break color-singlet strings into hadron-sized pieces. We note that asymmetries, such as the leading-particle effect discussed above, do not arise from the Lund string model. They arise because there is a significant probability for color-singlet strings with a relatively small invariant mass to simply coalesce into a single hadron. Coalescence is discussed below.

To describe the highlights of the Lund string model we use the (c, $\overline{u}_\pi$) string from Equation 1.3 as an example. This description is taken largely from the PYTHIA/JETSET manual[10]. We chose the center-of-mass of the (c, $\overline{u}_\pi$) system where the c quark is moving in the $+z_s$ direction and the $\overline{u}_\pi$ quark is moving in the $-z_s$ direction as our frame of reference. As the ends of the string move apart, the partons lose energy and the color field gains energy. This color field is able to spontaneously produce $q\overline{q}$ pairs.[3] The pairs have no transverse momenta with respect to the z_s-axis ($\vec{p}_{t_s,q} = -\vec{p}_{t_s,\overline{q}}$) and the x_s and y_s momenta of the q quark are selected independently from a Gaussian distribution with a mean of 0 and a width of 0.35 GeV. Beginning (arbitrarily) from the c end of the string, a $c\overline{q}$ meson is formed leaving behind a (q, $\overline{u}_\pi$) string, which is iteratively broken into smaller pieces. The transverse momentum of the $c\overline{q}$ meson with respect to the z_s-axis is determined by the transverse momentum of the $\overline{q}$ quark since the c quark contributes none. What remains to be determine is the energy E and longitudinal momentum p_{z_s} of the charm meson. Only one of these variables can be selected independently since the momentum of the meson is already constrained by its mass and transverse momentum:

$$(E + p_{z_s})(E - p_{z_s}) = M^2 + p_{x_s}^2 + p_{y_s}^2.$$

Considerations such as longitudinal boost invariance forces the Lund string model to determine the energy and longitudinal momentum of the meson by selecting what fraction z of $(E_c + p_{z_s,c})$ contributes to the $(E + p_{z_s})$ of the meson, where $(E_c + p_{z_s,c})$ is the original energy plus longitudinal momentum of the c quark. That is, $(E + p_{z_s}) = z(E_c + p_{z_s,c})$. The fragmentation function $f(z)$ gives the probability that a given z is selected. Because the Lund string model requires that the fragmentation process looks the same whether the iterative procedure is performed from the c end of the string or the $\overline{u}_\pi$ end, the fragmentation function for light quarks must be of the form:

$$f^{Lund}(z) \;\propto\; \frac{1}{z} z^{a_\alpha} \left(\frac{1-z}{z}\right)^{a_\beta} \exp\left(\frac{-bm_t^2}{z}\right), \tag{1.4}$$

where $m_t^2 = M^2 + p_{x_s}^2 + p_{y_s}^2$. The default PYTHIA/JETSET settings are $a_\alpha = a_\beta = 0.3$ and $b = 0.58\ \mathrm{GeV}^2$. For heavy quarks, Bowler has shown that f^{Lund} should be modified to

$$f^{Bow}(z) \;\propto\; \frac{1}{z^{bm_Q^2}}\, f^{Lund}(z), \tag{1.5}$$

[3] The production of $s\overline{s}$ pairs is suppressed by a factor of three compared to $u\overline{u}$ or $d\overline{d}$ pairs, and heavy-quark pairs are not allowed.

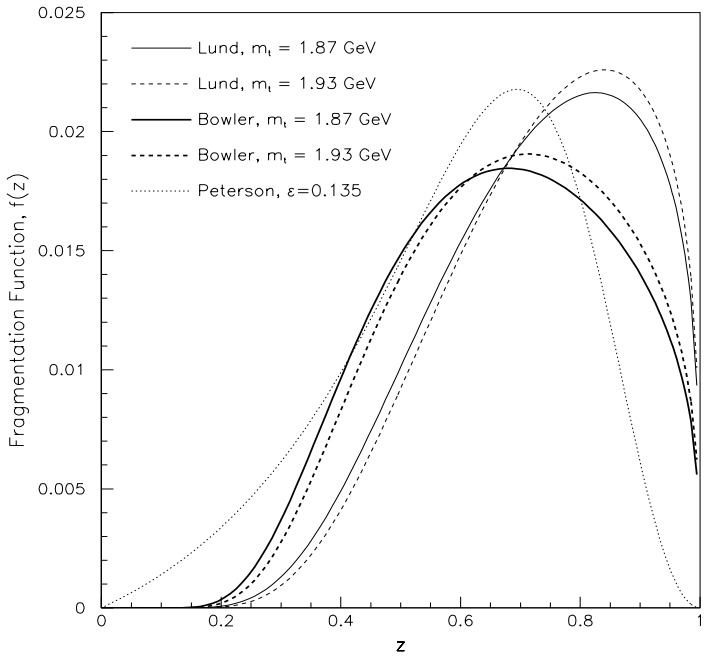

Figure 1.5: Common fragmentation functions: The PYTHIA/JETSET default for the hadronization of light quarks (LUND) for two values of $m_t \equiv \sqrt{M^2 + p_{x_s}^2 + p_{y_s}^2}$; the PYTHIA/JETSET default for heavy quarks (Bowler); and, lastly, the function commonly used to analyze e^+e^- data (Peterson), where $\epsilon = 0.135$ is derived from fits to CLEO and ARGUS D^0 data[19, 20]. See Eqs. 1.4-1.6.

where m_Q is the mass of the heavy quark. By default, the PYTHIA/JETSET event generator uses this fragmentation function for the hadronization of heavy quarks. Most e^+e^- experiments have used the Peterson fragmentation function:

$$f^{Pet}(z) \propto \frac{1}{z(1 - \frac{1}{z} - \frac{\epsilon}{1-z})^2}. \tag{1.6}$$

These three functions, f^{Lund}, f^{Bow}, and f^{Pet}, are compared in Figure 1.5.

With e^+e^- experiments, at leading-order, the only color-singlet string possible is (c, $\overline{c}$). Hence the fragmentation function, even if it is strongly peaked at large z, can only soften the longitudinal momentum distribution. In contrast, in the hadroproduction hadronization process, the longitudinal momentum distribution of the charm hadrons can be harder than the longitudinal momentum distribution of the charm quarks because of the dragging effect of the valence quarks from the colliding hadrons.

PYTHIA/JETSET Coalescence

As mentioned, in the PYTHIA/JETSET event generator a color-singlet string can simply coalesce into a single hadron rather than breaking into several hadron-sized pieces. To investigate the importance of coalescence in the PYTHIA/JETSET hadronization model we generate 100,000 $D\overline{D}$ events in which a 500 GeV π^- meson collides into a fix nuclear target. We use the default PYTHIA/JETSET settings for all parameters. We only allow events in which both the D and $\overline{D}$ rapidities are greater than -0.5 and less than 2.5 because our experimental acceptance goes to zero for rapidities outside those limits. To simulate the E791 experiment, we assume that one-fifth of the interactions occur in a platinum target, four-fifth in a carbon target (see Chapter 2). Since 50% of the nucleons in carbon are neutrons and 60% of the nucleons in platinum are neutrons, we force 52% of the PYTHIA/JETSET events interactions to be π^--neutron interactions and 48% to be π^--proton interactions. The PYTHIA/JETSET event generator does not include any nuclear effects. In other words, it assumes that the charm-pair cross section is proportional to the number of nucleons in the target material. This assumption is supported by recent results from experiment E769[21].

At fixed-target energies, the PYTHIA/JETSET event generator also assume that D^0, D^+, D^{*0}, D^{*+} and the respective charge-conjugate mesons are the only possible primary charm mesons, where a "primary" meson is produced directly in the fragmentation process, rather than via a decay such as $D^{*+} \rightarrow D^0\pi^+$. Contributions to the $D\overline{D}$ cross section from decays of higher-level excited D meson states or from decays of B mesons are assumed to be negligible. The PYTHIA/JETSET prediction for the relative production rates of the four types of primary $D\overline{D}$ pairs is

$$P_{nn} = 0.264, \quad P_{nc} = 0.332, \quad P_{cn} = 0.168, \quad P_{cc} = 0.236,$$

where, for example, P_{nc} is the probability for producing a neutral primary D meson and a charged primary $\overline{D}$ meson. The probability P_{nc} is largest because both the primary neutral D meson ($c\overline{u}$) and the primary charged $\overline{D}$ meson ($\overline{c}d$) can originate from coalescence with a π^- valence quark — that is, they are "leading" charm mesons. The primary charged $\overline{D}$ meson ($\overline{c}d$) can also arise from coalescence with the nucleon valence quark. In general, such "lagging" charm mesons, however, will be have negative rapidities that are outside our acceptance limits. The probability P_{cn} is the smallest because neither primary D meson

can originate from coalescence. If there were no coalescence mechanism, we would find $P_{nn} = P_{nc} = P_{cn} = P_{cc} = 0.25$.

Experimentally, only ground-state $D\overline{D}$ pairs can be fully reconstructed with reasonable efficiency. Because charged D^*'s can decay to neutral D's, reconstructing a neutral ground-state D does not unambiguously tell us the valence quark content of the primary charm meson. Therefore, some information regarding the importance of coalescence is lost when measuring the relative rate for ground-state $D\overline{D}$ pairs rather than for primary $D\overline{D}$ pairs. The PYTHIA/JETSET prediction for the relative production rates of the four types of ground-state $D\overline{D}$ pairs is

$$P_{D^0\overline{D^0}} = 0.581, \quad P_{D^0D^-} = 0.220, \quad P_{D^+\overline{D^0}} = 0.143, \quad P_{D^+D^-} = 0.057.$$

Because the contribution to the $D\overline{D}$ cross section from decays of higher-level excited D meson states or from decays of B mesons is assumed to be negligible, the $D\overline{D}$ production rates listed above can be derived from the primary $D\overline{D}$ production rates as follows:

$$\begin{aligned}
P_{D^0\overline{D^0}} &= P_{nn} + f_e f_n (P_{nc} + P_{cn}) + (f_e f_n)^2 P_{cc}, \\
P_{D^0D^-} &= (1 - f_e f_n) P_{nc} + (1 - f_e f_n)(f_e f_n) P_{cc}, \\
P_{D^+\overline{D^0}} &= (1 - f_e f_n) P_{cn} + (1 - f_e f_n)(f_e f_n) P_{cc}, \\
P_{D^+D^-} &= (1 - f_e f_n)^2 P_{cc},
\end{aligned}$$

where f_e is the fraction of primary D mesons that are excited D mesons and f_n is the fraction of excited charged D mesons that decay to neutral D mesons. The PYTHIA/JETSET default values are $f_e = 0.785$ and $f_n = 0.650$. Given no coalescence mechanism ($P_{nn} = P_{nc} = P_{cn} = P_{cc} = 0.25$.), the PYTHIA/JETSET event generator would find:

$$P_{D^0\overline{D^0}} = 0.570, \quad P_{D^0D^-} = 0.185, \quad P_{D^+\overline{D^0}} = 0.185, \quad P_{D^+D^-} = 0.060.$$

1.2 Theoretical Predictions for Charm-Pair Distributions

In the previous section, we introduced the theoretical framework used to describe the hadroproduction of $D\overline{D}$ pairs. In particular, we discussed:

- the leading-order perturbative QCD description of the hadroproduction of $c\overline{c}$ pairs;
- higher-order perturbative corrections to the leading-order calculation;

- the addition of intrinsic transverse momentum to the hard-scattering partons that collide to form the $c\overline{c}$ pair; and, lastly,
- the hadronization of $c\overline{c}$ pairs to observable $D\overline{D}$ pairs.

Using this framework, we investigate how sensitive single-charm and charm-pair distributions are to various theoretical assumptions. All predictions discussed in this section assume a 500 GeV π^- beam is incident on a nuclear target, mimicking the E791 environment.

The PYTHIA/JETSET event generator depends on hundreds of parameters. Unless otherwise mentioned, we use the default settings for all parameters. The next-to-leading order perturbative QCD calculation depends on the following six parameters:

- the mass of the charm quark, m_c;
- the beam and target parton distribution functions, f^π and f^N, respectively;
- Λ_{QCD}, the free parameter that must be determined experimentally, which roughly defines the mass scale below which quarks and gluons do not behave as independent, free partons — that is, below which perturbative QCD calculations are no longer valid; and
- the renormalization and factorization scales, μ_R and μ_F, respectively.

The pairs of pion and nucleon parton distribution functions considered in this section, obtained from the CERN computer library package PDFLIB [22], are listed in Table 1.2. Parton distribution functions depend on the fraction of the hadron momentum carried by the hard-scattering parton, x; on both the factorization and renormalization scales; and on Λ_{QCD}. Typically, collaborations extract parton distribution functions from data by first assuming a simple analytic form for the function, $f(x, \mu_0)$, at a fixed factorization scale μ_0. Perturbative QCD evolution equations then extend this 1-dimensional function $f(x, \mu_0)$ to any arbitrary factorization scale μ_F greater than μ_0. The evolution equations depend both on Λ_{QCD} and on the renormalization scale μ_R. Each fit assumes a fixed value for Λ_{QCD}. Since the choice of scales is arbitrary, the parton distribution functions accessible from PDFLIB have defined the renormalization scale to be the same as the factorization scale.

For each parton distribution function listed in Table 1.2, we specify the square of the minimum factorization scale allowed, μ_0^2; whether the evolution equations were cal-

Table 1.2: The pairs of pion and nucleon parton distribution functions considered in this section, obtained from the CERN FORTRAN package PDFLIB. The functions have been extracted from fits to data assuming a fixed value of Λ_{QCD}; and the functions are undefined below the minimum scale μ_0

Set		Name	μ_0^2[GeV^2]	$\Lambda^{(4)}_{\rm QCD}$ [MeV]	Order	Ref.
(1)[a]	f^π	SMRS-P2	5	190	NLO	[23]
	f^N	HMRS-B (4.90)	5	190	NLO	[24]
(2)	f^π	GRV-P	0.3	200	NLO	[25]
	f^N	GRV	0.3	200	NLO	[26]
(3)	f^π	SMRS-P2	5	190	NLO	[23]
	f^N	HMRS-B (8.90)	5	100	NLO	[27]
(4)	f^π	ABFKW-P3	2	281	NLO	[28]
	f^N	HMRS-B (8.90)	5	300	NLO	[27]
(5)[b]	f^π	OW-P1	4	200	LO	[29]
	f^N	CTEQ 2L	4	190	LO	[30]

[a] HVQMNR suggested default
[b] PYTHIA/JETSET default

culated to leading-order (LO) or to next-to-leading order (NLO)[4]; and the value of $\Lambda^{(4)}_{QCD}$ used in the fit[5]. Querying PDFLIB for the value of a parton distribution function at a scale below μ_0 gives undefined results. The default set of parton distribution functions for the PYTHIA/JETSET event generator is set (5) in Table 1.2; the default suggested by the authors of HVQMNR is set (1).

When possible, we choose pion and nucleon distribution functions that are fit assuming similar values for Λ_{QCD}. In Set (4) from Table 1.2, however, the pion functions were obtained assuming $\Lambda^{(4)}_{\rm QCD} = 190$ GeV, whereas the nucleon functions were obtained assuming $\Lambda^{(4)}_{\rm QCD} = 100$ GeV. To date, there are no pion distribution functions available that have been fit with $\Lambda^{(4)}_{\rm QCD} < 190$ GeV. The present uncertainties, however, suggest that $\Lambda^{(4)}_{\rm QCD}$ could range anywhere from 100 to 300 MeV[31]. In order to examine predictions for single-charm and charm-pair distributions assuming $\Lambda^{(4)}_{\rm QCD} = 100$ GeV, we use Set (4), ignoring the correlation between $\Lambda_{\rm QCD}$ and the pion distribution functions. For all predictions shown

[4] The modified minimal subtraction scheme is used for all NLO parton distribution functions listed in Table 1.2.

[5] Λ_{QCD} depends on the energy scale of the hard-scattering interaction. If the scale is much less than the mass of the $(n_f+1)^{\rm th}$ heaviest quark and much greater than the mass of the $(n_f)^{\rm th}$ heaviest quark, then $\Lambda^{(n_f)}_{QCD}$ should be used to determine the strong coupling constant. In our case, the energy scale is of the same order as the mass of the charm quark, making the choice more ambiguous. The MNR next-to-leading order calculation of the partonic $c\overline{c}$ cross section uses $\Lambda^{(3)}_{QCD}$. On the other hand, the parton distribution functions, which are convoluted with the partonic cross section to obtain the hadroproduction $c\overline{c}$ cross section, appear to use $\Lambda^{(4)}_{QCD}$.

below, the Λ_{QCD} used in the next-to-leading order calculation of the partonic cross section is defined to be the same as the Λ_{QCD} used to extract the nucleon parton distribution function f^N.

The degree to which the charm-pair distributions are sensitive to variations in μ_R and μ_F gives an indication of how important higher-order corrections are; that is, an indication of how much (or little) we can trust the α_S^3 calculation. In general, one tries to minimize higher-order contributions by choosing μ_R and μ_F to be of the same order as the energy scale Q of the hard-scattering process. This scale cannot be defined unambiguously. One reasonable choice is

$$Q \equiv \sqrt{m_c^2 + \frac{p_{t,c}^2 + p_{t,\overline{c}}^2}{2}}. \tag{1.7}$$

The default setting for the PYTHIA/JETSET event generator is $\mu_R = \mu_F = Q$, leading to factorization scales as low as the mass of the charm quark m_c, which by default is set to 1.35 GeV. The parton distribution functions used by the PYTHIA/JETSET event generator, however, are only defined for scales above 2 GeV. This problem is handled by setting the parton distribution function to $f(x, \mu_0)$ for all factorization scales less than μ_0.

The suggested default for the HVQMNR program is $\mu_R = Q$ and $\mu_F = 2Q$. Given the suggested default for the mass of the charm quark of $m_c = 1.5$ GeV, this choice ensures that the factorization scale will never go below the minimum allowed scale, $\mu_0 = \sqrt{5}$ GeV. On the other hand, this choice means that the α_S used in the calculation of the partonic cross section and the α_S used the evolution equations to determine the parton distribution function are evaluated at different scales, Q and $2Q$, respectively.

In Figures 1.7-1.12 we show single-charm and charm-pair distributions for a wide range of theoretical assumptions. When obtaining these theoretical predictions, we only allow charm-pair events in which both charm rapidities are greater than -0.5 and less than 2.5 — our experimental acceptance goes to zero for rapidities outside those limits. For the HVQMNR generator, which does not hadronize the $c\overline{c}$ pair to charmed mesons, the cut is on the charm quark rapidities. For the PYTHIA/JETSET generator, the cut is on the D meson rapidities. In Table 1.3, we show which generator (HVQMNR or PYTHIA/JETSET) and what theoretical assumptions are used in each figure.

The same set of single-charm and charm-pair distributions are shown in each figure. Each charm particle in a charm-pair event can be described using three variables. A common choice of independent variables for single-charm analyses is

Table 1.3: The settings used by the HVQMNR and PYTHIA/JETSET generators to obtain the single-charm and charm-pair distribution shown in Figures 1.7-1.12. The set of pion and nucleon parton distribution functions (PDF), labeled (1) through (5), are defined in Table 1.2. A "Y" indicates that parton showers (PS) are included in the PYTHIA/JETSET event generator; an "N" indicates that they are not included.

Generator		PDF	μ_R/Q	μ_F/Q	m_c [GeV]	σ_{k_t} [GeV]	PS	Figure	
MNR	NLO [a]	(1)	1.0	2.0	1.5	0		1.7	**solid**
MNR	LO [b]	(1)	1.0	2.0	1.5	0			dashed
P/J	$c\overline{c}$	(1)	1.0	1.0	1.5	0	Y		dotted
P/J	$c\overline{c}$	(1)	1.0	1.0	1.5	0.44	Y		solid
MNR	NLO [a]	(1)	1.0	2.0	1.5	0		1.8	solid
MNR	NLO	(1)	1.0	2.0	1.2	0			dashed
MNR	NLO	(1)	1.0	2.0	1.8	0			dotted
MNR	NLO [a]	(1)	1.0	2.0	1.5	0		1.9	**solid**
MNR	NLO	(2)	1.0	2.0	1.5	0			dashed
MNR	NLO	(3)	1.0	2.0	1.5	0			dotted
MNR	NLO	(4)	1.0	2.0	1.5	0			solid
MNR	NLO	(2)	0.5	0.5	1.5	0		1.10	solid
MNR	NLO	(2)	1.0	1.0	1.5	0			dashed
MNR	NLO	(2)	1.5	1.5	1.5	0			dotted
P/J	$D\overline{D}$ [c]	(5)	1.0	1.0	1.35	0.44	Y	1.11	**solid**
P/J	$c\overline{c}$	(5)	1.0	1.0	1.35	0	Y		dashed
P/J	$c\overline{c}$	(5)	1.0	1.0	1.35	0.44	N		dotted
P/J	$D\overline{D}$	(5)	1.0	1.0	1.35	0	N		solid
P/J	$D\overline{D}$ [c]	(5)	1.0	1.0	1.35	0.44	Y	1.12	**solid**
P/J	$D\overline{D}$	(5)	1.0	1.0	1.35	0.7	Y		dashed
P/J	$D\overline{D}$	(5)	1.0	1.0	1.35	1.0	Y		dotted
P/J	$D\overline{D}$	(5)	1.0	1.0	1.35	1.5	Y		solid

[a] Default next-to-leading order HVQMNR distributions
[b] Default leading-order HVQMNR distributions
[c] Default PYTHIA/JETSET $D\overline{D}$ distributions

- the longitudinal momentum of the charm particle in the center of mass of the colliding hadrons divided by the momentum of the beam hadron, x_F;
- the square of the transverse momentum of the charm particle, p_t^2; and
- the azimuthal angle of the charm particle with respect to the beam axis, ϕ.

We ignore the latter variable because all theoretical predictions give a flat ϕ distribution. Another common variable used in analyses is the rapidity in the center of mass of the

colliding hadrons

$$y \equiv \left[\frac{1}{2}\ln\left(\frac{E+p_z}{E-p_z}\right)\right]_{\rm CM}.$$

This variable is approximately related to x_F and p_t^2 as follows:

$$y \approx \sinh^{-1}\left(\frac{\sqrt{s}\,x_F}{2\sqrt{M^2+p_t^2}}\right),$$

where $\sqrt{s}$ is the center-of-mass energy of the colliding hadrons and M is the mass of the charm particle. Although x_F and y are very correlated, we show predictions for both distributions.

For each single-charm variable v, we obtain predictions for two charm-pair distributions: $\Delta v = v_c - v_{\overline{c}}$ and $\Sigma v = v_c + v_{\overline{c}}$. ($\Delta\phi$ is defined to be the minimum of $|\phi_c - \phi_{\overline{c}}|$ and $360^\circ - |\phi_c - \phi_{\overline{c}}|$.) As with the single-charm ϕ variable, we ignore the charm-pair $\Sigma\phi$ variable because all theoretical predictions give a flat $\Sigma\phi$ distribution. We do not, however, ignore the $\Delta\phi$ distribution which is very sensitive to theoretical assumptions. Two other commonly used charm-pair distributions that we examine are the square of the transverse momenta of the charm-pair, $p^2_{t,c\overline{c}} = |\vec{p}_{t,c} + \vec{p}_{t,\overline{c}}|^2$, and the invariant mass of the charm-pair, $M_{c\overline{c}}$.

The vertical axis of each distribution shown in Figures 1.7-1.12 gives the fraction of single-charm (charm-pair) events per variable v interval, $\frac{1}{N}\frac{{\rm d}N}{{\rm d}v}$, where N is the total number of single-charm (charm-pair) events generated. The number of single-charm events generated is, of course, just twice the number of charm-pair events generated.

Sensitivity to Higher-Order Perturbative Corrections

In Figure 1.7, we the compare the complementary methods used by the HVQMNR program and the PYTHIA/JETSET event generator to include higher-order perturbative corrections to the leading-order partonic cross section. As discussed in the previous section, the PYTHIA/JETSET event generator, beginning with leading-order matrix elements, uses parton showers to include higher-order perturbative effects. Whereas, the HVQMNR program calculates the next-to-leading order $c\overline{c}$ cross section. To more directly compare these two approaches, we change three of the default PYTHIA/JETSET settings — m_c, f^π and f^N — to match the default HVQMNR settings (See Table 1.3). We obtain PYTHIA/JETSET $c\overline{c}$ distributions assuming no intrinsic transverse momentum, as well as

assuming $\sigma_{k_t} = 0.44$ GeV which is the PYTHIA/JETSET default. As argued by T. Sjostrand, the intrinsic transverse momentum may, at least in part, be seen as a replacement for gluon emission that is truncated in the parton shower approach due to the introduction of an energy scale below which the parton shower evolution is stopped[32]. In Figure 1.7, we also show the HVQMNR leading-order distributions to emphasize which distributions are, and which are not, sensitive to higher-order corrections.

Figure 1.7 shows that higher-order perturbative corrections do not significantly affect the shapes of most of the single-charm and charm-pair distributions. That is, the HVQMNR leading-order and next-to-leading predictions for all distributions are very similar — except for the $|\Delta p_t^2|$, $\Delta\phi$, and $p_{t,c\overline{c}}^2$ distributions. In the leading-order calculation, these latter distributions are delta functions — at 0 GeV, 180° and 0 GeV, respectively — because the leading-order charm and anti-charm quark are back-to-back in the plane transverse to the beam axis.

The next-to-leading order predictions and the parton shower prediction are also quite similar. The slight difference between the HVQMNR and the PYTHIA/JETSET longitudinal (x_F and y) distributions may derive from cutting on the D meson rapidities ($-0.5 < y_D < 2.5$) rather than the charm quark rapidities for the PYTHIA/JETSET events. The $|\Delta p_t^2|$ and $\Delta\phi$ PYTHIA/JETSET distributions with no intrinsic transverse momentum included, indicate that the parton shower evolution is playing a very small role. The $\Delta\phi$ parton shower distribution, in particular, is closer to the leading-order delta-function prediction than to the next-to-leading order prediction. Adding intrinsic transverse momentum, with $\sigma_{k_t} = 0.44$ GeV, brings the PYTHIA/JETSET prediction very close to the next-to-leading order HVQMNR prediction. This result implies that the amount of intrinsic transverse momentum needed to agree with experimental results will depend on the method used to include higher-order perturbative corrections.

Sensitivity to the Mass of the Charm Quark

In Figure 1.8, we investigate the degree to which the single-charm and charm-pair distributions are sensitive to variations in the mass of the charm quark. All distributions are obtained from HVQMNR next-to-leading order calculations using the default values for all parameters — except for m_c. Higher-order effects play a larger role as the charm-quark mass decreases because the ratio Q/Λ_{QCD}, where Q gives the energy scale of the

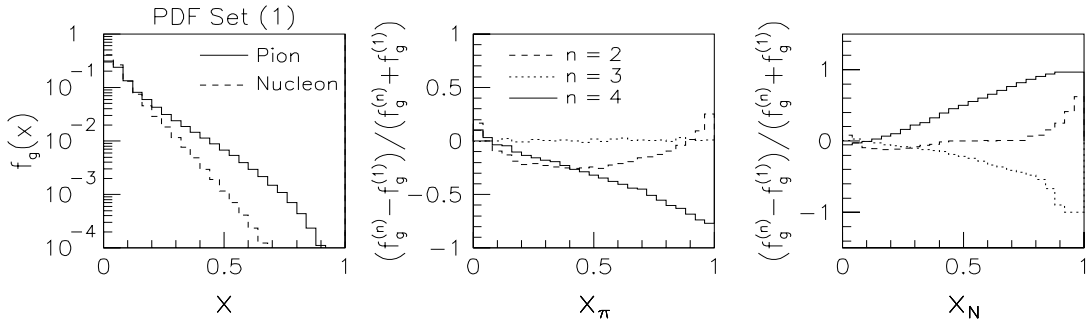

Figure 1.6: Comparison of the gluon distribution functions for Sets (1) through (4), defined in Table 1.2. The pion and nucleon functions for each set are obtained from PDFLIB after imposing the constraint $\sqrt{x_\pi x_N} \geq \frac{2m_c}{E_{CM}}$, where E_{CM} is the center-of-mass energy of the colliding hadrons.

interaction (Eq. 1.7), decreases. For $m_c = 1.2$ GeV, the single-charm x_F and p_t^2 distributions are steepest because the outgoing charm quark can more easily radiate gluons; the single-charm y distribution is less central ($y = 0$); and the invariant mass of the charm-pair is significantly steeper than the higher mass predictions. The increase in higher-order effects for smaller m_c is also evident in the $\Delta\phi$ distribution, which is flattest for $m_c = 1.2$ GeV.

Sensitivity to Parton Distribution Functions

In Figure 1.9, we investigate the degree to which the single-charm and charm-pair distributions are sensitive to variations in the parton distribution functions and Λ_{QCD}. All distributions are obtained from HVQMNR next-to-leading order calculations using the default values for all parameters — except for the parton distribution functions. We examine predictions for four pairs of pion and nucleon parton distribution functions, sets (1) through (4) defined in Table 1.2.

At fixed-target energies, the dominant contribution to the $c\overline{c}$ cross section is from gluon fusion. In Figure 1.6, we compare the gluon distribution functions, $f_g^{Set(n)}$, for Sets (1) through (4). By energy conservation, the energy of the two colliding partons must be at least twice the mass of a charm quark to produce a $c\overline{c}$ pair, that is, $\sqrt{x_\pi x_N} \geq \frac{2m_c}{E_{CM}}$ where $E_{CM} = 30.6$ GeV is the center-of-mass energy of the colliding hadrons. Hence, for each set, the pion and nucleon functions are obtained after imposing the constraint $x_\pi x_N \geq \frac{4m_c^2}{E_{CM}^2}$. We impose this constraint because we want to investigate how the four sets compare in the region of x that we explore, not in the very low x region where the functions are largest.

Although the four sets of parton distribution functions differ significantly, the

single-charm and charm-pair distributions shown in Fig. 1.9 are not very sensitive to these differences. The sensitivity of the $\Delta\phi$ distribution is due to the variation in Λ_{QCD} in Sets (1) through (4) (See Table 1.2). As the value of Λ_{QCD} increases, the ratio Q/Λ_{QCD}, where Q gives the energy scale of the interaction (Eq. 1.7), decreases, causing higher-order effects to play a larger role. Hence, the flattest $\Delta\phi$ distribution results from using Set (4) ($\Lambda^{(4)}_{QCD} = 300$ Gev); the steepest $\Delta\phi$ distribution, from using Set (3) ($\Lambda^{(4)}_{QCD} = 100$ Gev).

Sensitivity to Factorization and Renormalization Scales

In Figure 1.10, we investigate the degree to which the single-charm and charm-pair distributions are sensitive to variations in the renormalization and factorization scales. All distributions are obtained using the HVQMNR next-to-leading order calculation. We set the two arbitrary scales equal to each other, $\mu \equiv \mu_F = \mu_R$, and obtain distributions for $\mu = Q/2, Q$, and $2Q$, where Q gives the energy scale of the interaction (Eq. 1.7). We use the GRV parton distribution functions for both the pion and the nucleon (Set (2) in Table 1.2), which have been evolved down to $\mu_0^2 = 0.3$ GeV^2. With this choice, the factorization scale μ can go as low as $m_c/2$ without going below μ_0. As mentioned, the degree to which the distributions are sensitive to variations in the renormalization and factorization scales gives an indication of how much (or little) we can trust the α_S^3 calculation. As expected, the distributions that are most sensitive to variations in μ are those distributions that are trivial at leading-order: $|\Delta p_t^2|$, $\Delta\phi$, and $p^2_{t,c\bar{c}}$. The smaller the factorization and renormalization scales are, the broader these distributions are. That is, the higher-order α^3 terms play a larger role, compared to the leading-order α^2 terms, as renormalization and factorization scales decrease. The sensitivity to these arbitrary scales indicates that a next-to-leading order calculation is insufficient for obtaining accurate theoretical predictions for these transverse distributions.

Sensitivity to Higher-Order Non-perturbative Effects

In Figure 1.11, we look separately at the effects of parton showers, intrinsic transverse momentum, and hadronization. All distributions are obtained using the PYTHIA/JETSET event generator. The distributions obtained using the default settings (**solid**) include all three effects. We compare these default distributions to three set of distributions that are obtained by including

- *only* hadronization, but no parton shower evolution or intrinsic transverse momentum (solid);
- *only* the parton shower evolution, but no intrinsic transverse momentum or hadronization (dashed);
- *only* intrinsic transverse momentum, but no hadronization or parton shower evolution (dotted).

For the longitudinal momentum distributions (x_F, Σx_F, Δx_F, y, Σy, Δy), the determining factor is whether or not hadronization is included. The two sets of distributions that include hadronization effects are quite similar; the two sets of distributions that do not include hadronization effects are similar; but the latter two sets of distributions are significantly different than the former two sets. In the PYTHIA/JETSET hadronization model, the broadening of the longitudinal momentum distribution is the result of color-connecting the charm quark to a valence quark from one the colliding hadrons and the anti-charm quark to a valence quark from the other colliding hadron.

All three higher-order effects broaden the leading-order delta function prediction for the $\Delta\phi$ distribution. The broadening due to the parton shower evolution, however, is significantly smaller than the broadening due to either the hadronization process or the addition of intrinsic transverse momentum ($\sigma_{k_t} = 0.44$ GeV). The latter two effects broaden the $\Delta\phi$ distribution by roughly the same amount.

All three higher-order effects also broaden the leading-order delta function prediction for the $p^2_{t,c\overline{c}}$ distribution. In this case, however, the broadening due to the parton shower evolution is larger than the broadening due to either hadronization effects or the addition of intrinsic transverse momentum ($\sigma_{k_t} = 0.44$ GeV).

Sensitivity to Intrinsic Transverse Momentum

In Figure 1.12 we investigate the degree to which the single-charm and charm-pair distributions are sensitive to variations in the amount of intrinsic transverse momenta added to the hard-scattering partons that collide to form a $c\overline{c}$ pair. All distributions are obtained using the PYTHIA/JETSET event generator, with default settings for all parameters except for the width of the Gaussian intrinsic transverse momentum distribution, σ_{k_t}.

When intrinsic transverse momentum is included, the hard-scattering partons from

the colliding hadrons are no longer necessarily moving parallel to the colliding hadrons. The plane that is transverse to the axis of the parton-parton collision — which cannot be determined experimentally — is no longer the same as the plane that is transverse to the beam axis. Hence, including intrinsic transverse momentum smears the leading-order prediction, $\vec{p}_{t,c} = -\vec{p}_{t,\overline{c}}$. Not surprisingly, the distributions that are most sensitive to variations in σ_{k_t} are those transverse distributions that are trivial at leading-order: $|\Delta p_t^2|$, $\Delta\phi$, and $p^2_{t,c\overline{c}}$. As the width, σ_{k_t}, increase, these distributions become flatter.

Summary

In this section, we briefly summarize the results of the comparisons shown in Figures 1.7-1.12.

The longitudinal momentum distributions — x_F, Σx_F, Δx_F, y, Σy, and Δy — are relatively insensitive to all variations considered above, except for including, or not, the PYTHIA/JETSET hadroproduction hadronization (Figure 1.11). The steepness of the invariant mass distribution is also sensitive to the whether or not hadronization is included, as well as to the mass of the charm quark (Figure 1.8). Therefore, the measured distributions for these physics variables, discussed in Chapter 5, provide a test of the PYTHIA/JETSET hadronization model; in particular, a test of the string topology scheme that color-connects the charm quark to a valence quark from one the colliding hadrons and the anti-charm quark to a valence quark from the other colliding hadron.

The transverse distributions $|\Delta p_t^2|$, Σp_t^2, $\Delta\phi$, and $p^2_{t,c\overline{c}}$ are sensitive to almost all variations considered above because they are sensitive to degree of correlation between the charm and anti-charm transverse momenta. Varying m_c (Fig. 1.8), Λ_{QCD} (Fig. 1.9), or μ_R (Fig. 1.10) in the next-to-leading order calculation changes the definition of the running coupling constant α_S, which is approximately proportional to $1/\ln(\mu_R/\Lambda_{QCD})$. As the coupling constant increases — that is, as m_c decreases, Λ_{QCD} increases, or μ_R decreases — higher-order effects play a larger role, and consequently the charm and anti-charm transverse momenta become less correlated. The other methods we discussed for including higher-order effects were parton showers, intrinsic transverse momentum, and hadronization.

In Chapter 5, we quantify the degree of correlation between the transverse momenta of the D and $\overline{D}$ mesons from our $D\overline{D}$ data sample. Precise comparisons with next-to-leading order predictions, however, are not yet possible. The sensitivity of the

next-to-leading order predictions to the arbitrary renormalization and factorization scales (Fig. 1.10) indicates that higher-order perturbative corrections are important. In principal, one could determine the sets of theoretical parameters that generate predictions that are in good agreement with the full range of experimental results. Given the present theoretical uncertainties, however, such results would be difficult to interpret. The fit values of physical parameters (*e.g.* the mass of the charm quark) would depend on the values of the non-physical renormalization and factorization scales. For example, if a renormalization scale of $Q/2$, rather than Q, is assumed, then a smaller value for σ_{k_t} or a larger value for m_c would be required to fit the data.

Our goal in this analysis is to quantify the degree of correlation between the D and $\overline{D}$ mesons from our sample of approximately 800 $D\overline{D}$ signal events. In Chapter 5, we present our experimental results and compare them to the default HVQMNR and PYTHIA/JETSET predictions. Before presenting our results, we first introduce the E791 experiment (Chapter 2); discuss our event-selection methodology (Chapter 3); and describe how we obtain acceptance-corrected signal $D\overline{D}$ distributions (Chapter 4).

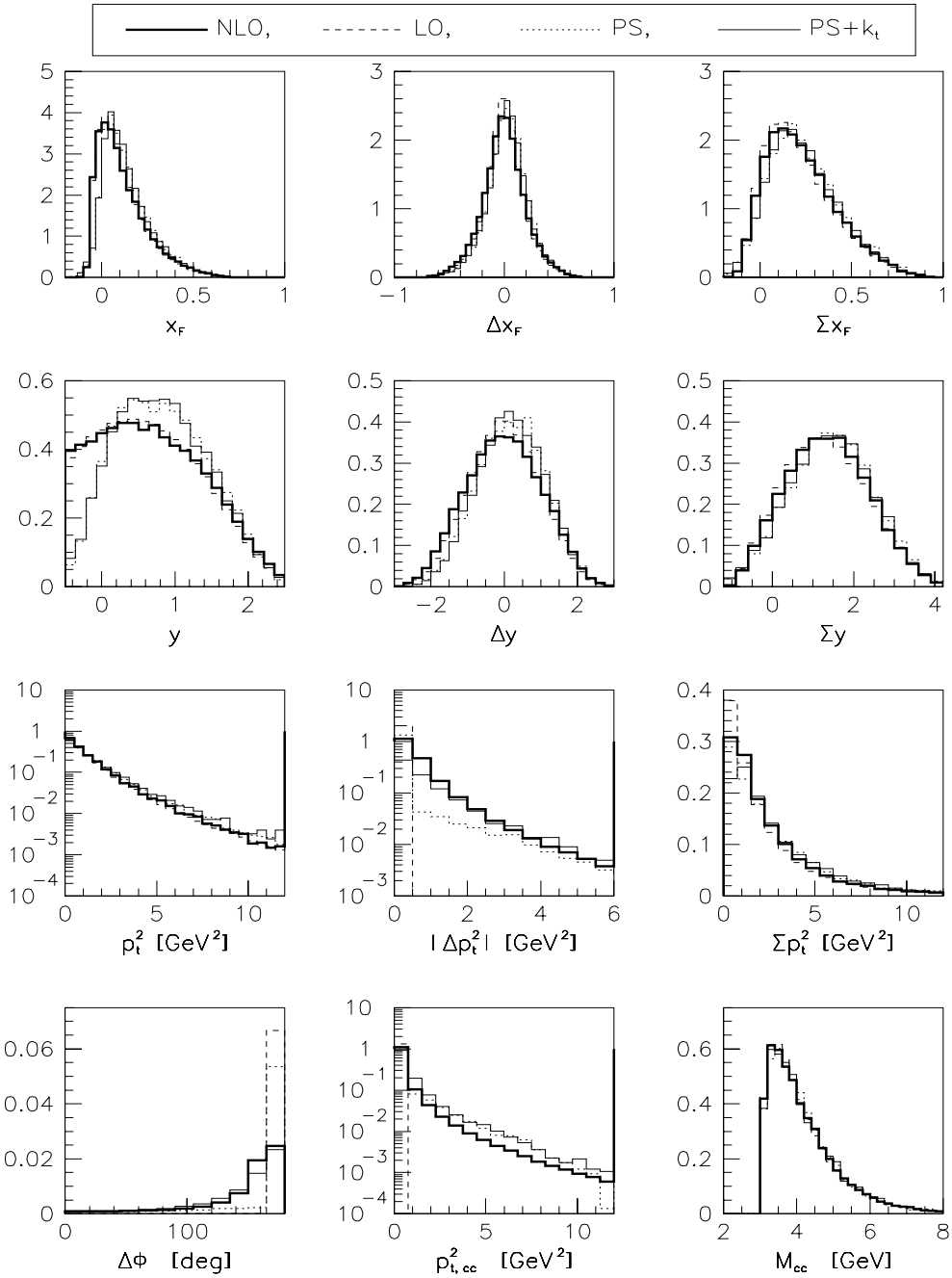

Figure 1.7: Sensitivity of single-charm and charm-pair distributions to higher-order perturbative corrections. The leading-order (LO) and next-to-leading order (NLO) distributions are obtained from the HVQMNR generator; the parton-shower (PS) distributions from the PYTHIA/JETSET generator. Table 1.3 shows the settings used for each set of distributions.

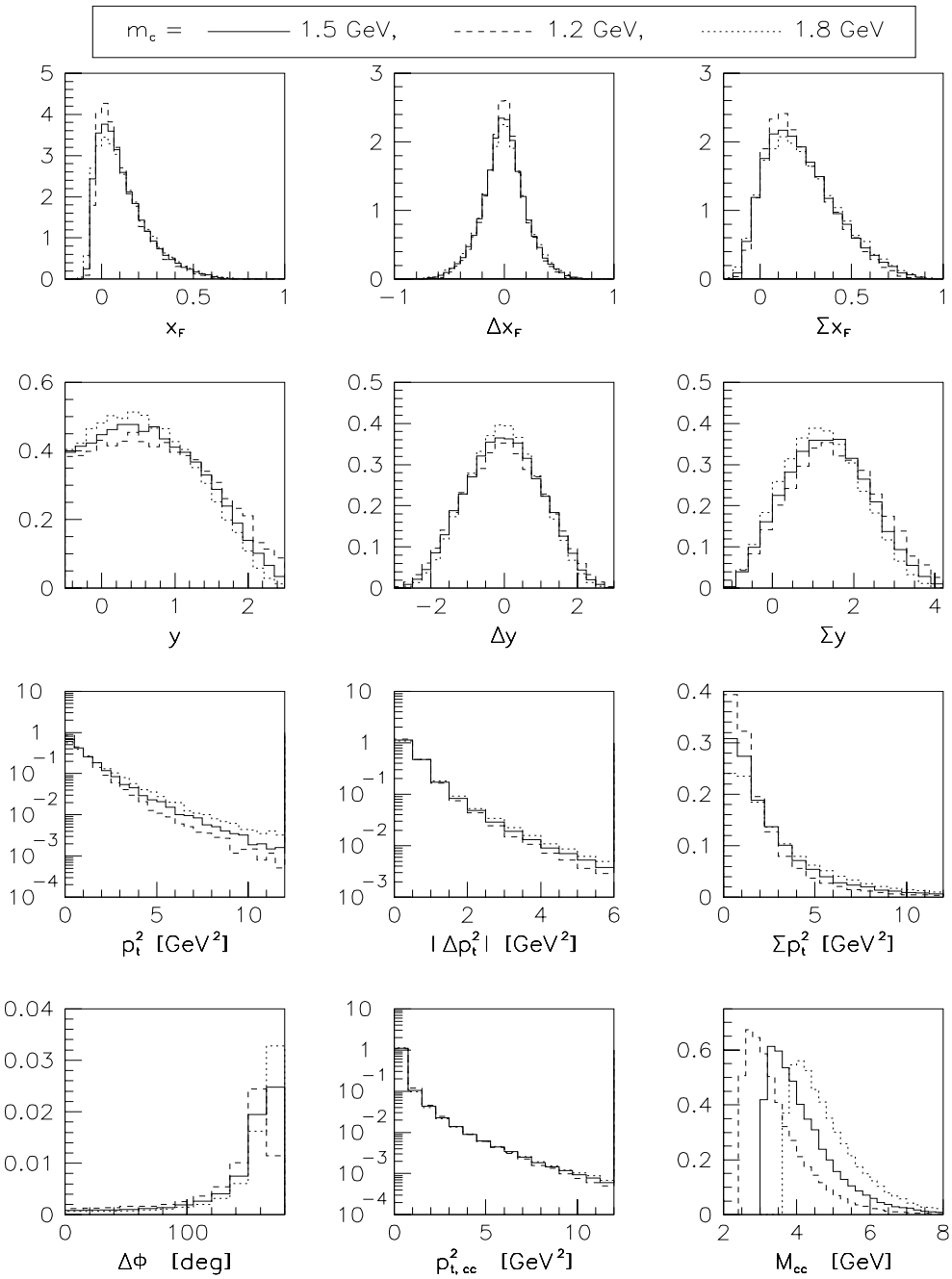

Figure 1.8: Sensitivity of single-charm and charm-pair distributions to variations in the mass of the charm quark. All distributions are obtained from HVQMNR next-to-leading order calculations using the default values for all parameters — except for m_c (see Table 1.3).

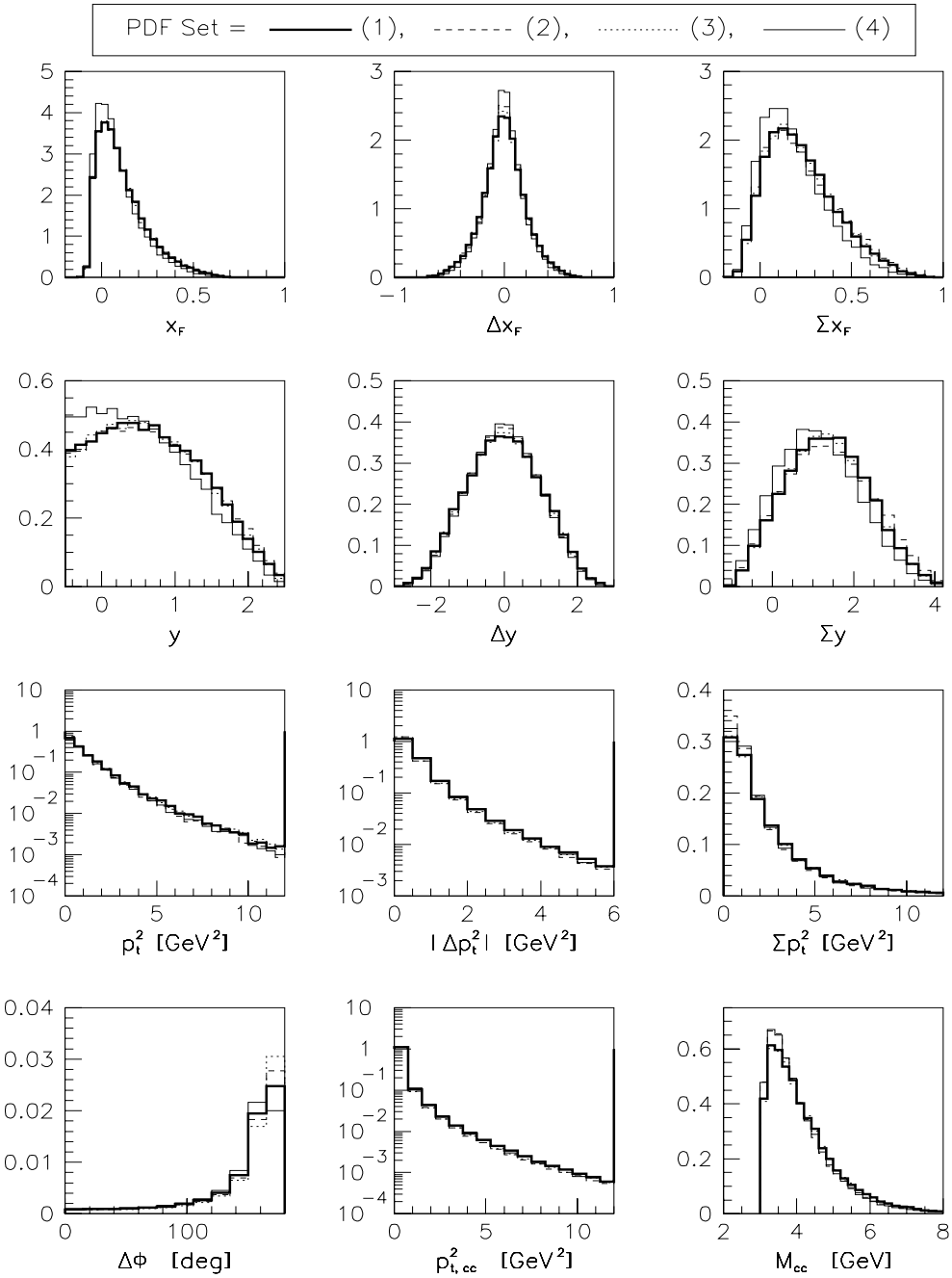

Figure 1.9: Sensitivity of single-charm and charm-pair distributions to variations in the parton distribution functions. Sets (1) through (4) are defined in Table 1.2. All distributions are obtained from HVQMNR next-to-leading order calculations using the default values for all parameters — except for the parton distribution functions (see Table 1.3).

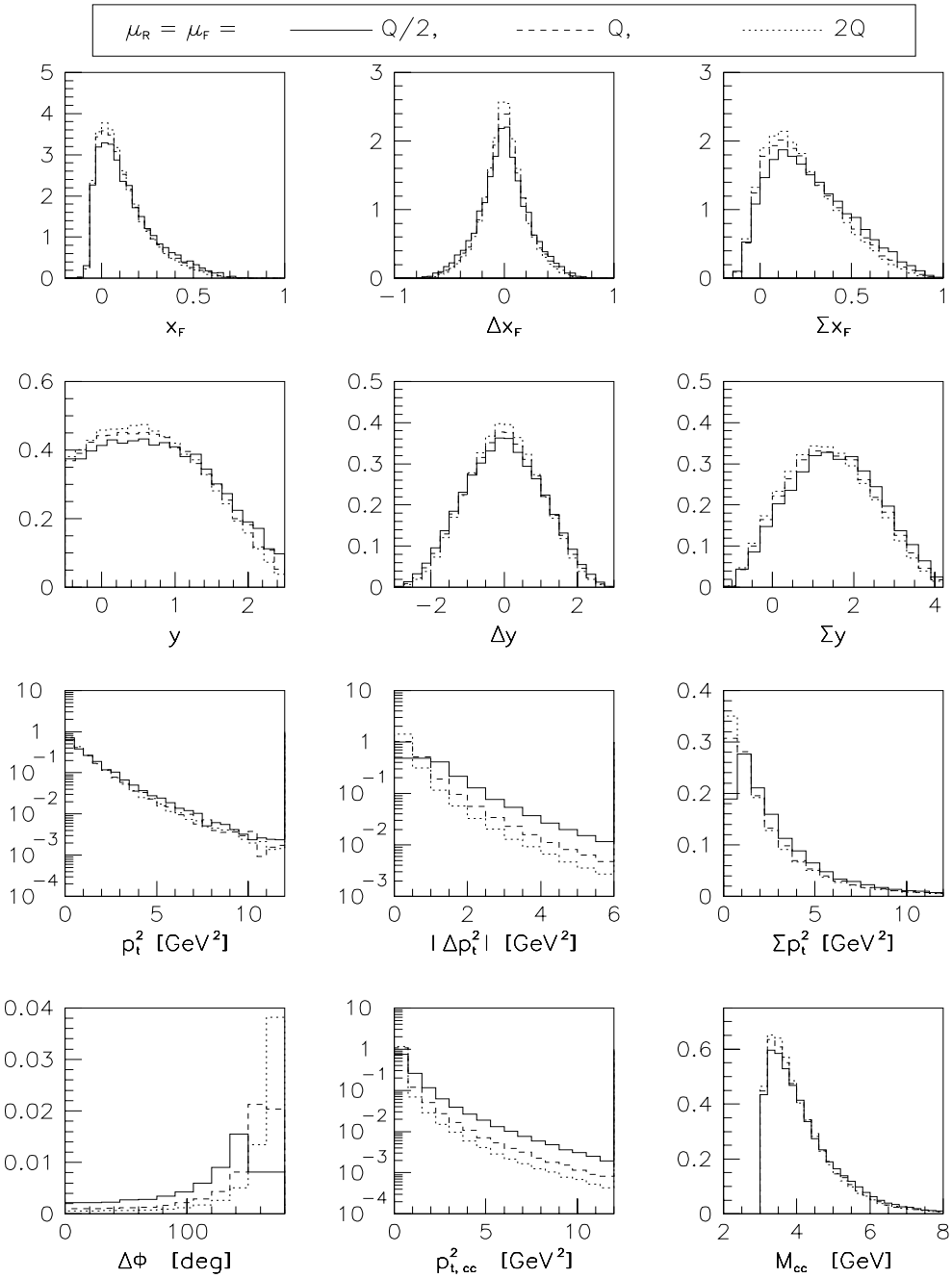

Figure 1.10: Sensitivity of single-charm and charm-pair distributions to variations in the factorization and renormalization scales. All distributions are obtained using HVQMNR next-to-leading order calculation. Equation 1.7 defines the energy scale Q. Rather than using the default set of parton distribution functions, we use the GRV functions, which are evolved down to $\mu_0^2 = 0.3$ GeV^2. See Tables 1.2 and 1.3.

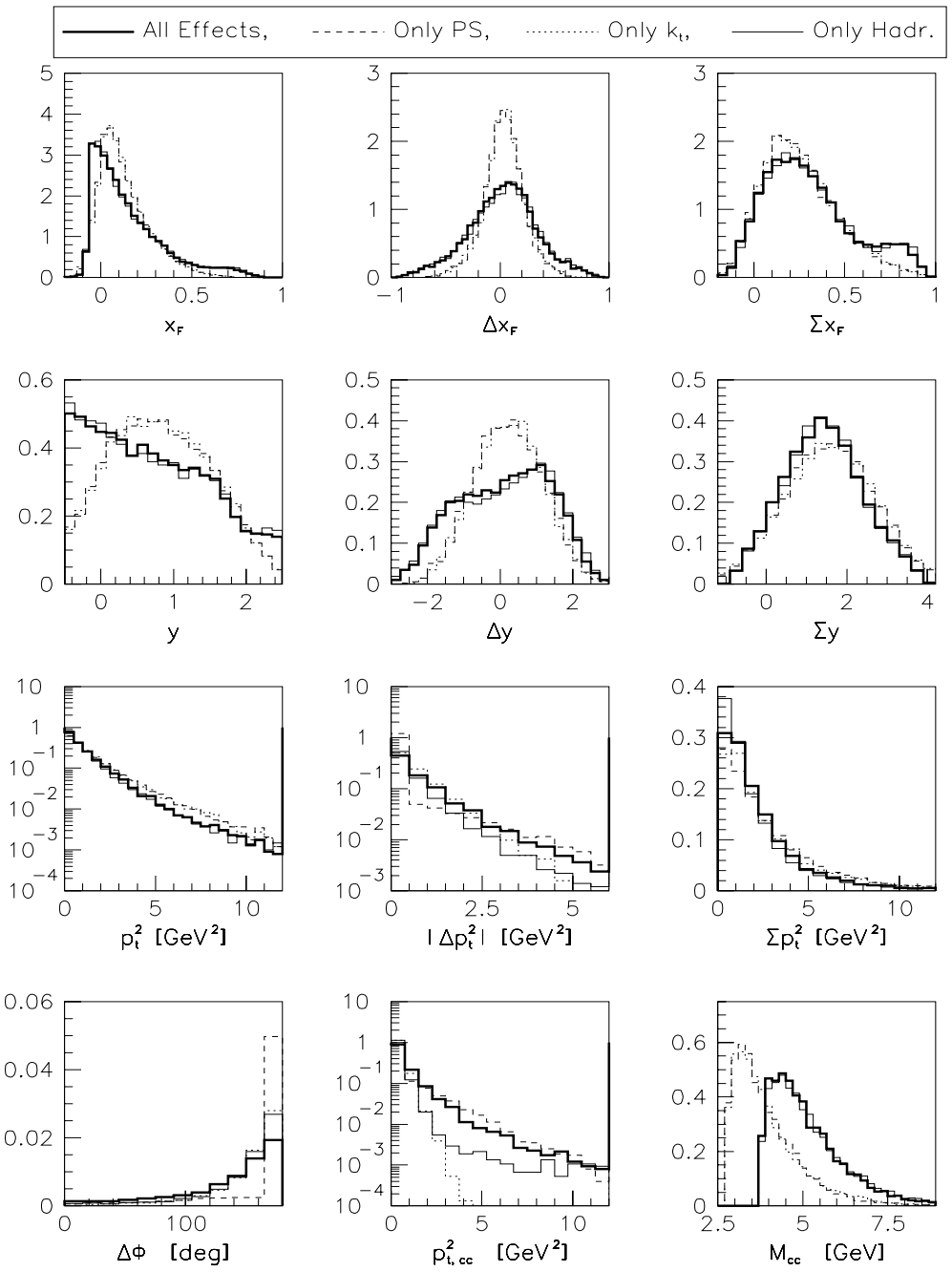

Figure 1.11: Sensitivity of the single-charm and charm-pair distributions to the parton shower evolution, the addition of intrinsic transverse momentum, and the hadronization process. All distribution are obtained using the PYTHIA/JETSET event generator. The **solid** distributions include all three effects; the dashed distributions include *only* the parton shower evolution: the dotted distributions include *only* intrinsic transverse momentum; the solid distributions include *only* hadronization. See Table 1.3

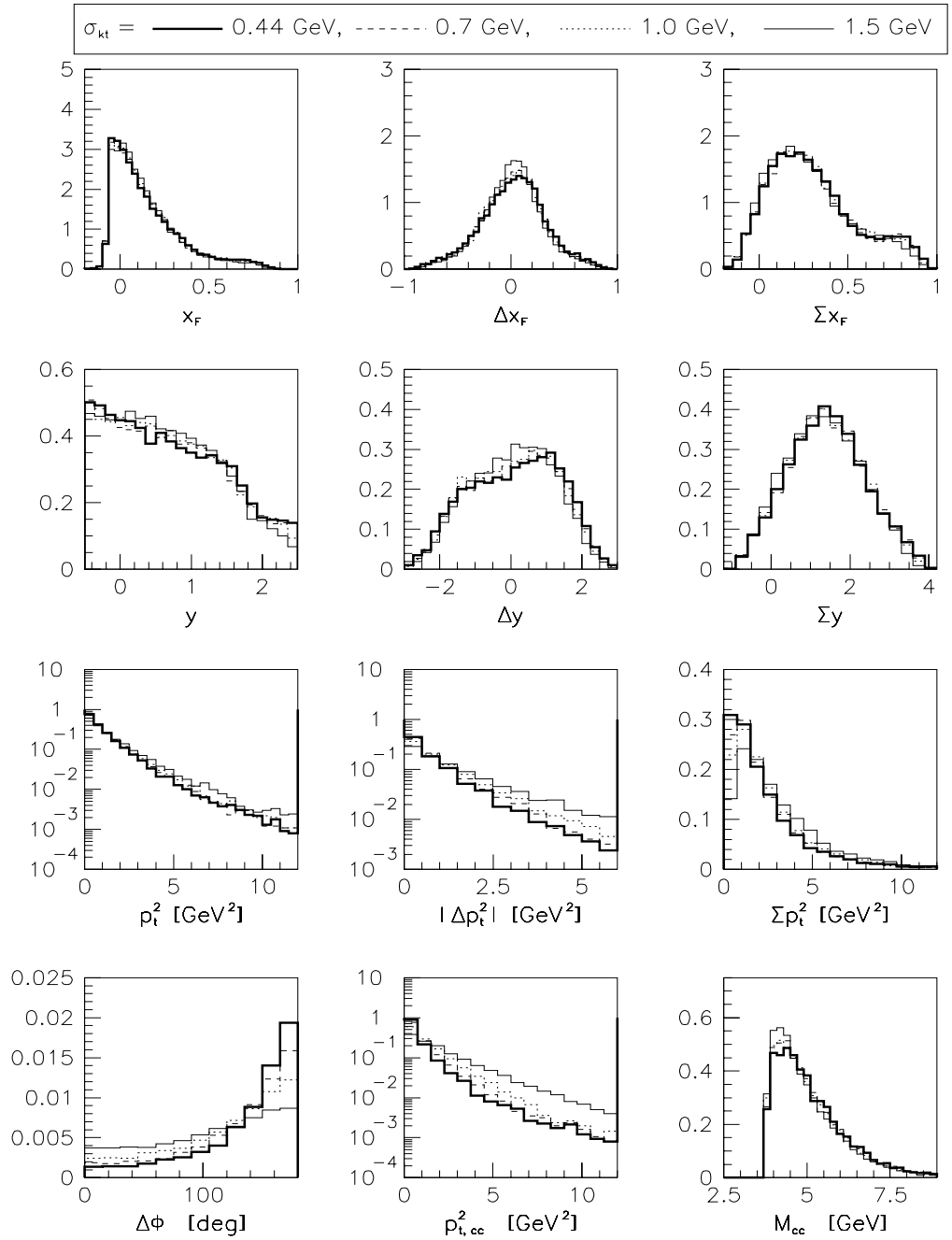

Figure 1.12: Sensitivity of single-charm and charm-pair distributions to variations in the amount of intrinsic transverse momenta added to the hard-scattering partons. All distributions are obtained using PYTHIA/JETSET event generator, using default settings for all parameters except σ_{k_t} (see Table 1.3).

Chapter 2

The E791 Experiment

Experiment 791 is the fourth in a series of fixed-target charmed-particle experiments conducted at Fermi National Accelerator Laboratory's Tagged Photon Laboratory: E516, E691, E769, and E791. During a six-month period ending in January 1992, E791 recorded 20 billion π^--nucleon interactions, producing 50 Terabytes of data. The goal, which has been realized and surpassed by a factor of 2, was to reconstruct 100,000 charmed particles — an order of magnitude more than any previous experiment [33].

In this chapter we discuss the characteristics of the E791 pion beam and the target used to produce charmed particles; the detectors of the Tagged Photon Spectrometer that allow us to detect the decay products of these charmed particles; and the data acquisition, reconstruction, and data reduction systems.

2.1 The Beam

During fixed-target runs, the 800 GeV proton beam from Fermilab's Tevatron is redirected to three fixed-target experimental stations approximately once per minute. With each spill from the Tevatron, 10^{12} protons are incident on a beryllium target upstream from the Tagged Photon Laboratory (TPL). The particles from this interaction — after being separated into positively and negatively charged particles, momentum filtered, and collimated by a series of magnets — result approximately in a 94% pure beam of negatively charged (500 ± 20) GeV pions. During the 23-second proton spills from the Tevatron, occuring once per minute, 2 million pions per second are incident on the E791 target.

"Photon" in the name Tagged Photon Laboratory comes from the previous use

of the TPL spectrometer, discussed below, for the photoproduction experiments E516 and E691. Although the charm cross section relative to the light-quark cross section is higher for high-energy photons than for pions, this advantage is out-weighed by the inability to produce the high beam rates possible with hadron beams. The E791 beam energy was twice that of the previous hadroproduction experiment at TPL, E769, increasing the charm cross section by approximately 80% [34].

2.2 The Target

The E791 target consists of five thin, circular foils oriented perpendicular to the beam axis and separated by approximately 1.5 cm. The most upstream foil is platinum; the four downstream foils are industrial diamond. The foils were chosen to be thin — 0.052 cm for the platinum foil and approximately 0.15 cm for the diamond foils — and separated by relatively large distances to maximize the volume of free space where the decay vertices of short-lived charmed particles are more easily reconstructed. A D^0, for example, produced in the primary interaction with a momentum of 100 GeV travels, on average, 0.7 cm beyond the primary vertex before decaying. Hence, it is very likely to decay outside the primary interaction foil and before the subsequent foil. Although not as relevant for our $D\overline{D}$ analysis, the thin foils are especially important for the reconstruction of Λ_c^+ and Ξ_c^+, which have mean lifetimes one half and one quarter, respectively, of the lifetime of the D^0.

With such thin foils, obtaining the necessary interaction rate required dense materials. The density of the platinum and diamond foils is approximately 21 and 3 grams per cubic centimeter, respectively, resulting in a 0.4% chance of a pion interacting in any given foil (or a 2% chance of interaction in the entire target for each pion).

Using two types of foils with significantly different atomic masses ($A = 195$ for platinum, $A = 12$ for diamond) allows for the possibility of measuring how the charm cross section depends on the nuclear target. If charm quarks are produced from hard parton-parton interactions, then one expects the cross section to be proportional to the number of partons and, therefore, to the atomic mass, $\sigma = A^\alpha \sigma_0$ with $\alpha = 1$. Early indirect measurements by WA78 and E613 found $\alpha \approx 0.75$, but more recent direct measurements find α to be consistent with 1 [21]. In this charm-pair analysis, we do not analyze the events originating from the platinum foil separately from events originating from the diamond foils.

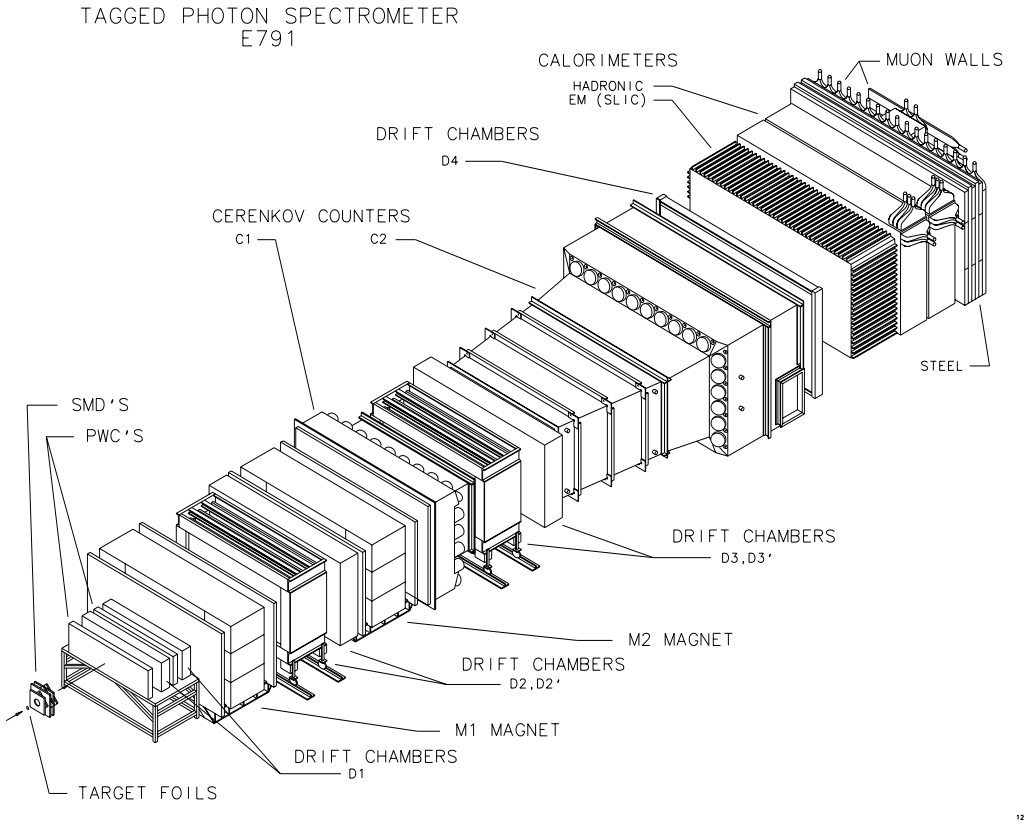

Figure 2.1: The E791 Tagged Photon Spectrometer

2.3 The Spectrometer

The Tagged Photon spectrometer, illustrated in Figure 2.1, is typical for a fixed-target experiment. Because the hard scattering that produces the charmed hadrons is boosted forward from its center of mass, almost all the detectors are positioned downstream of the target, approximately centered on the beam axis.

The downstream detectors perform three main functions:

- Vertexing both the primary interaction vertex and the secondary charm vertices;
- Tracking and determining the momenta of the charged particles; and
- Identifying the particle type of both neutral and charged particles.

Upstream detectors (not shown in Figure 2.1) track the π^- beam before it reaches the target. We discuss each of these functions separately in the following four sections. The

role that the calorimeters play in the E791 trigger is discussed in Section 2.4.

2.3.1 Tracking the π^- Beam

Eight planes of proportional wire chambers (PWC) and six planes of silicon microstrip detectors (SMD) are used to precisely track the transverse position and slope of the incoming pion beam. The PWC planes are located tens of meters upstream of the target to provide good angular resolution while the SMD planes are located tens of centimeters from the target to provide good spatial resolution.

In the E791 coordinate system, the x-axis points eastward, the y-axis upward, and the z-axis northward. In Figure 2.1, the arrow going into the target foils points along the z-axis. The origin of this coordinate system is just downstream of the target.

The path of the π^- beam varies slightly from event to event, but is always very close to the z-axis. The roughly Gaussian distribution of the x position of the beam has a mean and sigma of -0.2 ± 0.2 cm; and, for the y position, -0.7 ± 0.2 cm. The roughly Gaussian distribution of the beam angles in the xz plane has a mean and sigma of -0.3 ± 0.3 milliradians; and, for angles in the yz plane, 0.9 ± 0.1 milliradians.

2.3.2 Vertexing

Almost all E791 analyses depend on the ability to reconstruct the decays of short-lived charmed particles. The seventeen SMD planes positioned directly downstream from the target were designed for this purpose. Because of their proximity to the target — positioned from 3 to 50 cm from the last target foil — and their fine spatial resolution, this set of SMD planes is able to reconstruct secondary vertices with a z-position resolution of several hundred microns. Given a similar resolution for the primary interaction vertex, the decay vertex of a 100 GeV D^0, for example, decaying to $K^-\pi^+$ in its mean lifetime — that is, 0.7 cm downstream of the primary interaction — is measured to be significantly separated from the primary vertex. That is, the separation is $\Delta z = 0.7$ cm $= 7000$ μm and the error on this separation is on the order of $\sigma \approx \sqrt{300^2 + 300^2}\mu\text{m} \approx 400\mu\text{m}$, resulting in $\Delta z/\sigma \approx 18$.

All the SMD planes are oriented perpendicular to the z-axis, with the strips in a given plane perpendicular to the x, y, or v axis which is rotated from the x-axis 20.5° counter-clockwise about the z-axis. The dimensions are 5 cm by 5 cm for the first two

downstream planes, and 10 cm by 10 cm for the remaining 15 downstream planes, providing an overall geometric acceptance of approximately ± 100 milliradians.

Each SMD plane is a 300-μm-thick p-n junction diode operated at reverse bias, where the p-type silicon and the adjacent electrode have been segmented into strips to provide spatial resolution. The thinness of these planes ensures a minimum of multiple scattering. A relativistic charged particle passing through an SMD plane ionizes the n-type silicon producing, on average, 25,000 electron-hole pairs. The voltage drop across the diode forces the holes to drift towards the p-side electrode and the electrons towards the n-side electrode. This produces a signal (or a "hit") on one or more strips near the particle's trajectory. The spatial resolution of the detector depends on the strip pitch; the efficiency (*i.e.*, the probability of registering a hit when a particle traverses the detector); the noise level (*i.e.*, how often a hit is registered when no particle traverses); and the cross-talk (*i.e.*, when a particle passing through one strip produces hit(s) on neighboring strip(s)). The efficiency for all 23 SMD planes in the E791 spectrometer ranges from 83% to 99%. The inner strip pitch ranges from 25 to 50 μm; the outer strip pitch from 50 to 200 μm. The resulting spatial resolution, in the direction perpendicular to the given strip, ranges from 7 to 15 μm.

2.3.3 Tracking and Determining the Momenta of Charged Particles

Downstream of and complementing the SMD tracking and vertexing system, are two PWC planes, 35 drift chamber (DC) planes, and two magnets (Fig. 2.1). The long distance from the target, ranging from approximately 1 meter to almost 20 meters, allows charged tracks to be reconstructed with good angular resolution. The placement of DC planes before and after each magnet allows the momenta of charged tracks to be measured.

The DC planes are oriented perpendicular to the z-axis with the wires in a given plane perpendicular to the x, u, or v axis. The u and v axes are rotated about the z-axis $\pm 20.5^\circ$ beginning from the x-axis. The 35 drift chamber planes are divided into four modules, labeled D1 through D4 in Figure 2.1. Each module is made up of 1 to 4 assemblies; and each assembly is made up of 3 to 4 DC planes and is surrounded by a gas mixture which is 89% Argon, 10% Carbon, 1% CF_4,

Each DC plane alternates between sense wires maintained at 0 Volts, and field wires maintained at -2 kVolts. In between every two DC planes is a high voltage field plane

maintained at -2.4 Volts. A charged particle traversing a chamber ionizes gas molecules, producing free electrons that are then collected at the sense wires. Measuring the time it takes for the electrons to reach a given sense wire precisely indicates how far from that wire the particle passed. The spatial resolution for the DC planes ranges from 250 to 350 microns. Given three to four DC planes each with a different orientation and spaced closely together along the z-axis, an assembly is able to determine one point, in three-space, along the trajectory of a charged particle.

The two downstream PWC planes operate similarly to the DC planes. Each PWC plane, oriented perpendicular to the z-axis, is actually two planes, surrounded by a gas mixture which is 82.7% Argon, 17% CO_2, and 0.3% Freon. One plane with evenly-spaced wires which are perpendicular to the y-axis and maintained at a high, positive voltage is opposite another solid, grounded plane. Just as with a DC plane, a traversing charged particle will ionize gas molecules, producing free electrons that are collected at the nearest PWC wire(s). With the PWC detectors, we record only which wire(s) is hit, not any timing information. With the spacing between the wires at 2mm, the resulting resolution is approximately 600 microns.

The major component of the magnetic field for both of the large-aperture copper-coil magnets, labeled M1 and M2 in Figure 2.1, points vertically downward. A charged particle traveling in the $+z$ direction, therefore, accelerates horizontally; positive particles eastward and negative particles westward. The upstream magnet M1, with a maximum strength of about 5 kG, gives charged particles a transverse momentum kick of approximately 0.212 GeV/c; the downstream magnet M2, with a maximum strength of about 7 kG, gives a 0.324 GeV/c p_T kick. Given tracking information both upstream and downstream of each magnet and given a mapping of the magnetic field everywhere, the off-line reconstruction code can determine the momenta of charged particles.

2.3.4 Identifying particles

The particle-identification detectors of the Tagged Photon spectrometer consist of two Čerenkov counters, an electromagnetic calorimeter, a hadronic calorimeter and two muon walls. This charm-pair analysis only makes use of the particle-identification information from the two Čerenkov counters. References [35, 36] provide more details about the latter detectors.

A charged particle radiates Čerenkov radiation if its velocity is greater than the local phase velocity of light. The threshold velocity for such radiation to be emitted, therefore, depends on the mass of the particle and on the index of refraction of the medium the particle is traversing. The chambers of the two Čerenkov counters, labeled C1 and C2 in Figure 2.1, have different gas mixtures (and, therefore, different indices of refraction): C1 contains 100% Nitrogen and C2 contains 20% Nitrogen and 80% Helium. Assuming 100% efficiency for collecting the Čerenkov radiation, a charged kaon, for example, can be uniquely identified in the momentum range 20-36 GeV/c because no other charged particle produces radiation in both counters.

The Čerenkov radiation in each counter is collected by a plane of spherical mirrors which is perpendicular to the z-axis and downstream of the gas chamber. The light incident on each mirror is reflected into a different light-collecting Winston cone. Each Winston cone is coupled to a photomultiplier tube. The C1 plane is segmented into 28 mirrors and the C2 plane into 32 mirrors, with finer segmentation near the beam axis.

For each charged-particle type, we know the number of photons we expect to collect as a function of momentum for each Čerenkov counter. During off-line reconstruction, we are therefore able to assign to each charged particle, using Poisson statistics, the probability for being an electron, a muon, a pion, a kaon, or a proton.

2.4 Data Acquisition

As with the two preceding fixed-target experiments at TPL, the triggering philosophy of E791 was to use very loose constraints, recording as many events as possible with a minimum bias due to the triggering requirements. The tighter selection criteria necessary for obtaining significant charm signals are applied after the data is recorded, when time and computing resources are more available [37].

Specifically, an event is recorded if the following criteria are met:

- Only one π^- beam particle is detected in a scintillation counter upstream of the target;
- At least four charged tracks are detected in a scintillation counter downstream of the target; and
- A minimum of approximately 4.7 GeV of energy is deposited transverse to the beam line in the electromagnetic and hadronic calorimeters.

This choice is based on the desire for an unbiased trigger and on the ability of the data acquisition (DA) system, upgraded from the E769 experiment, to collect and record data very quickly. During the 23-second spills from the Tevatron, data from the detectors discussed in the previous section are digitized by various electronics systems. Data from one event, approximately 3 kbytes, is sent to memory buffers along eight parallel paths in approximately 10 microseconds.

The data, however, cannot be reassembled into events, compressed, and written to tape at 3 kbytes per 100 μseconds, i.e., 30 Mbytes per second. First-in-first-out (FIFO) memory buffers, able to hold 80 Mbytes of data each, feed the data more slowly ($\sim$9.5 Mbytes per second) to processors (CPU) housed in six VME crates during both the 23 second spill period and the 34 second interspill period. The processors assemble events in parallel and the events are written to tape in parallel. Seven Exabtye 8200 tape drives are controlled from each VME crate, resulting in a total of 42 tape drives each recording 0.24 Mb of data per second[38]. E791 ultimately wrote 50 Terabytes of data onto 24,000 2-Gbyte 8-mm tapes.

2.5 Data Processing

The 24,000 tapes of raw data which were collected during a six month period ending in January 1992 were processed in several stages. Figure 2.2 illustrates the pyramid-like structure of the data processing and Table 2.1 lists the number of distinct output streams as well as the number of tapes and events per output stream at each level (I-V) in the pyramid.

Table 2.1: The number of different output streams, as well as the number of tapes and events per output, at each level in the E791 data-processing scheme.

Level		Outputs per Level	Tapes per Output	Events per Output/10^3
I.	Raw Data	1	24,000	20,000,000
II.	Reconstruction/Filtering	1	13,000	3,000,000
III.	Stripping	2	3,500	1,000,000
IV.	Substripping	15	100-1,000	60,000[a]
V.	Analyses	30	1-10	4[b]

[a] Refers to the substrip used in this charm-pair analysis.

[b] Refers to the number of thousands of events, including background events, that passed the final charm-pair selection criteria (discussed in Chapter 4.)

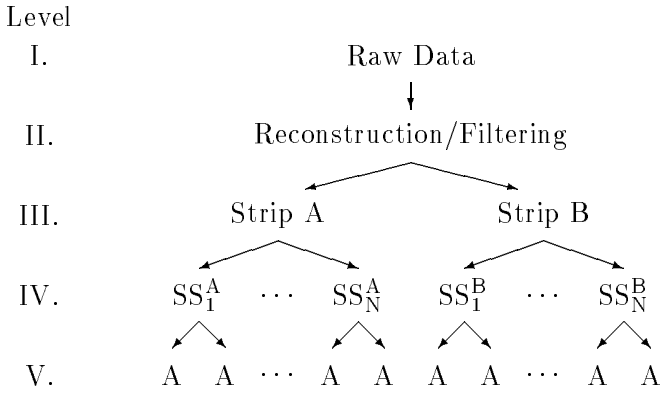

Figure 2.2: The E791 data-processing scheme, beginning with 24,000 raw data tapes and ending with approximately 30 different analyses processing 1 to 10 tapes each. See Table 2.1.

The first stage of data processing takes us from raw data to reconstructed and filtered data (i.e., from level I to level II, in Table 2.1). "Raw data" for an event is the compressed digitized output from each of the detector systems described in Section 2.3; for example, each SMD strip that was hit or the number of photons gathered from each Čerenkov counter mirror. "Reconstructed data" is the result of off-line processing of the raw data. For example, using all the SMD and DC hits, as well as a detailed map of the magnetic field for both magnets, a list of the positions, slopes and momenta, as well as the errors on these values, of all charged-track candidates is obtained.

Once the charged tracks have been reconstructed, including the π^- beam upstream of the target, the off-line reconstruction code searches for the primary interaction vertex and any secondary decay vertices downstream of this primary vertex. The E791 filter requires that the π^- beam is reconstructed and that at least one secondary decay vertex is found. This filter retains most events containing charmed particles while eliminating approximately 85% of the data.

The second stage of data processing, called stripping, is a search for all reconstructable charm decay modes. The stripping algorithm is a simple Boolean OR of sixteen physics filters, in which all events passing any of the first ten filters are saved on the so-called Stream A output and all events passing any of the latter six filters are saved on the Stream B output. Generally, Stream A corresponds to events with a secondary vertex significantly separated from the primary vertex while Stream B events contain a long-lived particle such as a K_S^0 or Λ^-. Our charm-pair analysis begins from the Stream A output.

For this analysis, the most significant physics filter is the one which searches for a pair of charged tracks in which at least one of the tracks has a significant probability, based on Čerenkov information, of being a kaon or a proton. The pair is required to form a vertex in which the χ^2 for the vertex fit is less than seven. In addition, the vertex must be downstream of and relatively well-separated from the primary vertex.

Both the first and second stage of data processing, discussed above, occured at four large computer "farms" — dedicated, parallel processing systems — at Kansas State University, The University of Mississippi, Fermi National Accelerator Laboratory, and Centro Brasileiro de Pesquisas Físicas in Brasil.

For our charm-pair analysis, the next stage of data processing (substripping in Table 2.1) was conducted at Fermi National Accelerator Laboratory. In this substrip, which uses a candidate-driven approach[1], we search for the following decay modes (and the respective charge conjugate modes): $D^0 \to K^-\pi^+$, $K^-\pi^+\pi^0$, $\pi^+\pi^-\pi^+\pi^-$, $K^-\pi^+\pi^-\pi^+$, $K^-K^+\pi^-\pi^+$, $K^-K^+K^-\pi^+$; and $D^+ \to K^-\pi^+\pi^+$. The final stage of data processing, in which we search for fully reconstructable charm-pair decays, is discussed in detail in the following chapter.

[1]The difference between a "candidate-driven" approach and a "topology-driven" approach is discussed in Section 3.1.

Chapter 3

Event Selection

3.1 Philosophy and Methodology

Our charm-pair search focuses exclusively on Cabibbo-favored decay modes of D mesons that can be fully reconstructed with relatively high efficiencies: $D^+ \to K^-\pi^+\pi^+$, $D^0 \to K^-\pi^+$, $D^0 \to K^-\pi^+\pi^+\pi^-$, and the respective charge conjugate modes. In this section, we motivate our event-selection philosophy, provide an overview of our methodology, and discuss how our approach differs from previous charm-pair searches.

3.1.1 Candidate-Driven Approach

Most E791 analyses use a "topology-driven" approach to reconstruct charm decays where secondary vertices are found topologically, after reconstructing the primary interaction vertex, without considering the effective mass of the reconstructed vertex. Instead, we use a "candidate-driven" approach, working on the premise that topological constraints can possibly be loosened if we use information about the masses of the charmed particles for which we are searching. In particular, we search for combinations of two, three, or four charged tracks — including tracks nominally from the primary interaction vertex — that have an effective mass within a window centered around the mass of real D mesons with a width roughly twenty times the expected experimental mass resolution. After finding two D candidates, the primary vertex is re-fit with any tracks now associated with either candidate removed.

The main disadvantage of a candidate-driven approach is that it is much more

CPU intensive than the topological approach. This approach also would not be effective for partially reconstructing charm vertices in which one or more of the decay products (*e.g.*, a neutrino) cannot be reconstructed. The conclusion of an E791 candidate-driven single-charm analysis, which reconstructed charged D mesons decaying to $K^{\mp}\pi^{\pm}\pi^{\pm}$, was that the most significant signal was obtained only after applying the tight topological constraints of the topology-driven method.

A charm-pair event, however, has many more variables to discriminate signal from background events than a single-charm event. If, in a single-charm search, we use the variables $(V_1, V_2, ..., V_N)$, then in a charm-pair search we use $(V_1^1, V_2^1, ..., V_N^1)$ for the first D meson candidate and $(V_1^2, V_2^2, ..., V_N^2)$ for the second. In addition, variables describing the separation of the vertices of the two candidates are also effective. This abundance of parameters that can be used to separate signal events from background events was our primary motivation for choosing the more CPU intensive, but more flexible, candidate-driven approach.

3.1.2 Parallel Search Algorithm

One algorithm used to find charm-pairs is to use tight selection criteria to find the first charmed meson candidate, followed by looser criteria to find the second candidate. Schematically, $\vec{V}^1 > \vec{h}$ and $\vec{V}^2 > \vec{l}$, where $\vec{V}$ is a set of discrimination variables, $\vec{h}$ is a set of stringent or "hard" selection criteria, and $\vec{l}$ is a set of less restrictive or "loose" selection criteria. Rather than using this sequential approach, we search for the two charmed particles in parallel. Specifically, for $m-n$ pronged candidates, where $D^m \rightarrow K\ (m-1)\pi$ and $D^n \rightarrow K\ (n-1)\pi$ and $m \neq n$, we iteratively select the "best" pair of selection criteria of the form

$$V_i^m > p_i \quad \text{and/or} \quad V_j^n > q_j. \tag{3.1}$$

We clarify what "best" means in Section 3.1.3 and the variables $\vec{V}$ used in this analysis are defined in Section 3.2.1. Equation 3.1 allows for the more traditional selection criteria of the form $(\vec{V}^m > \vec{h}$ and $\vec{V}^n > \vec{l})$, as well as many other possible types of selection criteria.

For $n-n$ pronged pairs, we require symmetric selection criteria:

$$V_i^n \ \text{and/or} \ V_i^{\overline{n}} > p_i. \tag{3.2}$$

As illustrated in Figure 3.1, Equation 3.2 allows $n-n$ pronged pairs to have selection criteria of the form $(\vec{V}^{MAX} > \vec{h}$ and $\vec{V}^{MIN} > \vec{l})$ — along with many other possibilities — where

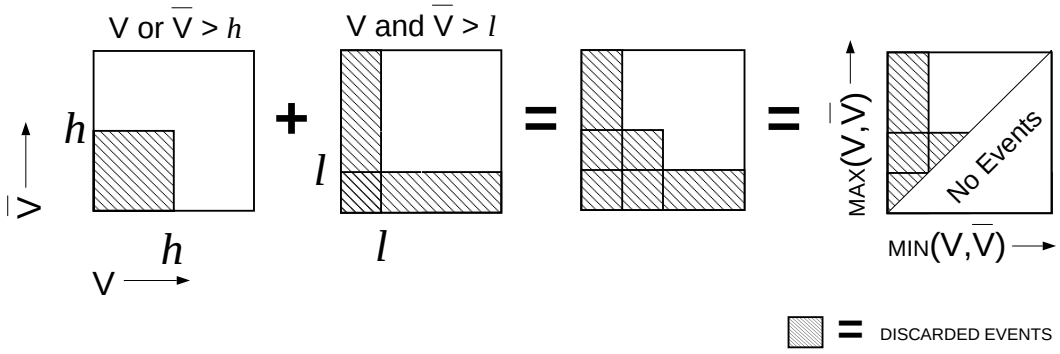

Figure 3.1: An illustration of how selection criteria of the form V^n and/or $V^{\overline{n}} > p$, which are symmetric between the two D candidates, can lead to cuts of the form ($\vec{V}^{MAX} > \vec{h}$ and $\vec{V}^{MIN} > \vec{l}$).

V_i^{MAX} is the maximum of the D and $\overline{D}$ discrimination variables V_i^n and $V_i^{\overline{n}}$ and V_i^{MIN} is the minimum of these two variables. The difference between this form and the more traditional form ($\vec{V}^1 > \vec{h}$ and $\vec{V}^2 > \vec{l}$) is that the former allows the more stringent cuts to be distributed between the D and the $\overline{D}$ candidates, whereas the latter requires that either the D or the $\overline{D}$ candidate survive all the hard cuts $\vec{h}$.

3.1.3 Iterative Optimization Procedure

The starting point of this analysis is a sample of "substripped" (Section 2.5) events, in which each event has at least one D candidate decaying to one of several modes: $K\pi$, $K\pi\pi$, $K\pi\pi\pi$, $KK\pi\pi$, $KKK\pi$, and $\pi\pi\pi\pi$. Consistent with our candidate-driven approach, the selected candidates have an effective mass in the approximate range 1.7 to 2 GeV and are subject to only very loose topological constraints. Our analysis focuses on the Cabibbo-favored modes: $K\pi$, $K\pi\pi$, and $K\pi\pi\pi$. At this substrip level, our signal-to-background ratio in the signal region is on the order of 10^{-5}.

In this section, we discuss how we iteratively proceed from this initial sample to the final sample shown in Figure 3.2, for which the signal-to-background ratio is greater by approximately five orders of magnitude. This figure shows a scatter plot of the mass of the D candidate, $M^{K^-n\pi}$, versus the mass of the $\overline{D}$ candidate, $M^{K^+n\pi}$, in each event, for candidate masses in the range 1.7 to 2.0 GeV. The number of pions n is not necessarily the same for the D and $\overline{D}$ in a given event. There are four types of events in this plot:

- Combinatoric background events consisting of a fake D and a fake $\overline{D}$.

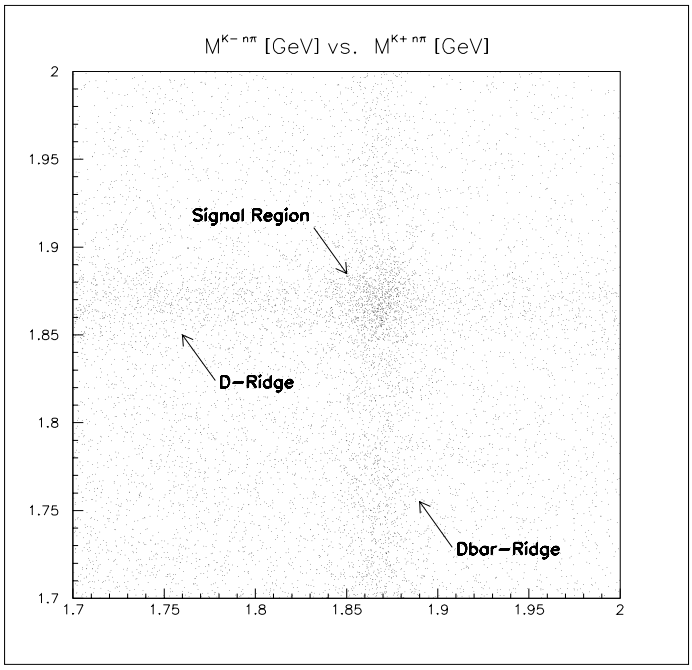

Figure 3.2: Scatter plot of $M^{K^-n\pi}$ versus $M^{K^+n\pi}$ for the final data sample of $D\overline{D}$ candidates. The plot contains four types of events: combinatoric background events spread over the entire region; D- and $\overline{D}$-ridge events, containing one real D and one fake D meson; and real $D\overline{D}$ events in the central signal region.

- D-ridge background events consisting of a real D and a fake $\overline{D}$. These events lie along a horizontal ridge in Fig. 3.2.
- $\overline{D}$-ridge background events consisting of a real $\overline{D}$ and a fake D. These events lie along a vertical ridge in Fig. 3.2.
- Signal events consisting of a real D and a real $\overline{D}$.

The combinatoric events are spread over the entire 2-dimensional mass window. Most of the D-ridge events, clearly seen as a horizontal band in Figure 3.2, are in the region

$$M_D - 2\sigma_{M_D} < M^{K^-n\pi} < M_D + 2\sigma_{M_D},$$

where M_D is the mean and σ_{M_D} is the resolution of the mass distribution of real D's. Most of the $\overline{D}$-ridge events are in the region

$$M_{\overline{D}} - 2\sigma_{M_{\overline{D}}} < M^{K^+n\pi} < M_{\overline{D}} + 2\sigma_{M_{\overline{D}}}.$$

Finally, most of the signal events are in the so-called "signal region:"

$$M_D - 2\sigma_{M_D} < M^{K^-n\pi} < M_D + 2\sigma_{M_D} \text{ and } M_{\overline{D}} - 2\sigma_{M_{\overline{D}}} < M^{K^+n\pi} < M_{\overline{D}} + 2\sigma_{M_{\overline{D}}}.$$

Along with signal events, this region contains all three types of background events.

Given an initial sample of data with a signal-to-background ratio on the order of 10^{-5}, we cannot reliably use our data to determine the distribution of discrimination variables for real $D\overline{D}$ events. Instead, we use the PYTHIA/JETSET Monte Carlo event generator, introduced in Chapter 1, to estimate our signal distributions, and use the data only to determine our background distributions. The events generated by the PYTHIA/JETSET Monte Carlo are passed through a simulation of the various E791 detectors discussed in Chapter 2, producing simulated "raw" data. With one exception, which we discuss in Section 3.2.2, we process the simulated Monte Carlo raw data and the real raw data in exactly the same manner. As discussed below, we explicitly exclude the signal region of our data to determine the background distributions once the signal-to-background ratio is on the order of 10^{-2}.

At any given level (*e.g.*, the substrip level), we begin with N_{MC} Monte Carlo "signal" events and N_{BK} background events from data. We then test all possible pairs of selection criteria (Equation 3.1 or 3.2), applying each to both the Monte Carlo and the real data events. For each pair of selection criteria, we determine how many Monte Carlo and how many background events survive: N'_{MC} and N'_{BK}, respectively. We consider only the subset of selection criteria that remove no more than $\sim 5\%$ of the Monte Carlo signal events. Specifically, we require $\Delta N_{MC}/N_{MC} = (N_{MC} - N'_{MC})/N_{MC}$ to fall within a fixed, narrow window; typically, $\Delta N_{MC}/N_{MC} = 0.05 \pm 0.01$. From this subset of selection criteria, we choose the one that yields the signal with maximum significance; i.e., with the maximum $N'_{MC}/\sqrt{N'_{BK}}$.[1] The shape of $N'_{MC}/\sqrt{N'_{BK}}$ as a function of all possible cuts does not depend on the relative size of the Monte Carlo and data samples.

We then apply the selection criteria which maximized the significance to both the Monte Carlo and data events and begin again, continuing the iterative procedure until further iterations decrease the statistical significance of the signal ($N'_{MC}/\sqrt{N'_{BK}} \leq N_{MC}/\sqrt{N_{BK}}$). We test the same set of discrimination variables $\vec{V}$ at every iteration, allowing a given variable V_i to be selected more than once as the most significant variable. We

[1] This formula for the significance is an approximation that is discussed in more detail below.

do this optimization procedure separately for each type of $m-n$ pronged pair: 2-2, 2-3, 2-4, 3-3, 3-4 and 4-4.

The optimization method described above attempts to maximize the significance $S = N_S/\sigma_{N_S}$ of our $D\overline{D}$ signal, where N_S is the number of signal events and σ_{N_S} is the statistical uncertainty on that number. We assume for a given sample of events that we are able to obtain a near perfect estimate of the number of background events in the signal region, N_B, by using the size and shape of the mass distribution outside the signal region. The number of signal events is then $N_S = N_{SR} - N_B$, where N_{SR} is the number of events in the signal region, and

$$\sigma_{N_S} = \sqrt{\sigma^2_{N_{SR}} + \sigma^2_{N_B}} \approx \sqrt{\sigma^2_{N_{SR}}} = \sqrt{N_{SR}} = \sqrt{N_S + N_B}.$$

For most iterations, the number of background events is much larger than the number of signal events, allowing the statistical significance $S = N_S/\sigma_{N_S} = N_S/\sqrt{N_S + N_B}$ to be approximated by $N_S/\sqrt{N_B}$.

As more and more selection criteria are applied to our data sample, the charm signal (both the D-ridge and $\overline{D}$-ridge single-charm signal and the charm-pair signal) becomes more significant. When these signals become noticeable ($\sim$1% of the events), we explicitly exclude both the signal region and the two ridge regions in the 2-dimensional mass plot (see Fig. 3.2) to obtain a sample of relatively pure combinatoric background events for determining our background distributions. When we begin to be dominated by the ridge background rather than the combinatoric background, we then exclude only the signal region when obtaining our background sample. Lastly, when the charm-pair signal in data becomes significant with respect to the backgrounds ($N_S/N_B \sim 0.1$), at each iteration we maximize $N'_{MC}/\sqrt{N'_{MC} + N'_{BK}}$ rather than $N'_{MC}/\sqrt{N'_{MC}}$. This requires properly normalizing the sample size of the background events with respect to Monte Carlo events.

When we begin to see a charm-pair signal in data, we also require that the selection criteria chosen at any given iteration does not degrade the true significance of our charm-pair signal (*i.e.*, the significance obtained using the signal from data rather than the signal from the Monte Carlo).[2] Given the relatively small sample of real charm-pair events, we risk tuning on statistical fluctuations if we use the signal from data to optimize the selection criteria. Hence, we only use the true significance to determine whether the chosen selection criteria should be loosened slightly. This additional step during the later

[2]Section 4.1.3 describes how to determine the significance of the charm-pair signal from our data sample.

part of our optimization procedure helps avoid the possible problem of the Monte Carlo inaccurately simulating the detector, usually producing distribution that are "too good", and, therefore, selection criteria that are too stringent.

3.1.4 Comparison with Other Approaches to Signal Optimization

A standard method of signal optimization is to first select a set of discrimination variables $\vec{V}$ and then examine, for each variable V_i, the statistical significance of the signal as a function of p_i, where background and signal events survive if $V_i > p_i$. The selection criteria that maximizes the significance is applied to both the signal and background samples and the procedure is repeated, until the significance no longer increases.

Geometrically, the significance of a signal is a multi-dimensional function of all possible selection criteria and selecting a set of discrimination variables determines the axes along which we explore this function. In the standard signal optimization method described above, one iteratively projects the significance onto each axis, determining for a given iteration the axis V_i and the value p_i that maximizes the significance of the signal.

The optimization method we use in this $D\overline{D}$ analysis is slightly more elaborate than the standard method. As well as making 2-dimensional projections in discrimination-variable space (i.e., examining both charm candidates simultaneously) and allowing both or- and and-type cuts, we also explicitly take smaller steps along the discrimination-variable axes by selecting the most significant cut at a fixed $\Delta N_S/N_S$, with $\Delta N_S/N_S \sim 0.05$. Taking smaller step sizes, in principal, allows us to stay closer to the path of steepest ascent which may be, for example, along a linear combination of cut variable axes. Smaller step sizes also allow us to distribute the selection criteria among more discrimination variables, making us less dependent on the predictions of the Monte Carlo event generator for a particular discrimination variable.

One limitation of both the standard optimization method and our method is that each iteration effectively eliminates an entire region of discrimination-variable space from further exploration. Other optimization methods that are becoming more and more popular, based for example on neural-network or binary-decision-tree algorithms[39], allow a more systematic exploration of the entire multi-dimensional space of possible selection criteria. We believe such algorithms could be effectively applied to future charm-pair searches.

3.2 Highlights of the Event Selection Procedure

In this section, we first define the variables used in our charm-pair search to discriminate signal events from background. We then discuss selection criteria applied early in the charm-pair search to the primary vertex, to all candidate decay tracks, and to all single-charm D candidates. Lastly, we show results from the first iteration of choosing charm-pair selection criteria of the form shown in Equations 3.1 and 3.2.

3.2.1 Definition of Discrimination Variables

The fourteen variables used in our charm-pair search are defined below. Each variable name is followed either by (>), indicating that a candidate passes the criteria if the variable is greater than some minimum value; or by (<), indicating that a candidate passes if the variable is less than some maximum value. The variables that begin with "S" are so-called "scaled" variables, constructed by dividing a variable, estimated from the reconstructed positions and/or momenta of particles in an event, by the one-standard-deviation experimental uncertainty on the measurement of that variable.

CHIS (<) χ^2 per degree of freedom for the fit of the tracks in a candidate D decay to a common vertex.

DIP (<) The distance, in a plane transverse to the beam axis, between the primary interaction vertex and the projection of the candidate D momentum vector back to the z-position of the primary vertex.

SDIP (<) DIP, defined above, divided by the uncertainty on DIP.

KPRB (>) Probability that the candidate kaon track is a kaon, based on Čerenkov information.

PTB (<) The component of the candidate-D momentum vector that is perpendicular to the candidate's line-of-flight, as determined by the positions of the primary and secondary vertices.

PTDK (>) Scalar sum, over the decay tracks of the D candidate, of the square of the momentum transverse to the candidate-D momentum vector.

SDZ (>) The separation, along the z-axis, of the primary vertex and the candidate D vertex, divided by the uncertainty on the separation.

SDISO (>) The smallest SDCA[1] of all the tracks from the primary vertex to the candidate-D vertex.

SPISO (>) The smallest SDCA[1] of all the decay tracks of a D candidate to the primary vertex.

SPRAT (<) The product of the SDCA[1] of the decay tracks of a D candidate to its own vertex divided by the product of the SDCA of these tracks to the primary vertex.

SSISO (>) The smallest SDCA[1] of all the decay tracks of a D candidate to the vertex of the other D candidate. Given an $m-n$ pronged charm-pair candidate, SSISO^{m} uses the tracks of the m-pronged candidate and the vertex of the n-pronged candidate.

SSRAT (<) The product of the SDCA[1] of the decay tracks of a D candidate to its own vertex divided by the product of the SDCA of these tracks to the vertex of the other D candidate. Given an $m-n$ pronged charm-pair candidate, SSRAT^{m} uses the tracks of the m-pronged candidate and, in the denominator, the vertex of the n-pronged candidate.

STRG (>) Separation, along the beam direction, of the candidate-D vertex from the nearest edge of a target, divided by the uncertainty on the separation.

TAU (>, <) Lifetime of the D candidate. The lifetime distribution for real D events is exponential. Background events cluster both at very small lifetimes, when the primary vertex is split into a primary plus a fake D vertex; and at very large lifetimes when interactions in target foils downstream of the primary interaction mimic D decay vertices.

3.2.2 Preliminary Selection Criteria

Prior to the iterative procedure to find the optimum charm-pair selection criteria, constraints are imposed (1) on the primary vertex, (2) on the tracks used to form D

[1]SDCA is the distance of closest approach of a particular track to a particular vertex, divided by the uncertainty in that distance.

candidate vertices, and (3) on the single-charm candidates used to form the charm-pair candidates. For the primary vertex, which is re-fit after removing any tracks from either of the two candidate-D decay vertices that were originally associated with the primary vertex, we require:

- at least three tracks;
- the z-position to be consistent with an interaction occurring inside a target foil; and
- the χ^2 per degree of freedom of the vertex fit to be less than 15.

For the candidate-D decay tracks, we require:

- tracking information (*i.e.*, hits) in the silicon microstrip detectors downstream of the target and, for momentum determination, in the drift chamber planes both upstream and downstream of the first magnet.
- the χ^2 per degree of freedom of the track fit to be less than 6; and
- the measured momentum to be between 1 and 300 GeV.

For the single-charm candidates, we require:

- the effective mass to be between 1.7 and 2 GeV;
- the χ^2 per degree of freedom of the vertex fit to be less than 25;
- the momentum to be less than 500 GeV; and
- SDZ (defined in Section 3.2.1) to be greater than 1.

From these three sets of selection criteria, applied to our sample of substripped events, we obtain our initial sample of charm-pair candidates. For each three-pronged D candidate, the sum of the charges of the candidate decay tracks must be either $+1$ or -1, and the kaon is defined to be the oddly charged tracked. For each two- and four-pronged D candidate, the sum of the charges must be 0 and the kaon is defined to be the track with the greatest probability for being a kaon, based on Čerenkov information.

Given such loose criteria, finding multiple $D\overline{D}$ candidates per event is possible. For our data sample, which we use to determine the distribution of discrimination variables for background events, we allow multiple candidates per event — until near the end of

the optimization procedure. For our Monte Carlo sample, allowing multiple candidates per event smears the estimate of the real $D\overline{D}$ distributions. That is, only one candidate is the true signal candidate; the others are background. For each charged-particle Monte Carlo track, we have both reconstructed track parameters — obtained from simulated raw data in exactly the same way as real data — and the original track parameters from the physics simulation. We allow only one Monte Carlo candidate per event by choosing the candidate for which the track parameters of the reconstructed D meson decay tracks and the original simulated decay tracks are in the best agreement. The track parameters we consider in our comparison are the slopes with respect to the z-axis — $\mathrm{d}x/\mathrm{d}z$ and $\mathrm{d}y/\mathrm{d}z$ — and the x and y intercepts at z=0. Also we only accept Monte Carlo candidates with the same number of decay tracks, for both D mesons, as produced in the physics simulation.

Before beginning the iterative search for the optimum charm-pair selection criteria described in Section 3.1, for a few iterations, we optimize our single-charm signal. Specifically, we form three sub-samples of single-charm D candidates (with two such candidates per charm-pair candidate) from both data and Monte Carlo events: all 2-pronged ($K^{\mp}\pi^{\pm}$) candidates, all 3-pronged candidates, and all 4-pronged candidates. For each sample, we test all possible selection criteria of the form $V_i > p_i$ or $V_i < p_i$ where $\vec{V}$ = (CHIS, DIP, PTDK, PTB, SDIP, SDZ, STRG, SPISO, SPRAT, SDISO, TAU). At each iteration, just as with the charm-pair search, we select the criteria that maximizes the significance, $N'_{MC}/\sqrt{N'_{BK}}$, while eliminating only $\sim 5\%$ of the signal, $\Delta N_{MC}/N_{MC} = 0.05 \pm 0.01$.

Results from the first iteration of selecting the optimum criteria for the $K\pi$ candidates are shown in Figure 3.3. Figure 3.3a shows $N'_{MC}/\sqrt{N'_{BK}}$, given $\Delta N_{MC}/N_{MC} \approx 0.05$, for each discrimination variable $V_i, i = 1 \ldots 11$. We arbitrarily normalize the number of Monte Carlo signal events to 1 and the number of background events to 10,000. Hence, $N'_{MC}/\sqrt{N'_{BK}} < 1/\sqrt{10000} = 0.01$ implies that imposing the selection criteria worsens the significance of the signal. In this figure, results are shown for both "unweighted" and "weighted" background candidates, where the latter are weighted according to the inverse of the number of D candidates in the given event. We were concerned in the early stages of the optimization procedure that a few events with anomalously large numbers of candidates would distort the background distributions. We find, however, that weighting the events never significantly affects which criteria are selected. Figure 3.3a indicates that PTDK is the variable that maximizes the significance given $\Delta N_{MC}/N_{MC} \approx 0.05$. As discussed in Sec. 3.2.1, PTDK is the scalar sum, over the decay tracks of the D candidate, of the square

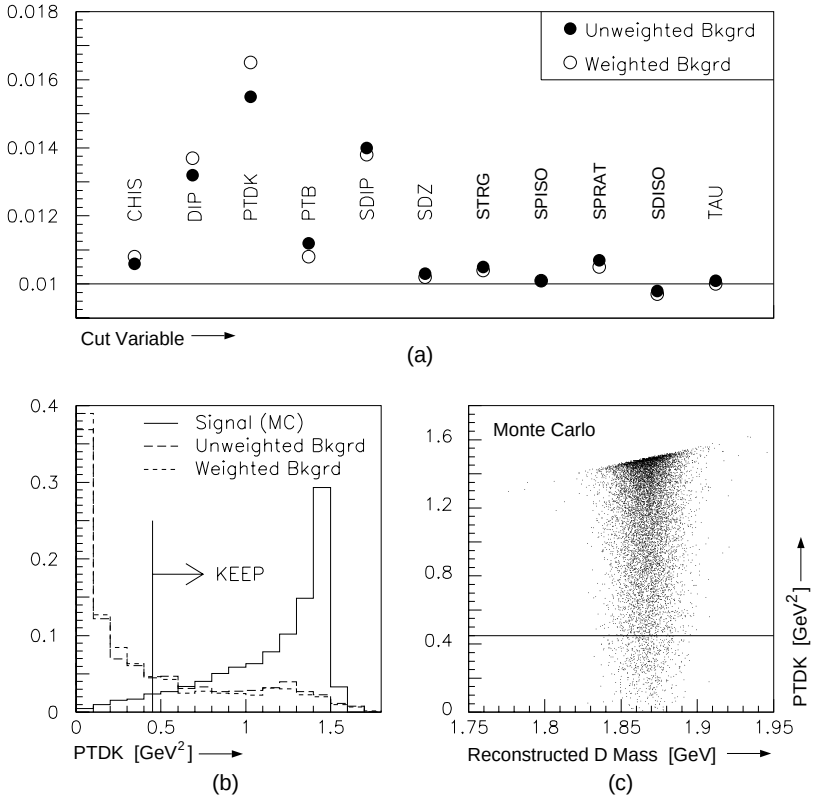

Figure 3.3: Results from the first iteration of optimizing 2-pronged single-charm selection criteria: (a) $N'_{MC}/\sqrt{N'_{BK}}$ (given $\Delta N_{MC}/N_{MC} \approx 0.05$) vs. Cut Variable, indicating that PTDK is the best cut variable for the first iteration. The constraint $\Delta N_{MC}/N_{MC} \approx 0.05$ determines the value at which the cut is made. (b) PTDK distributions, normalized to the same area, for both the Monte Carlo signal events and the weighted and unweighted background events (c) Scatter plot of PTDK versus the reconstructed mass of the 2-prong D meson from the Monte Carlo sample, indicating that PTDK is not significantly correlated to the mass of the D meson for PTDK < 0.45 GeV^2.

of the momentum transverse to the candidate-D momentum vector. Figure 3.3b shows the distributions, normalized to the same area, for both the Monte Carlo signal events and the weighted and unweighed background events. The optimum cut PTDK > 0.45 GeV^2, consistent with $\Delta N_{MC}/N_{MC} \approx 0.05$, is indicated.

The variable PTDK is effective at discriminating signal events from background events because decay products of heavy charmed mesons are produced at large transverse momenta with respect to the direction of the charmed meson, whereas background candidates, often formed from random tracks from the π^--nucleon interaction, are more likely to have the candidate parent momentum vector and decay tracks all aligned very closely to

Table 3.1: Selection criteria applied to all D candidates before beginning the charm-pair optimization procedure. Variables are defined in Sec. 3.2.1.

Selection Criteria		$K\pi$	$K\pi\pi$	$K\pi\pi\pi$
CHIS	$<$	25	25	15
DIP [μm]	$<$	45	45	
PTDK [GeV^2]	$>$	0.45		0.25
SDIP	$<$			1.8
SDZ	$>$	1	1	3.5
SPRAT	$<$		0.1	0.055
STRG	$>$			1

the z-axis. We are careful, however, not to choose selection criteria that effectively make a cut on the mass of the D candidates. Imposing such criteria would distort the linear mass distribution of background events. As discussed in Chapter 4, understanding the distribution of background events is essential for determining the number of signal events. In Figure 3.3c, we demonstrate that, although PTDK is correlated to the mass of D meson, the correlation is not significant below 0.45 GeV^2 where the cut is made.

Imposing a few single-charm selection criteria before beginning our charm-pair search dramatically reduces the computer processing time involved in selecting a sample of charm-pair candidates from our data. The final single-charm selection criteria are listed in Table 3.1.

3.2.3 First Iteration Results

After imposing the preliminary selection criteria discussed in the previous section, we begin our optimization of charm-pair selection criteria of the form

$$V_i^m > p_i \quad \text{and/or} \quad V_j^n > q_j$$

for $m-n$ pronged pairs with $m \neq n$, and

$$V_i^n \ \text{ and/or } \ V_i^{\overline{n}} > p_i$$

for $n-n$ pronged pairs, where $\vec{V}$ = (CHIS, DIP, PTDK, PTB, SDIP, SDZ, STRG, SPISO, SPRAT, SDISO, TAU, KPRB, SSRAT, SSISO). (See Sec. 3.2.1 for variable definitions.) As discussed in Sec. 3.1.3, for each type of $m-n$ pronged pair, we iteratively select the criteria that maximizes the significance, $N'_{MC}/\sqrt{N'_{BK}}$, while eliminating only $\sim 5\%$ of the signal.

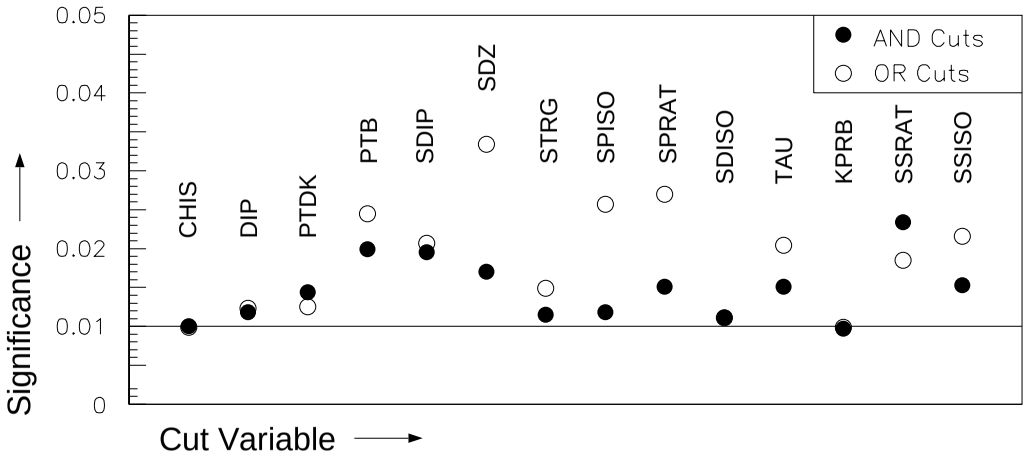

Figure 3.4: Results from the first iteration of optimizing 3-3 pronged charm-pair selection criteria: A plot of $N'_{MC}/\sqrt{N'_{BK}}$ (given $\Delta N_{MC}/N_{MC} \approx 0.05$) versus cut variable, indicating that an or-type cut on the variable SDZ is the best first iteration cut. The constraint $\Delta N_{MC}/N_{MC} \approx 0.05$ determines at what value the cut is made. The Monte Carlo and data samples are normalized such that $N_{MC}/\sqrt{N_{BK}} = 0.01$ before any cuts are applied. Open circles show results for or-type cuts and solid circles for and-type cuts.

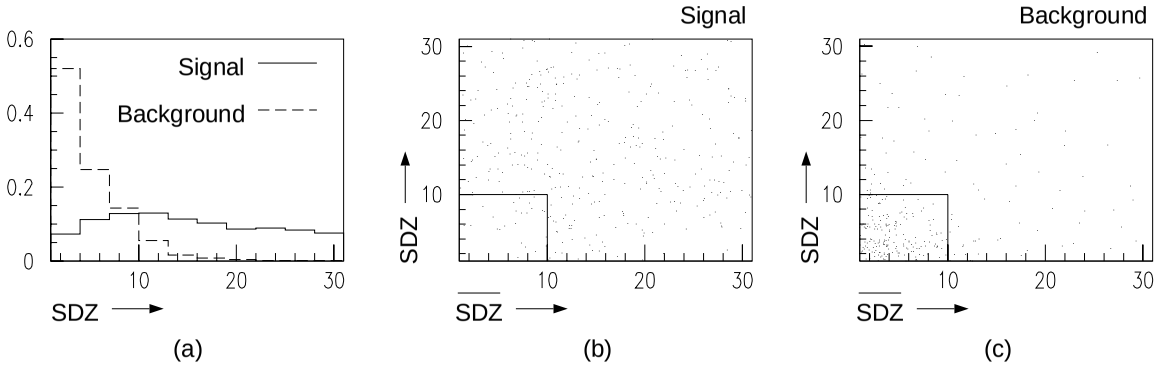

Figure 3.5: Monte Carlo (signal) and data (background) SDZ distributions for the 3-3 pronged candidates. (a) Single-charm SDZ distributions normalized to unit area. (b) $\mathrm{SDZ_D}$ versus $\mathrm{SDZ_{\overline{D}}}$ for Monte Carlo signal events. (c) $\mathrm{SDZ_D}$ versus $\mathrm{SDZ_{\overline{D}}}$ for background events from data. The boxes in the lower left-hand corner of (b) and (c) show the candidates that are eliminated by the cut ($\mathrm{SDZ_3}$ or $\mathrm{SDZ_{\overline{3}}}$) > 10.

Results from the first iteration of testing all selection criteria on the 3-3 pronged Monte Carlo (signal) and data (background) candidates is shown in Figure 3.4. As with the single-charm results shown in Figure 3.3, we show the value of $N'_{MC}/\sqrt{N'_{BK}}$, given $\Delta N_{MC}/N_{MC} \approx 0.05$, for each discrimination variable $V_i, i = 1 \ldots 14$, where the number of Monte Carlo events is normalized to 1 and the number of background events is normalized to 10,000. The significance for the or-type and and-type cuts are shown with open and

filled circles, respectively. We find that for $\Delta N_{MC}/N_{MC} \approx 0.05$, an or-type cut on SDZ is the optimum cut: SDZ_3 or $\mathrm{SDZ}_{\overline{3}} > 10$, where SDZ is the separation, along the z-axis, between the primary vertex and the candidate D vertex, divided by the uncertainty on the separation.

Figure 3.5 shows the SDZ distributions for signal and background events, indicating which candidates are discarded by applying this cut. Or-type cuts remove charm-pair candidates in which neither single-D candidate looks like a real D, whereas and-type cuts accept candidates in which both single-D candidates looks like a real D. In the early stages of the optimization procedure, when we are dominated by combinatoric backgrounds, or-type cuts are often found to be more effective than and-type cuts. As the D- and $\overline{D}$-ridge background events become more significant, and-type cuts become more effective. For example, after several iterations, the and-type cut (SDZ_3 and $\mathrm{SDZ}_{\overline{3}}$) > 4 is determined to be the most significant, effectively removing D- and $\overline{D}$-ridge background events. The combination of the two cuts, $\mathrm{SDZ}^{\mathrm{MAX}} > 10$ and $\mathrm{SDZ}^{\mathrm{MIN}} > 4$, effectively removes all three types of background events.

Each iteration in the optimization procedure for $m - n$ pronged pairs with $m \neq n$ requires testing $14 \times 14 = 196$ combinations of discrimination variables:

$$V_i^m > p_i \quad \text{and/or} \quad V_j^n > q_j,\ i, j = 1, \ldots, 14.$$

We show the first-iteration result for the 2-3 pronged candidates in Figure 3.6 for a 9×9 subset of variables:

$$\vec{V}_2, \vec{V}_3 = (\mathrm{SDZ}, \mathrm{SPISO}, \mathrm{SPRAT}, \mathrm{STRG}, \mathrm{SDIP}, \mathrm{PTB}, \mathrm{TAU}, \mathrm{SSRAT}, \mathrm{SSISO})$$

(The variable combinations not shown were among the least effective in optimizing the significance of the signal.) There are nine plots, one for each of the nine 2-pronged variables $\vec{V}_2$. Each plot shows $N'_{MC}/\sqrt{N'_{BK}}$, given $\Delta N_{MC}/N_{MC} \approx 0.05$, for each of the nine 3-pronged variables $\vec{V}_3$. The cut ($\mathrm{TAU}_2 > 0.25$ psec or $\mathrm{SDZ}_3 > 10$) is found to be the most significant first iteration cut.

3.3 Final Selection Criteria

As discussed in Section 3.1.3, we continue the iterative procedure to optimize the charm-pair selection criteria until applying further selection criteria does not improve

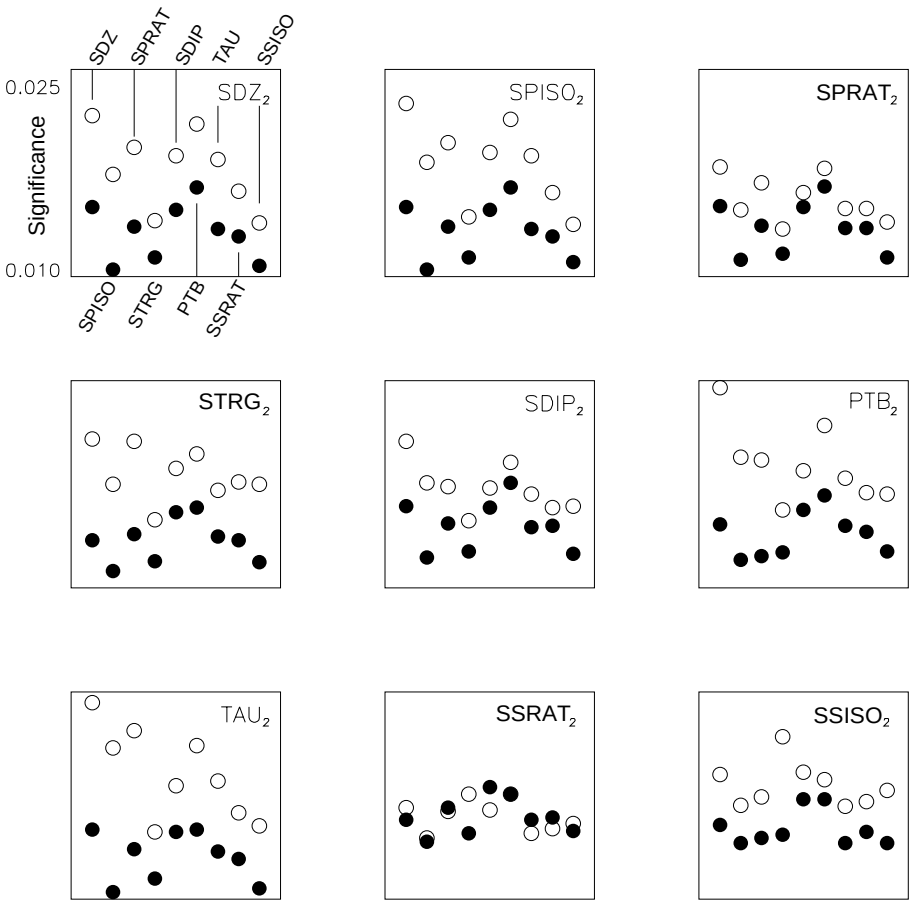

Figure 3.6: Results from the first iteration of optimizing 2-3 pronged charm-pair selection criteria. Each plot shows $N'_{MC}/\sqrt{N'_{BK}}$ (given $\Delta N_{MC}/N_{MC} \approx 0.05$) versus the 3-pronged cut variables. And each plot is associated with a particular 2-pronged cut variable. Open circles show results for or-type cuts and solid circles for and-type cuts. The left-most open circle in the bottom left-hand plot, for example, indicates that applying the cut ($\mathrm{TAU}_2 > p$ or $\mathrm{SDZ}_3 > q$) brings the significance, $N'_{MC}/\sqrt{N'_{BK}}$, to approximately 0.025. The values of p and q, not shown in the plot, meet the requirement that $\Delta N_{MC}/N_{MC} \approx 0.05$. The Monte Carlo and data samples are normalized such that $N_{MC}/\sqrt{N_{BK}} = 0.01$ before any cuts are applied.

the significance. The final results, for all six types of $m - n$ pronged pairs, are shown in Tables 3.2-3.5. The symmetric $n - n$ pronged criteria are in Table 3.2, the 2-3 pronged criteria in Table 3.3, the 2-4 criteria in Table 3.4, and the 3-4 criteria in Table 3.5.

In Figures 3.7-3.9, we test the validity of our optimization procedure by comparing the shapes of the Monte Carlo distributions of cut variables (defined in 3.2.1) to the shapes

Table 3.2: Charm-pair selection criteria for $n-n$ pronged events. The entry "90" in the first row, for example, means all 4-4 pronged candidates must pass the cut ($\mathrm{DIP}_4 < 90\mu$m AND $\mathrm{DIP}_{\overline{4}} < 90\ \mu$m). Variables are defined in Section 3.2.1.

Selection Criteria			$K\pi$ $2-\overline{2}$	$K\pi\pi$ $3-\overline{3}$	$K\pi\pi\pi$ $4-\overline{4}$
DIP [μm]	$<$	AND			90
PTB [GeV]	$<$	AND	1.4	0.85	
		OR	0.4		0.4
PTDK [GeV^2]	$>$	AND		0.17	
SDIP	$<$	OR		1.	
SDZ	$>$	AND		4.3	
		OR		10	8
SPISO	$>$	OR	4.9	4.9	
SPRAT	$<$	OR	0.024	0.01	
SSRAT	$<$	AND		0.004	0.002
		OR			0.001
STRG	$>$	OR	5.2		5.0
TAU [psec]	$>$	AND		0.214	
		OR	0.25		

of the background-subtracted distributions from data[3]. This test is not fool-proof: We can obtain statistically significant distributions from data only after applying all selection criteria, and having similar Monte Carlo and data distributions *after* applying the selection criteria does not guarantee that the distributions are similar *before* applying the selection criteria. It is encouraging, nonetheless, that the Monte Carlo signal distributions and the data signal distributions are in good agreement for all cut variables. In addition, the Monte Carlo and data signal distributions for most variables are significantly different from the distribution for the combinatoric background events (*i.e.,* events for which neither candidate-D mass is in the region $M_D - 2\sigma_D < M^{Kn\pi} < M_D + 2\sigma_D$). Not surprisingly, the optimization procedure does not find variables in which the combinatoric background distribution is very similar to the signal distributions (*e.g.,* CHIS) to be very effective at discriminating signal from background. We do not show the distributions for the variable SDISO because it is not selected as an optimum cut variable at any iteration. For the variable PTDK, we show the distributions for the 2-, 3-, and 4-pronged candidates separately because the distribution is so dependent on the number of decay tracks.

[3]We use the method discussed in Section 4.1.2 to obtain background-subtracted distributions.

Table 3.3: Charm-pair selection criteria for 2-3 pronged events. The third entry "1 OR 5.4" in the first row, for example, means all 2-3 pronged candidates must pass the cut ($PTB_2 < 1$ GeV OR $STRG_3 > 5.4$). Variables are defined in Section 3.2.1.

V^3 / V^2	PTB [GeV] <	PTDK [GeV^2] >	SDIP <	SDZ >	SPISO >	SPRAT >	STRG <
PTB [GeV] <	0.3 OR 0.33			5 AND 2.3	5.4 OR 1		
SPISO >						0.01 OR 7	
SSISO >							4 OR 4
SSRAT <	0.4 AND 0.06	0.2 AND 0.1					
STRG >			1 AND 1				
TAU [psec] >				10 OR 0.25			2 OR 0.15

For several variables (*e.g.*, SPRAT shown in Figure 3.8), although the shape of the data signal distribution resembles the Monte Carlo distribution more than the combinatoric background distribution, the shape of the data signal distribution is somewhat intermediary between the background and Monte Carlo signal distributions. As discussed Section 3.1.3, such differences between the Monte Carlo and the real data distributions can lead to the optimization procedure suggesting selection criteria that are too stringent. As mentioned, this problem is dealt with during the latter part of the optimization procedure by loosening a selected cut if that cut degrades the true significance of the charm-pair signal (*i.e.*, the significance obtained using the signal from data rather than the signal from the Monte Carlo).

In Figures 3.10-3.12 we organize the final selection criteria by cut variable, rather than by the type of $D\overline{D}$ candidate. Although these figures contain much of the same

Table 3.4: Charm-pair selection criteria for 2-4 pronged events. The entry "0.18 OR 0.01" in the first row, for example, means all 2-4 pronged candidates must pass the cut ($KPRB_2 > 0.18$ OR $SSRAT_4 < 0.01$). Variables are defined in Section 3.2.1.

V^4 / V^2	DIP [μm] <	KPRB >	PTB [GeV] <	SPISO >	SPRAT <	SSRAT <	STRG >	TAU [psec] >	TAU [psec] <
KPRB >						0.01 OR 0.18			
PTB [GeV] <				5.4 OR 0.4					
PTDK [GeV^2] >								0.3 OR 0.81	
SDIP <		0.15 OR 1	0.85 AND 2						
SDZ >	45 AND 2 / 32 OR 7								
SSRAT <					0.02 AND 0.03				
SSISO >							5 OR 5.6		
STRG >		0.17 OR 2							
TAU [psec] >					0.003 OR 0.3				2.14 OR 0.1

information as Tables 3.2-3.5, they allow us to more easily see patterns in the selection criteria. Each of the plots in these figures contains information regarding one cut variable. The x-axes of plots indicate at what value a cut is made. The y-axes indicate on what type of candidate a cut is made (*e.g.*, the y label"4-2" indicates that a cut is made on

Table 3.5: Charm-pair selection criteria for 3-4 pronged events. The entry "23 OR 0.4" in the first row, for example, means all 3-4 pronged candidates must pass the cut ($DIP_3 < 23$ μm OR $PTB_4 < 0.4$ GeV). Variables are defined in Section 3.2.1.

V^3 \ V^4	DIP [μm] <	KPRB >	PTB [GeV] <	SPRAT <	SSISO >	SSRAT <	STRG >
DIP [μm] <			0.4 OR 23				
PTB [GeV] <				0.001 OR 0.3			
PTDK [GeV^2] >					0.9 AND 0.22		
SDIP <			1.2 AND 1.3				
SDZ >	98 AND 5					0.001 OR 3	
SPISO >		0.28 OR 3.8					5 OR 6
SPRAT <			0.4 OR 0.0004			0.002 AND 0.004	
SSRAT <					6 OR 0.003		
STRG >		0.25 OR 1.4					

the 4-pronged candidates from the 4-2 pronged pairs). The symbols on the plots indicate whether the cut is an and-type (solid circle), an or-type (open circle), or a single-charm (star) cut, where the latter cuts are applied to all n-pronged D candidates regardless of the number of decay tracks of the companion D candidate. We group the plots into several categories according to how the cut variables (defined in Section 3.2.1) discriminate signal from background:

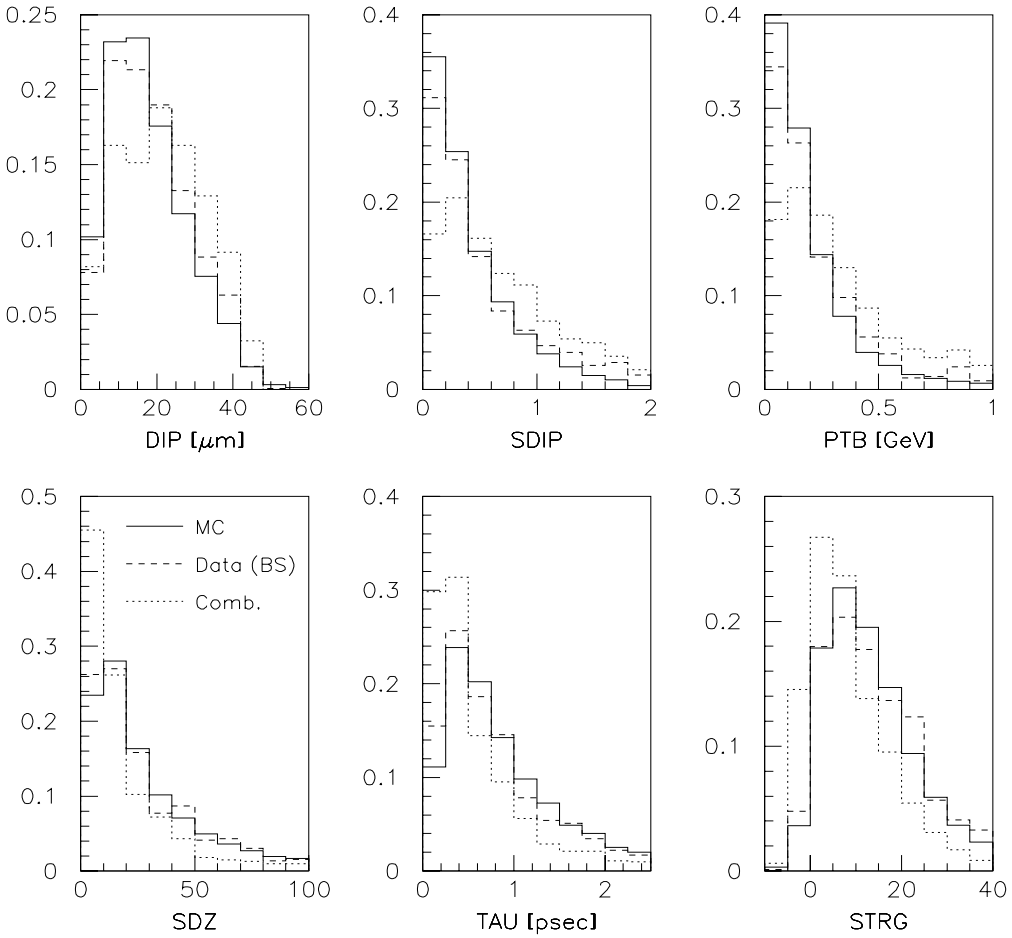

Figure 3.7: Normalized distributions of cut variables for the Monte Carlo sample (solid), the background-subtracted data sample (dashed), and the combinatoric background sample (dotted) after all selection criteria have been applied. The distributions of both D candidates from each $D\overline{D}$ candidate are added. The cut variables are defined in Section 3.2.1.

DIP, SDIP, PTB Is the D candidate consistent with originating from the primary interaction vertex? (Top plots in Figure 3.10.)

SDZ, STRG, TAU Is the vertex of the D candidate well separated from the primary interaction vertex? The latter two variables also indicate whether the D candidate looks like a secondary interaction in a foil downstream of the primary interaction foil. (Bottom plots in Figure 3.10.)

SPISO, SPRAT Do any of the decay tracks of the D candidate look like they originate from the primary vertex? (Top plots in Figure 3.11.)

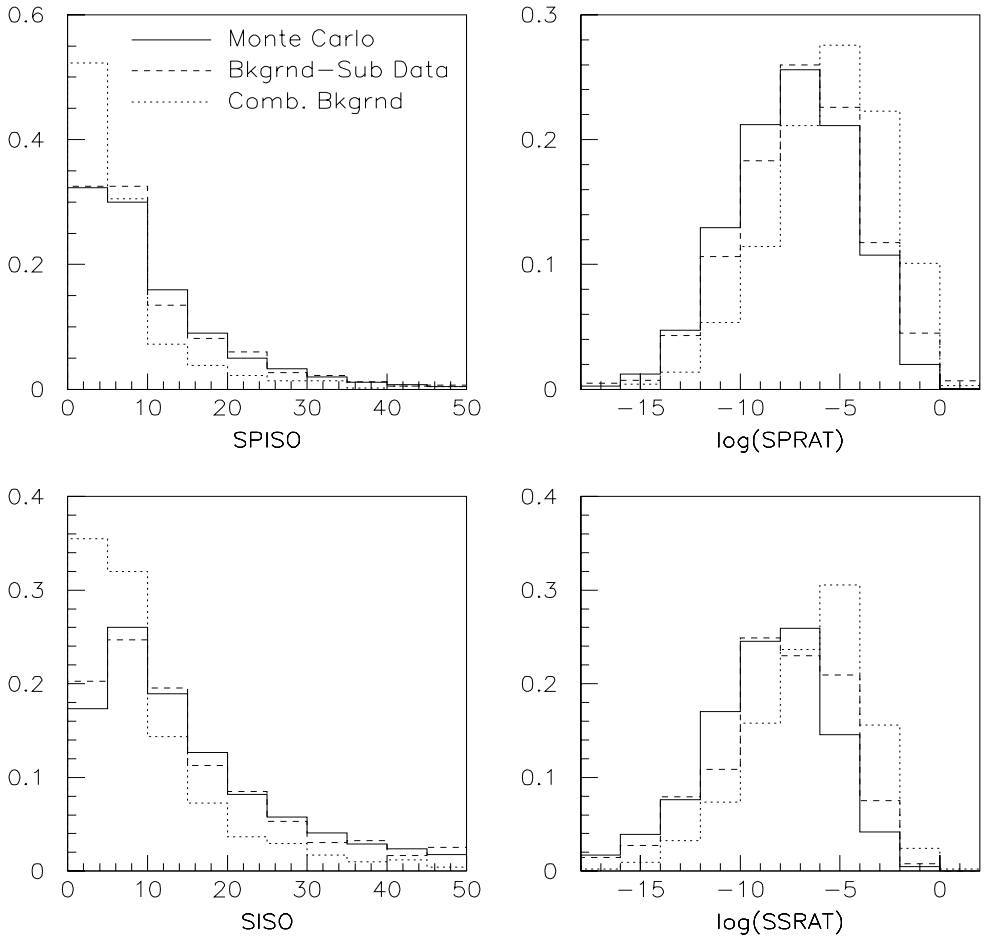

Figure 3.8: Normalized distributions of cut variables for the Monte Carlo sample (solid), the background-subtracted data sample (dashed), and the combinatoric background sample (dotted) after all selection criteria have been applied. The distributions of both D candidates from each $D\overline{D}$ candidate are added. The cut variables are defined in Section 3.2.1.

SSISO, SSRAT Do any of the decay tracks of one D candidate look like they originate from the other D candidate vertex? (Bottom plots in Figure 3.11.)

PTDK Are the transverse momenta of the candidate-D decay tracks, with respect to the candidate-D trajectory, indicative of a heavy meson decay? (Right plot in Figure 3.12.)

KPRB Based on Čerenkov information, is the candidate kaon likely to be a real kaon? (Left plot in Figure 3.12.)

CHIS Do the decay tracks of the D candidate form a good vertex? (Middle plot in Fig-

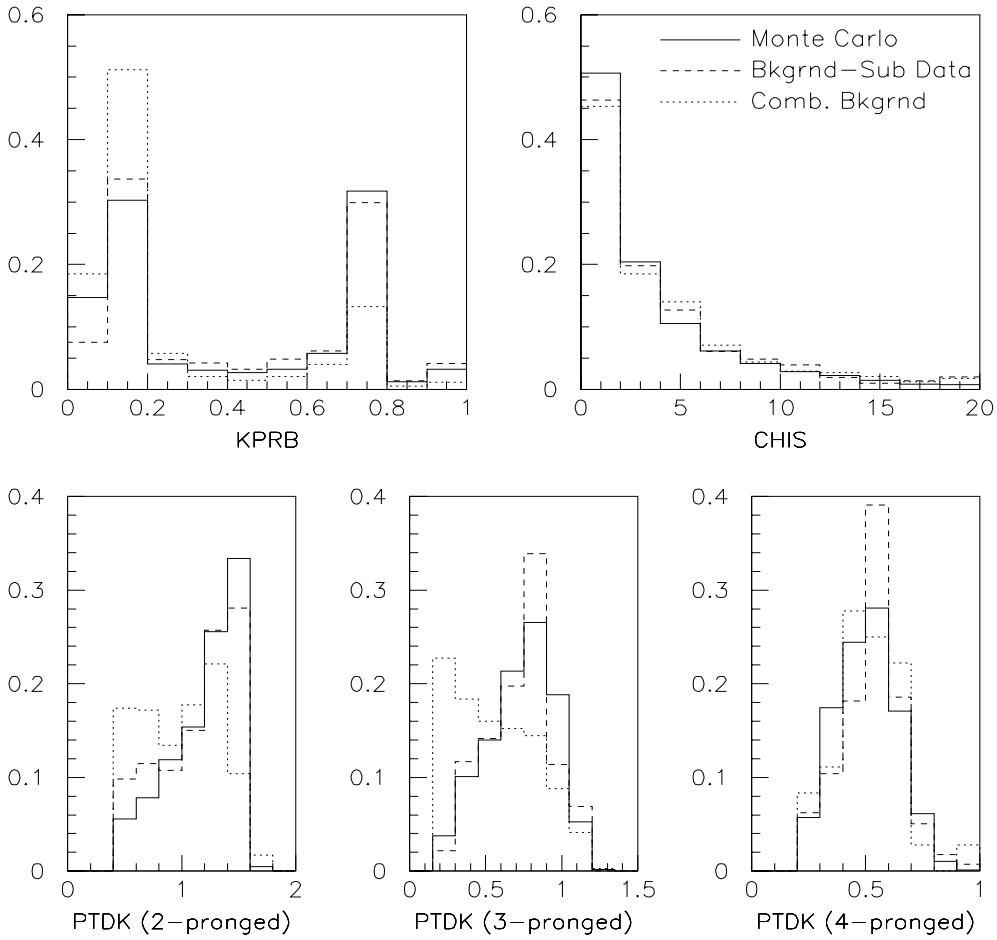

Figure 3.9: Normalized distributions of cut variables for the Monte Carlo sample (solid), the background-subtracted data sample (dashed), and the combinatoric background sample (dotted) after all selection criteria have been applied. The distributions of both D candidates from each $D\overline{D}$ candidate are added. The cut variables are defined in Section 3.2.1.

ure 3.12.)

All categories, except the latter two, seem to be important for discriminating signal $D\overline{D}$ events from background. We do not show the cut variable SDISO, which quantifies whether any tracks from the primary look like they could be associated with a candidate-D vertex, because it is never chosen as an optimum cut variable at any iteration.

The main conclusion from Figures 3.10-3.12 is that results look reasonable:

- For any given cut variable the range of selected cuts is fairly narrow compared to the widths of the distributions shown in Figures 3.7-3.9.

- The cut values for or-type cuts are generally more stringent than the values for and-

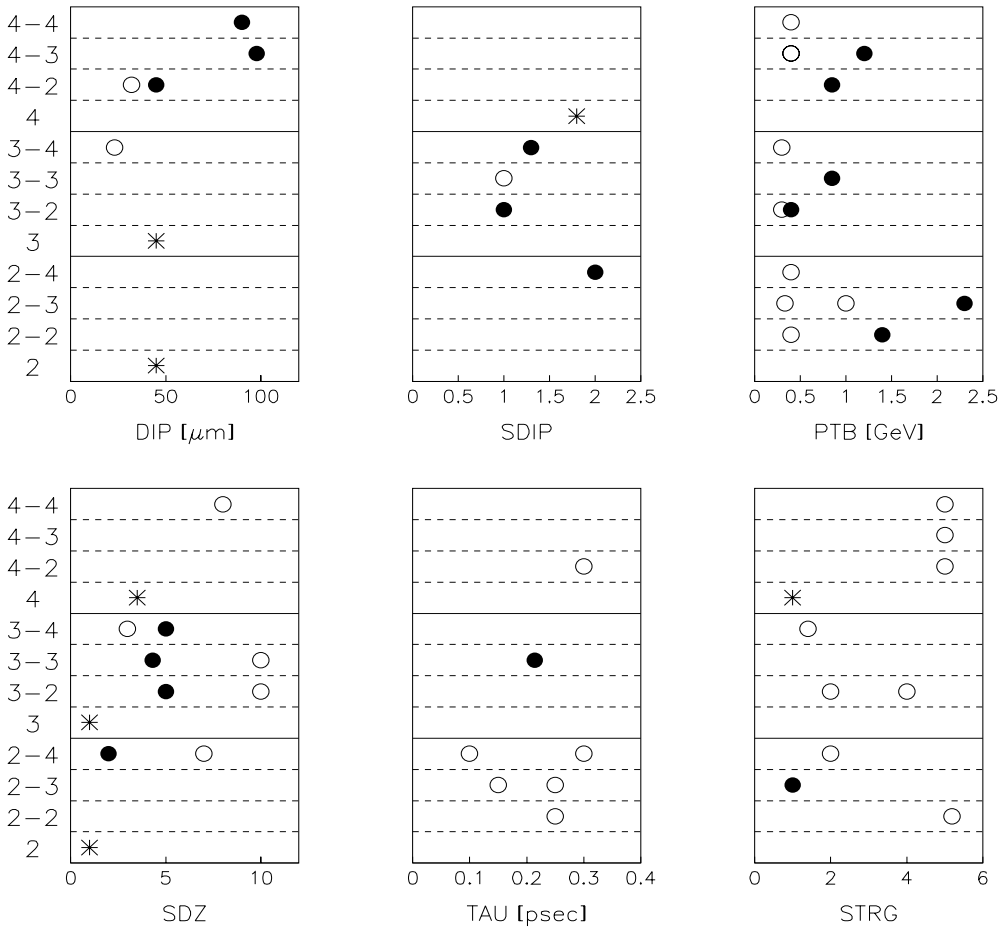

Figure 3.10: The distribution of selection criteria for the cut variables DIP, SDIP, PTB, SDZ, TAU, and STRG. The x-axes indicate the value at which a cut is made; the y-axes indicate on what type of candidate a cut is made. For example, the y label "4-2" indicates that a cut is made on the 4-pronged candidates from the 4-2 pronged pairs. The symbols on the plots indicate whether the cut is an and-type (solid circle), an or-type (open circle), or a single-charm (star) cut. The cut variables are defined in Section 3.2.1.

type cuts because the area of the cut-variable space removed by or-type cuts is smaller than the area removed by and-type cuts (See Figure 3.1).

- There are several examples of a less stringent and-type cut combined with a more stringent or-type cut (*e.g.*, the PTB cuts on the 2-pronged candidates from 2-2 and 2-3 pronged pairs, and the SDZ cuts on the 3-pronged candidates from 3-2 and 3-3 pronged pairs). As discussed in the previous section, this pattern is reasonable because our sample of $D\overline{D}$ candidates contains two types of background events: combinatoric events in which neither D candidate is real, and ridge events in which one of the two

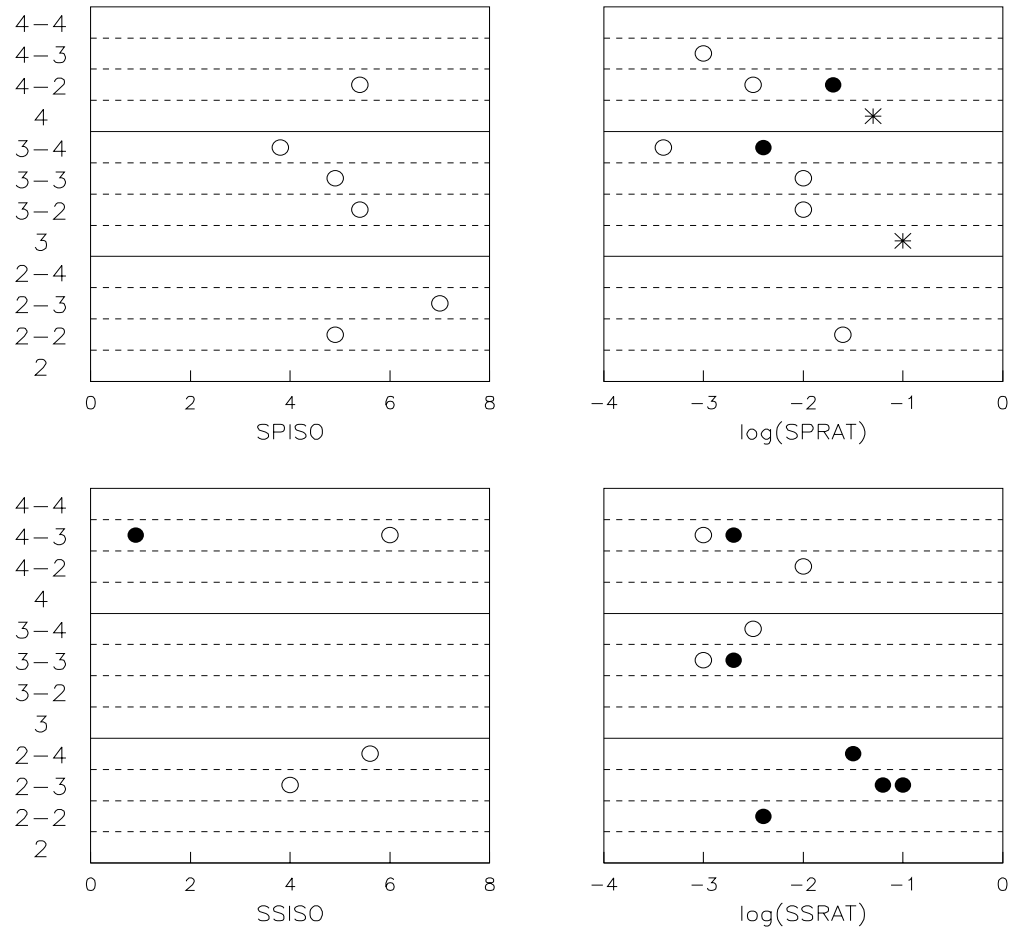

Figure 3.11: The distribution of selection criteria for the cut variables SPISO, SPRAT, SSISO and SSRAT. The x-axes indicate the value at which a cut is made; the y-axes indicate on what type of candidate a cut is made. For example, the y label "4-2" indicates that a cut is made on the 4-pronged candidates from the 4-2 pronged pairs. The symbols on the plots indicate whether the cut is an and-type (solid circle), an or-type (open circle), or a single-charm (star) cut. The cut variables are defined in Section 3.2.1.

D candidates is a real D.

- The PTDK cuts selected for 2-pronged candidates is looser that the cuts selected for 3-pronged candidates, consistent with the PTDK distributions shown in Figure 3.9.

Other comments regarding Figures 3.10-3.12 are:

- Or-type cuts are selected almost twice as often as and-type cuts.
- There are two examples of selection criteria that become obsolete because another cut selected later in the optimization procedure is more stringent: the SDZ cuts on the

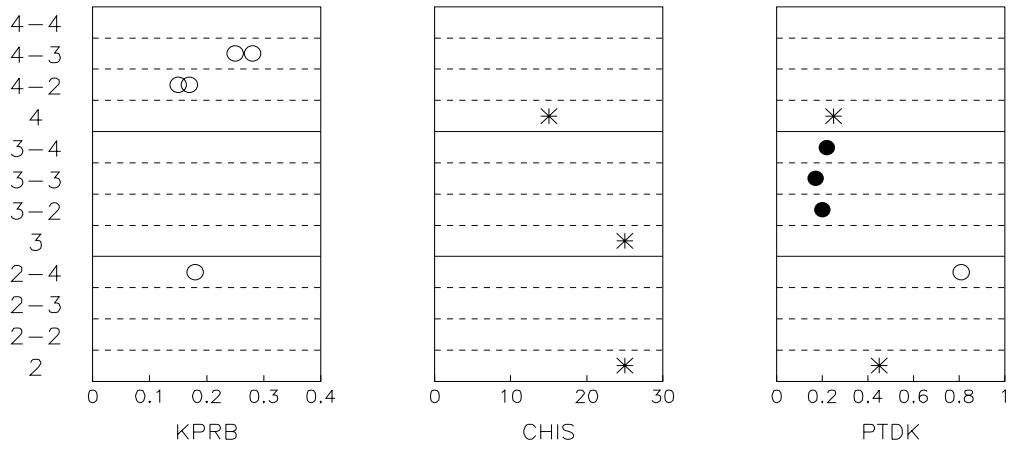

Figure 3.12: The distribution of selection criteria for the cut variables KPRB, CHIS, and PTDK. The x-axes indicate the value at which a cut is made; the y-axes indicate on what type of candidate a cut is made. For example, the y label "4-2" indicates that a cut is made on the 4-pronged candidates from the 4-2 pronged pairs. The symbols on the plots indicate whether the cut is an and-type (solid circle), an or-type (open circle), or a single-charm (star) cut. The cut variables are defined in Section 3.2.1.

3-pronged candidates from 3-4 pronged pairs, and the SSRAT cuts on the 2-pronged candidates from the 2-3 pronged pairs.

- Comparing the variables SDZ and TAU, SDZ seems more effective for 3-pronged D candidates, whereas TAU seems more effective for 2-pronged candidates.

- The SxRAT variables appear to be more effective than the SxISO variables at discriminating signal from background events.

- The variables CHIS and KPRB are not found to be very important in this analysis.

Applying the final selection criteria discussed in this section to our data sample gives us the $D\overline{D}$ signal evident in the scatter plot of Figure 3.2. In the following chapter, we discuss how to extract the number of real $D\overline{D}$ events from this scatter plot, and, finally, in Chapter 5 we present the results of this $D\overline{D}$ analysis.

Chapter 4

Data Analysis

To obtain physics distributions (*e.g.*, the transverse momentum of the $D\overline{D}$ pair), we need a method for determining the number of charm-pair signal events in each bin of a given physics variable, and for correcting our distributions to account for the acceptance and smearing effects of the reconstruction and data selection processes. These two issues are discussed in Sections 4.1 and 4.2, respectively.

4.1 Determining Yields and Significances

4.1.1 Normalized Mass

In the previous chapter, we show the results from our final data sample as a scatter plot of the reconstructed mass of each D candidate versus the reconstructed mass of each $\overline{D}$ candidate (Figure 3.2). To analyze our data, we use normalized masses M_n rather than reconstructed masses M, where $M_n \equiv (M - M_D)/\sigma_{M_D}$. If we correctly determine the mean M_D and resolution σ_{M_D} for the reconstructed mass distribution, then the distribution of M_n for reconstructed D mesons will be Gaussian with a mean of 0 and a variance of 1.

The motivation for using normalized masses is that the mass resolution for D mesons decaying to $Kn\pi$ in the E791 spectrometer depends on both the number of decay tracks and on the x_F of the D meson, where x_F is the longitudinal momentum of the D in the center of mass of the π^--nucleon system divided by the maximum possible longitudinal momentum. In addition, the experimental means — slightly different from the Particle Data Group values[40] — range from 1.866 to 1.872 GeV. In other words, the distribution

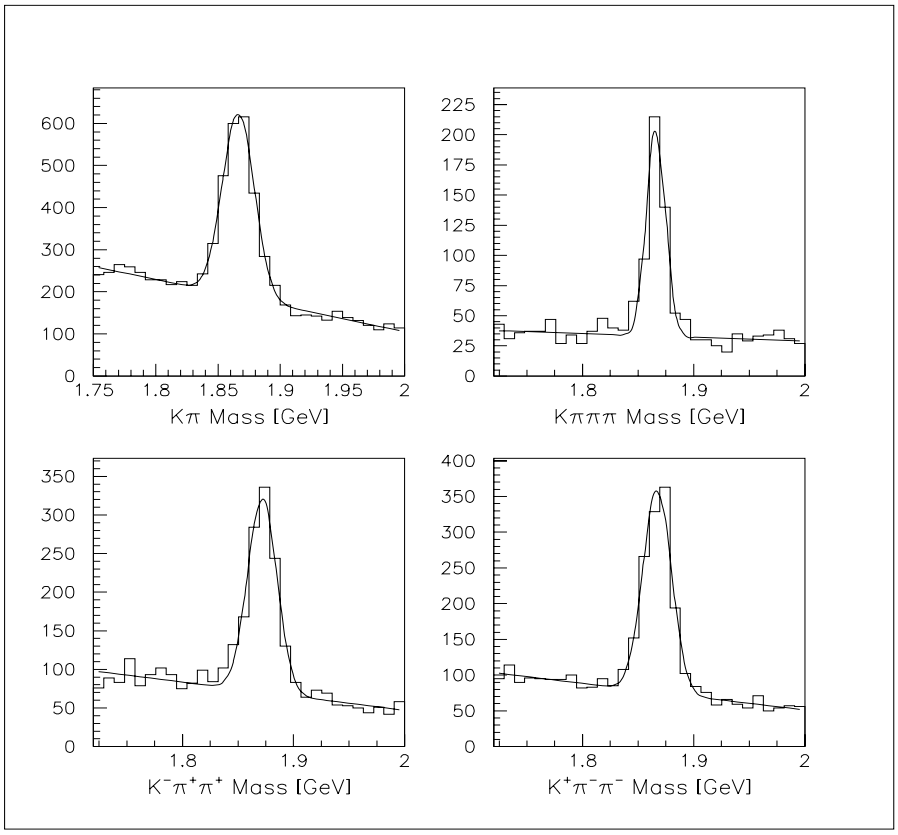

Figure 4.1: One-dimensional measured mass distributions from the final data sample with fits to a Gaussian plus linear distribution superimposed. The parameters of the Gaussians extracted from the fits are given in Table 4.1.

of D (and $\overline{D}$) meson masses in Figure 3.2 is approximately a superposition of Gaussians with a discrete number of means and a continuum of variances. As described below, we use our higher statistics single-charm one-dimensional mass distributions to measure the parameters that transform these D and $\overline{D}$ reconstructed mass distributions to normalized mass distributions that are approximately Gaussian with means of 0 and variances of 1. Then, as discussed in Section 4.1.3, when fitting to the two-dimensional charm-pair mass distribution ($M_n^{K^-n\pi}$ vs. $M_n^{K^+n\pi}$) we can fix the D signal distributions to be Gaussian with a mean of 0 and a variance of 1.

As shown in Figure 4.1, to make the transformation to normalized masses, we first fit the following four single-charm mass distributions from our final data sample to a Gaussian distribution for the signal D events, plus a linear distribution for the background events: all 2-pronged $D^0/\overline{D^0}$ candidates, all 4-pronged $D^0/\overline{D^0}$ candidates, all D^- candi-

Table 4.1: The parameters of the Gaussian extracted from the fits to the one-dimensional measured mass distributions from the final data sample shown in Figure 4.1

Decay Mode	Mean, M_D [GeV]	σ_{M_D} [MeV]
$D \to K^{\mp}\pi^{\pm}$	1.866 ± 0.001	12.7 ± 0.5
$D \to K^{\mp}\pi^{\mp}\pi^{\pm}\pi^{\pm}$	1.866 ± 0.001	8.4 ± 0.6
$D^+ \to K^-\pi^+\pi^+$	1.872 ± 0.001	13.1 ± 0.7
$D^- \to K^+\pi^-\pi^-$	1.867 ± 0.001	12.8 ± 0.6

Table 4.2: The sigma σ_{M_D}, in MeV, of the Gaussian extracted from the fits to the one-dimensional measured mass distributions from the final data sample. The means of the Gaussians are fixed to the values shown in Table 4.1.

	$K\pi$	$K\pi\pi$	$K\pi\pi\pi$
$x_F < 0.0$	10.6 ± 0.9	14.9 ± 3.5	
$0.0 < x_F < 0.1$	11.1 ± 0.7	10.7 ± 0.5	
$0.1 < x_F < 0.2$	14.1 ± 0.9	14.1 ± 0.8	
$0.2 < x_F$	23.9 ± 2.4	19.8 ± 1.9	
$x_F < 0.15$			7.6 ± 0.6
$x_F > 0.15$			13.7 ± 1.8

dates, and lastly all D^+ candidates. The D^- and D^+ signal distributions have slightly different experimental means because of a small asymmetry in the E791 spectrometer between the reconstruction of positively and negatively charged tracks. Table 4.1 shows the parameters of the Gaussian extracted from each fit. We then divide the 2-pronged and both 3-pronged single-charm samples into four x_F bins. Due to the small number of events, we divide the 4-pronged sample into only two x_F bins. We again fit each mass distribution to

Table 4.3: The parameters of the Gaussian extracted from the fits to the one-dimensional normalized mass M_n distributions from the final data sample shown in Figure 4.2, where $M_n = (M - M_D)/\sigma_{M_D}$ and M_D and σ_{M_D} are taken from Tables 4.1 and 4.2, respectively.

Decay Mode	Mean	Sigma
$D \to K^{\mp}\pi^{\pm}$	-0.01 ± 0.04	1.08 ± 0.05
$D \to K^{\mp}\pi^{\mp}\pi^{\pm}\pi^{\pm}$	0.07 ± 0.08	0.99 ± 0.08
$D^+ \to K^-\pi^+\pi^+$	0.09 ± 0.05	0.95 ± 0.06
$D^- \to K^+\pi^-\pi^-$	0.03 ± 0.06	1.00 ± 0.05

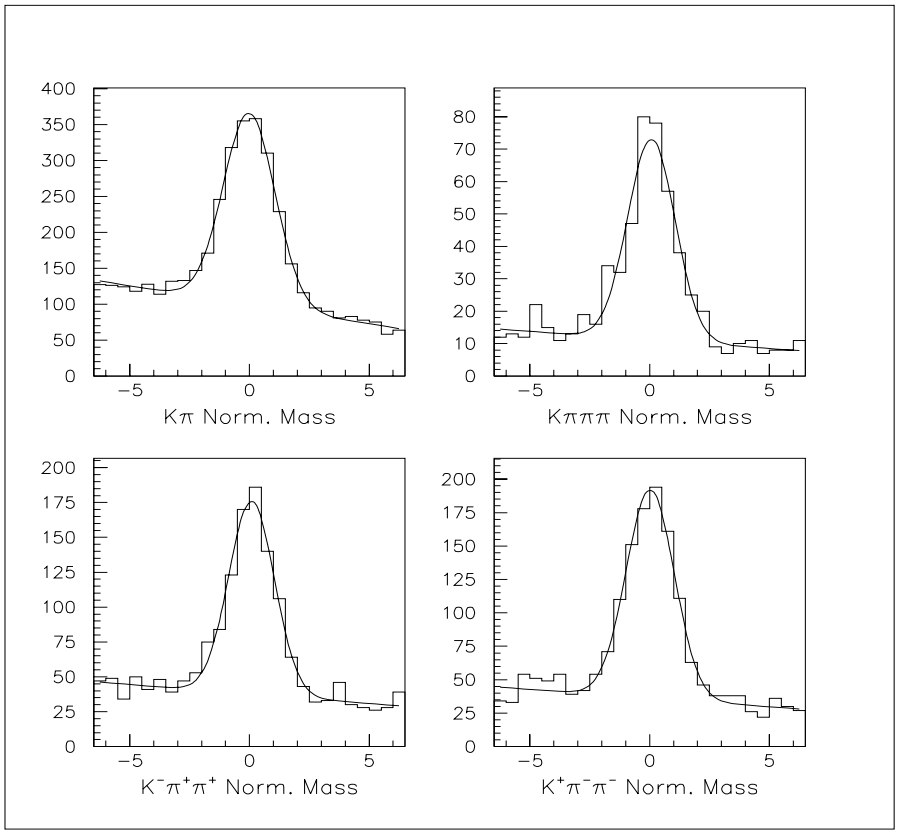

Figure 4.2: One-dimensional normalized mass distributions from the final data sample with fits to a Gaussian plus linear distribution superimposed. The parameters of the Gaussians extracted from the fits are given in Table 4.3.

a Gaussian signal distribution plus a linear background distribution, but we fix the means of the Gaussian using the values from the previous four fits (Table 4.1). The widths of the Gaussians extracted from these fits are shown in Table 4.2. Although the means of the D^+ and D^- distributions differ, we do not expect the resolutions to differ. Hence, in Table 4.2, we show the averages of the D^+ and D^- mass resolutions, which were all consistent within one standard deviation.

To check this procedure, we transform the four initial single-charm reconstructed mass distributions (Figure 4.1) to normalized mass distributions, $M_n \equiv (M - M_D)/\sigma_{M_D}$, using M_D from Table 4.1 and σ_{M_D} from Table 4.2. Once again, as shown in Figure 4.2, we fit each distribution to a Gaussian plus a linear distribution. The parameters of the Gaussians extracted from the fits are given in Table 4.3. The means and the sigmas extracted from all four fits are within 0.1 of 0 and 1, respectively. We expect this level of accuracy because

both the means and the sigmas of the measured-mass fits are known to approximately 1 MeV. For example, if we have a Gaussian distribution for which the true mean is 1870 MeV and the true sigma is 10 MeV, but we transform to a normalized distribution assuming a mean of 1871 GeV and a sigma of 11 MeV, then the normalized mass distribution will have a mean of $\frac{1}{11}$ and a sigma of $\frac{10}{11}$. That is, if we assume

$$M_n = \frac{M - (M_D + \Delta M_D)}{\sigma_{M_D} + \Delta\sigma_{M_D}},$$

then the distribution that we fit to is proportional to

$$\exp\left(-\frac{1}{2}\left(\frac{(\sigma_{M_D} + \Delta\sigma_{M_D})M_n + (M_D + \Delta M_D) - M_D}{\sigma_{M_D}}\right)^2\right) =$$

$$\exp\left(-\frac{1}{2}\left(\frac{M_n + \Delta M_D/(\sigma_{M_D} + \Delta\sigma_{M_D})}{\sigma_{M_D}/(\sigma_{M_D} + \Delta\sigma_{M_D})}\right)^2\right).$$

4.1.2 Binned Method for Background Subtraction

As discussed in the following section, we ultimately use an unbinned maximum-likelihood fit to estimate the number of signal $D\overline{D}$ events in our data sample. In this section, we describe a simpler binned method for subtracting background events in order to emphasize the difference between the two approaches.

Figure 4.3 shows the two-dimensional normalized mass distribution for our final sample of $D\overline{D}$ candidates. In this figure, four regions are defined according to their cross-hatching:

- Region 1, with N_1 events, contains mostly combinatoric background events;
- Region 2, with N_2 events, contains both combinatoric background events and D-ridge background events;
- Region 3, with N_3 events, contains both combinatoric background events and $\overline{D}$-ridge background events; and, lastly,
- Region 4 — the signal region — with N_4 events, contains signal events as well as all three types of background events.

In order to determine the number of signal events in the signal region, we must be able to estimate the number of each type of background event in this region. Region 1, which

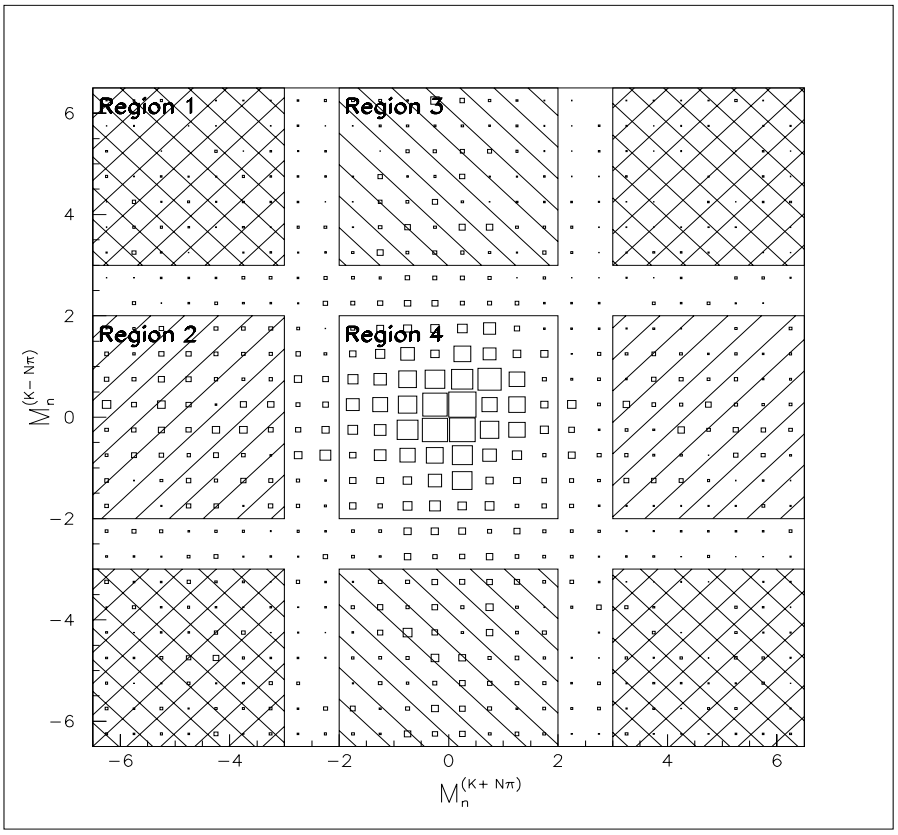

Figure 4.3: Distribution of normalized masses for the final sample of $D\overline{D}$ candidates. (The length, not the area, of the boxes in each bin is proportional to the number of events in the bin.)

symmetrically surrounds the signal region, contains N_1 combinatoric background events and covers an area of 4 × 3.5 GeV × 3.5 GeV = 49 GeV^2. Hence, assuming that the distribution of combinatoric events is linear in both $M^{K^-n\pi}$ and $M^{K^+n\pi}$, the number of combinatoric events in the signal region, which covers an area of 4 GeV × 4 GeV = 16 GeV^2, is approximately 16/49 N_1. Region 2 covers an area of 2 × 4 GeV × 3.5 GeV = 28 GeV^2. Hence, the number of D-ridge events in the signal region is approximately 16/28 N_2 - 16/49 N_1, where the number of combinatoric events in the signal region is subtracted because Region 2 contains *both* D-ridge events and combinatoric events. Similarly, the number of $\overline{D}$-ridge events in the signal region is 16/28 N_3 - 16/49 N_1. Therefore, an estimate for the number of signal events is

$$N_S = N_4 - 16/49N_1 - (16/28N_2 - 16/49N_1) - (16/28N_3 - 16/49N_1), \text{ or}$$

$$N_S = N_4 - 4/7(N_2 + N_3) + 16/49N_1,$$

and the error on this estimate is

$$\sigma_{N_S} = \sqrt{N_4 + (4/7)^2(N_2 + N_3) + (16/49)^2 N_1}.$$

4.1.3 Unbinned Maximum Likelihood Fit

A more powerful method for determining the number of signal events is an unbinned maximum-likelihood fit. Using every event in the determination of the shape and dominance of both the signal and the three types of background distributions allows us to estimate our backgrounds more precisely than the simple binned method discussed above. That is, we are able to reduce σ_{N_S} from $\sqrt{N_4 + (4/7)^2(N_2 + N_3) + (16/49)^2 N_1}$, to approximately $\sqrt{N_4}$.

In general, the maximum likelihood method assumes we have N independent measurements of one or more quantities and that these quantities $\vec{z}$ are distributed according to some probability distribution function $f(\vec{z};\vec{\alpha})$ where $\vec{\alpha}$ is an unknown set of parameters to be determined. To determine the set of values $\hat{\alpha}$ that maximizes the joint probability for all events, we solve the set of likelihood equations[40]:

$$\frac{\partial \ln L(\vec{\alpha})}{\partial \alpha_j} = 0 \quad \text{where} \quad L(\vec{\alpha}) = \prod_{i=1}^{N} f(\vec{z}_i;\vec{\alpha}).$$

In this analysis, the quantities that we measure for each event are the normalized mass of both the D and $\overline{D}$ candidate; *i.e.*, $\vec{z} = (M_n^{K^-m\pi}, M_n^{K^+m\pi})$. (The number of pions m is not necessarily the same for the D candidate and the $\overline{D}$ candidate.) The unknown parameters that we want to determine are the number of signal events, combinatoric events, D-ridge events, and $\overline{D}$-ridge events — N_S, N_C, N_D, and $N_{\overline{D}}$, respectively — and the slopes of the background $K^-m\pi$ and $K^+m\pi$ distributions — S^D and $S^{\overline{D}}$, respectively. That is,

$$\vec{\alpha} = (N_S, N_C, N_D, N_{\overline{D}}, S^D, S^{\overline{D}}).$$

We construct our probability distribution function using the following two assumptions: (i) the normalized mass distribution for background $K^-m\pi$ and $K^+m\pi$ is linear in $M_n^{K^-m\pi}$ and $M_n^{K^+m\pi}$, and (ii) the normalized mass distribution of real D's and real $\overline{D}$'s is Gaussian with mean of 0 and sigma of 1. Under these assumptions, the probability distribution functions — normalized to unit area in the two-dimensional window defined by $|M_n^{(K^-m\pi)}| < 6.5$ and $|M_n^{(K^+m\pi)}| < 6.5$ — for each class of events is:

Combinatoric background events: $P_C = 1/169 + S^D M_n^{K^-m\pi} + S^{\overline{D}} M_n^{K^+m\pi}$,

D-Ridge background events: $P_D = (\frac{1}{13\sqrt{2\pi}} + \frac{N_C}{N_D} S^{\overline{D}} M_n^{K^+m\pi})\ e^{-(M_n^{K^-m\pi})^2/2}$,

$\overline{D}$-Ridge background events: $P_{\overline{D}} = (\frac{1}{13\sqrt{2\pi}} + \frac{N_C}{N_{\overline{D}}} S^D M_n^{K^-m\pi})\ e^{-(M_n^{K^+m\pi})^2/2}$,

Signal events: $P_S = \frac{1}{2\pi} e^{-((M_n^{K^-m\pi})^2 + (M_n^{K^+m\pi})^2)/2}$.

The overall probability distribution function is then:

$$f(\vec{z};\vec{\alpha}) = \frac{N_C P_C + N_D P_D + N_{\overline{D}} P_{\overline{D}} + N_S P_S}{N_C + N_D + N_{\overline{D}} + N_S}.$$

In this analysis, we use the extended maximum likelihood method[41, pg. 249] in which the number of $D\overline{D}$ candidates found, $N_{D\overline{D}}$, is considered one more measurement with a Gaussian probability distribution $G(N_{D\overline{D}})$ of mean $\mu = N_C + N_D + N_{\overline{D}} + N_S$ and $\sigma = \sqrt{\mu}$. Our likelihood function is then

$$L = G(N_{D\overline{D}}, \mu) \prod_{i=1}^{N_{D\overline{D}}} f(\vec{z}_i;\vec{\alpha}). \tag{4.1}$$

To solve the likelihood equation, we use the function minimization and error analysis FORTRAN package MINUIT [42]. Figure 4.4 shows the function $N_{D\overline{D}} f(\vec{z};\hat{\alpha})$ that maximizes the likelihood function for the final sample of $D\overline{D}$ candidates shown in Figures 3.2 and 4.3. In Figure 4.5, to qualitatively demonstrate how well this function fits our data we show various one-dimensional projections of both the data and the fit function.

4.2 Acceptance and Smearing Corrections

Using the fitting method described above, we can now obtain distributions of variables describing the correlations between the two charmed mesons. For example, to determine the distribution of the invariant mass of the $D\overline{D}$ pairs, we divide the charm-pair candidates into N samples where each candidate in the i^{th} sample has $k_i < M_{D\overline{D}} < k_{i+1}$. We then do N likelihood fits as described in the previous section, obtaining an estimate for the number of $D\overline{D}$ signal events for each range of $M_{D\overline{D}}$. The resulting distribution

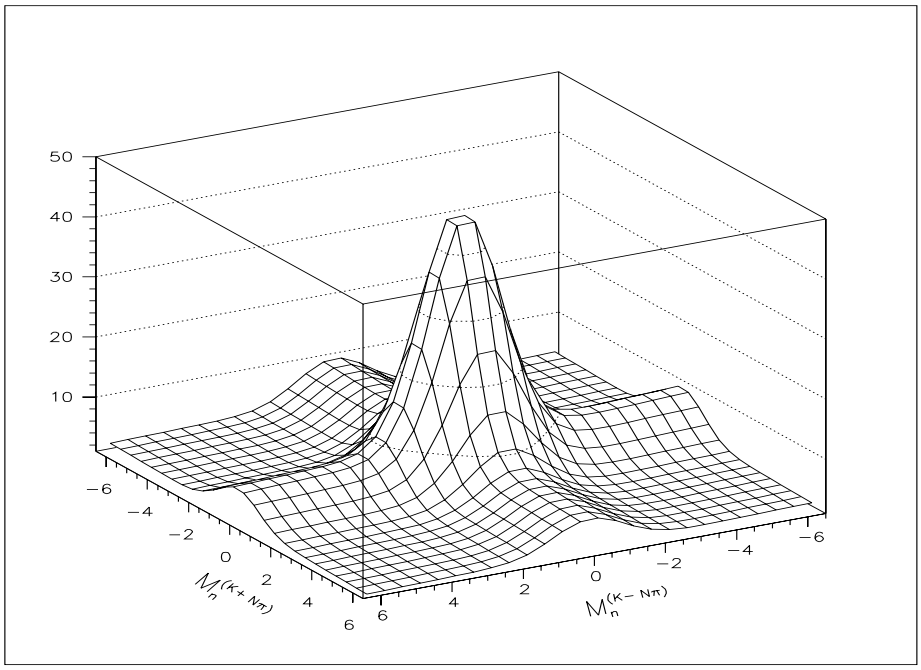

Figure 4.4: The function $N_{D\overline{D}} f(\vec{z};\hat{\alpha})$ that maximizes the likelihood function for the final sample of $D\overline{D}$ candidates shown in Figures 3.2 and 4.3.

of $M_{D\overline{D}}$, however, may be distorted from the true $M_{D\overline{D}}$ distribution for two reasons: (i) the efficiency for reconstructing an event may vary with $M_{D\overline{D}}$, and (ii) an event produced with an invariant mass $M_{D\overline{D}}$ may actually be reconstructed at a slightly different invariant mass. We use the PYTHIA/JETSET Monte Carlo event generator, combined with the E791 detector simulation, to quantify these acceptance and smearing effects.

We generate approximately two million $D\overline{D}$ Monte Carlo events, where each D decays to $Kn\pi$, $n = 1$, 2, or 3. We pass these events through the detector simulation, producing "raw" data (hits in silicon microstrip detectors, energy depositions in the calorimeter, *etc.*). We then pass this simulated raw data through the same reconstruction code and event selection criteria as real data. We are left with approximately 7000 Monte Carlo events. This sample size is roughly eight times the number of signal $D\overline{D}$ events found in our final data sample.

Throughout this chapter and in the following chapter (where we present our results), we explicitly remove all data $D\overline{D}$candidates and Monte Carlo events in which the center-of-mass rapidity is less than -0.5 or greater than 2.5. Our acceptance in this region is approximately zero because of the limited coverage of our spectrometer. This cut removes

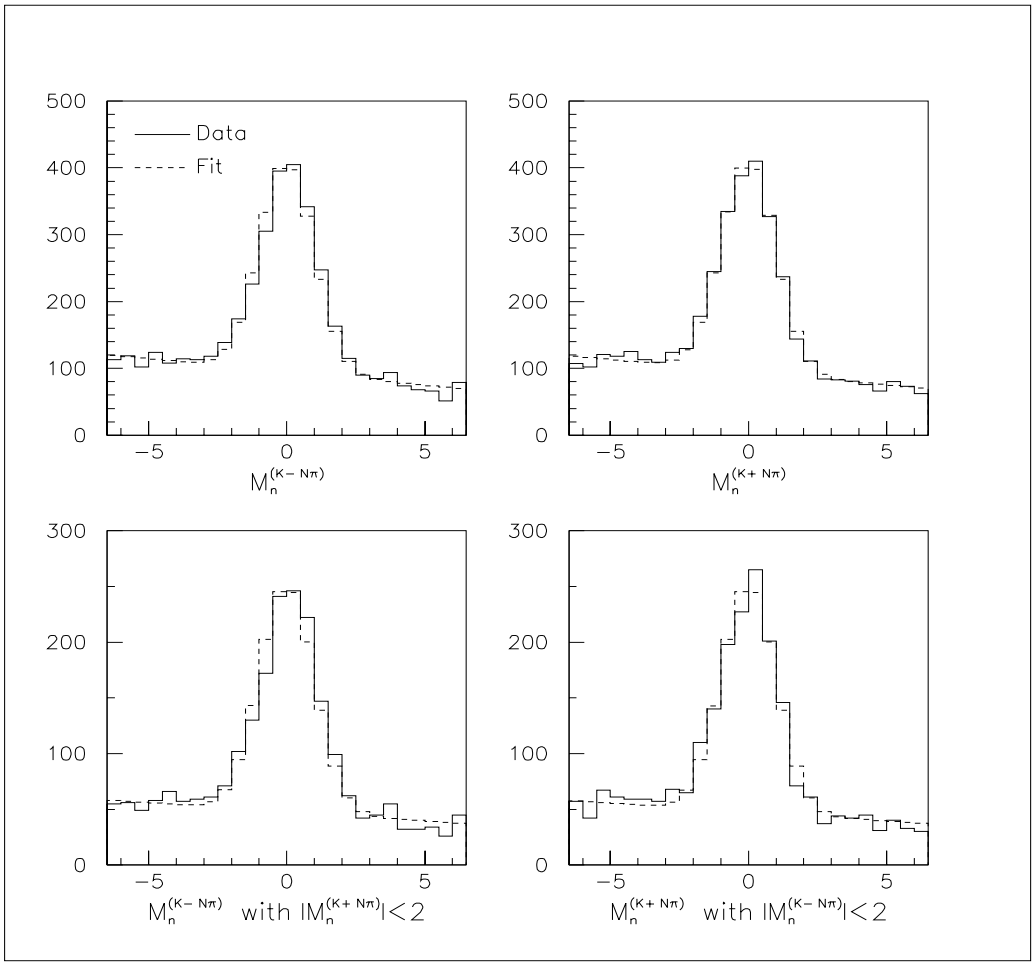

Figure 4.5: One-dimensional projections of charm-pair normalized mass distributions for both the maximum-likelihood fit function (dashed histogram) and the final data sample (solid histogram). The top plots are projections of the full data sample shown in Figure 3.2. The bottom plots include only the data from the $\overline{D}$-ridge region (left plot) and the D-ridge region (right plot).

approximately 60% of the original Monte Carlo events, 4% of the Monte Carlo events that survive all selection criteria, and less than 2% of all $D\overline{D}$ candidates from our final data sample.

From our two Monte Carlo samples — generated events and accepted events — we have three distributions of the physics parameters $\vec{x}$:

- $P^{MC}(\vec{x})$, the original generated distribution for $D\overline{D}$ events;
- $Q^{MC}(\vec{x})$, the generated distribution for accepted $D\overline{D}$ events; and

- $R^{MC}(\vec{x})$, the reconstructed distribution for accepted $D\overline{D}$ events.

Through the relationship

$$R^{MC}(\vec{x}') = \int S(\vec{x},\vec{x}')\; Q^{MC}(\vec{x})\; d\vec{x} \quad \text{where} \quad Q^{MC}(\vec{x}) = A(\vec{x})P^{MC}(\vec{x}),$$

the two Monte Carlo samples can be used to determine the acceptance function $A(\vec{x})$, which gives us the probability for a $D\overline{D}$ event generated at $\vec{x}$ to be accepted, and the smearing function $S(\vec{x},\vec{x}')$, which gives us the probability for an accepted $D\overline{D}$ event generated at $\vec{x}$ to be reconstructed at $\vec{x}'$.

4.2.1 One-Variable Case

If a $D\overline{D}$ pair could be fully described using only one variable x and we divide the appropriate range of x into N bins, then

$$\begin{bmatrix} R_1^{MC} \\ \vdots \\ R_N^{MC} \end{bmatrix} = \begin{bmatrix} S_{11}A_1 & \cdots & S_{1N}A_N \\ \vdots & \ddots & \vdots \\ S_{N1}A_1 & \cdots & S_{NN}A_N \end{bmatrix} \begin{bmatrix} P_1^{MC} \\ \vdots \\ P_N^{MC} \end{bmatrix},$$

$$\text{or} \quad R^{MC} = TP^{MC},$$

where A_i is the fraction of $D\overline{D}$ events originating in the i^{th} bin that survive all selection criteria; S_{ji} is the fraction of the surviving $D\overline{D}$ events originating in the i^{th} bin that are reconstructed in the j^{th} bin ($\sum_j S_{ji} = 1$); and the transformation matrix T_{ji} equals $S_{ji}A_i$ ($\sum_j T_{ji} = A_i$). Applying the inverse transformation matrix T^{-1} to the x distribution measured from data would provide an estimate for the true x distribution.

Although this method does rely on the E791 detector simulation, in this simplified example in which we assume that a $D\overline{D}$ pair can be described using one variable, this method does not depend on the generated distribution of x being the same in the Monte Carlo and data — as long as the simulated events span at least the range of x spanned by real $D\overline{D}$ events.

To illustrate the technique discussed above, we assume for the moment that a $D\overline{D}$ event can be completely described using just the invariant mass of the $D\overline{D}$ pair, $M_{D\overline{D}}$. Figure 4.6(a) shows the three $M_{D\overline{D}}$ distributions from the two Monte Carlo samples — P^{MC}, Q^{MC}, and R^{MC} — each normalized to unit area. The last bin of these distributions is an "overflow" bin containing all events with $M_{D\overline{D}} > 6.6$ GeV. (There are no events

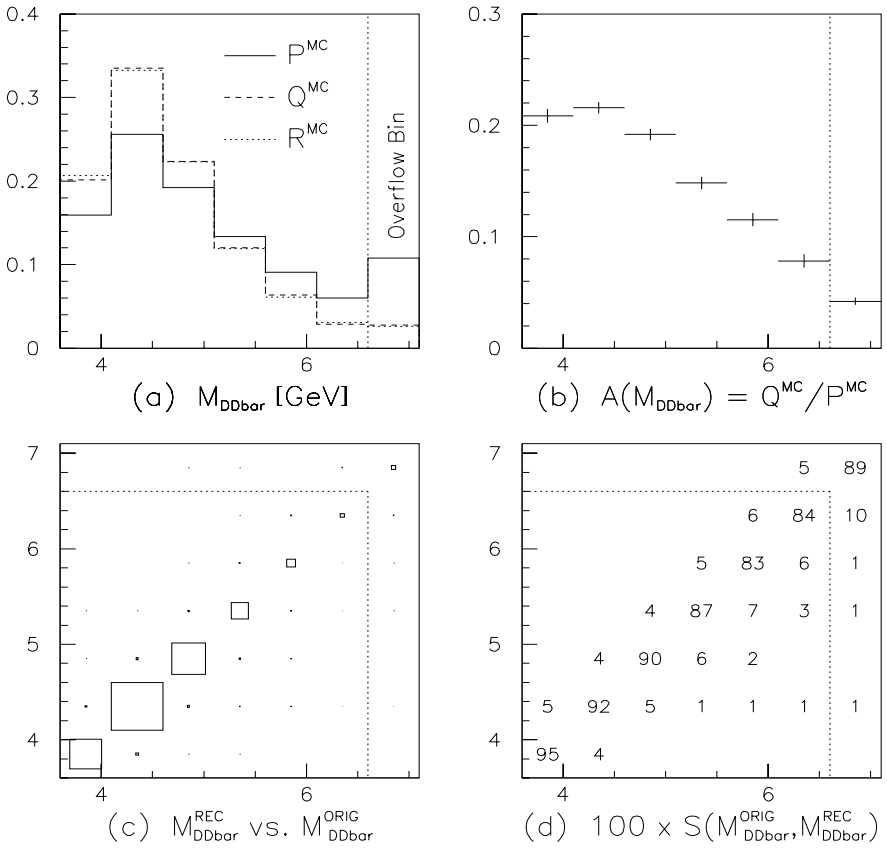

Figure 4.6: (a) Normalized Monte Carlo distributions of the invariant mass of $D\overline{D}$ pairs: the original generated distribution (P^{MC}), the generated distribution for accepted $D\overline{D}$ events (Q^{MC}), and the reconstructed distribution for accepted $D\overline{D}$ events (R^{MC}). (b) The acceptance as a function of the invariant mass (arbitrary vertical scale). (c) Reconstructed $M_{D\overline{D}}$ vs. generated $M_{D\overline{D}}$ for the subset of Monte Carlo events that survive all selection criteria. (d) The smearing matrix ($\times$ 100) for the invariant mass, obtained from (c) by normalizing each column to 1.

with $M_{D\overline{D}} < 2M_D = 3.6$ GeV.) We construct the acceptance function $A(M_{D\overline{D}})$, shown in Figure 4.6(b), by dividing Q^{MC} by P^{MC}. This acceptance function is also normalized to unit area because in this analysis we determine only the shapes, not the absolute value, of the physics distributions.

In Figure 4.6(c) we show, for the subset of Monte Carlo events that survive all selection criteria, the reconstructed invariant mass $M^{REC}_{D\overline{D}}$ versus the generated invariant mass $M^{GEN}_{D\overline{D}}$. By normalizing each column of the distribution in Figure 4.6(c) to 1, we obtain the smearing function $S(M^{REC}_{D\overline{D}}, M^{GEN}_{D\overline{D}})$ shown in Figure 4.6(d). By normalizing each column of $S(M^{REC}_{D\overline{D}}, M^{GEN}_{D\overline{D}})$ to $A(M_{D\overline{D}})$, we obtain the transformation matrix

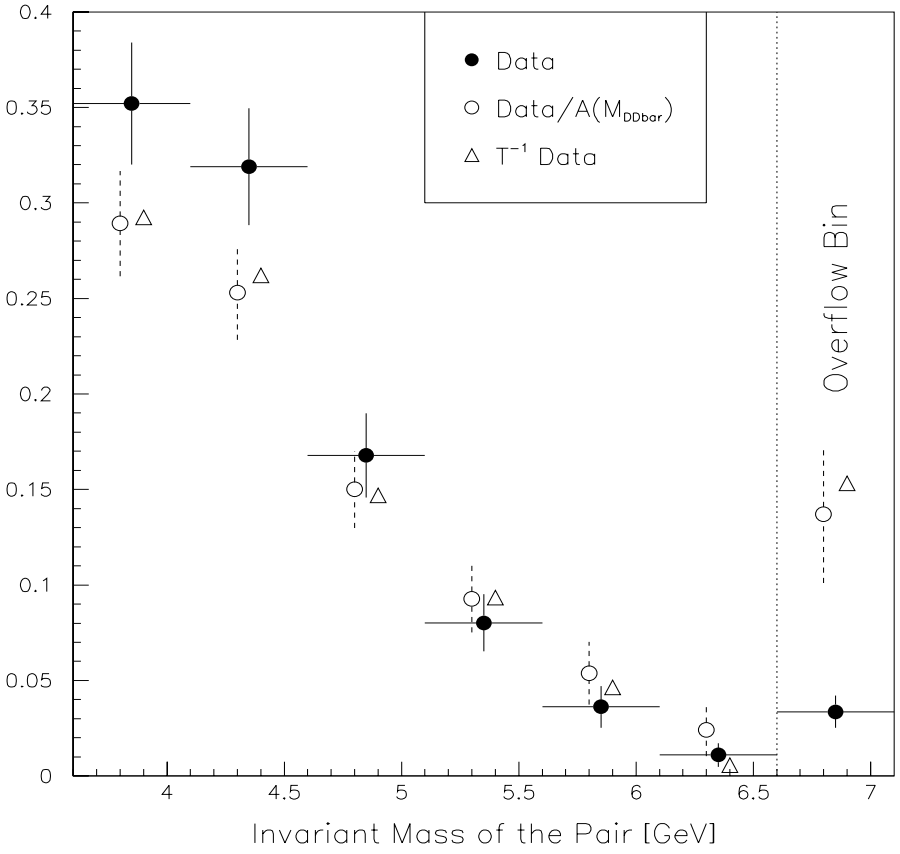

Figure 4.7: Distributions of the invariant mass of the $D\overline{D}$ pair from the final data sample: uncorrected distribution (solid circle), acceptance corrected distribution (open circle), acceptance and smearing corrected distribution (triangle).

$$T = \begin{bmatrix} & & & & & .004 & .037 \\ & & & & .008 & .066 & .004 \\ & & & .008 & .095 & .005 & \\ .001 & & .007 & .128 & .008 & .003 & \\ & .008 & .173 & .010 & .003 & & \\ .010 & .198 & .011 & .001 & .002 & .001 & \\ .197 & .010 & .001 & .001 & & & \end{bmatrix}$$

that transforms the generated distribution of $D\overline{D}$ invariant masses for the original Monte Carlo sample of events (P^{MC} in Fig. 4.6a) into the reconstructed distribution of invariant masses for the sample of accepted Monte Carlo events (R^{MC} in Fig. 4.6a). Because smearing effects are small, S is approximately the identity matrix and T is approximately a diagonal

matrix with $T_{ii} \approx A_i$.

Figure 4.7 shows three $M_{D\overline{D}}$ distributions obtained from our final data sample, all normalized to the same area: the uncorrected distribution $R(M_{D\overline{D}})$, obtained from doing a maximum likelihood fit for the sample of events in each $M_{D\overline{D}}$ bin; the acceptance corrected distribution $R(M_{D\overline{D}})/A(M_{D\overline{D}})$; and lastly, the smearing and acceptance-corrected distribution $T^{-1}R(M_{D\overline{D}})$. The difference between these latter two distributions is quite small compared to the statistical errors because the smearing effects are not significant. We find that the smearing effects are negligible for all the physics distributions considered in this analysis. For all final corrected distributions, shown in Chapter 5, we assume that the smearing matrix S is the identity matrix.

4.2.2 Two-Variable Toy Model

A $D\overline{D}$ event cannot be fully described using one variable. Six parameters are necessary to describe the momenta of both D candidates and two (discrete) parameters are necessary to specify the number of decay tracks of each candidate. In this section, using a simple two-variable toy model, we illustrate why one must be careful when correcting data distributions for acceptance effects when more than one variable is required to fully describe an event.

In this hypothetical example, a $D\overline{D}$ event can be completely described using two independent, but correlated, parameters — x and y where $-1 < (x, y) < 1$. From our imaginary data sample, we obtain the uncorrected distribution of the variable x, $D(x)$. We want to correct this distribution for acceptance effects to obtain an estimate for the true x distribution, $T(x)$. Suppose the original distribution of Monte Carlo events is

$$P^{MC}(x, y) = \frac{3}{4(1+c^2)}(x - cy)^2 \tag{4.2}$$

which is normalized to unit area in the two-dimensional window defined by $-1 < (x, y) < 1$. Further suppose that the distribution of Monte Carlo events that survive all selection criteria is

$$Q^{MC}(x, y) = (1 - y^2/2)P^{MC}(x, y). \tag{4.3}$$

That is, the acceptance function $A(x, y) = Q^{MC}(x, y)/P^{MC}(x, y)$ equals $(1 - y^2/2)$ — that is, flat in x and varying in y by a factor of two over the range $-1 < y < 1$). Figure 4.8a shows $P^{MC}(x, y)$ for $c = 1$ and Figure 4.8b show the acceptance function $A(x, y)$.

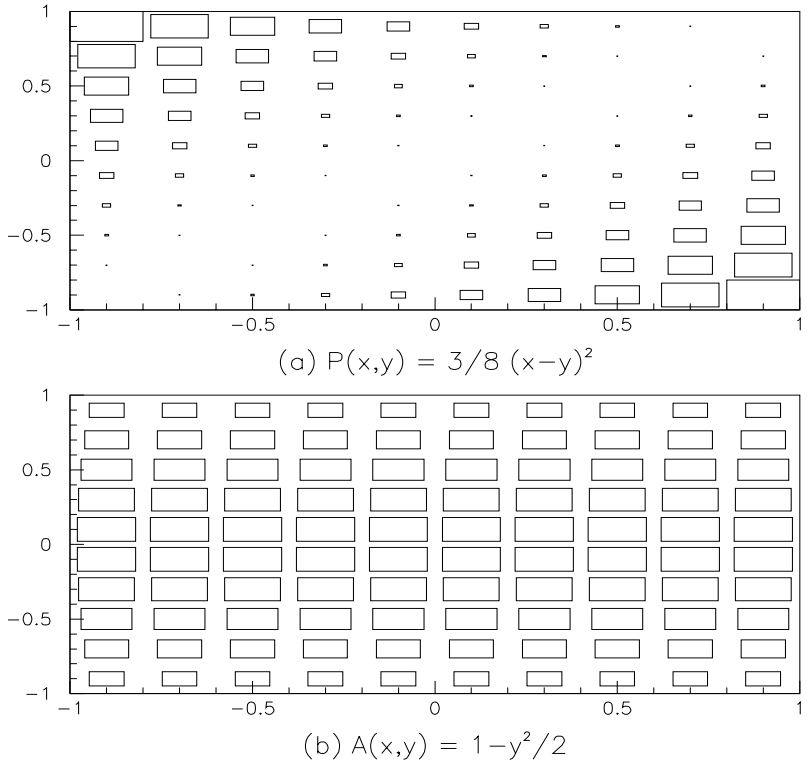

Figure 4.8: Two-variable toy model discussed in Section 4.2.2. (a) Monte Carlo probability distribution function for parameters x and y. (b) Acceptance function for parameters x and y.

If we assume that the variables x and y are uncorrelated in the true data distribution of $D\overline{D}$ events, then no acceptance correction in x is necessary because the acceptance function is flat in x. The true x distribution $T(x)$ is simply proportional to the measured x distribution $D(x)$. On the other hand, if we assume that the variables x and y are correlated in the true data distribution of $D\overline{D}$ events just as they are in the Monte Carlo distribution of events, then we obtain $T(x)$ by dividing $D(x)$ by the acceptance function

$$A^{MC}(x) = \frac{\int_{-1}^{1} Q^{MC}(x,y)\mathrm{d}y}{\int_{-1}^{1} P^{MC}(x,y)\mathrm{d}y} = \frac{\int_{-1}^{1} A(x,y)P^{MC}(x,y)\mathrm{d}y}{\int_{-1}^{1} P^{MC}(x,y)\ \mathrm{d}y} = \frac{1}{10}\frac{25x^2+7c^2}{3x^2+c^2}. \tag{4.4}$$

This acceptance correction depends on the physics assumption of the Monte Carlo. Given that one of the goals of this analysis is to experimentally determine the correlations between the D and $\overline{D}$ in a $D\overline{D}$ event, we do not want our acceptance corrections to depend on *ad hoc* assumptions regarding correlations among the variables that describe a $D\overline{D}$ event. We emphasize that the function $A^{MC}(x)$ can depend on the physics assumptions of the Monte

Carlo if *either* $P^{MC}(x,y)$ or $A(x,y)$ does not factorize into a function of x times a function of y.

Event-Weighting Technique

We can correct distributions from data for acceptance effects without making such *ad hoc* assumptions by using an event-weighting technique[41, pg. 253]. We assign each candidate a weight w that is proportional to the inverse of the acceptance function, $w \propto 1/A(x,y)$, where the weights are normalized such that $\sum_{i=1}^{N_{D\overline{D}}} w_i = N_{D\overline{D}}$ where $N_{D\overline{D}}$ is the number of $D\overline{D}$ candidates. Just as we did to obtain the uncorrected distribution $D(x)$, we first divide our sample of $N_{D\overline{D}}$ candidates into N samples where each candidate in the i^{th} sample has $k_i < x < k_{i+1}$. We then do N likelihood fits, but rather than using the likelihood function L from Eq. 4.1, we use

$$L = G(N_{D\overline{D}}, \vec{\alpha}) \prod_{i=1}^{N_{D\overline{D}}} f(\vec{z}_i; \vec{\alpha})^{w_i}, \tag{4.5}$$

where the probability distribution function f is taken to the power w_i. In other words, one candidate with a weight of $w = 2$ is effectively counted as two candidates. The distribution obtained using this method gives an estimate of the acceptance-corrected x distribution $T(x)$ that does not depend on whether, or to what degree, the variables x and y are correlated in data.

4.2.3 From the Two-Variable Toy Model to Eight-Variable Reality

As mentioned above, a real $D\overline{D}$ event cannot be fully described using one or even two variables. In this section, we discuss how we obtain an estimate for the eight-dimensional acceptance function $A(\vec{x})$ using the Monte Carlo distributions $P^{MC}(\vec{x})$ (the original generated distribution for $D\overline{D}$ events) and $Q^{MC}(\vec{x})$ (the generated distribution for accepted $D\overline{D}$ events). As discussed in Section 4.2.1, the smearing that occurs in going from the generated distribution $Q^{MC}(\vec{x})$ to the reconstructed distribution is negligible.

We use the eight variables $\vec{x} = ((y, p_t, \phi, n)_D, (y, p_t, \phi, n)_{\overline{D}})$ to describe the D and $\overline{D}$ degrees of freedom, where y is the rapidity of the D in the center of mass of the π^--nucleon system (Eq. 1.2), p_t is the transverse momentum of the D with respect to the beam axis, ϕ is the angle of the D in the plane transverse to the beam axis, and lastly n is the number of decay tracks of the D meson. Given an estimate for the acceptance function $A(\vec{x})$, we

can then assign a weight $w \propto 1/A(\vec{x})$ to each $D\overline{D}$ candidate from our data sample and, as discussed above, obtain an acceptance-corrected distribution for any physics variable (*i.e.*, any function of $\vec{x}$, such as the invariant mass of the $D\overline{D}$ pair).

Ideally, we would obtain an estimate for the acceptance function $A(\vec{x})$ by dividing the events from both Monte Carlo samples into $9N^6$ bins (*i.e.*, N bins for each of the 6 continuous physics variables and 3 values for each of the 2 discrete variables). The value of the acceptance function in the i^{th} bin would be the number of Monte Carlo events in that bin that survived all selection criteria divided by the original number generated in that bin. The problem with this method is that the fractional statistical uncertainty on the acceptance function must be added in quadrature to the fractional statistical error from our data sample. With $9N^6$ bins, even with $N = 3$, the number of accepted Monte Carlo events necessary for obtaining reasonable statistical errors is beyond our computing capacity.

In order to reduce the statistical uncertainties due to the acceptance correction without introducing large systematic uncertainties, we need to understand both how the acceptance function $A(\vec{x})$ and how the original Monte Carlo distribution of events $P^{MC}(\vec{x})$ factorize. If we could establish, for example, that these distributions factorize as follows:

$$P^{MC}(\vec{x}) = P_0^{MC}((y, p_t, \phi, n)_D)\ P_1^{MC}((y, p_t, \phi, n)_{\overline{D}}) \text{ and}$$

$$A(\vec{x}) = A_0((y, p_t, \phi, n)_D)\ A_1((y, p_t, \phi, n)_{\overline{D}})$$

then, rather than $9N^6$ bins, we would need only $2(3N^3) = 6N^3$ bins to obtain an estimate of the acceptance function $A(\vec{x})$ that does not depend on the physics assumptions of the Monte Carlo.

Correlations in Original Monte Carlo Distribution

Each Monte Carlo $D\overline{D}$ event can be described by eight independent, but possibly correlated, variables. One measure of the correlation between any two of these variables is the linear correlation coefficient[41, pg. 40] $\rho(x_i, x_j) = V_{ij}/(\sigma_i \sigma_j)$ where the mean of x_i is μ_i, the variance σ_i^2 is the mean of the square of $(x_i - \mu_i)$, and the covariance matrix V_{ij} is the mean of $(x_i - \mu_i)(x_j - \mu_j)$. The correlation coefficient measures how well a straight line describes the relationship between two variables. It is positive if an increase in one variable corresponds to an increase in the other, and negative if an increase in one corresponds to a decrease in the other. These coefficients are bounded between -1 and 1, and two

Table 4.4: Correlation coefficients $\rho(x_i, x_j) = V_{ij}/(\sigma_i \sigma_j)$ for the variables $((y, p_t, \phi, n)_D$, $(y, p_t, \phi, n)_{\overline{D}})$ from the original Monte Carlo sample of events.

	y_D	$y_{\overline{D}}$	$p_{t,D}$	$p_{t,\overline{D}}$	ϕ_D	$\phi_{\overline{D}}$	n_D	$n_{\overline{D}}$
y_D	1.00							
$y_{\overline{D}}$	-.32	1.00						
$p_{t,D}$	-.04	-.11	1.00					
$p_{t,\overline{D}}$	-.05	-.09	.10	1.00				
ϕ_D	.00	.00	.00	-.01	1.00			
$\phi_{\overline{D}}$	.01	-.01	.01	.00	-.27	1.00		
n_D	.02	-.01	.00	.00	.00	.00	1.00	
$n_{\overline{D}}$	.02	-.03	.00	.00	.00	.00	.00	1.00

random variables with $\rho(x_i, x_j) = +1(-1)$ are said to be completely positively (negatively) correlated.

The correlation coefficients for the variables $\vec{x} = ((y, p_t, \phi, n)_D, (y, p_t, \phi, n)_{\overline{D}})$ from the original Monte Carlo sample are shown in Table 4.4. Given the discussion in Chapter 1, the results are not surprising. The most significant correlations are between the variables y_D and $y_{\overline{D}}$, and between the variables ϕ_D and $\phi_{\overline{D}}$, with $\rho(y_D, y_{\overline{D}})$ and $\rho(\phi_D, \phi_{\overline{D}})$ approximately equal to -0.3. We ignore the slight correlations between the rapidities and the transverse momenta.

From Chapter 1 and Table 4.4, we conclude that to a good approximation the distribution of Monte Carlo events factorizes as follows:

$$P^{MC}(\vec{x}) = B_{n_D n_{\overline{D}}}\, C_{n_D n_{\overline{D}}}(y_D, y_{\overline{D}})\; E(p_{t,D})\; F(p_{t,\overline{D}})\; G(\phi_D, \phi_{\overline{D}}) \tag{4.6}$$

where the functions $C_{n_D n_{\overline{D}}}$, E, F, and G are normalized (*e.g.*, $\int\int C_{n_D n_{\overline{D}}}(y_D, y_{\overline{D}})\, \mathrm{d}y_D\, \mathrm{d}y_{\overline{D}} = 1$) and where $B_{n_D n_{\overline{D}}}$ gives the number of each type of event. The correlations between y_D and $y_{\overline{D}}$ depend on the type of $D\overline{D}$ event; that is, on whether the event is a $D^0\overline{D^0}$, a $D^0 D^-$, a $D^+\overline{D^0}$, or a D^+D^- event.

Correlations in the Acceptance Function

In the previous section, we determined approximately how the distribution of Monte Carlo events $P^{MC}(\vec{x})$ factorizes. In this section, we want to determine how the acceptance function $A(\vec{x})$ factorizes. We are, of course, in a catch-22: How can we determine how $A(\vec{x})$ factorizes without knowing what $A(\vec{x})$ is?

As an approximation, we determine, for each variable x_i, whether the function $A^{MC}(x_i)$ depends significantly on the value of any other variable x_j, where, for a restricted range of x_j,

$$A^{MC}(x_i;\ a < x_j < b) = \frac{\int_a^b \mathrm{d}x_j \ \prod_{k\neq i,j}(\int \mathrm{d}x_k)\ Q^{MC}(\vec{x})}{\int_a^b \mathrm{d}x_j \ \prod_{k\neq i,j}(\int \mathrm{d}x_k)\ P^{MC}(\vec{x})}. \tag{4.7}$$

As discussed in Section 4.2.2, the function $A^{MC}(x_i)$ may depend on the physics assumptions of the Monte Carlo. We emphasize that $A^{MC}(x_i;\ a < x_j < b)$ is not the same as a projection of the the eight-dimensional acceptance function $A(\vec{x})$ onto the x_i axis,

$$A(x_i;\ a < x_j < b) = \int_a^b \mathrm{d}x_j \ \prod_{k\neq i,j}(\int \mathrm{d}x_k)\frac{Q^{MC}(\vec{x})}{P^{MC}(\vec{x})}.$$

We use A^{MC} only as a gross indication of whether the acceptance as a function of variable x_i depends on the value of x_j.

Figure 4.9 shows A^{MC} as a function of rapidity, y; Fig. 4.10, as a function of the transverse momenta, p_t; Fig. 4.11, as a function of the azimuthal angle, ϕ; and, lastly, Fig. 4.12, as a function of the number of decay tracks, n In each of these four figures, we show six plots. For example, in Figure 4.9 we show

(a) $A^{MC}(y_D)$ and $A^{MC}(y_{\overline{D}})$,

(b) $A^{MC}(y_D; a < y_{\overline{D}} < b)$ for two ranges of $y_{\overline{D}}$;

(c) $A^{MC}(y_{\overline{D}}; a < y_D < b)$ for two ranges of y_D,

(d) $A^{MC}(y_D; a < p_{t,D} < b) + A^{MC}(y_{\overline{D}}; a < p_{t,\overline{D}} < b)$ for three ranges p_t;

(e) $A^{MC}(y_D; a < \phi_D < b) + A^{MC}(y_{\overline{D}}; a < \phi_{\overline{D}} < b)$ for three ranges of ϕ; and

(f) $A^{MC}(y_D; n_D = i) + A^{MC}(y_{\overline{D}}; n_{\overline{D}} = i)$ for $i = 2$, 3, and 4.

As we are interested only in the shapes of the distributions, all functions are normalized to the same area.

The conclusions we draw from these figures are:

- With a few exceptions, which are noted below, the acceptance as a function of any variable x_i does not depend significantly on the value of any other variable x_j. That is, the eight dimensional acceptance function, to a good approximation, factorizes completely.

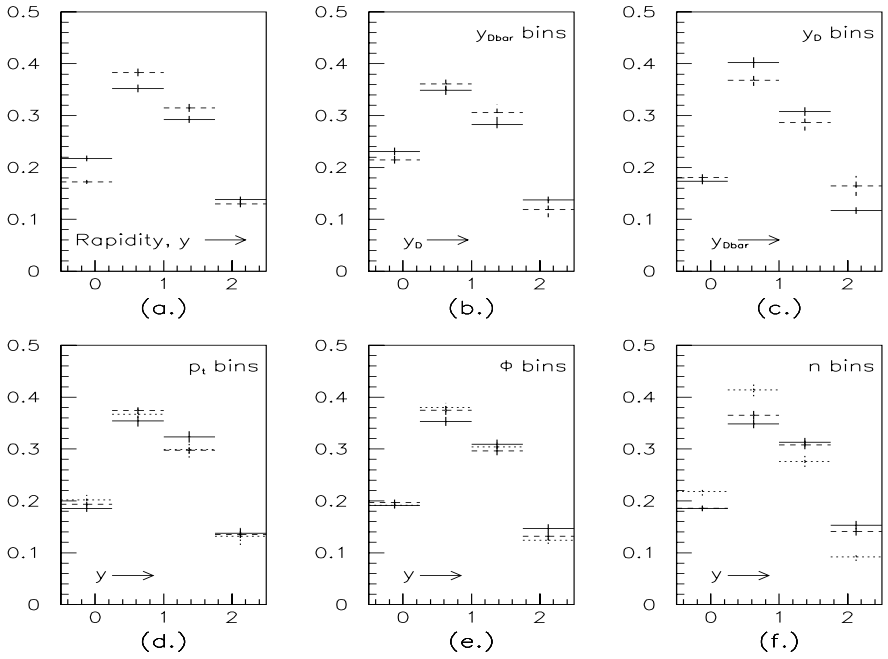

solid	(a.) $A^{MC}(y_D)$	(b.) $A^{MC}(y_D;\ -0.5 < y_{\overline{D}} < 1.0)$	(c.) $A^{MC}(y_{\overline{D}};\ -0.5 < y_D < 1.0)$
dashed	$A^{MC}(y_{\overline{D}})$	$A^{MC}(y_D;\ 1.0 < y_{\overline{D}} < 2.5)$	$A^{MC}(y_{\overline{D}};\ 1.0 < y_D < 2.5)$

solid	(d.)	$A^{MC}(y_D;\ p_{t,D} < 0.5\ \text{GeV})$	+	$A^{MC}(y_{\overline{D}};\ p_{t,\overline{D}} < 0.5\ \text{GeV})$
dashed		$A^{MC}(y_D;\ 0.5 < p_{t,D} < 1.5\ \text{GeV})$	+	$A^{MC}(y_{\overline{D}};\ 0.5 < p_{t,\overline{D}} < 1.5\ \text{GeV})$
dotted		$A^{MC}(y_D;\ 1.5 < p_{t,D} < 3.0\ \text{GeV})$	+	$A^{MC}(y_{\overline{D}};\ 1.5 < p_{t,\overline{D}} < 3.0\ \text{GeV})$
solid	(e.)	$A^{MC}(y_D;\ 0^\circ < \phi_D < 120^\circ)$	+	$A^{MC}(y_{\overline{D}};\ 0^\circ < \phi_{\overline{D}} < 120^\circ)$
dashed		$A^{MC}(y_D;\ 120^\circ < \phi_D < 240^\circ)$	+	$A^{MC}(y_{\overline{D}};\ 120^\circ < \phi_{\overline{D}} < 240^\circ)$
dotted		$A^{MC}(y_D;\ 240^\circ < \phi_D < 360^\circ)$	+	$A^{MC}(y_{\overline{D}};\ 240^\circ < \phi_{\overline{D}} < 360^\circ)$
solid	(f.)	$A^{MC}(y_D;\ n_D = 2)$	+	$A^{MC}(y_{\overline{D}};\ n_{\overline{D}} = 2)$
dashed		$A^{MC}(y_D;\ n_D = 3)$	+	$A^{MC}(y_{\overline{D}};\ n_{\overline{D}} = 3)$
dotted		$A^{MC}(y_D;\ n_D = 4)$	+	$A^{MC}(y_{\overline{D}};\ n_{\overline{D}} = 4)$

Figure 4.9: A^{MC}, defined in Eq. 4.7, as a function of rapidity. The meaning of the solid, dashed, and dotted curves is given in the table below the figures. All distributions are normalized to the same area.

- Not surprisingly, the acceptance function does not depend on the azimuthal angle of either the D or $\overline{D}$ meson, thereby reducing our eight-dimensional acceptance function to a six-dimensional function.

- The dependence of the acceptance function on the transverse momenta of the D mesons is relatively flat, varying by approximately 30% over the entire range of transverse momenta. The steepness depends on the number of decay tracks n of the D meson.

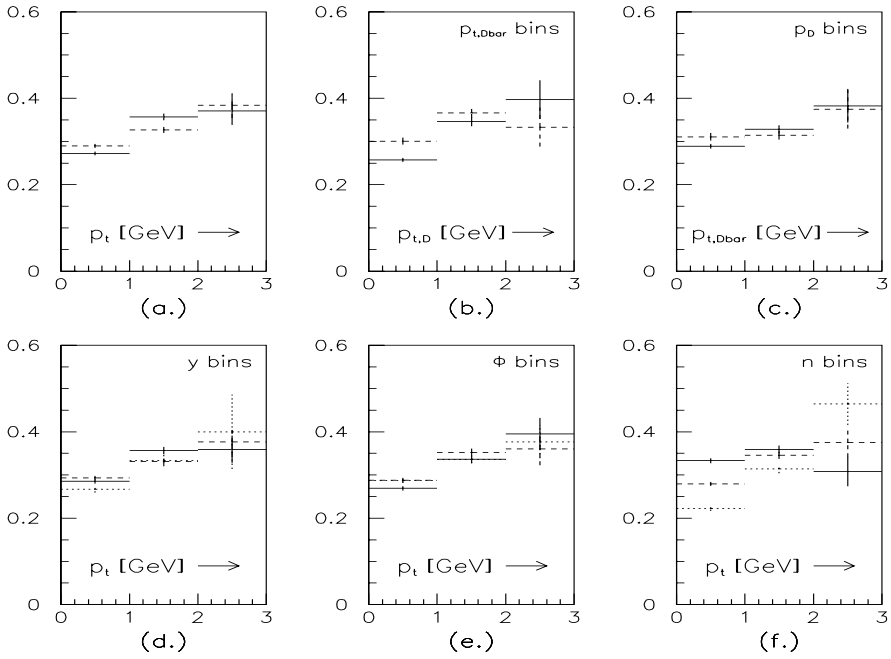

solid	(a.) $A^{MC}(p_{t,D})$	(b.) $A^{MC}(p_{t,D};\ p_{t,\overline{D}} < 1$ GeV)	(c.) $A^{MC}(p_{t,\overline{D}};\ p_{t,D} < 1$ GeV)
dashed	$A^{MC}(p_{t,\overline{D}})$	$A^{MC}(p_{t,D};\ 1 < p_{t,\overline{D}} < 3$ GeV)	$A^{MC}(p_{t,\overline{D}};\ 1 < p_{t,D} < 3$ GeV)

solid	(d.)	$A^{MC}(p_{t,D};\ -0.5 < y_D < 0.5)$	+	$A^{MC}(p_{t,\overline{D}};\ -0.5 < y_{\overline{D}} < 0.5)$
dashed		$A^{MC}(p_{t,D};\ 0.5 < y_D < 1.5)$	+	$A^{MC}(p_{t,\overline{D}};\ 0.5 < y_{\overline{D}} < 1.5)$
dotted		$A^{MC}(p_{t,D};\ 1.5 < y_D < 2.5)$	+	$A^{MC}(p_{t,\overline{D}};\ 1.5 < y_{\overline{D}} < 2.5)$
solid	(e.)	$A^{MC}(p_{t,D};\ 0° < \phi_D < 120°)$	+	$A^{MC}(p_{t,\overline{D}};\ 0° < \phi_{\overline{D}} < 120°)$
dashed		$A^{MC}(p_{t,D};\ 120° < \phi_D < 240°)$	+	$A^{MC}(p_{t,\overline{D}};\ 120° < \phi_{\overline{D}} < 240°)$
dotted		$A^{MC}(p_{t,D};\ 240° < \phi_D < 360°)$	+	$A^{MC}(p_{t,\overline{D}};\ 240° < \phi_{\overline{D}} < 360°)$
solid	(f.)	$A^{MC}(p_{t,D};\ n_D = 2)$	+	$A^{MC}(p_{t,\overline{D}};\ n_{\overline{D}} = 2)$
dashed		$A^{MC}(p_{t,D};\ n_D = 3)$	+	$A^{MC}(p_{t,\overline{D}};\ n_{\overline{D}} = 3)$
dotted		$A^{MC}(p_{t,D};\ n_D = 4)$	+	$A^{MC}(p_{t,\overline{D}};\ n_{\overline{D}} = 4)$

Figure 4.10: A^{MC}, defined in Eq. 4.7, as a function of transverse momentum. The meaning of the solid, dashed, and dotted curves is given in the table below the figures. All distributions are normalized to the same area.

- The acceptance for 2- and 3-pronged D mesons is approximately five times the acceptance for 4-pronged D mesons. This relative acceptance among the three types of decay modes does not depend significantly on any other variables.

- The dependence of the acceptance function on the rapidity of D mesons is quite steep. In addition, the shapes of the projections $A^{MC}(y_D)$ and $A^{MC}(y_{\overline{D}})$ are slightly different; and the shape of $A^{MC}(y)$ for 2- and 3-pronged D mesons differs from the shape of $A^{MC}(y)$ for 4-pronged D mesons.

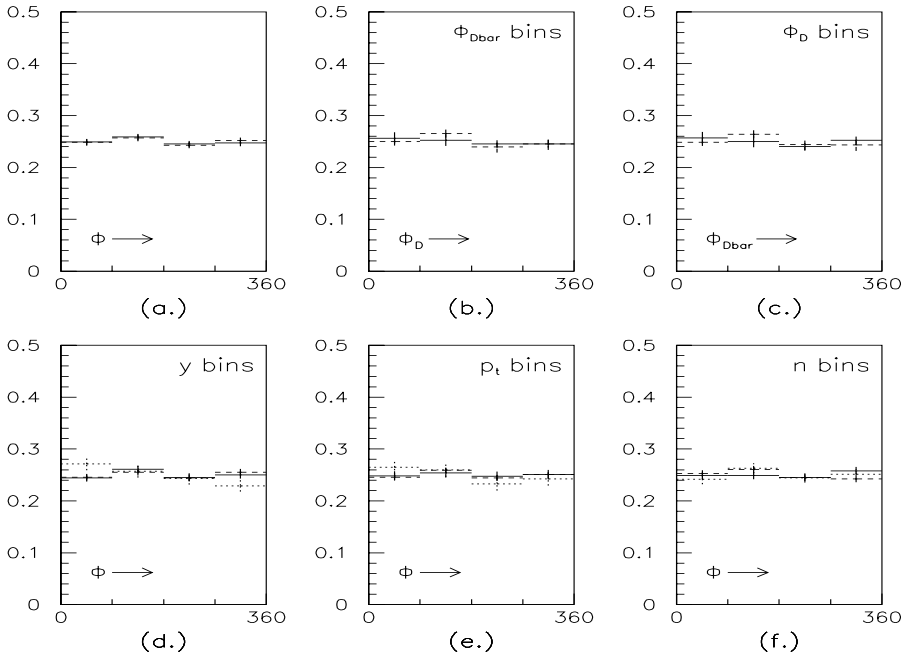

solid	(a.) $A^{MC}(\phi_D)$	(b.) $A^{MC}(\phi_D;\ \phi_{\overline{D}} < 180°)$	(c.) $A^{MC}(\phi_{\overline{D}};\ \phi_D < 180°)$
dashed	$A^{MC}(\phi_{\overline{D}})$	$A^{MC}(\phi_D;\ \phi_{\overline{D}} > 180°)$	$A^{MC}(\phi_{\overline{D}};\ \phi_D > 180°)$

solid	(d.)	$A^{MC}(\phi_D;\ -0.5 < y_D < 0.5)$	+	$A^{MC}(\phi_{\overline{D}};\ -0.5 < y_{\overline{D}} < 0.5)$
dashed		$A^{MC}(\phi_D;\ 0.5 < y_D < 1.5)$	+	$A^{MC}(\phi_{\overline{D}};\ 0.5 < y_{\overline{D}} < 1.5)$
dotted		$A^{MC}(\phi_D;\ 1.5 < y_D < 2.5)$	+	$A^{MC}(\phi_{\overline{D}};\ 1.5 < y_{\overline{D}} < 2.5)$
solid	(e.)	$A^{MC}(\phi_D;\ p_{t,D} < 0.5\ \mathrm{GeV})$	+	$A^{MC}(\phi_{\overline{D}};\ p_{t,\overline{D}} < 0.5\ \mathrm{GeV})$
dashed		$A^{MC}(\phi_D;\ 0.5 < p_{t,D} < 1.5\ \mathrm{GeV})$	+	$A^{MC}(\phi_{\overline{D}};\ 0.5 < p_{t,\overline{D}} < 1.5\ \mathrm{GeV})$
dotted		$A^{MC}(\phi_D;\ 1.5 < p_{t,D} < 3.0\ \mathrm{GeV})$	+	$A^{MC}(\phi_{\overline{D}};\ 1.5 < p_{t,\overline{D}} < 3.0\ \mathrm{GeV})$
solid	(f.)	$A^{MC}(\phi_D;\ n_D = 2)$	+	$A^{MC}(\phi_{\overline{D}};\ n_{\overline{D}} = 2)$
dashed		$A^{MC}(\phi_D;\ n_D = 3)$	+	$A^{MC}(\phi_{\overline{D}};\ n_{\overline{D}} = 3)$
dotted		$A^{MC}(\phi_D;\ n_D = 4)$	+	$A^{MC}(\phi_{\overline{D}};\ n_{\overline{D}} = 4)$

Figure 4.11: A^{MC}, defined in Eq. 4.7, as a function of azimuthal angle. The meaning of the solid, dashed, and dotted curves is given in the table below the figures. All distributions are normalized to the same area.

From these figures, we assume that to a good approximation the acceptance factorizes as follows:

$$A(\vec{x}) = b_{n_D}\, b_{n_{\overline{D}}}\, c^{D}_{n_D}(y_D)\, c^{\overline{D}}_{n_{\overline{D}}}(y_{\overline{D}})\, e_{n_D}(p_{t,D})\, e_{n_{\overline{D}}}(p_{t,\overline{D}}). \tag{4.8}$$

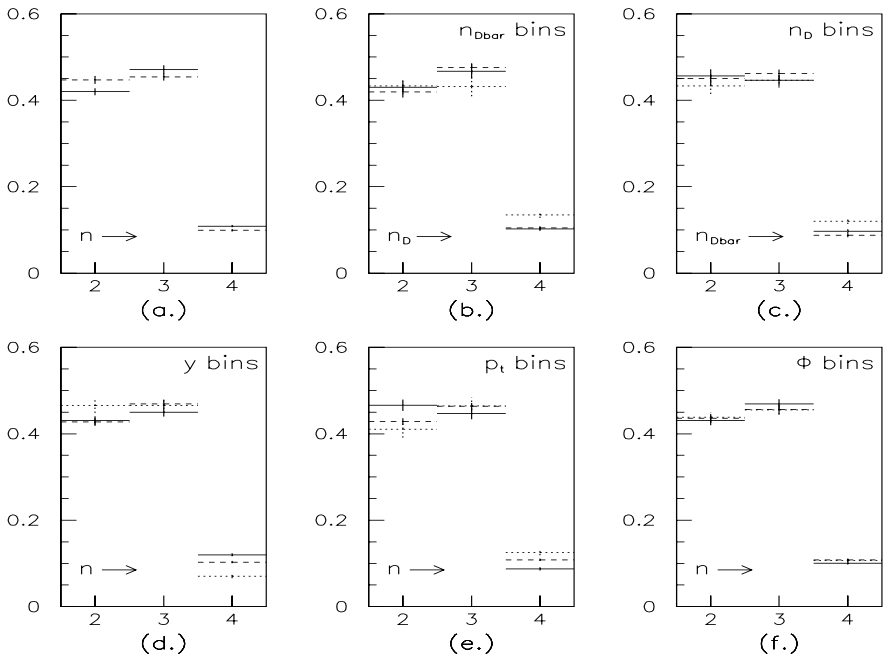

solid	(a.) $A^{MC}(n_D)$	(b.) $A^{MC}(n_D;\ n_{\overline{D}}=2)$	(c.) $A^{MC}(n_{\overline{D}};\ n_D=2)$
dashed	$A^{MC}(n_{\overline{D}})$	$A^{MC}(n_D;\ n_{\overline{D}}=3)$	$A^{MC}(n_{\overline{D}};\ n_D=3)$
dotted		$A^{MC}(n_D;\ n_{\overline{D}}=4)$	$A^{MC}(n_{\overline{D}};\ n_D=4)$

solid	(d.)	$A^{MC}(n_D;\ -0.5 < y_D < 0.5)$	+	$A^{MC}(n_{\overline{D}};\ -0.5 < y_{\overline{D}} < 0.5)$
dashed		$A^{MC}(n_D;\ 0.5 < y_D < 1.5)$	+	$A^{MC}(n_{\overline{D}};\ 0.5 < y_{\overline{D}} < 1.5)$
dotted		$A^{MC}(n_D;\ 1.5 < y_D < 2.5)$	+	$A^{MC}(n_{\overline{D}};\ 1.5 < y_{\overline{D}} < 2.5)$
solid	(e.)	$A^{MC}(n_D;\ p_{t,D} < 0.5\ \mathrm{GeV})$	+	$A^{MC}(n_{\overline{D}};\ p_{t,\overline{D}} < 0.5\ \mathrm{GeV})$
dashed		$A^{MC}(n_D;\ 0.5 < p_{t,D} < 1.5\ \mathrm{GeV})$	+	$A^{MC}(n_{\overline{D}};\ 0.5 < p_{t,\overline{D}} < 1.5\ \mathrm{GeV})$
dotted		$A^{MC}(n_D;\ 1.5 < p_{t,D} < 3.0\ \mathrm{GeV})$	+	$A^{MC}(n_{\overline{D}};\ 1.5 < p_{t,\overline{D}} < 3.0\ \mathrm{GeV})$
solid	(f.)	$A^{MC}(n_D;\ 0^\circ < \phi_D < 120^\circ)$	+	$A^{MC}(n_{\overline{D}};\ 0^\circ < \phi_{\overline{D}} < 120^\circ)$
dashed		$A^{MC}(n_D;\ 120^\circ < \phi_D < 240^\circ)$	+	$A^{MC}(n_{\overline{D}};\ 120^\circ < \phi_{\overline{D}} < 240^\circ)$
dotted		$A^{MC}(n_D;\ 240^\circ < \phi_D < 360^\circ)$	+	$A^{MC}(n_{\overline{D}};\ 240^\circ < \phi_{\overline{D}} < 360^\circ)$

Figure 4.12: A^{MC}, defined in Eq. 4.7, as a function of the number of decay tracks. The meaning of the solid, dashed, and dotted curves is given in the table below the figures. All distributions are normalized to the same area.

An Estimate for the Eight-Dimensional Acceptance Function

We now need estimates for the functions b_n, $c^D_{n_D}(y_D)$, $c^{\overline{D}}_{n_{\overline{D}}}(y_{\overline{D}})$, and $e_n(p_t)$. Given our estimates for how the distribution of Monte Carlo events factorizes:

$$P^{MC}(\vec{x}) = B_{n_D\, n_{\overline{D}}}\, C_{n_D\, n_{\overline{D}}}(y_D, y_{\overline{D}})\ E(p_{t,D})\ F(p_{t,\overline{D}})\ G(\phi_D, \phi_{\overline{D}}),$$

and how the acceptance function factorizes:

$$A(\vec{x}) = b_{n_D}\; b_{n_{\overline{D}}}\; c^D_{n_D}(y_D)\; c^{\overline{D}}_{n_{\overline{D}}}(y_{\overline{D}})\; e_{n_D}(p_{t,D})\; e_{n_{\overline{D}}}(p_{t,\overline{D}}),$$

obtaining an estimate for e_n is straight-forward. For example, $A^{MC}(p_{t,D};\; n_D = 2)$ equals

$$\frac{\int\int\int\int\int\; (\; \sum_{n_{\overline{D}}}\; b_2\; b_{n_{\overline{D}}}\; c^D_2\; c^{\overline{D}}_{n_{\overline{D}}}\; e_2\; e_{n_{\overline{D}}}\; B_{2n_{\overline{D}}}\; C_{2n_{\overline{D}}}\; E\; F\; G\;)\; \mathrm{d}y_D\; \mathrm{d}y_{\overline{D}}\; \mathrm{d}p_{t,\overline{D}}\; \mathrm{d}\phi_D\; \mathrm{d}\phi_{\overline{D}}}{\int\int\int\int\int\; (\; \sum_{n_{\overline{D}}} B_{2n_{\overline{D}}}\; C_{2n_{\overline{D}}}\; E\; F\; G\;)\; \mathrm{d}y_D\; \mathrm{d}y_{\overline{D}}\; \mathrm{d}p_{t,\overline{D}}\; \mathrm{d}\phi_D\; \mathrm{d}\phi_{\overline{D}}}$$

$$= e_2(p_{t,D})\; \frac{E}{E}\; b_2\; \frac{\int\int\int c_2^D\; F\; (\; \sum_{n_{\overline{D}}} b_{n_{\overline{D}}}\; c^{\overline{D}}_{n_{\overline{D}}}\; e_{n_{\overline{D}}}\; B_{2n_{\overline{D}}}\; C_{2n_{\overline{D}}}\;)\; \mathrm{d}y_D\; \mathrm{d}y_{\overline{D}}\; \mathrm{d}p_{t,\overline{D}}}{\int\int\int F\; (\; \sum_{n_{\overline{D}}} B_{2n_{\overline{D}}}\; C_{2n_{\overline{D}}}\;)\; \mathrm{d}y_D\; \mathrm{d}y_{\overline{D}}\; \mathrm{d}p_{t,\overline{D}}}\; \frac{\int\int G\; \mathrm{d}\phi_D\; \mathrm{d}\phi_{\overline{D}}}{\int\int G\; \mathrm{d}\phi_D\; \mathrm{d}\phi_{\overline{D}}}.$$

Nothing to the right of $e_2(p_{t,D})$ depends on $p_{t,D}$; that is, $A^{MC}(p_{t,D};\; n_D = 2) \propto e_2(p_{t,D})$. Hence, the solid-, dashed-, and dotted-lined $A^{MC}(p_t)$ functions shown in Figure 4.10f are good estimates for e_2, e_3, and e_4, respectively.

Obtaining estimates for b_n, $c^D_{n_D}$, and $c^{\overline{D}}_{n_{\overline{D}}}$ is a little less straight-forward because the y_D and $y_{\overline{D}}$ distributions in the original Monte Carlo are correlated and because the functions B, C, c^D, $c^{\overline{D}}$, and e all depend on the number of decay tracks. For example, $A^{MC}(y_D; n_D = 2)$ equals

$$c_2^D(y_D)\; \frac{\int\int F\; (\; \sum_{n_{\overline{D}}}\; b_{n_{\overline{D}}}\; e_{n_{\overline{D}}}\; B_{2n_{\overline{D}}}\; c^{\overline{D}}_{n_{\overline{D}}}(y_{\overline{D}})\; C_{2n_{\overline{D}}}(y_D, y_{\overline{D}})\;)\; \mathrm{d}y_{\overline{D}}\; \mathrm{d}p_{t,\overline{D}}}{\int\int F\; (\; \sum_{n_{\overline{D}}}\; B_{2n_{\overline{D}}}\; C_{2n_{\overline{D}}}(y_D, y_{\overline{D}})\;)\; \mathrm{d}y_{\overline{D}}\; \mathrm{d}p_{t,\overline{D}}}$$

where the term to the right of $c_2^D(y_D)$ does depend on y_D. To obtain estimates for b_n, c^D and $c^{\overline{D}}$ that do not depend significantly on the physics assumptions of the Monte Carlo, we examine the two-dimensional functions $A^{MC}(y_D, y_{\overline{D}};\; n_D, n_{\overline{D}})$ for each of the nine combinations of $n_D n_{\overline{D}}$ pairs, where $A^{MC}(y_D, y_{\overline{D}};\; n_D, n_{\overline{D}})$ equals

$$\frac{b_{n_D}\; b_{n_{\overline{D}}}\; c^D_{n_D}(y_D)\; c^{\overline{D}}_{n_{\overline{D}}}(y_{\overline{D}})\; B_{n_D n_{\overline{D}}}\; C_{n_D n_{\overline{D}}}(y_D, y_{\overline{D}})}{B_{n_D n_{\overline{D}}}\; C_{n_D n_{\overline{D}}}(y_D, y_{\overline{D}})}\; \frac{\int e_{n_D}\; E\; \mathrm{d}p_{t,D}}{\int E\; \mathrm{d}p_{t,D}}\; \frac{\int e_{n_{\overline{D}}}\; F\; \mathrm{d}p_{t,\overline{D}}}{\int F\; \mathrm{d}p_{t,\overline{D}}}$$

$$=\; b_{n_D}\; b_{n_{\overline{D}}}\; c^D_{n_D}(y_D)\; c^{\overline{D}}_{n_{\overline{D}}}(y_{\overline{D}})\; \frac{\int e_{n_D}\; E\; \mathrm{d}p_{t,D}}{\int E\; \mathrm{d}p_{t,D}}\; \frac{\int e_{n_{\overline{D}}}\; F\; \mathrm{d}p_{t,\overline{D}}}{\int F\; \mathrm{d}p_{t,\overline{D}}}.$$

Because the e_n functions are relatively flat, ignoring their slight dependence on the number of decay tracks does not introduce large errors. Therefore, to a good approximation

$$A^{MC}(y_D, y_{\overline{D}};\; n_D, n_{\overline{D}}) \propto b_{n_D}\; b_{n_{\overline{D}}}\; c^D_{n_D}(y_D)\; c^{\overline{D}}_{n_{\overline{D}}}(y_{\overline{D}}).$$

In other words, to a good approximation, the nine $A^{MC}(y_D, y_{\overline{D}};\; n_D, n_{\overline{D}})$ functions, shown in Figure 4.13, do not depend on the physics assumptions of the Monte Carlo.

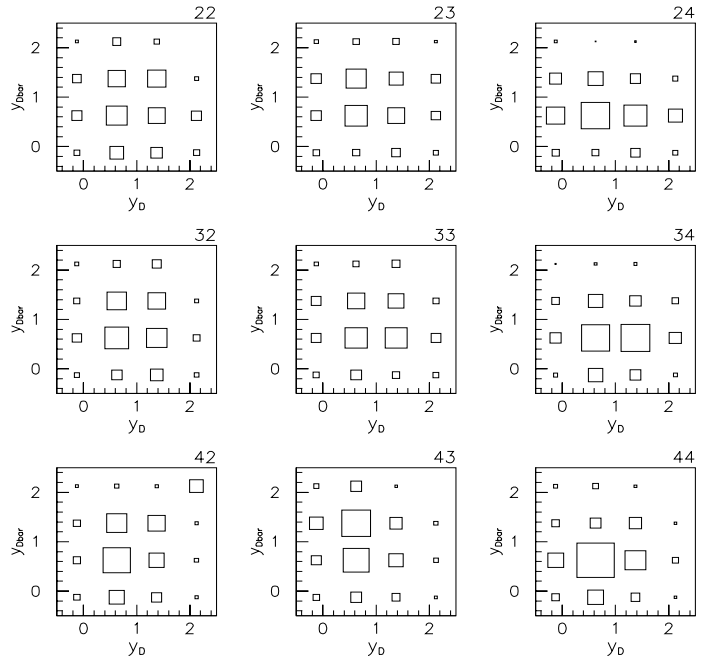

Figure 4.13: The nine $A^{MC}(y_D, y_{\overline{D}};\ n_D, n_{\overline{D}})$ projections (one for each $n_D n_{\overline{D}}$ combination). Each projection is normalized to the same area and plotted on the same scale.

To obtain estimates for b_{n_D} and $b_{n_{\overline{D}}}$, we integrate each of the nine functions over both y_D and $y_{\overline{D}}$ and sum over $n_{\overline{D}}$ and n_D, respectively:

$$\begin{aligned} b^D_{n_D} &= \sum_{n_{\overline{D}}} \int\int A^{MC}(y_D, y_{\overline{D}};\ n_D, n_{\overline{D}})\ \mathrm{d}y_D\ \mathrm{d}y_{\overline{D}} \\ &= (0.427 \pm 0.011,\ 0.466 \pm 0.012,\ 0.107 \pm 0.002), \end{aligned} \tag{4.9}$$

and

$$\begin{aligned} b^{\overline{D}}_{n_{\overline{D}}} &= \sum_{n_D} \int\int A^{MC}(y_D, y_{\overline{D}};\ n_D, n_{\overline{D}})\ \mathrm{d}y_D\ \mathrm{d}y_{\overline{D}} \\ &= (0.440 \pm 0.012,\ 0.472 \pm 0.011,\ 0.088 \pm 0.003), \end{aligned} \tag{4.10}$$

where the functions are arbitrarily normalized such that

$$\sum_{n_D}\sum_{n_{\overline{D}}} \int\int A^{MC}(y_D, y_{\overline{D}};\ n_D, n_{\overline{D}})\ \mathrm{d}y_D\ \mathrm{d}y_{\overline{D}} = 1.$$

We note that

$$b_{n_{\overline{D}}} \otimes b_{n_D} = \begin{bmatrix} 0.440 \\ 0.472 \\ 0.088 \end{bmatrix} \otimes \begin{bmatrix} 0.427 & 0.466 & 0.107 \end{bmatrix} = \begin{bmatrix} 0.188 & 0.205 & 0.047 \\ 0.202 & 0.223 & 0.050 \\ 0.038 & 0.041 & 0.009 \end{bmatrix}$$

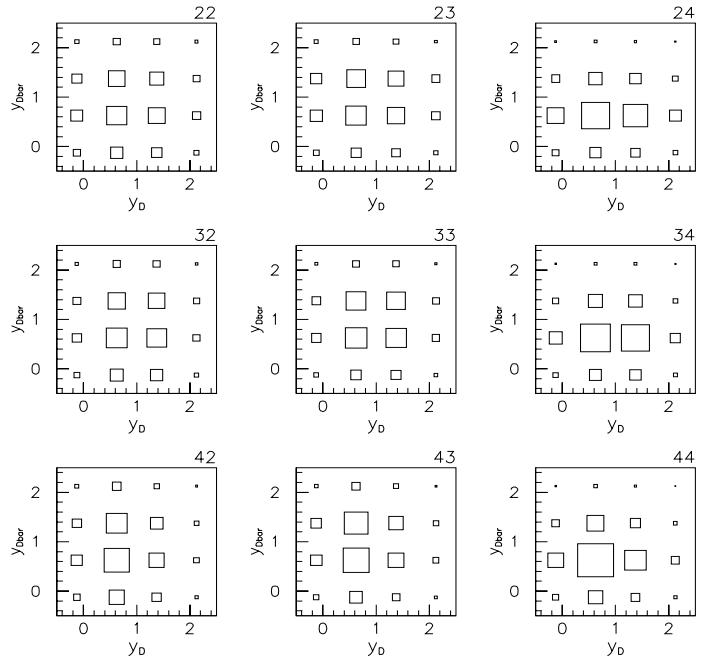

Figure 4.14: Using the estimates for the $c^D_{n_D}(y_D)$ and $c^{\overline{D}}_{n_{\overline{D}}}(y_{\overline{D}})$ distributions in Figure 4.15, we construct nine two-dimensional functions: $c^D_{n_D}(y_D)c^{\overline{D}}_{n_{\overline{D}}}(y_{\overline{D}})$, one for each $n_D n_{\overline{D}}$ combination. Comparing these distributions to the nine distributions in Figure 4.13 confirms that $A^{MC}(y_D, y_{\overline{D}};\ n_D, n_{\overline{D}})$ approximately factorizes.

is approximately equal to

$$\int\int A^{MC}(y_D, y_{\overline{D}};\ n_D, n_{\overline{D}})\ \mathrm{d}y_D\ \mathrm{d}y_{\overline{D}} = \begin{bmatrix} 0.187 & 0.205 & 0.048 \\ 0.202 & 0.223 & 0.047 \\ 0.038 & 0.038 & 0.012 \end{bmatrix},$$

confirming that, to a good approximation,

$$\int\int A^{MC}(y_D, y_{\overline{D}};\ n_D, n_{\overline{D}})\ \mathrm{d}y_D\ \mathrm{d}y_{\overline{D}},$$

which is a function of both n_D and $n_{\overline{D}}$, factorizes into a function of n_D times a function of $n_{\overline{D}}$.

Our estimates for b_{n_D} and $b_{n_{\overline{D}}}$ are very similar to the projections $A^{MC}_{n_D}$ and $A^{MC}_{n_{\overline{D}}}$ shown in Figure 4.12a. We emphasize, however, that we could not simply assume, for example, that the one-dimensional projection $A^{MC}_{n_D}$, which is approximately proportional to

$$b_{n_D}\frac{\int\int \sum_{n_{\overline{D}}} B_{n_D n_{\overline{D}}}\ b_{n_{\overline{D}}}\ c^D_{n_D}(y_D)\ c^{\overline{D}}_{n_{\overline{D}}}(y_{\overline{D}})\ C_{n_D n_{\overline{D}}}(y_D, y_{\overline{D}})\ \mathrm{d}y_D\ \mathrm{d}y_{\overline{D}}}{\int\int \sum_{n_{\overline{D}}} B_{n_D n_{\overline{D}}}\ C_{n_D n_{\overline{D}}}(y_D, y_{\overline{D}})\ \mathrm{d}y_D\ \mathrm{d}y_{\overline{D}}},$$

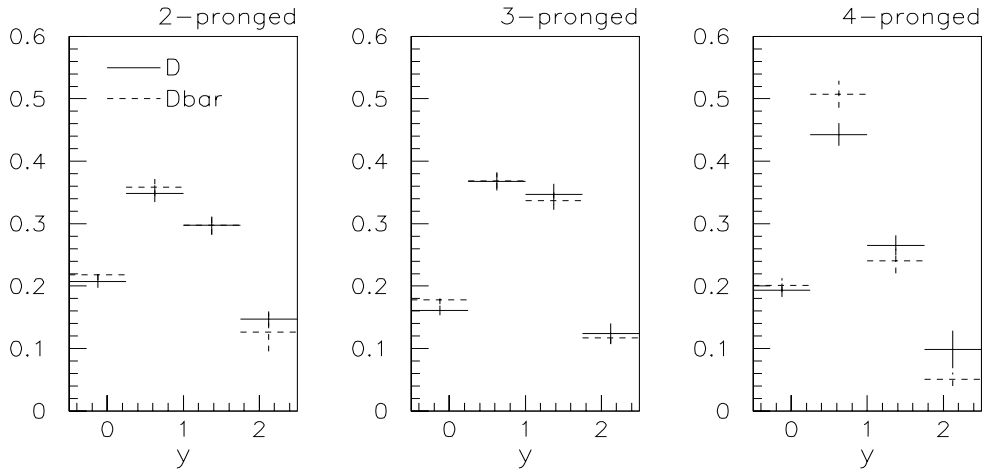

Figure 4.15: Estimates for $c^{D}_{n_D}(y_D)$ and $c^{\overline{D}}_{n_{\overline{D}}}(y_{\overline{D}})$ obtained by summing and integrating over the two-dimensional projection $A^{MC}(y_D, y_{\overline{D}};\ n_D, n_{\overline{D}})$.

is the same as summing and integrating over the nine two-dimensional projections. Determining b_n, $c^{D}_{n_D}$, and $c^{\overline{D}}_{n_{\overline{D}}}$ from the nine two-dimensional projections in Figure 4.13, we explicitly avoid obtaining estimates that depend on the physics assumptions of the Monte Carlo.

To find estimates for $c^{D}_{n_D}$ and $c^{\overline{D}}_{n_{\overline{D}}}$, we first normalize each of the nine projections:

$$\int\int A^{MC}(y_D, y_{\overline{D}};\ n_D, n_{\overline{D}})\ \mathrm{d}y_D\ \mathrm{d}y_{\overline{D}} \ =\ 1.$$

and then sum over $n_{\overline{D}}$ (n_D) and integrate over $y_{\overline{D}}$ (n_D):

$$c^{D}_{n_D}(y_D) \ =\ \int \sum_{n_{\overline{D}}} A^{MC}(y_D, y_{\overline{D}};\ n_D, n_{\overline{D}})\ \mathrm{d}y_{\overline{D}}$$

and

$$c^{\overline{D}}_{n_{\overline{D}}}(y_{\overline{D}}) \ =\ \int \sum_{n_D} A^{MC}(y_D, y_{\overline{D}};\ n_D, n_{\overline{D}})\ \mathrm{d}y_D\,.$$

The resulting six distributions are shown in Figure 4.15. In Figure 4.14 we show the nine two-dimensional distributions obtained by multiplying each of the three $c^{D}_{n_D}(y_D)$ distributions with each of the three $c^{\overline{D}}_{n_{\overline{D}}}(y_{\overline{D}})$ distributions. These nine distributions are very similar to the nine $A^{MC}(y_D, y_{\overline{D}};\ n_D, n_{\overline{D}})$ projections shown in Figure 4.13, confirming that the projections $A^{MC}(y_D, y_{\overline{D}};\ n_D, n_{\overline{D}})$, to a good approximation, factorize.

Weighting the $D\overline{D}$ Candidates from the Data Sample

We now have an estimate for our acceptance function:

$$A(\vec{x}) = b^D_{n_D}\, b^{\overline{D}}_{n_{\overline{D}}}\, c^D_{n_D}(y_D)\; c^{\overline{D}}_{n_{\overline{D}}}(y_{\overline{D}})\; e_{n_D}(p_{t,D})\; e_{n_{\overline{D}}}(p_{t,\overline{D}}),$$

where the $b^D_{n_D}$ and $b^{\overline{D}}_{n_{\overline{D}}}$ distributions are given in Equations 4.9-4.10; the $c^D_{n_D}(y_D)$ and $c^{\overline{D}}_{n_{\overline{D}}}(y_{\overline{D}})$ distributions are shown in Figure 4.15; and the $e_n(p_t)$ distributions are shown in Figure 4.10f. We transform the $c(y)$ and $e(p_t)$ functions into piece-wise linear functions, making straight lines from the center of each bin to the center of the neighboring bins. As discussed above, we can obtain acceptance corrected distributions from our final data sample by assigning a weight $w \propto 1/A(\vec{x})$ to each $D\overline{D}$ candidate and using the weighted likelihood function (Equation 4.5) when executing the unbinned maximum likelihood fits.

As shown in Eqs. 4.9-4.10, the acceptance for D mesons that decay to $K3\pi$ is roughly 4.5 times smaller than the acceptance for either 2- or 3-pronged decays. Hence, the acceptance for 4-4 pronged decays is approximately 20 times smaller than n-m decays, where both n and m are equal to 2 or 3. That is, we have very few 4-4 candidates with very large weights. For most charm-pair distributions, discussed in the following chapter, eliminating the 4-4 pronged candidates from our data sample improves the significance of our signal distributions. All the results in the next chapter, therefore, are obtained after eliminating all 4-4 pronged candidates.

The weights w must also be proportional to $\frac{1}{B(D)B(\overline{D})}$ where, for neutral D candidates, B is the sum of the branching fractions of the two D^0 modes we reconstruct, and, for charged D candidates, B is branching fraction to $K\pi\pi$. The relevant branching fractions are[40]

$$\begin{aligned} B(D^+ \to K^-\pi^+\pi^+) &= (9.1 \pm 0.6)\%, \\ B(D^0 \to K^-\pi^+\pi^-\pi^+) &= (8.1 \pm 0.5)\%, \text{ and} \\ B(D^0 \to K^-\pi^+) &= (4.01 \pm 0.14)\%. \end{aligned}$$

Because we eliminate 4-4 pronged candidates, the branching fraction for $D^0\overline{D}^0$ candidates is actually

$$B(D^0 \to K^-\pi^+)B(D^0 \to K^-\pi^+) \;+\; 2B(D^0 \to K^-\pi^+)B(D^0 \to K^-\pi^+\pi^-\pi^+),$$

or $(0.81 \pm 0.05)\%$. Weighting events by the inverse of the the branching fraction is necessary because, for example, the distribution of invariant masses for $D^0\overline{D^0}$ may differ from the

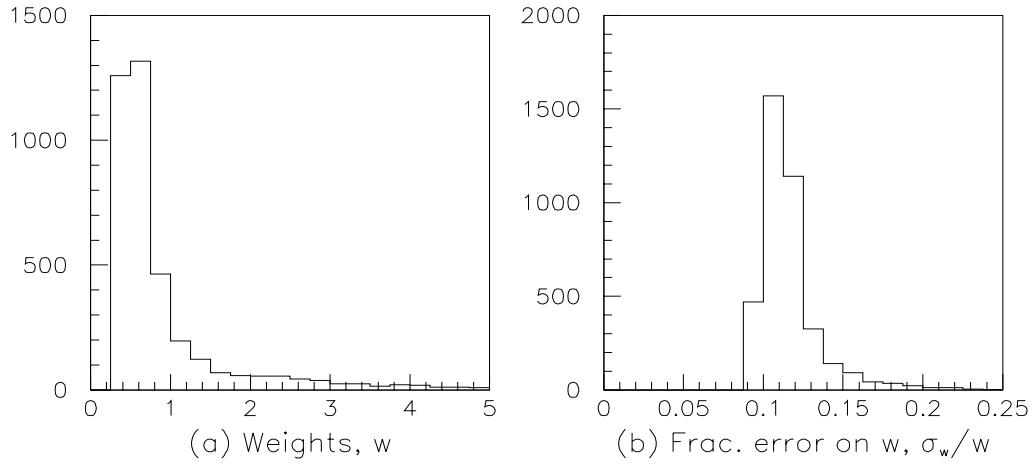

Figure 4.16: (a) The distribution of weights, $w \propto \frac{1}{A(\vec{x})B(D)B(\overline{D})}$, for the final sample of $D\overline{D}$ candidates. The mean of the distribution, by construction, is one; the standard deviation about the mean is 1.3, with the largest weight (not shown) at 23. (b) The distribution of the fractional errors on the weights, with a mean of 12%.

distribution for D^+D^-. Such weighting ensures that $D\overline{D}$ distributions extracted from our data sample, shown in Chapter 5, reflect the true production rates for the four types of $D\overline{D}$ pairs ($D^0\overline{D^0}$, D^0D^-, $D^+\overline{D^0}$, and D^+D^-), rather than the production rates for the subset of $D\overline{D}$ pairs in which both D mesons decay to $K^{\mp}\pi^{\pm}$, $K^{\mp}\pi^{\pm}\pi^{\pm}$, or $K^{\mp}\pi^{\pm}\pi^{\mp}\pi^{\pm}$.

The distribution of weights for all $D\overline{D}$ candidates in the two-dimensional normalized mass window defined by $|M_n^{(K^-N\pi)}| < 6.5$ and $|M_n^{(K^+N\pi)}| < 6.5$ is shown in Figure 4.16a. The weights w, proportional to $\frac{1}{A(\vec{x})B(D)B(\overline{D})}$, are normalized such that $\sum_{i=1}^{N_{D\overline{D}}} w_i = N_{D\overline{D}}$ where $N_{D\overline{D}}$ is the number of $D\overline{D}$ candidates. Given the choice of normalization, the mean of this distribution is 1; the standard deviation about the mean is 1.3. Less than 2% of the candidates lie beyond the range shown in Figure 4.16a and 23 is the largest weight. The distribution of the fractional errors of the weights, σ_{w_i}/w_i, is shown in Figure 4.16b, where σ_{w_i} is

$$w_i\sqrt{\left(\frac{\sigma_{b_D}}{b^D_{n_D}}\right)^2+\left(\frac{\sigma_{b_{\overline{D}}}}{b^{\overline{D}}_{n_{\overline{D}}}}\right)^2+\left(\frac{\sigma_{c_D}}{c^D_{n_D}}\right)^2+\left(\frac{\sigma_{c_{\overline{D}}}}{c^{\overline{D}}_{n_{\overline{D}}}}\right)^2+\left(\frac{\sigma_{e_D}}{e_{n_D}}\right)^2+\left(\frac{\sigma_{e_{\overline{D}}}}{e_{n_{\overline{D}}}}\right)^2+\left(\frac{\sigma_B}{B(D\overline{D})}\right)^2}.$$

This error accounts for the Monte Carlo statistical error and the uncertainties on the branching fractions, but not for possible systematic errors due to the Monte Carlo not accurately representing the detector.

The first step in obtaining acceptance-corrected distributions for any given physics variable $z(\vec{x})$ is to divide our sample of $N_{D\overline{D}}$ candidates into N sub-samples where each candidate in the i^{th} sub-sample has $k_i < z < k_{i+1}$. Although the sum of the weights of all $D\overline{D}$ candidates, by definition, equals $N_{D\overline{D}}$, the sum of the weights of a particular sub-sample of events may not equal the true (unweighted) number of events in that sample N_{SMPL}. The error on the number of signal events σ_{N_S} obtained from each weighted likelihood fit reflects the number of reconstructed candidates in the sample, N_{SMPL}, and must be rescaled to reflect the estimate for the number of generated candidates, $\sum_{i=1}^{N_{SMPL}} w_i$. That is,

$$\sigma_{N_S} \rightarrow \sqrt{\frac{\sum_{i=1}^{N_{SMPL}} w_i}{N_{SMPL}}}\, \sigma_{N_S}.$$

All of the acceptance-corrected $D\overline{D}$ distributions shown in the following chapter are obtained using the weighted maximum likelihood fits discussed in this chapter. We currently do not account for the statistical errors σ_w on the weights w.

Chapter 5

Results and Conclusions

In this chapter, we present charm-pair results from approximately 90% of the full E791 data sample. As discussed in the previous chapter, all distributions, experimental and theoretical, are obtained after excluding any candidates in which the center-of-mass rapidity of either the D or $\overline{D}$ is less than -0.5 or greater than 2.5. In addition, all 4-4 pronged $D\overline{D}$ candidates are eliminated from the data sample because the large weights of these candidates degrade the significance of the signal distributions.

For the experimental results, the acceptance-corrected distributions are obtained from maximizing the weighted likelihood function (Section 4.2); the uncorrected distributions, from maximizing the unweighted likelihood function (Section 4.1.3). The errors on the acceptance-corrected results do not yet include the errors associated with each weight; nor are systematic errors included. The total number of signal $D\overline{D}$ events found in the unweighted fit is $N_s = 791 \pm 44$. For the weighted likelihood fit, we find $N_s = 910 \pm 45$.[1]

This chapter is divided into five sections. Before comparing with theoretical predictions, we first use two methods to examine the degree of correlation between the D and $\overline{D}$ mesons from our $D\overline{D}$ signal events. If the two charmed mesons in each $D\overline{D}$ event are completely uncorrelated, then the charm-pair distributions contain no more information than the single-charm distributions. In Section 5.1, we use the single-charm distributions to predict what the charm-pair distributions would be if the D and $\overline{D}$ were uncorrelated. Comparing the measured charm-pair distributions to these single-charm predictions pro-

[1]Since the sum over all weights is normalized to equal the number of $D\overline{D}$ candidates, the fact that the number of signal events is significantly larger for the weighted data sample than for the unweighted sample indicates that, on average, the weights for signal events are larger than for background events.

vides one measure of the degree of correlation between the D and $\overline{D}$. In Section 5.2, we look directly for correlations by examining several two-dimensional distributions. For example, by finding the number of signal $D\overline{D}$ events per y_D interval per $y_{\overline{D}}$ interval, where y is the rapidity of the charm particle, we can determine whether the shape of the y_D distribution depends on the value of $y_{\overline{D}}$.

In Section 5.3, we compare our experimental distributions to three sets of theoretical predictions:

- the distribution of $c\overline{c}$ pairs from the MNR next-to-leading order perturbative QCD calculation,
- the distribution of $c\overline{c}$ pairs from the PYTHIA/JETSET event generator, which uses a parton-shower model to include higher-order perturbative effects, and
- the distribution of $D\overline{D}$ pairs from the PYTHIA/JETSET event generator, which uses the LUND string model to transform $c\overline{c}$ pairs to $D\overline{D}$ pairs.

In Section 5.4, we look for production asymmetries among the four types of $D\overline{D}$ pairs — $D^0\overline{D^0}$, D^0D^-, $D^+\overline{D^0}$, and D^+D^- — and compare our experimental results to the predictions from the the PYTHIA/JETSET event generator For all theoretical predictions, we use the default settings for all parameters (see Table 1.3).

Finally, in Section 5.5 we summarize the results of this $D\overline{D}$ analysis.

5.1 Single-Charm Predictions

In Figure 5.1 we show the measured single-charm distributions for x_F, y, p_t^2 and ϕ, which are defined in Section 1.2. Each distribution is obtained from summing the D and $\overline{D}$ distributions from signal $D\overline{D}$ events. The contribution to the single-charm signal from the D- and $\overline{D}$-ridge events is not included. The vertical axis of each distribution gives the fraction of signal mesons per variable v interval, $P(v) = \frac{1}{N_D}\frac{\mathrm{d}N_D}{\mathrm{d}v}$, where the total number of signal D mesons N_D is simply twice the number of signal $D\overline{D}$ events N_s. Table 5.1 shows the integrals, $\int_{v_{min}}^{v_{max}} P(v)dv$, for all single-charm and charm-pair acceptance-corrected distributions discussed in this section, showing that only a very small fraction of the signal events lie outside any of the domains ($v_{min} < v < v_{max}$) used in Figures 5.1-5.6.

For each single-charm variable v, we obtain two measured charm-pair distributions: $\Delta v = v_D - v_{\overline{D}}$ and $\Sigma v = v_D + v_{\overline{D}}$. ($\Delta\phi$ is defined to be the minimum of $|\phi_D - \phi_{\overline{D}}|$ and

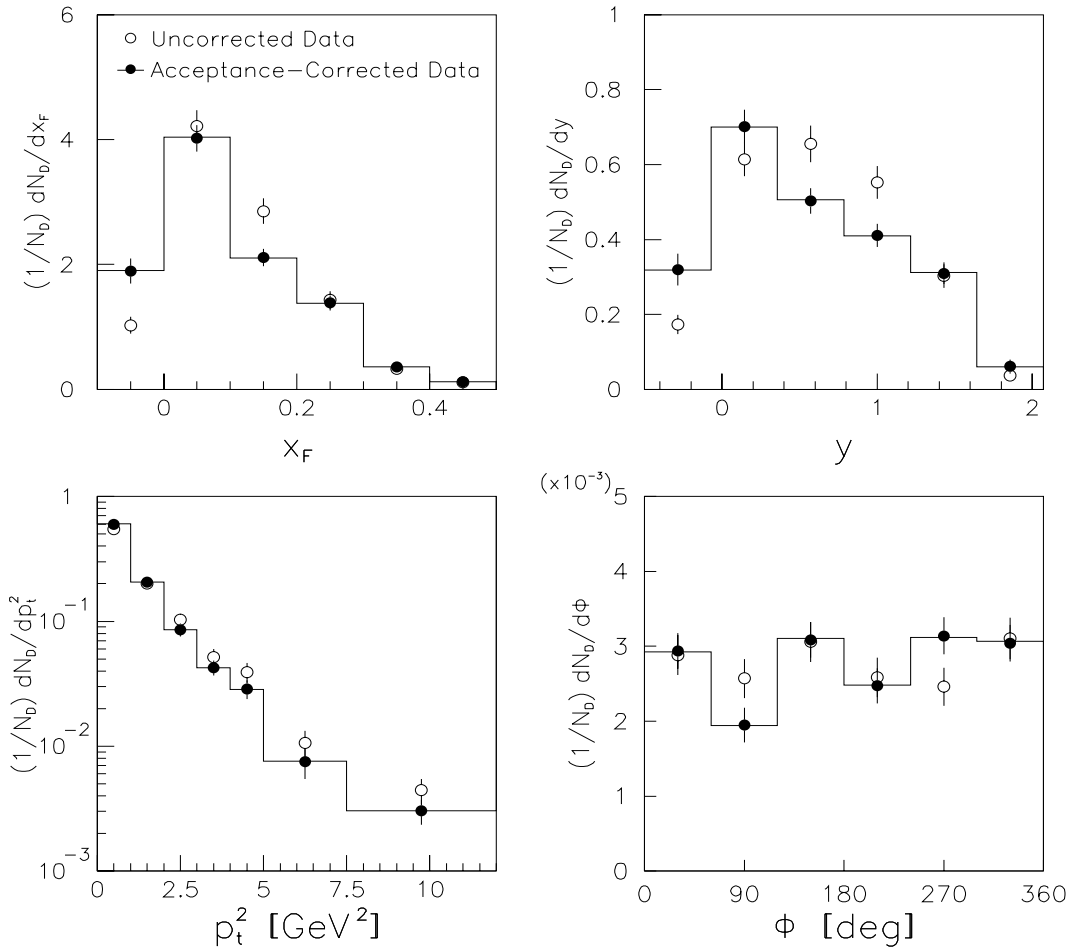

Figure 5.1: Single-charm distributions for the variables x_F, y, p_t^2 and ϕ, obtained from summing the D and $\overline{D}$ distributions from our signal $D\overline{D}$ events. The total number of signal D mesons, N_D, is simply twice the number of signal $D\overline{D}$ events N_s.

$360° - |\phi_D - \phi_{\overline{D}}|$, and $\Sigma\phi$ is defined to be $\phi_D + \phi_{\overline{D}}$ modulo 360°.) In Figures 5.2-5.5, we compare these measured charm-pair distributions to the following single-charm predictions:

$$Q(\Delta v) = \delta(\Delta v - v_D + v_{\overline{D}})P(v_D)P(v_{\overline{D}}) \times \begin{cases} \frac{v_{max}-v_{min}-|\Delta v|}{(v_{max}-v_{min})^2} & \text{if } v_{min} - v_{max} < \Delta v < v_{max} - v_{min} \\ 0 & \text{if } |\Delta v| > v_{max} - v_{min} \end{cases} \quad (5.1)$$

and

$$Q(\Sigma v) = \delta(\Sigma v - v_D - v_{\overline{D}})P(v_D)P(v_{\overline{D}}) \times \quad (5.2)$$

Table 5.1: The integrals, $\int_{v_{min}}^{v_{max}} P(v)dv$, for all single-charm and charm-pair acceptance-corrected distributions shown in Figures 5.1-5.6, showing the fraction of signal events within the domain $v_{min} < v < v_{max}$.

v	v_{min}	v_{max}		$\int_{v_{min}}^{v_{max}} P(v)\mathrm{d}v$	Figure
x_F	-0.1	0.5		0.99	5.1
y	-0.5	2.07		0.99	5.1
p_t^2	0	12	GeV^2	0.99	5.1
ϕ	0	360	deg.	1.00	5.1
Δx_F	-0.5	0.5		0.97	5.2
Σx_F	-0.1	0.64		0.97	5.2
Δy	-2	2		1.00	5.3
Σy	-0.8	3.3		1.00	5.3
$\lvert\Delta p_t^2\rvert$	0	6	GeV^2	0.96	5.4
Σp_t^2	0	12	GeV^2	0.98	5.4
$\Delta\phi$	0	180	deg.	0.99	5.5
$\Sigma\phi$	0	360	deg.	1.00	5.5
$p_{t,D\overline{D}}^2$	0	12	GeV^2	0.99	5.6
$M_{D\overline{D}}$	3.7	7.5	GeV	0.99	5.6

$$\begin{cases} \frac{\Sigma v - 2v_{min}}{(v_{max}-v_{min})^2} & \text{if } 2v_{min} < \Sigma v < v_{max} + v_{min} \\ \frac{\Sigma v - 2v_{max}}{(v_{max}-v_{min})^2} & \text{if } v_{max} + v_{min} < \Sigma v < 2v_{max} \\ 0 & \text{if } \Sigma v < 2v_{min} \text{ or } \Sigma v > 2v_{max} \end{cases}$$

where $P(v)$ refers to the single-charm distributions shown in Figure 5.1. The triangular functions to the right of $P(v_D)P(v_{\overline{D}})$ in Equation 5.1 and 5.2 give the probability distribution functions for $v_D \pm v_{\overline{D}}$ assuming a flat probability distribution function for v_D and $v_{\overline{D}}$ within the domain $v_{min} < v < v_{max}$ and zero probability outside this domain.

If the D and $\overline{D}$ from our signal $D\overline{D}$ events are completely uncorrelated, then the measured charm-pair distributions for Δv and Σv would agree with the single-charm predictions. With the exception of the $\Delta\phi$ distribution (Figure 5.5), the measured distributions are quite similar to the single-charm predictions, indicating both that the correlation between the D and $\overline{D}$ longitudinal momenta is small and that the correlation between the amplitudes of the D and $\overline{D}$ transverse momenta is small. The measured Δx_F, Δy, and Δp_t^2 distributions, however, are somewhat more peaked near zero than the single-charm

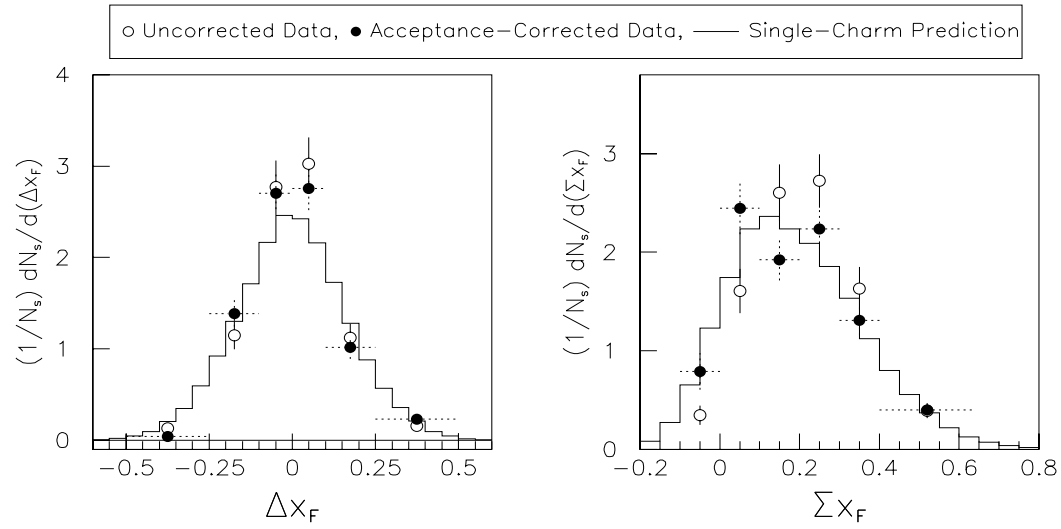

Figure 5.2: Charm-pair distributions for $\Delta x_F = x_{F,D} - x_{F,\overline{D}}$ and $\Sigma x_F = x_{F,D} + x_{F,\overline{D}}$. The single-charm predictions for Δx_F and Σx_F are defined in Eqs. 5.1 and 5.2.

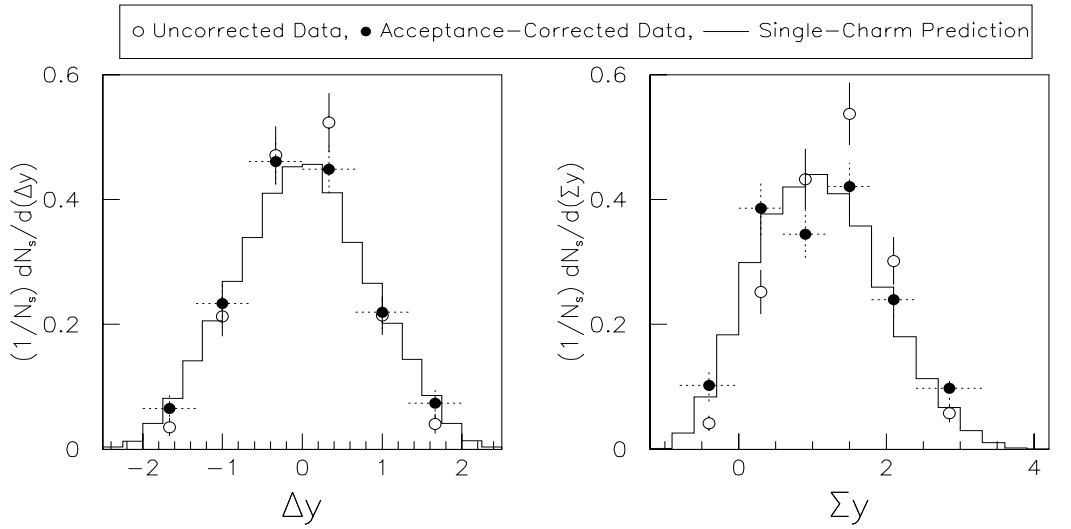

Figure 5.3: Charm-pair distributions for $\Delta y = y_D - y_{\overline{D}}$ and $\Sigma y = y_D + y_{\overline{D}}$. The single-charm predictions for Δy and Σy are defined in Eqs. 5.1 and 5.2.

predictions, indicating slight correlations.

Two other commonly used charm-pair variables are the square of the transverse momenta of the charm-pair, $p^2_{t,D\overline{D}} = |\vec{p}_{t,D} + \vec{p}_{t,\overline{D}}|^2$, and the invariant mass of the charm-pair $M_{D\overline{D}}$. The measured distributions and the single-charm predictions for these two variables are shown in Figure 5.6. Obtaining single-charm predictions for $p^2_{t,D\overline{D}}$ and $M_{D\overline{D}}$ is slightly more involved than for the Δv and Σv variables because $p^2_{t,D\overline{D}}$ and $M_{D\overline{D}}$ are not linear

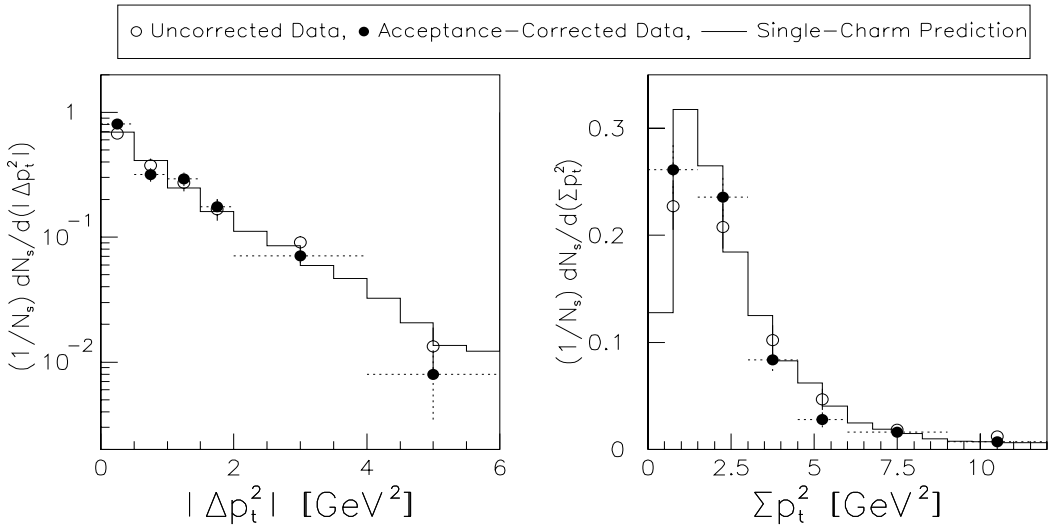

Figure 5.4: Charm-pair distributions for $|\Delta p_t^2| = |p_{t,D}^2 - p_{t,\overline{D}}^2|$ and $\Sigma p_t^2 = p_{t,D}^2 + p_{t,\overline{D}}^2$. The single-charm predictions for Δp_t^2 and Σp_t^2 are defined in Eqs. 5.1 and 5.2.

functions of $x_{F,D}$, $x_{F,\overline{D}}$, ϕ_D, $\phi_{\overline{D}}$, $p_{t,D}^2$, and $p_{t,\overline{D}}^2$. Rather, in terms of these single-charm variables,

$$p_{t,D\overline{D}}^2 = p_{t,D}^2 + p_{t,\overline{D}}^2 + 2\sqrt{p_{t,D}^2 p_{t,\overline{D}}^2}\cos(\phi_D - \phi_{\overline{D}}), \text{ and}$$

$$M_{D\overline{D}} = \sqrt{2M_D^2 + 2E_D E_{\overline{D}} - 2\sqrt{p_{t,D}^2 p_{t,\overline{D}}^2}\cos(\phi_D - \phi_{\overline{D}}) - \frac{s\, x_{F,D}\, x_{F,\overline{D}}}{2}},$$

where the D meson energy E is $\sqrt{M_D^2 + p_t^2 + \frac{s\, x_F^2}{4}}$, and s is the square of the center-of-mass energy of the colliding hadrons. We obtain single-charm predictions by randomly generating 10^8 $D\overline{D}$ events in which all three variables (x_F, ϕ, and p_t^2) for both D mesons from each $D\overline{D}$ event are selected independently and randomly from a probability distribution function that is flat within the domains shown in Figure 5.1 and zero elsewhere. Each event is weighted by

$$\frac{1}{|J|} P(x_{F,D}) P(\phi_D) P(p_{t,D}^2) P(x_{F,\overline{D}}) P(\phi_{\overline{D}}) P(p_{t,\overline{D}}^2),$$

where $P(v)$ refers the single-charm distributions shown in Figure 5.1 and $|J|$ is the Jacobian determinant of the transformation from the complete and independent set of variables ($x_{F,D}$, $x_{F,\overline{D}}$, ϕ_D, $\phi_{\overline{D}}$, $p_{t,D}^2$, and $p_{t,\overline{D}}^2$) to the set ($x_{F,D}$, $x_{F,\overline{D}}$, ϕ_D, $\phi_{\overline{D}}$, $p_{t,D\overline{D}}^2$, and $M_{D\overline{D}}$). Specifically,

$$|J| \equiv \left| \frac{\partial(x_{F,D}, x_{F,\overline{D}}, \phi_D, \phi_{\overline{D}}, p_{t,D\overline{D}}^2, M_{D\overline{D}})}{\partial(x_{F,D}, x_{F,\overline{D}}, \phi_D, \phi_{\overline{D}}, p_{t,D}^2, p_{t,\overline{D}}^2)} \right| \tag{5.3}$$

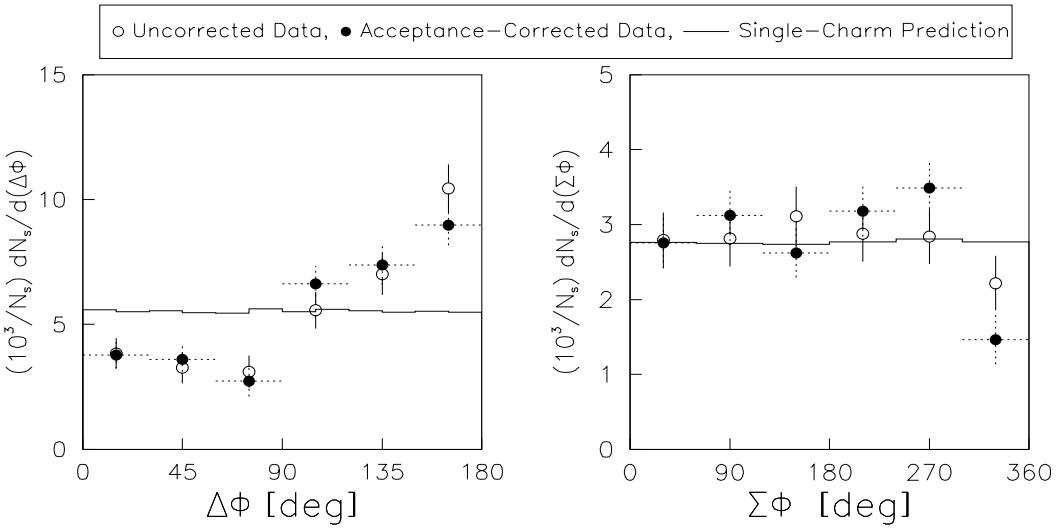

Figure 5.5: Charm-pair distributions for $\Delta\phi =$ (minimum of $|\phi_D - \phi_{\overline{D}}|$ and $360° - |\phi_D - \phi_{\overline{D}}|$) and $\Sigma\phi = (\phi_D + \phi_{\overline{D}}$ modulo $360°)$. The single-charm predictions for $\Delta\phi$ and $\Sigma\phi$ are defined in Eqs. 5.1 and 5.2.

$$= \left| \begin{array}{cc} 1 + \sqrt{\frac{p^2_{t,\overline{D}}}{p^2_{t,D}}}\cos(\phi_D - \phi_{\overline{D}}) & 1 + \sqrt{\frac{p^2_{t,D}}{p^2_{t,\overline{D}}}}\cos(\phi_D - \phi_{\overline{D}}) \\ \frac{1}{2\sqrt{2}M_{D\overline{D}}}\left(\frac{E_{\overline{D}}}{E_D} - \sqrt{\frac{p^2_{t,\overline{D}}}{p^2_{t,D}}}\cos(\phi_D - \phi_{\overline{D}})\right) & \frac{1}{2\sqrt{2}M_{D\overline{D}}}\left(\frac{E_D}{E_{\overline{D}}} - \sqrt{\frac{p^2_{t,D}}{p^2_{t,\overline{D}}}}\cos(\phi_D - \phi_{\overline{D}})\right) \end{array} \right| .$$

The measured distribution for $M_{D\overline{D}}$ agrees quite well with the single-charm prediction. The measured distribution for $p^2_{t,D\overline{D}}$, however, is noticeably steeper than the single-charm prediction, indicating significant correlations between $\vec{p}_{t,D}$ and $\vec{p}_{t,\overline{D}}$. The dashed histogram in Figure 5.6 demonstrates that this lack of agreement is not due to the correlations between ϕ_D and $\phi_{\overline{D}}$ evident in the $\Delta\phi$ distribution in Figure 5.5. This latter prediction is obtained by assuming that $x_{F,D}$ and $x_{F,\overline{D}}$ are uncorrelated and that $p^2_{t,D}$ and $p^2_{t,\overline{D}}$ are uncorrelated, but that ϕ_D and $\phi_{\overline{D}}$ are correlated as shown in Figure 5.5. The following section investigates correlations between $\vec{p}_{t,D}$ and $\vec{p}_{t,\overline{D}}$ in more detail.

5.2 Two-Dimensional Distributions

A direct method for investigating whether two variables, v_D and $v_{\overline{D}}$, are correlated is to determine the number of $D\overline{D}$ signal events per v_D interval per $v_{\overline{D}}$ interval. Such two-dimensional distributions show us whether the v_D distribution depends on the value of $v_{\overline{D}}$, and vice-versa. Given our limited statistics, we must use very course binning. In

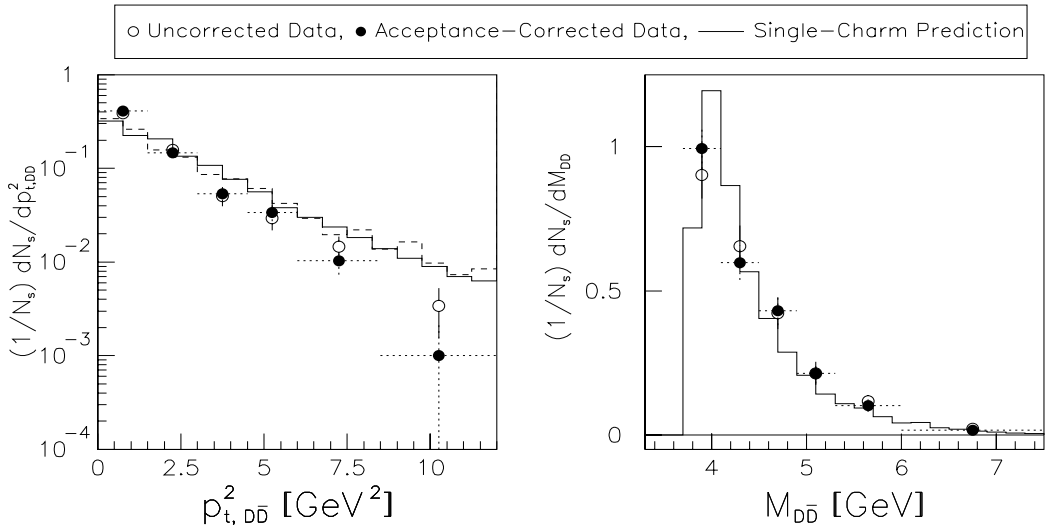

Figure 5.6: Charm-pair distributions for $p^2_{t,D\overline{D}}$ and $M_{D\overline{D}}$. The solid histograms show the single-charm predictions. The dashed $p^2_{t,D\overline{D}}$ histogram assumes that $x_{F,D}$ and $x_{F,\overline{D}}$ are uncorrelated and that $p^2_{t,D}$ and $p^2_{t,\overline{D}}$ are uncorrelated, but that ϕD and $\phi\overline{D}$ are correlated as shown in Figure 5.5.

Figures 5.7-5.9, we show the results for $v = x_F, y,$ and p_t^2, respectively. In each figure, we first show the number of acceptance-corrected $D\overline{D}$ signal events reconstructed in nine (v_D, $v_{\overline{D}}$) bins — three v_D bins times three $v_{\overline{D}}$ bins. Using the information in this 2-dimensional plot, several normalized 1-dimensional plots are created, facilitating our ability to detect differences in the shapes of the distributions. In particular, plot (b) in each figure shows the v_D distribution for each $v_{\overline{D}}$ bin, $N_i \frac{dN_s}{dv_D}$, where N_i is chosen such that the integral over each v_D distribution equals one. Similarly, plot (c) in each figure shows the normalized $v_{\overline{D}}$ distribution for each v_D bin. Lastly, plots (d)-(f) simply rearrange the information shown in (b) and (c). Plot (d) shows the normalized v_D and $v_{\overline{D}}$ distribution for the first $v_{\overline{D}}$ and v_D bin, respectively; plot (e) shows results for the second bins; and plot (f) shows results for the third bins. We reiterate that the two-dimensional plots show the actual number of acceptance-corrected $D\overline{D}$ signal events in each bin; whereas, the one-dimensional plots, proportional to $\frac{dN_s}{dv_D}$, take into account the variation in bin size.

Figure 5.7 indicates some correlation between x_D and $x_{\overline{D}}$. In particular, the first-bin distributions are more peaked at low x_F than the second- and third-bin distributions. This result is consistent with Figure 5.2, discussed above, which shows that the measured Δx_F distribution is somewhat steeper than the single-charm prediction. Because x_F and y

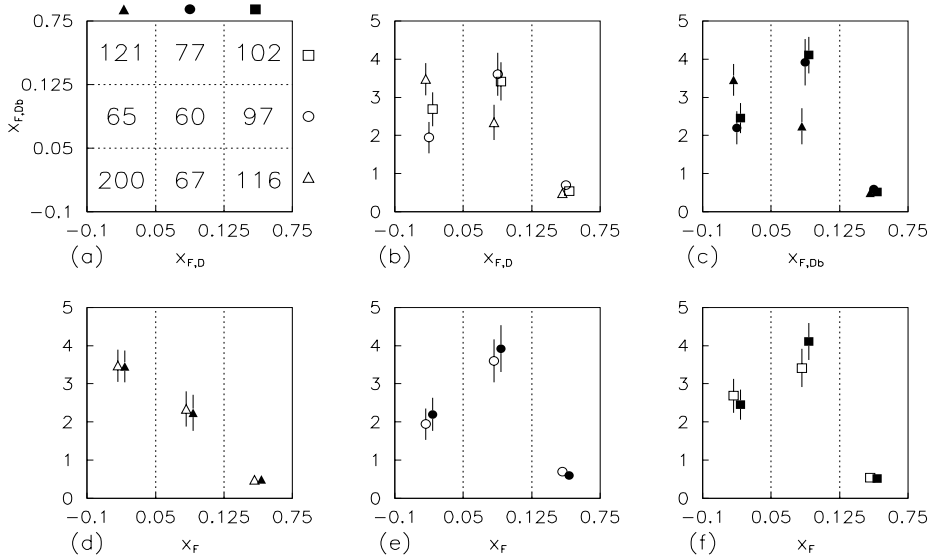

Figure 5.7: (a) Number of acceptance-corrected $D\overline{D}$ signal events $\mathrm{d}N_s$ found in nine ($x_{F,D}$, $x_{F,\overline{D}}$) bins. (b) $x_{F,D}$ distribution $N_i(\mathrm{d}N_s/\mathrm{d}x_{F,D})$ for each $x_{F,\overline{D}}$ bin, where N_i is chosen such that the integral over $x_{F,D}$ equals one. (c) $x_{F,\overline{D}}$ distribution for each $x_{F,D}$ bin. (d)-(f) $x_{F,D}$ ($x_{F,\overline{D}}$) distribution for the first, second and third $x_{F,\overline{D}}$ ($x_{F,D}$) bins, respectively. The open symbols show the x_D distributions; the closed symbols the $x_{\overline{D}}$ distributions.

are quite correlated, Figure 5.8 shows the same trends as Figure 5.7. Figure 5.9 indicates that $p^2_{t,D}$ and $p^2_{t,\overline{D}}$ are also slightly correlated: The second-bin $p^2_{t,D}$ and $p^2_{t,\overline{D}}$ distributions are enhanced in the second bin; and the third-bin $p^2_{t,D}$ and $p^2_{t,\overline{D}}$ distributions are enhanced in the third bin. This result is consistent with Figure 5.4, discussed above, which shows that the measured Δp_t^2 distribution is somewhat steeper than the single-charm prediction. In all three figures (5.7-5.9), the shapes of the three v_D distributions are remarkably similar to the shapes of the respective $v_{\overline{D}}$ distributions.

In Figure 5.10 we investigate whether the separation in azimuthal angle between the D and $\overline{D}$ is correlated to the amplitude of the transverse momenta of the D and $\overline{D}$. In particular, we determine the number of signal $D\overline{D}$ events per $\Delta\phi$ interval per Σp_t^2 interval and the number of signal $D\overline{D}$ events per $\Delta\phi$ interval per $|\Delta p_t^2|$ interval. Although we find no significant correlation between $\Delta\phi$ and $|\Delta p_t^2|$, we do find that $\Delta\phi$ and Σp_t^2 are quite correlated. The $\Delta\phi$ distribution is more peaked at large Σp_t^2 and the Σp_t^2 distribution is flatter at large $\Delta\phi$. A theoretical explanation for these correlations is discussed in the following section.

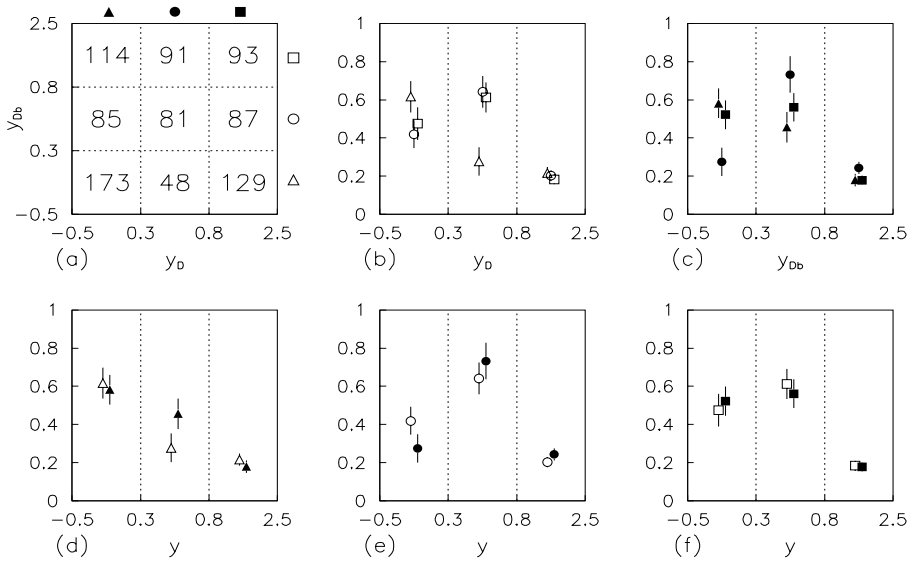

Figure 5.8: (a) Number of acceptance-corrected $D\overline{D}$ signal events $\mathrm{d}N_s$ found in nine (y_D, $y_{\overline{D}}$) bins. (b) y_D distribution $N_i(\mathrm{d}N_s/\mathrm{d}y_D)$ for each $y_{\overline{D}}$ bin, where N_i is chosen such that the integral over y_D equals one. (c) $y_{\overline{D}}$ distribution for each y_D bin. (d)-(f) y_D ($y_{\overline{D}}$) distribution for the first, second and third $y_{\overline{D}}$ (y_D) bins, respectively.

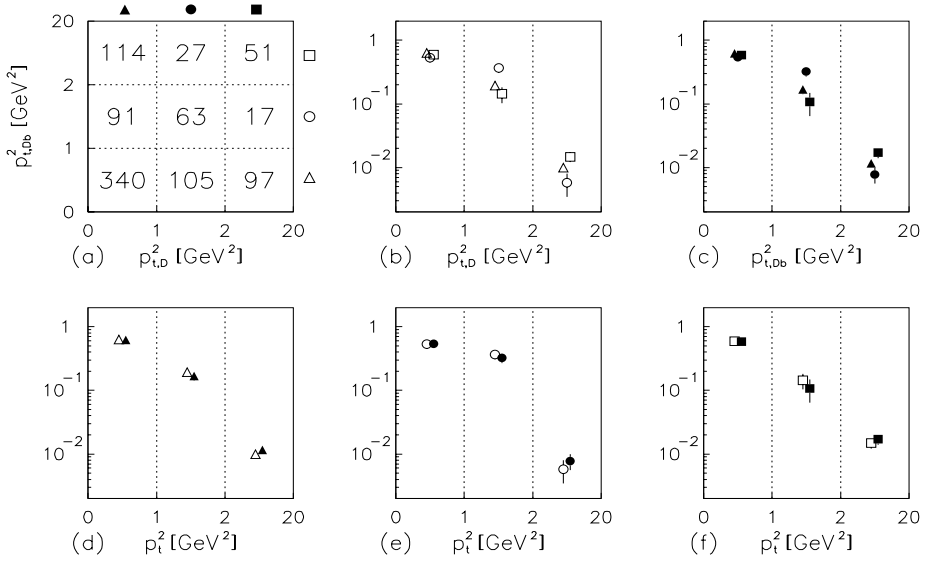

Figure 5.9: (a) Number of acceptance-corrected $D\overline{D}$ signal events $\mathrm{d}N_s$ found in nine ($p^2_{t,D}$, $p^2_{t,\overline{D}}$) bins. (b) $p^2_{t,D}$ distribution $N_i(\mathrm{d}N_s/\mathrm{d}p^2_{t,D})$ for each $p^2_{t,\overline{D}}$ bin, where N_i is chosen such that the integral over $p^2_{t,D}$ equals one. (c) $p^2_{t,\overline{D}}$ distribution for each $p^2_{t,D}$ bin. (d)-(f) $p^2_{t,D}$ ($p^2_{t,\overline{D}}$) distribution for the first, second and third $p^2_{t,\overline{D}}$ ($p^2_{t,D}$) bins, respectively.

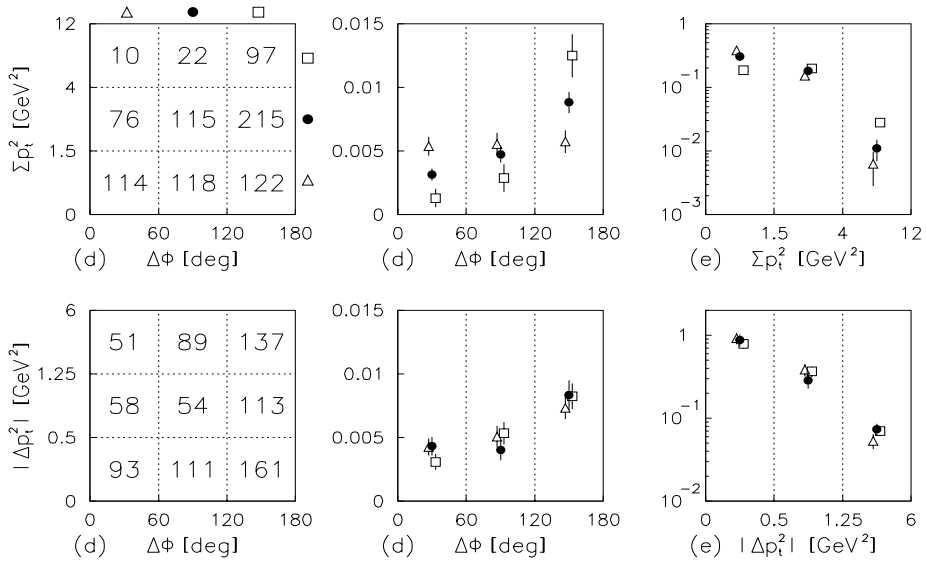

Figure 5.10: (a) Number of acceptance-corrected $D\overline{D}$ signal events $\mathrm{d}N_s$ found in nine ($\Delta\phi$, Σp_t^2) bins. (b) $\Delta\phi$ distribution $N_i(\mathrm{d}N_s/\mathrm{d}\Delta\phi)$ for each Σp_t^2 bin, where N_i is chosen such that the integral over $\Delta\phi$ equals one. (c) Σp_t^2 distribution for each $\Delta\phi$ bin. (d) Number of acceptance-corrected $D\overline{D}$ signal events $\mathrm{d}N_s$ found in 9 ($\Delta\phi$,$|\Delta p_t^2|$) bins. (e) $\Delta\phi$ distribution for each $|\Delta p_t^2|$ bin. (f) $|\Delta p_t^2|$ distribution for each $\Delta\phi$ bin.

5.3 Comparisons with Theory

In this section, we compare all the acceptance-corrected distributions discussed in the previous two sections (Figs. 5.1-5.10) to three sets of theoretical predictions:

- the distribution of $c\overline{c}$ pairs from the MNR next-to-leading order perturbative QCD calculation,
- the distribution of $c\overline{c}$ pairs from the PYTHIA/JETSET event generator, which uses a parton-shower model to include higher-order perturbative effects, and
- the distribution of $D\overline{D}$ pairs from the PYTHIA/JETSET event generator, which uses the LUND string model to transform $c\overline{c}$ pairs to $D\overline{D}$ pairs.

For all theoretical predictions, we use the default parameters suggested by the respective authors, which are discussed in Chapter 1 (Table 1.3). All distributions are obtained after excluding any candidates in which the center-of-mass rapidity of either the D or $\overline{D}$ is less than -0.5 or greater than 2.5.

Single-Charm Distributions

Lack of agreement between an experimental charm-pair distribution and a theoretical prediction can arise if the theory does not model the correlations between the two charm particles correctly. Lack of agreement, however, can also arise if the theory models the correlations correctly but does not correctly model the single-charm distributions. Hence, in Figure 5.11, before comparing our experimental charm-pair distributions to theory, we first compare our acceptance-corrected single-charm distributions (x_F, y, p_t^2 and ϕ) to theory.

For the longitudinal momentum distributions, x_F and y, the experimental results and theoretical predictions do not agree. The experimental distributions are most similar to the NLO and PYTHIA/JETSET $c\overline{c}$ distributions, but are narrower than all three. The difference between the PYTHIA/JETSET $c\overline{c}$ and the PYTHIA/JETSET $D\overline{D}$ longitudinal distributions shows the effect of the hadronization scheme that color-attaches one charm quark to the remnant beam and the other to the remnant target, broadening out the longitudinal distributions.

The experimental p_t^2 distribution agrees quite well with all three theoretical distributions. The PYTHIA/JETSET $c\overline{c}$ distribution is slightly too flat; the PYTHIA/JETSET

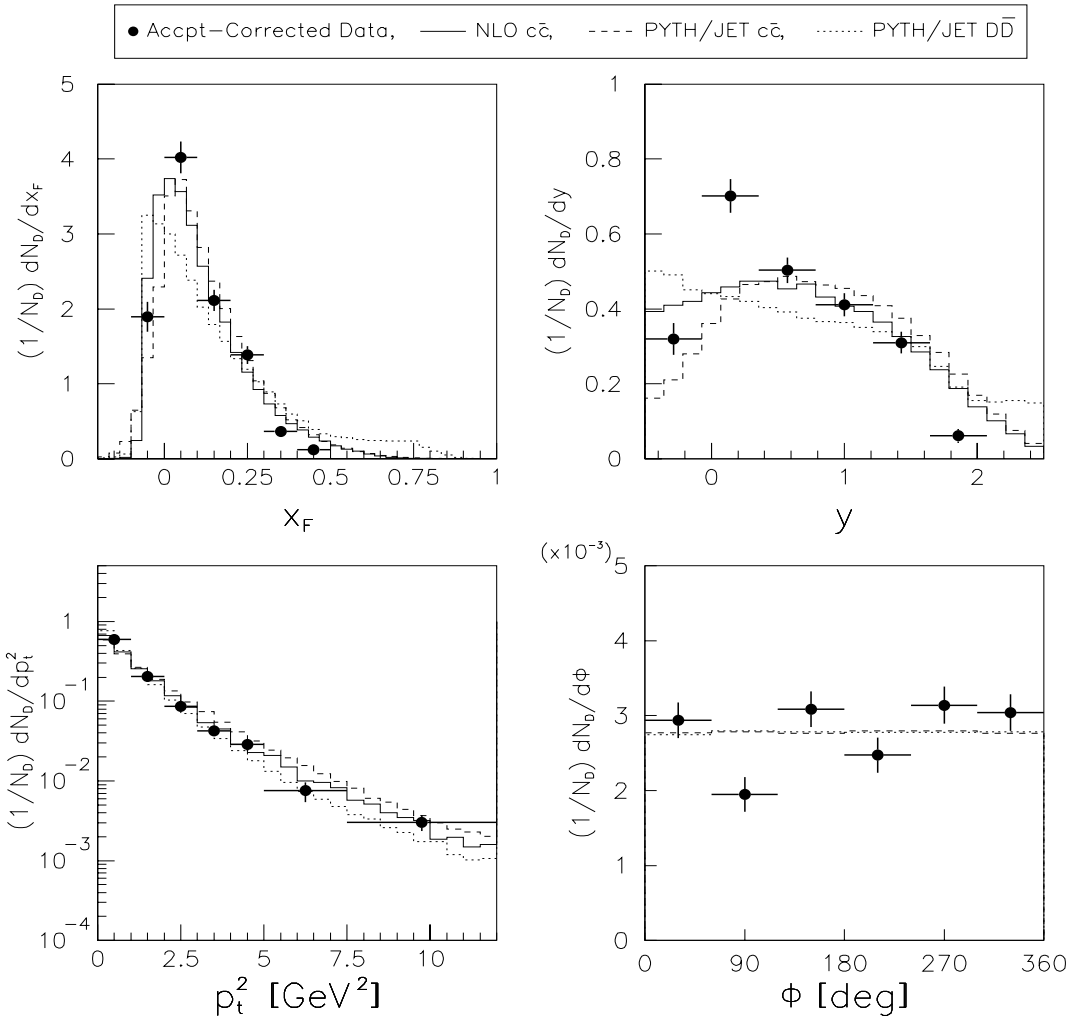

Figure 5.11: Experimental single-charm distributions for x_F, y, p_t^2 and ϕ compared to three sets of theoretical predictions: the next-to-leading order perturbative QCD prediction, the PYTHIA/JETSET charm quark prediction, and the PYTHIA/JETSET D meson prediction. All distributions are obtained from summing the charm and anti-charm distributions from charm-pair events.

$D\overline{D}$ distribution, slightly too steep. As expected, both the theoretical and experimental ϕ distributions are flat.

Longitudinal Distributions

Given the lack of agreement between the experimental and theoretical single-charm longitudinal distributions, it is not surprising that the experimental Δx_F and Σx_F distributions (Figure 5.12) and the Δy and Σy distributions (Figure 5.13) do not agree with

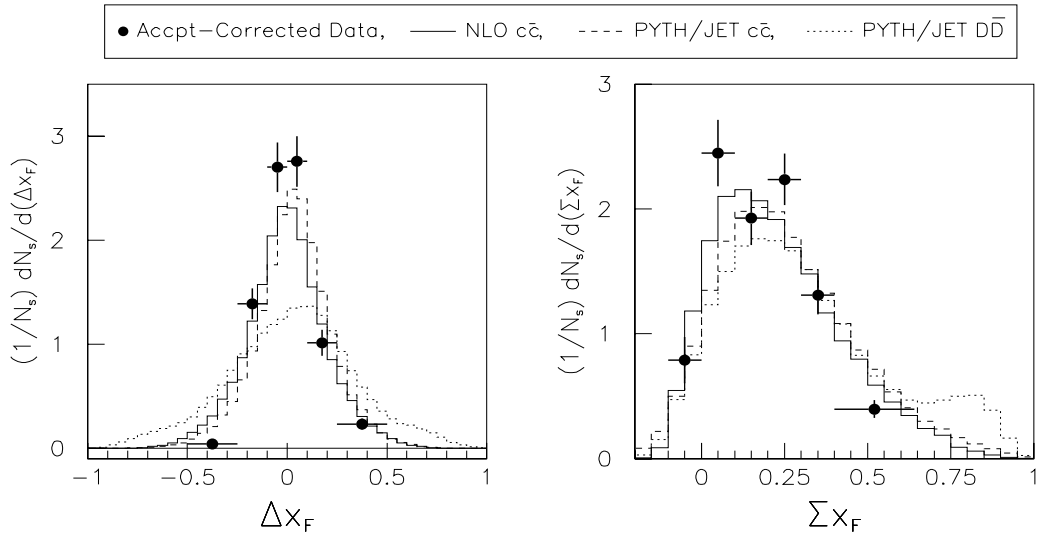

Figure 5.12: Experimental Δx_F and Σx_F distributions compared to three sets of theoretical predictions: the next-to-leading order perturbative QCD prediction, the PYTHIA/JETSET $c\overline{c}$ prediction, and the PYTHIA/JETSET $D\overline{D}$ prediction.

theoretical predictions. As with the single-charm distributions, the experimental results are much closer to the two $c\overline{c}$ predictions than to the PYTHIA/JETSET $D\overline{D}$ prediction, but narrower than all three predictions. As discussed in Chapter 1, the PYTHIA/JETSET hadronization scheme introduces a strong correlation between the D and $\overline{D}$ which significantly broadens the Δy distribution. In other words, as shown in Figure 5.14, the PYTHIA/JETSET $D\overline{D}$ Δy distribution is broader than the single-charm prediction

$$Q_{MC}(\Delta y) = P_{MC}(y_D)P_{MC}(y_{\overline{D}})\delta(\Delta y - y_D + y_{\overline{D}}) \times \begin{cases} \frac{y_{max}-y_{min}-|\Delta y|}{(y_{max}-y_{min})^2} & \text{if } y_{min} - y_{max} < \Delta y < y_{max} - y_{min} \\ 0 & \text{if } |\Delta y| > y_{max} - y_{min} \end{cases} \quad (5.4)$$

where $P_{MC}(y)$ refers to the PYTHIA/JETSET $D\overline{D}$ single-charm rapidity distribution from Figure 5.11. In contrast, the experimental Δy distribution is slightly narrower than its single-charm prediction (Fig. 5.3).

Transverse Distributions

In Figures 5.15-5.17, we compare experimental distributions to theoretical predictions for the following transverse variables: $|\Delta p_t^2|$, Σp_t^2, $\Delta\phi$, $\Sigma\phi$, and $p_{t,D\overline{D}}^2$. The discrepancy

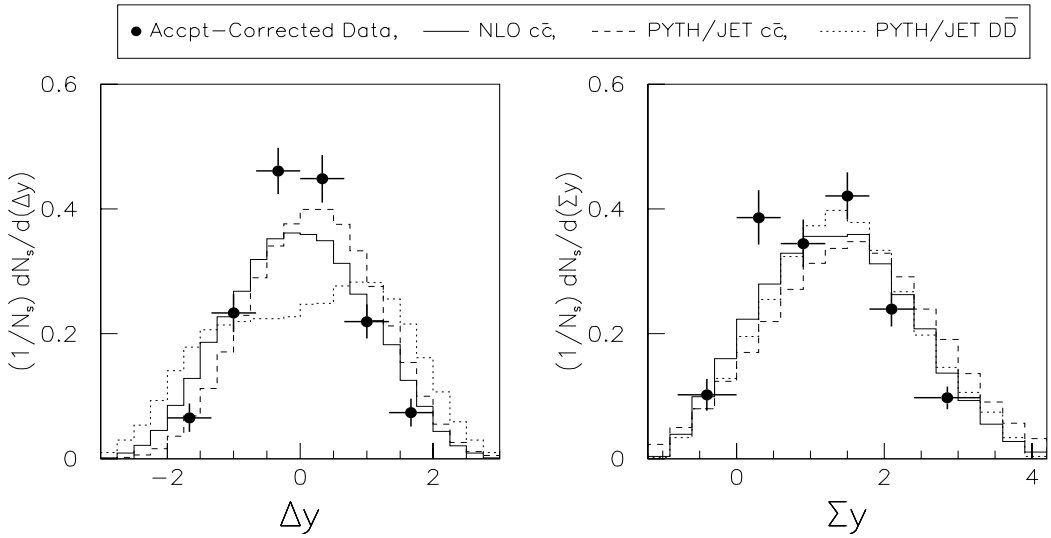

Figure 5.13: Experimental Δy and Σy distributions compared to three sets of theoretical predictions: the next-to-leading order perturbative QCD prediction, the PYTHIA/JETSET $c\overline{c}$ prediction, and the PYTHIA/JETSET $D\overline{D}$ prediction.

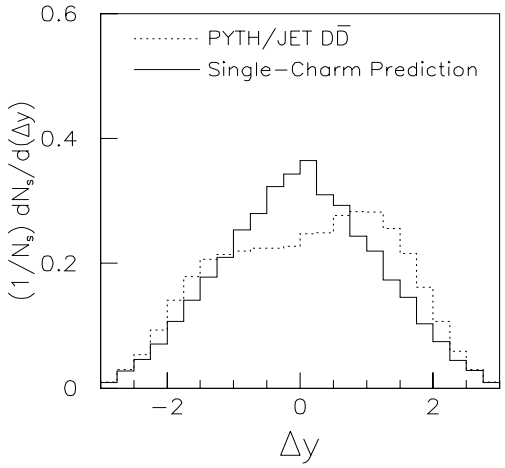

Figure 5.14: PYTHIA/JETSET $D\overline{D}$ prediction for Δy compared to the PYTHIA/JETSET single-charm prediction, which is obtained by assuming that the D and $\overline{D}$ mesons are completely uncorrelated (See Eq. 5.4).

between theory and data for the $|\Delta p_t^2|$, $\Delta\phi$, and $p^2_{t,D\overline{D}}$ distributions is noteworthy because the single-charm p_t^2 and ϕ experimental distributions agree quite well with theory. The discrepancy, therefore, must derive from the theory modeling the correlation between $\vec{p}_{t,D}$ and $\vec{p}_{t,\overline{D}}$ incorrectly.

If $\vec{p}_{t,D}$ and $\vec{p}_{t,\overline{D}}$ were completely uncorrelated, then the single-charm predictions (Figures 5.4-5.6) would provide good estimates for these three distributions. At the opposite

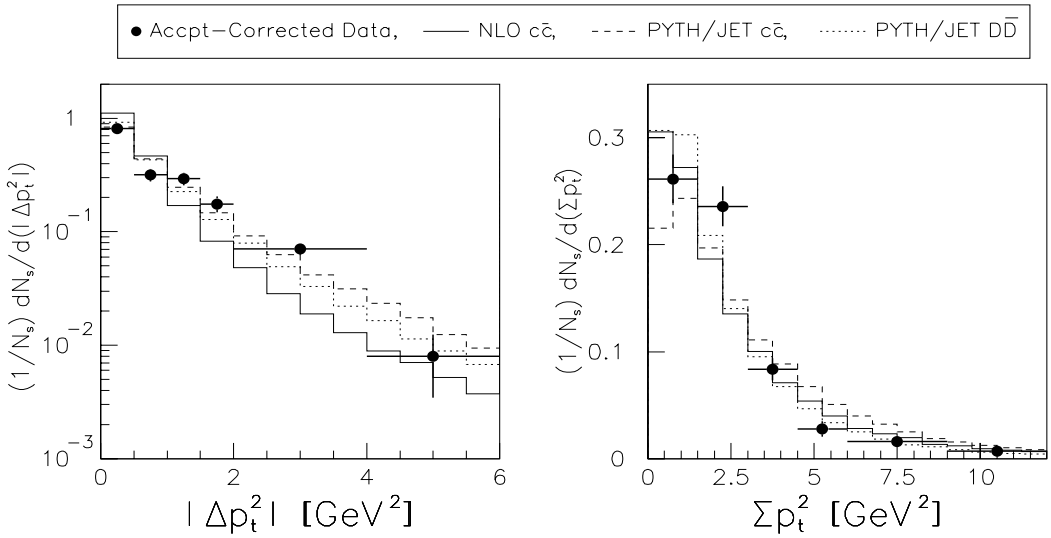

Figure 5.15: Experimental $|\Delta p_t^2|$ and Σp_t^2 distributions compared to three sets of theoretical predictions: the next-to-leading order perturbative QCD prediction, the PYTHIA/JETSET $c\overline{c}$ prediction, and the PYTHIA/JETSET $D\overline{D}$ prediction.

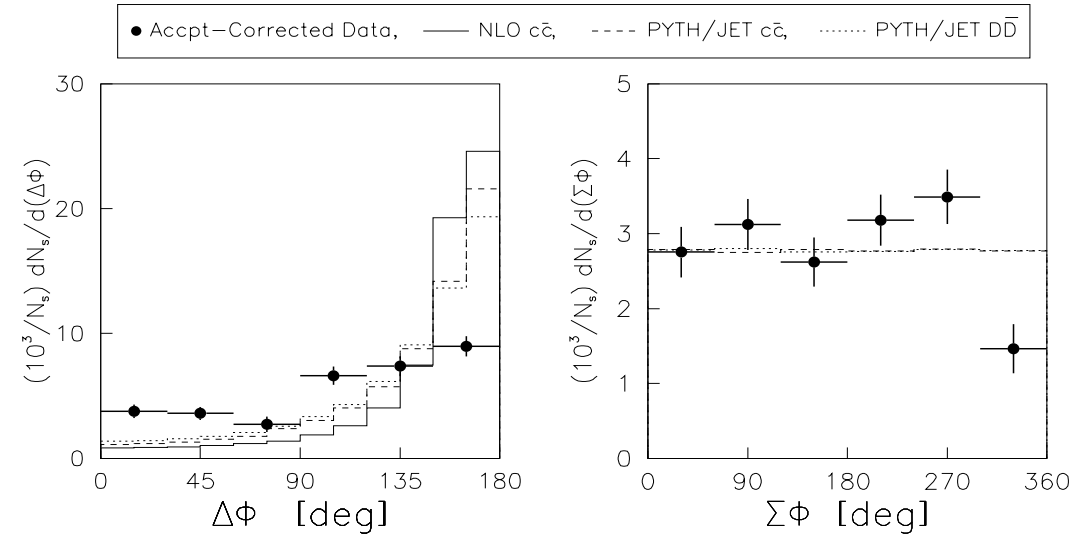

Figure 5.16: Experimental $\Delta\phi$ and $\Sigma\phi$ distributions compared to three sets of theoretical predictions: the next-to-leading order perturbative QCD prediction, the PYTHIA/JETSET $c\overline{c}$ prediction, and the PYTHIA/JETSET $D\overline{D}$ prediction.

extreme, if $\vec{p}_{t,D}$ and $\vec{p}_{t,\overline{D}}$ were completely, negatively correlated — as in the leading-order perturbative QCD prediction — then the Δp_t^2 distribution would be a delta function at $\Delta p_t^2 = 0$ GeV^2; the $p^2_{t,D\overline{D}}$ distribution a delta function at $p^2_{t,D\overline{D}} = 0$ GeV^2; and the $\Delta\phi$ distribution a delta function at $\Delta\phi = 180°$. Both the experimental distributions and the

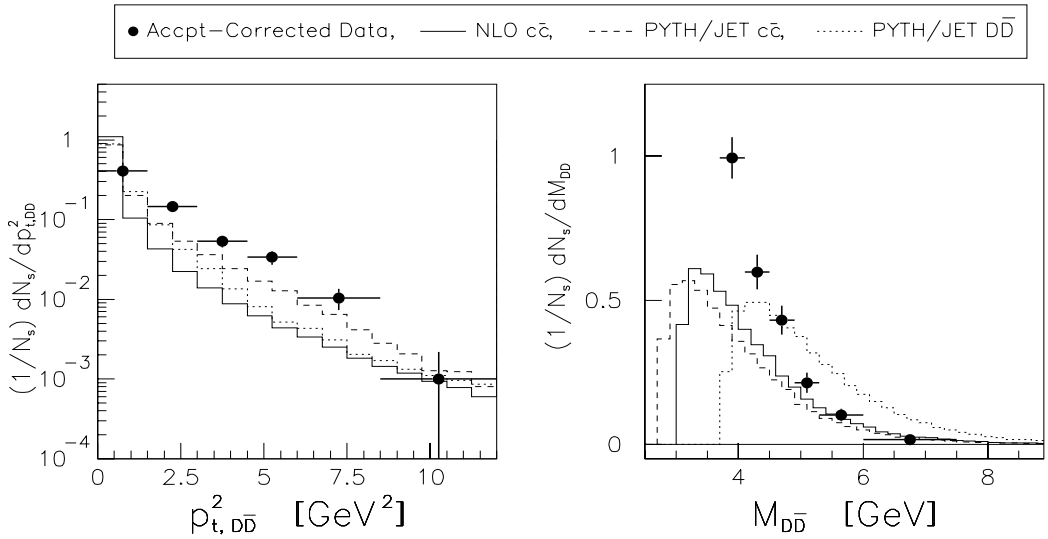

Figure 5.17: Experimental $p^2_{t,D\overline{D}}$ and $M_{t,D\overline{D}}$ distributions compared to three sets of theoretical predictions: the next-to-leading order perturbative QCD prediction, the PYTHIA/JETSET $c\overline{c}$ prediction, and the PYTHIA/JETSET $D\overline{D}$ prediction.

three sets of theoretical predictions lie between these two extremes. None of the three experimental distributions, however, are as steep as any of the theoretical predictions. The next-to-leading order predictions are the steepest — that is, the next-to-leading calculation predicts the most correlation between $\vec{p}_{t,D}$ and $\vec{p}_{t,\overline{D}}$.

The PYTHIA/JETSET hadronization scheme broadens the $\Delta\phi$ distribution, bringing it closer to the experimental result. The same hadronization scheme, however, softens the $p^2_{t,D\overline{D}}$ and Δp^2_t distributions, taking them further from the experimental results. One mechanism that would both flatten the $\Delta\phi$ distribution and harden the $p^2_{t,D\overline{D}}$ and Δp^2_t distributions would be more intrinsic transverse momenta for the partons in the colliding hadrons.

Charm-Pair Invariant Mass

In Figure 5.17, we compare the experimental charm-pair invariant mass distribution to theoretical predictions. The $c\overline{c}$ invariant mass predictions are shifted to the left because the mass of the charm quark is less than the mass of the D meson.[2] We expect the experimental $M_{D\overline{D}}$ distribution to be steeper than the theoretical predictions because the

[2]The default settings for the charm quark mass are 1.5 Gev for the MNR NLO calculation and 1.35 GeV for the PYTHIA/JETSET event generator.

experimental single-charm x_F (or y) distribution is steeper than the theoretical predictions. In addition, the correlations introduced by the PYTHIA/JETSET hadronization scheme broaden the invariant mass distribution.

Two-Dimensional Distributions

In Figures 5.18-5.22, we examine the same two-dimensional experimental distributions discussed in Section 5.2. We now compare these experimental results to the three sets of theoretical predictions. In each figure, the top row shows the NLO perturbative QCD prediction; the middle row, the PYTHIA/JETSET $c\overline{c}$ prediction; and the bottom row, the PYTHIA/JETSET $D\overline{D}$ prediction. The experimental results are repeated in each row.

The longitudinal distributions, x_F and y, are shown in Figures 5.18 and 5.19, respectively. The three theoretical predictions are quite different. The NLO $c\overline{c}$ predictions show no significant correlation between $x_{F,D}$ and $x_{F,\overline{D}}$ (or between y_D and $y_{\overline{D}}$) and the $x_{F,D}$ and $x_{F,\overline{D}}$ distributions are quite similar. The PYTHIA/JETSET $c\overline{c}$ predictions show a slight correlation and, surprisingly, the $x_{F,D}$ and $x_{F,\overline{D}}$ distributions are somewhat different. Due to the PYTHIA/JETSET hadronization scheme, the PYTHIA/JETSET $D\overline{D}$ prediction shows the strongest correlation between $x_{F,D}$ and $x_{F,\overline{D}}$. Interestingly, in the PYTHIA/JETSET $D\overline{D}$ prediction, $x_{F,D}$ and $x_{F,\overline{D}}$ are negatively correlated; whereas, in PYTHIA/JETSET $c\overline{c}$ prediction they are positively correlated. The correlation patterns in the experimental results, although inconsistent with any of the theoretical predictions, are closest to the PYTHIA/JETSET $c\overline{c}$ predictions.

Figure 5.20 investigates the correlations between $p^2_{t,D}$ and $p^2_{t,\overline{D}}$. The three theoretical predictions and the experimental results all show similar trends. Although all the distributions are broader than the leading-order perturbative QCD prediction — a delta function at $p^2_{t,D} = p^2_{t,\overline{D}}$ — they all shows signs of an enhancement in the $p^2_{t,D} = p^2_{t,\overline{D}}$ bins. The PYTHIA/JETSET $c\overline{c}$ distributions and the PYTHIA/JETSET $D\overline{D}$ distributions are very similar and resemble the experimental results more so than the NLO $c\overline{c}$ distributions. All of the third bin theoretical distributions are significantly flatter than the experimental third bin distributions. In contrast to the longitudinal distributions, all the $p^2_{t,D}$ are very similar to the respective $p^2_{t,\overline{D}}$ distributions.

In Figure 5.21, we investigate correlations between $\Delta\phi$ and Σp_t^2. For the $\Delta\phi$ dependence, a leading-order perturbative QCD calculation predicts a delta function at $\Delta\phi = 180°$.

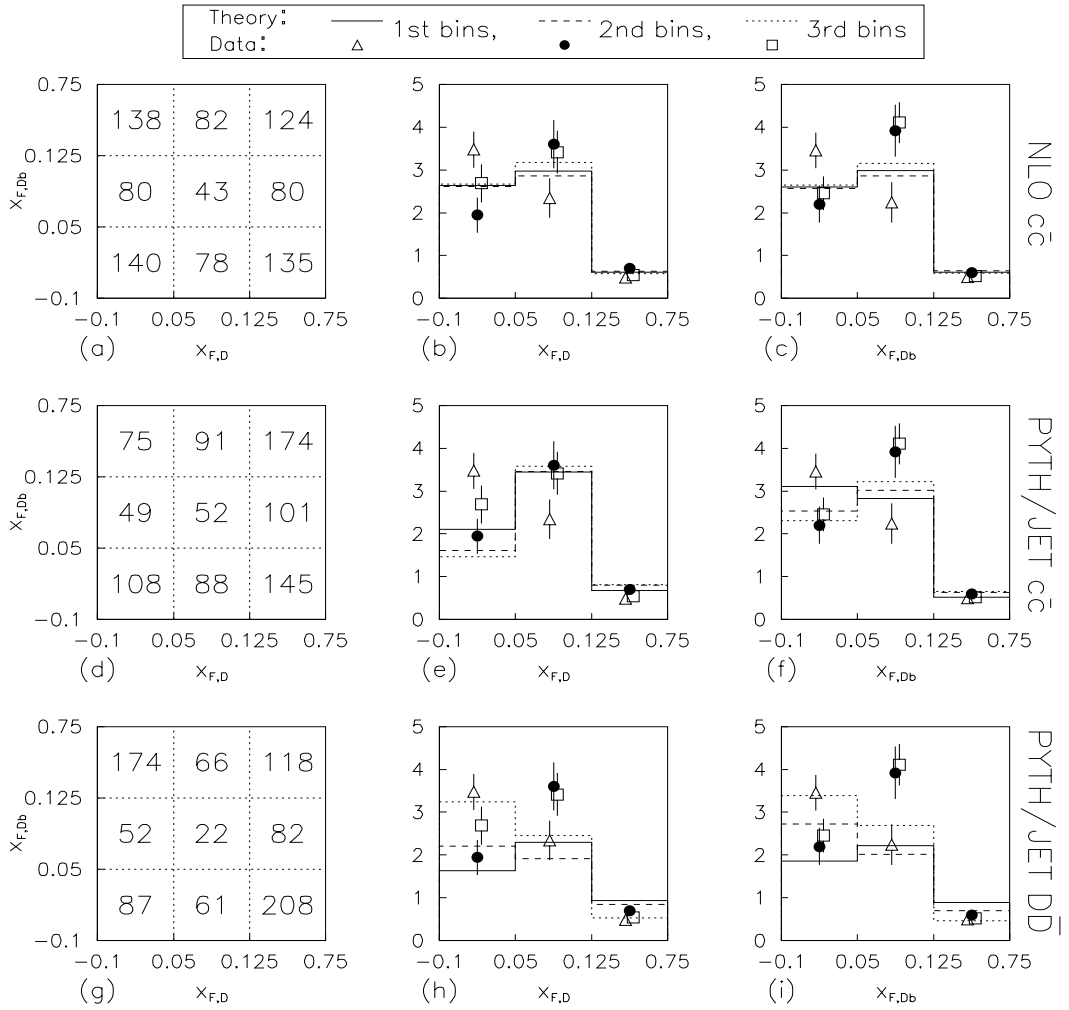

Figure 5.18: (a) The NLO perturbative QCD prediction for the number of $c\overline{c}$ events in 9 ($x_{F,D}$,$x_{F,\overline{D}}$) bins, normalized such that the number of generated NLO events equals the number of acceptance-corrected $D\overline{D}$ signal events. (b) Experimental $x_{F,D}$ distribution for each $x_{F,\overline{D}}$ bin compared to the NLO perturbative QCD predictions. Each $x_{F,D}$ distribution is normalized such that the integral over $x_{F,D}$ equals one. (c) Same as (b) for the $x_{F,\overline{D}}$ distributions. (d)-(f) Same as (a)-(c) for the PYTHIA/JETSET $c\overline{c}$ prediction. (g)-(i) Same as (a)-(c) for the PYTHIA/JETSET $D\overline{D}$ prediction.

We expect the leading-order prediction to be more accurate as the energy scale Q of the partonic hard scattering increases (See Eq. 1.7). That is, we expect the $\Delta\phi$ distribution to be more peaked at 180° for $D\overline{D}$ events with larger Σp_t^2. This behavior is clearly evident in our experimental distributions as well as in all three theoretical predictions. The theoretical $\Delta\phi$ distributions, however, for all three Σp_t^2 bins, are significantly steeper than the

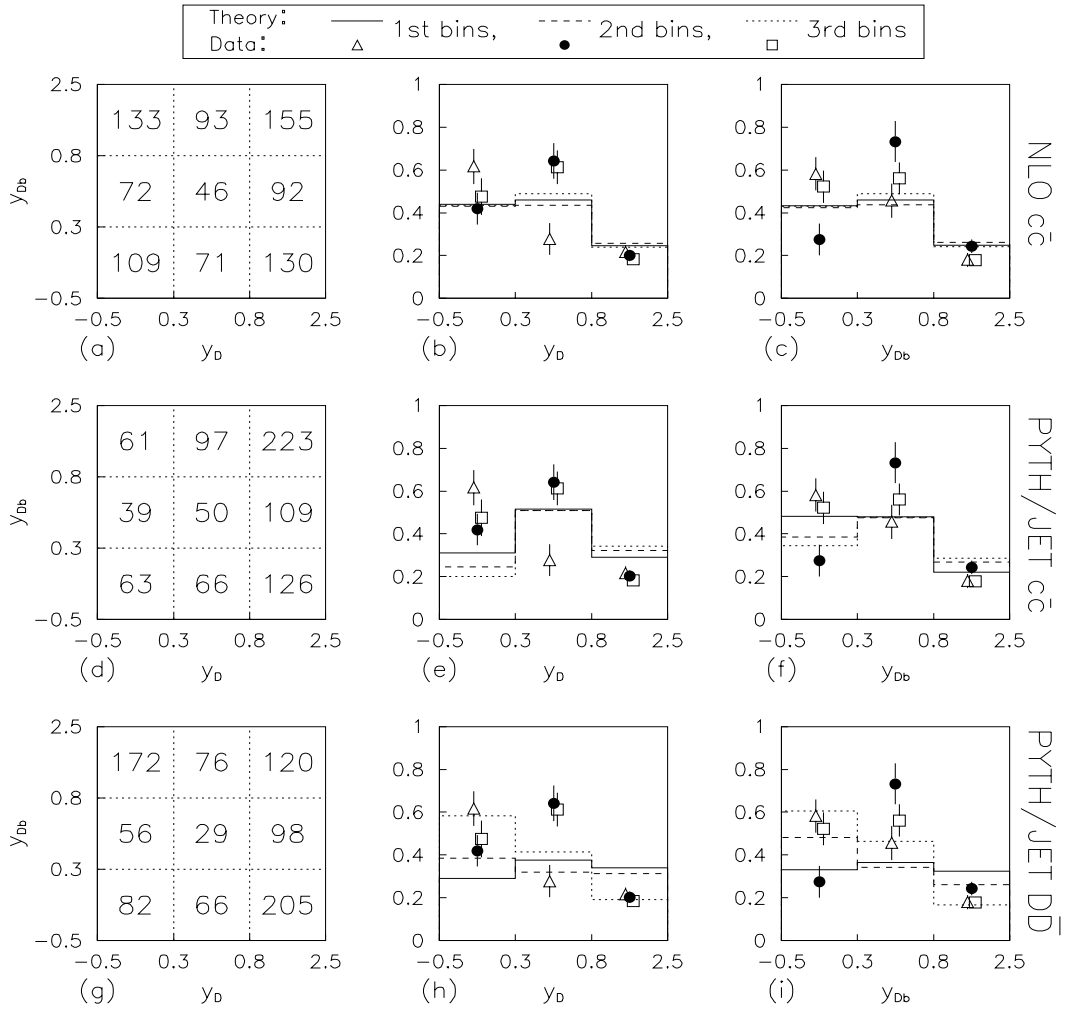

Figure 5.19: (a) The NLO perturbative QCD prediction for the number of $c\overline{c}$ events in 9 (y_D,$y_{\overline{D}}$) bins, normalized such that the number of generated NLO events equals the number of acceptance-corrected $D\overline{D}$ signal events. (b) Experimental y_D distribution for each $y_{\overline{D}}$ bin compared to the NLO perturbative QCD predictions. Each y_D distribution is normalized such that the integral over y_D equals one. (c) Same as (b) for the $y_{\overline{D}}$ distributions. (d)-(f) Same as (a)-(c) for the PYTHIA/JETSET $c\overline{c}$ prediction. (g)-(i) Same as (a)-(c) for the PYTHIA/JETSET $D\overline{D}$ prediction.

respective experimental distributions. The NLO $c\overline{c}$ $\Delta\phi$ distributions are the steepest. The experimental and theoretical Σp_t^2 distributions are in fairly good agreement, with the Σp_t^2 distribution broadening as $\Delta\phi$ increases. In Figure 5.22, we show that $\Delta\phi$ and $|\Delta p_t^2|$ are not significantly correlated in either theory or data.

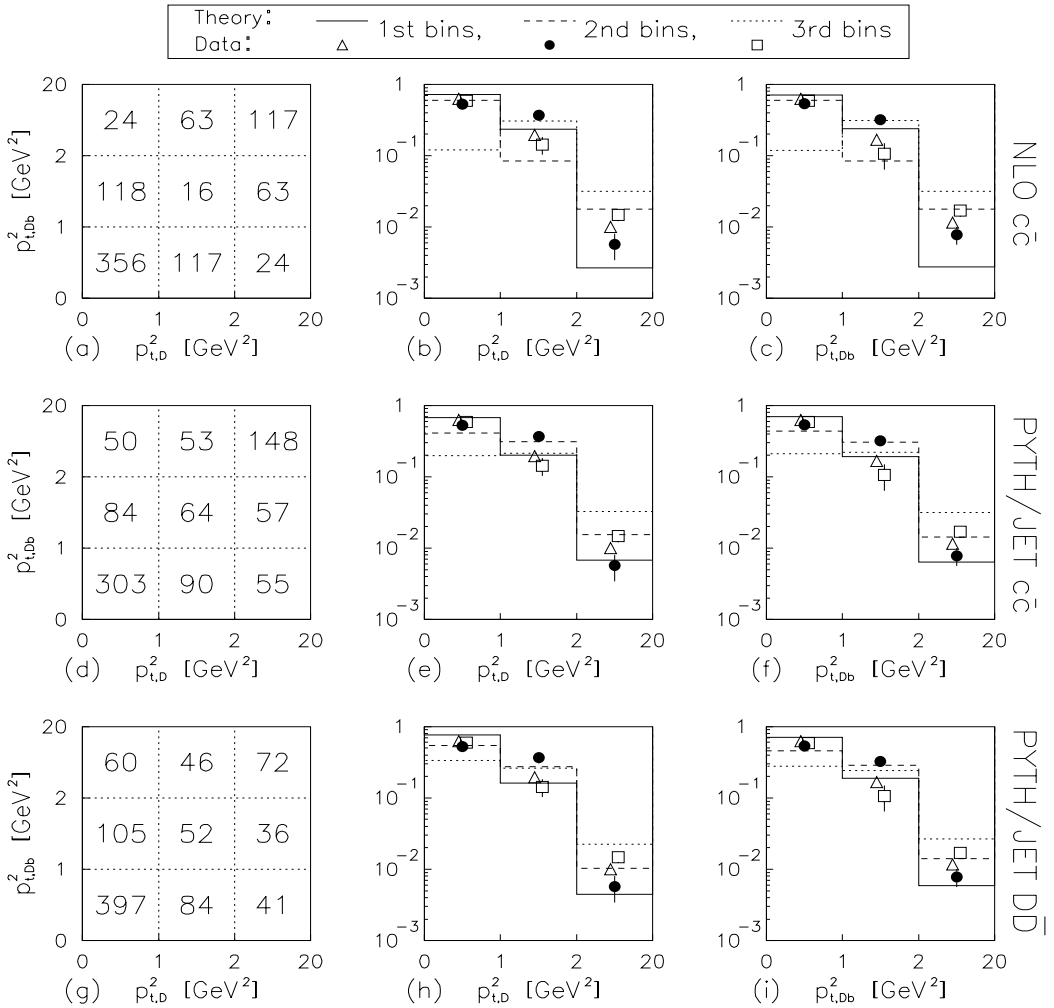

Figure 5.20: (a) The NLO perturbative QCD prediction for the number of $c\overline{c}$ events in 9 ($p^2_{t,D}$,$p^2_{t,\overline{D}}$) bins, normalized such that the number of generated NLO events equals the number of acceptance-corrected $D\overline{D}$ signal events. (b) Experimental $p^2_{t,D}$ distribution for each $p^2_{t,\overline{D}}$ bin compared to the NLO perturbative QCD predictions. Each $p^2_{t,D}$ distribution is normalized such that the integral over $p^2_{t,D}$ equals one. (c) Same as (b) for the $p^2_{t,\overline{D}}$ distributions. (d)-(f) Same as (a)-(c) for the PYTHIA/JETSET $c\overline{c}$ prediction. (g)-(i) Same as (a)-(c) for the PYTHIA/JETSET $D\overline{D}$ prediction.

5.4 Asymmetries Among the Four Types of $D\overline{D}$ Pairs

Yields

In Table 5.2, we compare the experimental yields for each type of $D\overline{D}$ pair to the predictions from the PYTHIA/JETSET event generator. The experimental results are

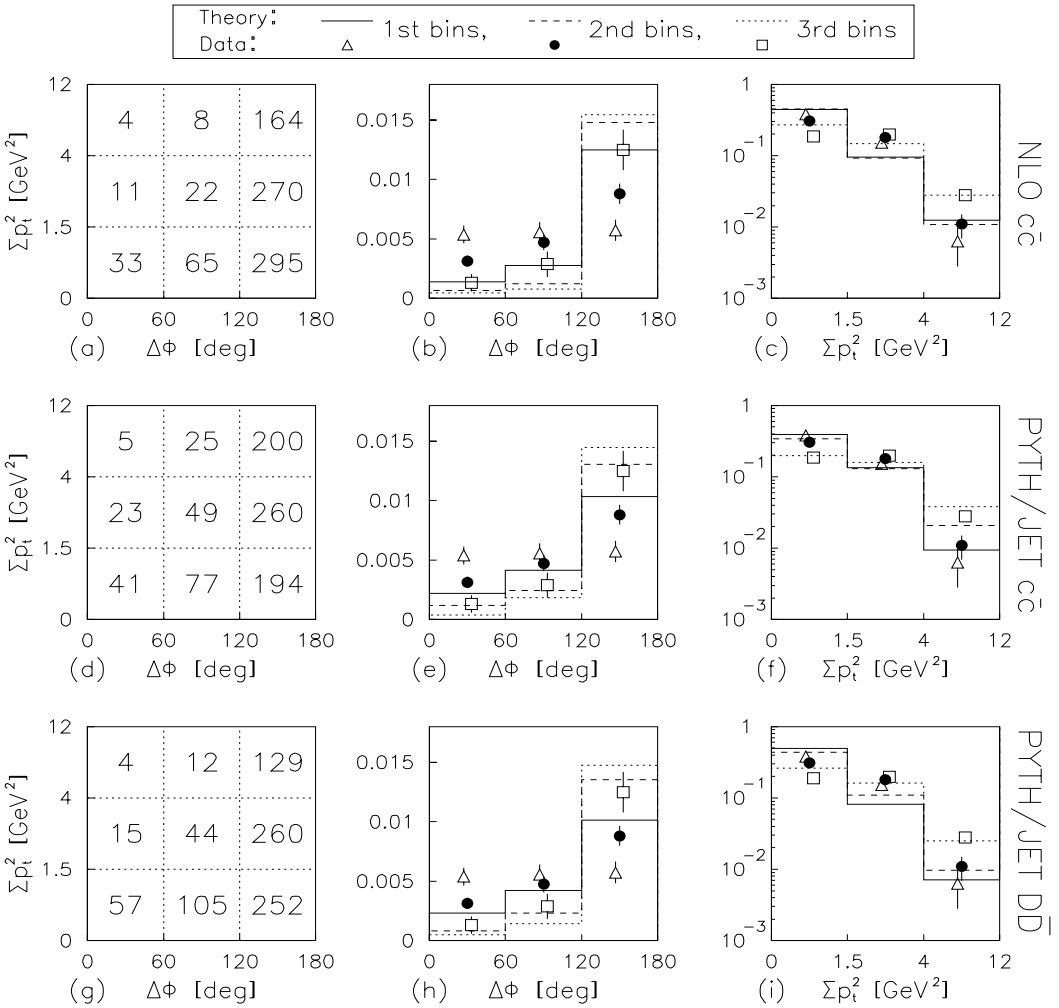

Figure 5.21: (a) The NLO perturbative QCD prediction for the number of $c\overline{c}$ events in 9 ($\Delta\phi$,Σp_t^2) bins, normalized such that the number of generated NLO events equals the number of acceptance-corrected $D\overline{D}$ signal events. (b) Experimental $\Delta\phi$ distribution for each Σp_t^2 bin compared to the NLO perturbative QCD predictions. Each $\Delta\phi$ distribution is normalized such that the integral over $\Delta\phi$ equals one. (c) Same as (b) for the Σp_t^2 distributions. (d)-(f) Same as (a)-(c) for the PYTHIA/JETSET $c\overline{c}$ prediction. (g)-(i) Same as (a)-(c) for the PYTHIA/JETSET $D\overline{D}$ prediction.

obtained by maximizing the weighted likelihood function where the weights account for both acceptance effects and for the relative branching fractions of the reconstructed decay modes (Section 4.2). In this analysis, we do not determine absolute cross sections; hence, for ease of comparison, we normalize the sum of the four yields to one for both theory and data. The experimental results and PYTHIA/JETSET predictions agree on the ordering

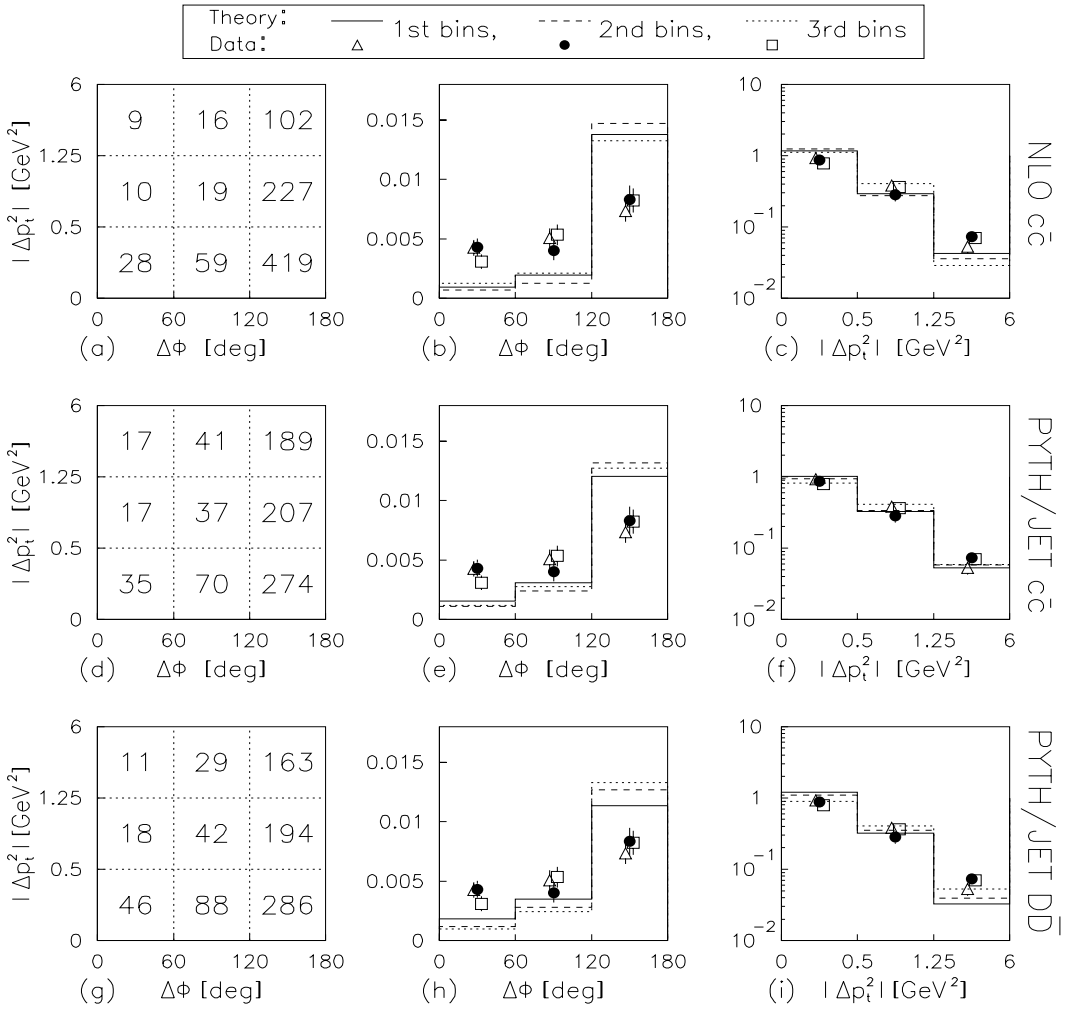

Figure 5.22: (a) The NLO perturbative QCD prediction for the number of $c\overline{c}$ events in 9 ($\Delta\phi$,$|\Delta p_t^2|$) bins, normalized such that the number of generated NLO events equals the number of acceptance-corrected $D\overline{D}$ signal events. (b) Experimental $\Delta\phi$ distribution for each $|\Delta p_t^2|$ bin compared to the NLO perturbative QCD predictions. Each $\Delta\phi$ distribution is normalized such that the integral over $\Delta\phi$ equals one. (c) Same as (b) for the Δp_t^2 distributions. (d)-(f) Same as (a)-(c) for the PYTHIA/JETSET $c\overline{c}$ prediction. (g)-(i) Same as (a)-(c) for the PYTHIA/JETSET $D\overline{D}$ prediction.

of the relative rates — with the greatest production rate for $D^0\overline{D^0}$ pairs and the lowest for D^+D^- pairs. The PYTHIA/JETSET event generator, however, predicts a significantly smaller D^+D^- production rate than is found in data, and a larger $D^0\overline{D^0}$ rate.

At fixed-target energies, the PYTHIA/JETSET event generator assumes that the contribution to the $D\overline{D}$ cross section from the decays of B mesons or from the decays

Table 5.2: Experimental yields for the four types of $D\overline{D}$ pairs compared to predictions from the PYTHIA/JETSET event generator. Both experimental and theoretical yields are obtained after excluding any candidates in which the center-of-mass rapidity of either the D or $\overline{D}$ is less than -0.5 or greater than 2.5.

			Normalized	
	Data	PYTH/JET	Data	PYTH/JET
$D^0\overline{D^0}$	460 ± 34	58086	0.50 ± 0.04	0.581 ± 0.002
D^0D^-	185 ± 19	22012	0.20 ± 0.02	0.220 ± 0.001
$D^+\overline{D^0}$	160 ± 19	14250	0.18 ± 0.02	0.1425 ± 0.001
D^+D^-	106 ± 16	5652	0.12 ± 0.02	0.0565 ± 0.001
Totals	911	100,000	1.00	1.00

of hyper-excited D meson states (*i.e.*, D mesons more massive than $D^*(2010\ \mathrm{MeV})^{\pm}$) is negligible. As discussed in Section 1.1.4, if this assumption is correct, then the relative yields for the four types of $D\overline{D}$ pairs can be parameterized using the following variables:

- The fraction f_e of primary D mesons that are excited D mesons, where "primary" means produced directly in the fragmentation process, rather than via a decay such as $D^{*+} \rightarrow D^0 + \pi^+$.

- The fraction f_n of excited charged D mesons that decay to neutral D mesons. Kinematically, excited neutral D mesons cannot decay to charged D mesons.

- The relative probabilities for producing each of the four types of primary charm pairs — P_{nn}, P_{nc}, P_{cn}, and P_{cc} — where, for example, P_{nc} is the probability for producing a neutral primary charm meson and a charged primary anti-charm meson; and $P_{nn} + P_{nc} + P_{cn} + P_{cc} = 1$. As discussed in Chapter 1, if coalescence does not occur at any significant level, then $P_{nn} = P_{nc} = P_{cn} = P_{cc} = 0.25$.

The measured relative yields are related to these parameters as follows:

$$\begin{aligned}
P_{D^0\overline{D^0}} &= P_{nn} + f_e f_n (P_{nc} + P_{cn}) + (f_e f_n)^2 P_{cc}, \\
P_{D^0D^-} &= (1 - f_e f_n) P_{nc} + (1 - f_e f_n)(f_e f_n) P_{cc}, \\
P_{D^+\overline{D^0}} &= (1 - f_e f_n) P_{cn} + (1 - f_e f_n)(f_e f_n) P_{cc}, \\
P_{D^+D^-} &= (1 - f_e f_n)^2 P_{cc},
\end{aligned}$$

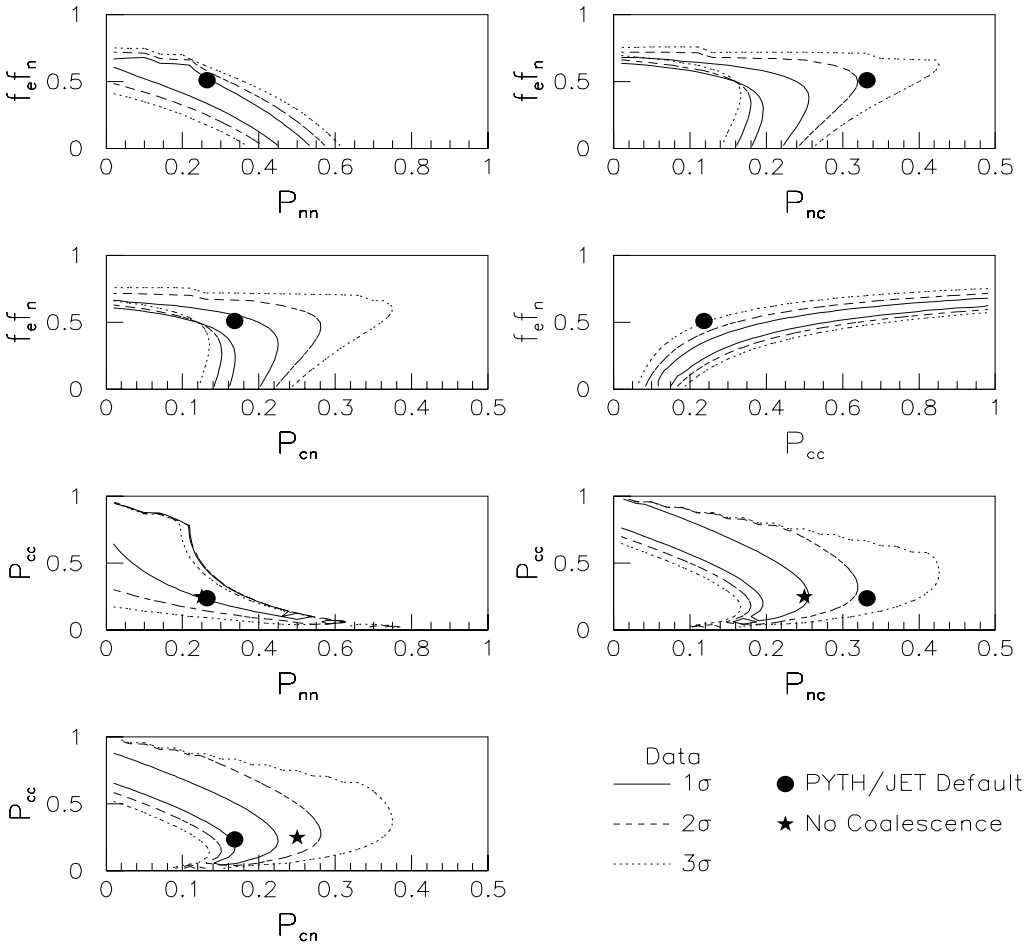

Figure 5.23: Several 2-dimensional projections onto the (P_{nn}, P_{nc}, P_{cn}, P_{cc}, f) parameter space, showing the regions that are one (solid line), two (dashed), and three (dotted) standard deviations from our experimental results. The default PYTHIA/JETSET prediction and the no-coalescence prediction are also shown.

where $P_{D^0\overline{D^0}} + P_{D^0D^-} + P_{D^+\overline{D^0}} + P_{D^+D^-} = 1$. Because the variables f_e and f_n always appear as a product, the relative yields can only provide information about $f \equiv f_e f_n$. Given four independent parameters and only three independent measurements, we cannot use the measured yields to obtain a unique prediction for P_{nn}, P_{nc}, P_{cn}, P_{cc}, and f. We can, however, determine which regions of parameter space are consistent with our experimental measurements.

In Figure 5.23, for several 2-dimensional projections onto this five dimensional parameter space, we show the regions that are within one (solid line), two (dashed), and three (dotted) standard deviations from our experimental results. In each plot, we also mark where the default PYTHIA/JETSET prediction lies and where the no-coalescence

prediction ($P_{nn} = P_{nc} = P_{cn} = P_{cc} = 0.25$) lies. In the ($P_{cn}$, f), (P_{cc}, f), and (P_{cn}, P_{cc}) projections the PYTHIA/JETSET prediction is more than two standard deviations away from the experimental results, possibly indicating that the default PYTHIA/JETSET settings for f and P_{cn} are somewhat too large, and that the setting for P_{cc} is somewhat too small. The no-coalescence prediction is within approximately 1.5 standard deviations from our experimental results. If the PYTHIA/JETSET assumption $f_e f_n = 0.785 \times 0.651 = 0.511$ is correct, then the data suggest that the probability that both primary charmed mesons are charged, P_{cc}, is larger than the other three probabilities. This would be difficult to explain in terms of a simple coalescence model, in which the probability P_{cn} should be the largest because both the primary neutral D meson ($c\overline{u}$) and the primary charged $\overline{D}$ meson ($\overline{c}d$) can originate from coalescence with a π^- valence quark.

Correlations Between the D and $\overline{D}$ Longitudinal Momenta

As shown in Figure 5.24, in the PYTHIA/JETSET hadronization scheme, the correlation between y_D and $y_{\overline{D}}$ is quite different for each of the four types of $D\overline{D}$ pairs. In Figure 5.25, we investigate whether this is also true for data. Given the limited statistics of our data sample, we can only search for gross asymmetries in the (y_D, $y_{\overline{D}}$) distribution. We obtain the four plots in Figure 5.25 by bisecting the 2-dimensional (y_D, $y_{\overline{D}}$) distribution along the following four lines, respectively ($v = a$): $\Delta y = 0$, $\Sigma y = 1.2$, $y_D = 0.6$, and $y_{\overline{D}} = 0.6$. These four lines are indicated by dashed lines in Figure 5.24.

To search for possible asymmetries, we determine whether the fraction of signal events on one side of a given line depends on the type of $D\overline{D}$ pair. Specifically, for both theory and data we show

$$A_v(i) = \frac{N_i(v > a) - N_i(v < a)}{N_i(v < a) + N_i(v < a)} \tag{5.5}$$

where $i = (D^0\overline{D^0}, D^0D^-, D^+\overline{D^0}, D^+D^-)$ and N_i is the number of signal $D\overline{D}$ events of type i. The PYTHIA/JETSET $A_{\Sigma y}$ distribution is fairly flat, indicating no significant asymmetries among the four $D\overline{D}$ types for the Σy distribution. The PYTHIA/JETSET $A_{\Delta y}$, A_{y_D}, and $A_{y_{\overline{D}}}$ distributions, however, indicate significant asymmetries, all of which are easily interpreted in terms of the PYTHIA/JETSET coalescence mechanism discussed in Chapter 1. Unfortunately, the degree of asymmetry in the PYTHIA/JETSET predictions is of the same order as our experimental errors. The experimental A_{y_D} distribution, for

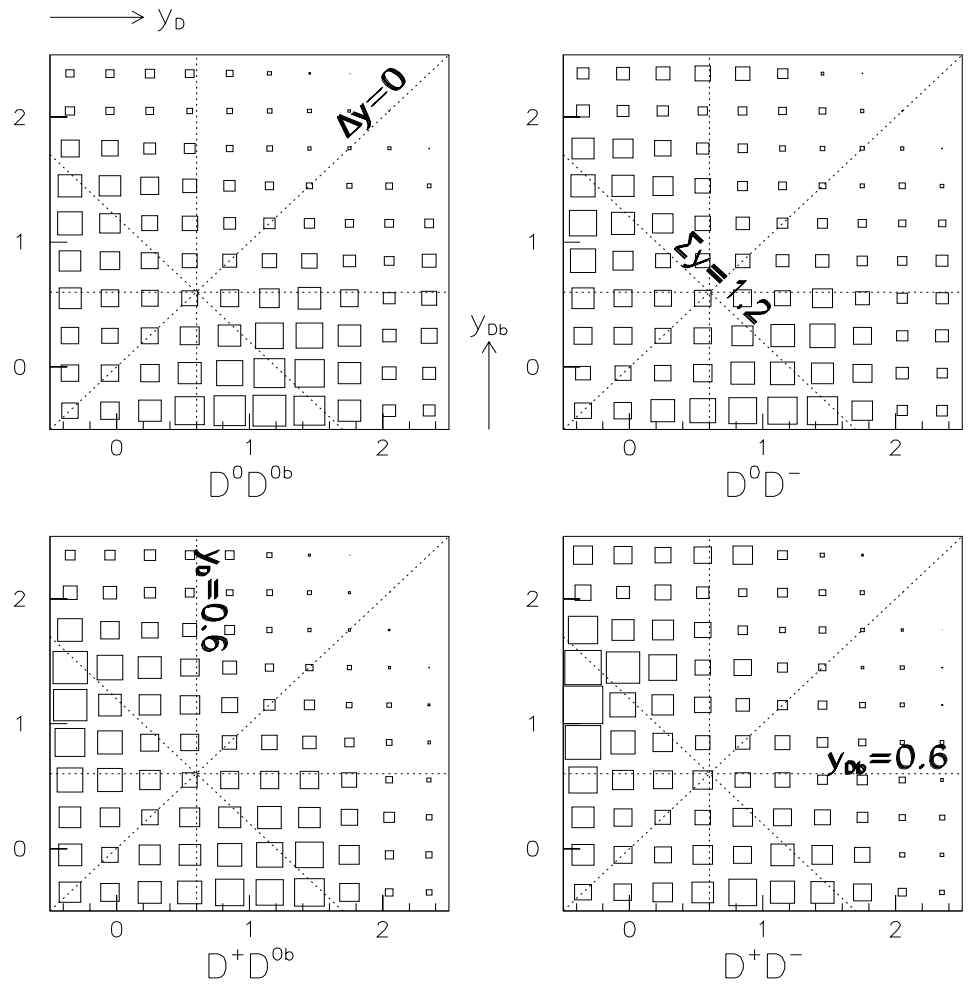

Figure 5.24: PYTHIA/JETSET prediction for the $(y_D, y_{\overline{D}})$ distribution for each of the four types of $D\overline{D}$ pairs. The dashed lines help define the asymmetry functions $A_v(i)$ (Eq. 5.5) which are shown, for both theory and data, in Fig. 5.25.

example, is consistent with the PYTHIA/JETSET prediction, but it is also consistent with being flat. Similarly, the experimental $A_{\Sigma y}$ distribution is fairly consistent with the flat PYTHIA/JETSET prediction, but it also shows some indication of an asymmetry between $D^0\overline{D^0}$ and D^+D^-. The most significant difference between the experimental results and the PYTHIA/JETSET predictions occurs for the $D\overline{D}$ types $D^0\overline{D^0}$ and D^+D^- in the $A_{y_{\overline{D}}}$ distribution. Both theory and data indicate an asymmetry between $D^0\overline{D^0}$ and D^+D^-; but the experimental result finds $A_{y_{\overline{D}}}(D^0\overline{D^0}) > A_{y_{\overline{D}}}(D^+D^-)$, whereas, the PYTHIA/JETSET model finds $A_{y_{\overline{D}}}(D^+D^-) > A_{y_{\overline{D}}}(D^0\overline{D^0})$.

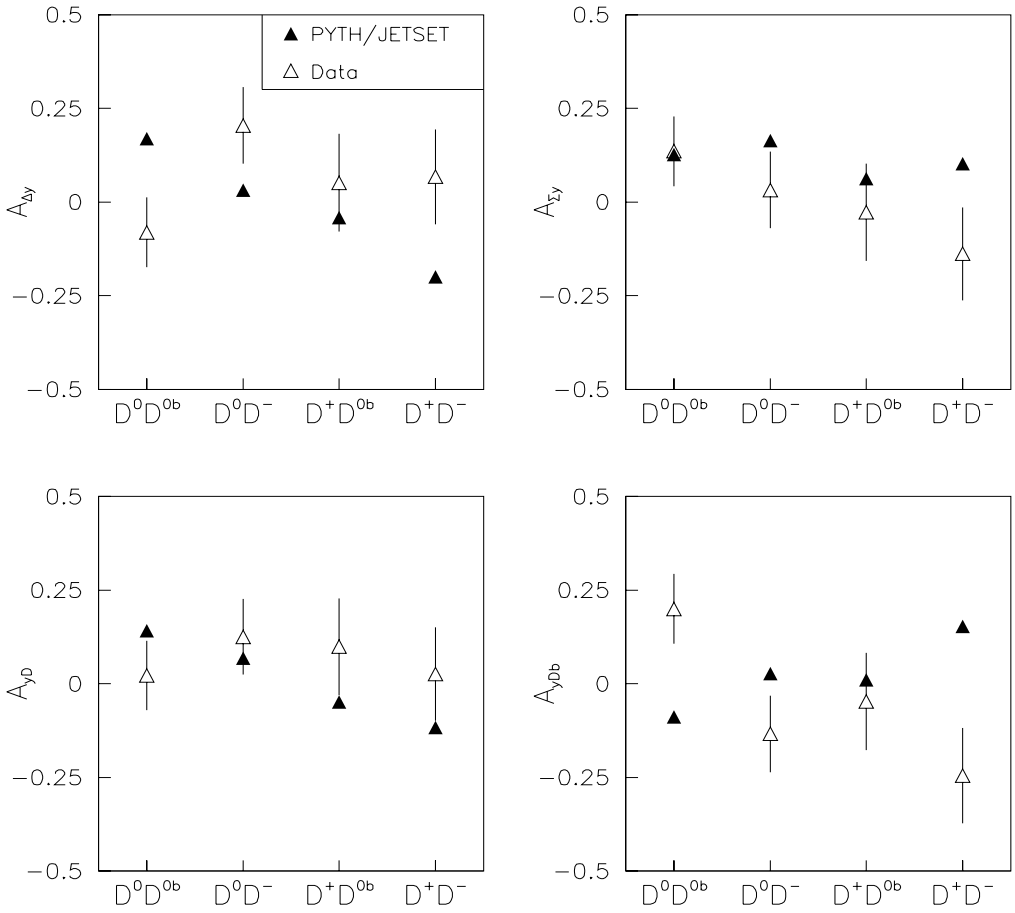

Figure 5.25: The asymmetry function $A_v(i) = \frac{N_i(v>a)-N_i(v<a)}{N_i(v<a)+N_i(v<a)}$, where i =($D^0\overline{D^0}$, D^0D^-, $D^+\overline{D^0}$,D^+D^-) and N_i is the number of signal $D\overline{D}$ events of type i, for $(v,\ a)$ = (Δy, 0), (Σy, 1.2), (y_D, 0.6), and ($y_{\overline{D}}$, 0.6). All functions are obtained after excluding any PYTHIA/JETSET $D\overline{D}$ events and $D\overline{D}$ candidates from data in which the center-of-mass rapidity of either the D or $\overline{D}$ is less than -0.5 or greater than 2.5.

5.5 Conclusions

In this analysis, we fully reconstructed 791 ± 44 $D\overline{D}$ events, the largest sample of charm-pair events collected to date. We thoroughly investigated the degree of correlation between the D and $\overline{D}$ momenta. We also compared the measured charm-pair distributions to predictions from the fully differential next-to-leading calculation as well as to prediction from the PYTHIA/JETSET Monte Carlo event generator.

Longitudinal Correlations

Our measurements indicate that the longitudinal momenta of the D and $\overline{D}$ from charm-pair events are slightly correlated. The measured Δx_F and Δy distributions (Figs. 5.2-5.3) are somewhat narrower than the single-charm predictions; and the $x_{F,D}$ (y_D) distribution depends slightly on the value of $x_{F,\overline{D}}$ ($y_{\overline{D}}$), and vice-versa (Figs. 5.7-5.8).

The single-charm x_F and y distributions from all three sets of theoretical predictions (Figs. 5.11) do not agree with each other nor with the measured distributions. In addition, all three sets have different predictions for the correlation between the charm and anti-charm longitudinal momenta (Figs. 5.18-5.19). The next-to-leading order calculation predicts no significant correlation; the PYTHIA/JETSET $c\overline{c}$ prediction indicates a slight positive correlation; and the PYTHIA/JETSET $D\overline{D}$ prediction indicates a strong negative correlation. The data agrees best with the PYTHIA/JETSET $c\overline{c}$ prediction. The measured longitudinal distributions suggest that the string topology scheme of the PYTHIA/JETSET hadroproduction hadronization model — which color-connects the charm quark to a valence quark from one the colliding hadrons and the anti-charm quark to a valence quark from the other colliding hadron — is incorrect.

Transverse Correlations

Our measurements indicate that the transverse momenta of the D and $\overline{D}$ from charm-pair events are correlated in several ways. The square of the amplitudes of the D and $\overline{D}$ transverse momenta are slightly correlated (Fig 5.9). The directions of the D and $\overline{D}$ in the plane transverse to the beam axis are significantly correlated (Fig. 5.5), which has been observed by several experiments[3, 4, 6, 7, 8]. Lastly, we find that the separation in azimuthal angle $\Delta\phi$ is significantly correlated to the sum of the squares of the D and $\overline{D}$ transverse momenta Σp_t^2 (Fig. 5.10). Although all three sets of theoretical predictions show the same correlation trends as we find in data, none are consistent with the experimental results. The theories predict that the transverse momenta of the D and $\overline{D}$ are significantly more correlated than we find in data, indicating that the theories do not include enough higher-order effects.

Bibliography

[1] Mangano, M., P. Nason and G. Ridolfi, 1992, Nucl. Phys. **B373**, 295.

[2] Aguilar-Benitez, M., *et al.*, (NA27 Collaboration), 1985, Phys. Lett. **B164**, 405.

[3] Aguilar-Benitez, M., *et al.*, (NA27 Collaboration), 1988, Z. Phys. **C40**, 321.

[4] Aoki, S., *et al.*, (WA75 Collaboration), 1988, Phys. Lett. **B209**, 113.

[5] Barlag, S., *et al.*, (NA32 Collaboration), 1991, Phys. Lett. **B257**, 519.

[6] Barlag, S., *et al.*(NA32 Collaboration), 1993, Phys. Lett. **B302**, 112.

[7] Kodama, K., *et al.*, (E653 Collaboration), 1991, Phys. Lett. **B263**, 579.

[8] Adamovich, M., *et al.*, (WA92 Collaboration), 1995, Phys. Lett. **B256**, 256.

[9] Mangano, M., P. Nason and G. Ridolfi, 1993, Nucl. Phys. **B405**, 507.

[10] Sjöstrand, T., *PYTHIA 5.6 and JETSET 7.3: Physics and Manual*, CERN preprint CERN-TH.6488/92.

[11] Frixione, S., M.L. Mangano, P. Nason, and G. Ridolfi, 1994, Nucl. Phys. **B431**, 453.

[12] Erhan, S., *et al.*, (UCLA-Saclay Collaboration), 1979, Phys. Lett. **B85**, 447.

[13] Basile, M., *et al.*, (CERN-Bologna-Frascati Collaboration), 1984, Lett. Nuovo Cimento **30**, 487.

[14] Ritchie, J.L., *et al.*, (E595 Collaboration), 1984, Phys. Lett. **B138**, 213.

[15] Adamovich, M., *et al.*, (WA82 Collaboration), 1993, Phys. Lett. **B402**, 402.

[16] Alves, G.A., *et al.*, (E769 Collaboration), 1994, Phys. Rev. Lett. **72**, 812.

[17] Aitala, E.M., *et al.*(E791 Collaboration), 1996, to be published.

[18] Vogt, R. and S.J. Brodsky, 1995, Nucl. Phys. **B438**, 438.

[19] Bortoletto, D., *et al.*, 1988, Phys. Rev. **D37**, 1719.

[20] Albrecht, H., *et al.*, 1991, Z. Phys. **C52**, 353.

[21] Gay, C.W., 1991, PhD Dissertation, Univ. Toronto, Toronto, Canada, unpublished.

[22] Plothow-Besch, H., 1994, CERN Program Library Pool, PDFLIB, W5051.

[23] Sutton, P.J., A.D. Martin, R.G. Roberts, and W.J. Stirling, 1992, Phys. Rev. **D45**, 2349.

[24] Harriman, P.N., A.D. Martin, R.G. Roberts and W.J. Stirling, 1990, Phys. Rev. **D42**, 798.

[25] Gluck, M., E. Reya, and A. Vogt, 1992, Z. Phys. **C53**, 651.

[26] Gluck, M., E. Reya, and A. Vogt, 1992, Z. Phys. **C53**, 127.

[27] Harriman, P.N., A.D. Martin, R.G. Roberts and W.J. Stirling, 1990, unpublished.

[28] Aurenche, P., *et al.*, 1989, Phys. Lett. **B233**, 517.

[29] Owens, J.F., 1984, Phys. Rev. **D30**, 943.

[30] Botts, J., *et al.*(CTEQ Collaboration), 1993, Phys. Lett. **B304**, 159.

[31] Martin, A.D., W.J. Stirling and R.G. Roberts, 1991, Phys. Lett. **B266**, 173.

[32] Sjostrand, T. (private communication).

[33] Anjos, J.C., *et al.*, 1988, *P791: Continued Study of Heavy Flavors at TPL*, A Proposal to Fermi National Accelerator Laboratory.

[34] Ellis, R.K. and C. Quigg, 1987, FERMILAB-FN-445.

[35] Appel, J.A., P.M. Mantsch, M.E. Streetman, and R.M. Robertson, 1986,

[36] Gagnon, P., 1993, PhD Dissertation, Univ. of California, Santa Cruz, CA, USA. Nucl. Instr. and Meth. **A243**, 361.

[37] Amato, S., *et al.*, 1992, Nucl. Instr. Meth. A **324**, 535.

[38] Exabyte Corp., 1745 38th Street, Boulder, CO 80301, USA.

[39] Breiman, L., J. Friedman, R. Olshen, and C. Stone, 1984, *Classification and Regression Trees* (Chapman & Hall, Great Britain).

[40] Particle Data Group, Review of Particle Properties, 1994, Phys. Rev. D **50**, 1173.

[41] Frodesen, A.G., O. Skjeggestad, and H. Tofte, 1979, *Probability and Statistics in Particle Physics* (Universitetsforlaget, Norway).

[42] CERN Applications Software Group, 1992, CERN Program Library Pool, MINUIT Reference Manual, D506.